mpipks

Many-Body Floquet Engineering
in Periodically Driven Optical Lattices

Dissertation

zur Erlangung des akademischen Grades

Doctor rerum naturalium
(Dr. rer. nat.)

vorgelegt

der Fakultät Mathematik und Naturwissenschaften
der Technischen Universität Dresden

von

M.Sc. Christoph Sträter

geboren am 30.05.1986 in Bochum

Dresden, 2017

To my parents and my mentors

Zusammenfassung

Die vorliegende Arbeit behandelt Quantensimulationen von stark wechselwirkenden Systemen ultrakalter Atome in optischen Gittern. Dabei fokussiert sich diese theoretische Arbeit auf die Möglichkeit, diese Systeme mit Hilfe eines hochfrequenten Antriebs kohärent zu kontrollieren. Diese Form des Quantenengineering nennt man Floquet-Engineering. Experimentell wurden mit Hilfe eines zeitperiodischen Antriebs des optischen Gitters bereits viele physikalische Phänomene und Modelle realisiert, insbesondere im Bereich geringer Wechselwirkungen. Hier beschreiben wir zwei neue Vorschläge für interessante Phänomene im Bereich starker Wechselwirkungen, welche durch zeitperiodisches Gitterschütteln ermöglicht werden: Das Schmelzen eines Mott-Isolators in einen angeregte superfluiden Zustand durch kohärentes Koppeln von Bloch-Bändern, sowie die Erzeugung von eindimensionalen Gitter-Anyonen. Außerdem wird die Rolle von Multiphoton-Übergängen in angetriebenen Gittern untersucht, da diese Prozesse zu ungewolltem Heizen und damit zur Verhinderung von erfolgreichem Floquet-Engineering führen können.

Das einleitende Kapitel 1 gibt einen Überblick über das Feld der Quantensimulationen mit ultrakalten Atomen und beschreibt den experimentellen Fortschritt der letzten Jahre auf diesem Gebiet. In Kapitel 2 wird die Floquet-Theorie eingeführt, die einen exzellenten Rahmen dafür bietet zeitperiodische Hamiltonians zu behandeln und die Grundlage für die folgenden Kapitel ist. Kapitel 3 stellt den Vorschlag vor, Bloch-Bänder in optischen Gittern durch das Schütteln des Gitters kohärent miteinander zu koppeln. Insbesondere wird im Detail gezeigt, wie dieses Bandkoppeln zu einem orbital getriebenen Phasenübergang von einem Mott-Isolator zu einem Suprafluid führen kann. In Kapitel 4 wird der Vorschlag erläutert, wie eindimensionale Anyonen durch stark wechselwirkende Bosonen erzeugt werden können, indem das Gitter gekippt und geschüttelt wird. Außerdem wird vorgeschlagen, Friedel-Oszillationen im Ortsraum als im Experiment messbare Signatur für die Anyonisierung zu nutzen. Schließlich werden in Kapitel 5 Multiphoton-Übergänge in höhere Bloch-Bänder untersucht, im Falle eines geschüttelten und eines Amlitudenmodulierten Gitters. Die Stärke und die Lage der Resonanzen, welche zu Heizen führen, werden hierbei theoretisch und numerisch beschrieben.

Abstract

The present thesis is devoted to quantum simulation of strongly interacting systems of ultra-cold atoms in optical lattices. It is a theoretical work which focuses on the possibility to employ strong time-periodic forcing for the coherent control of these system. This form of quantum engineering is called Floquet engineering. Experimentally, time-periodic forcing has been successfully applied to realize a variety of physical models and phenomena, especially in the regime of weak interactions. We describe two novel proposals for interesting phenomena in the regime of strong interactions that rely on lattice shaking: melting of a Mott-insulator into an excited-state superfluid via coherent coupling of Bloch bands and the creation of 1D lattice anyons. Furthermore, the role of multiphoton excitations in a driven lattice is analyzed since these processes can lead to unwanted heating and thereby impeding of successful Floquet engineering in the experiment.

The introductory Chapter 1 gives an overview over the field of quantum simulations with ultra-cold atoms in optical lattices and describes the experimental progress that has been made in the recent years. In Chapter 2, Floquet theory is reviewed, which provides an excellent framework to deal with time-periodic Hamiltonians and which is the basis of the analysis presented in the following chapters. Chapter 3 deals with the proposal of coherently coupling Bloch bands of an optical lattice via resonant lattice shaking. In particular, the orbital-driven phase transition from a Mott insulating to a superfluid ground state is described in detail. In Chapter 4, a proposal of realizing 1D lattice anyons from strongly interacting bosons in a shaken and tilted lattice is worked out. Furthermore, Friedel oscillations are proposed to provide a measurable real-space signature for the anyonization. Finally, in Chapter 5 multiphoton excitations to higher Bloch bands are analyzed for the cases of a shaken and an amplitude-modulated lattice. The strength and the location of resonances, which are associated with heating, are described theoretically and numerically.

Contents

Contents

1. Introduction

The title of this work is "Many-Body Floquet Engineering in Periodically Driven Optical Lattices". About each of these key words one can fill entire books and this has aleady been done. However, the composition of these words and the underlying physics is a new and very specific issue and needs to be discussed. The purpose of this introduction is to explain the title, the background, and the purpose of this work. Moreover, the reader is invited to embrace the fascination for the mentioned quantum experiments, which has captured the author and many scientists before him and which has thereby driven their efforts.

1.1. Experiments with Ultra-Cold Atoms - A Quantum Playground

For many years after its discovery, quantum physics has been a primarily theoretical construct. Performing a "standard" experiment - characterized by preparation, execution and read-out - in a quantum system, is generally limited by the short time- and high energy scales that we encounter therein. Especially many-body quantum experiments, i.e. those where the collective behavior of a lot of quantum particles is investigated, has been a special challenge. This is because it is very hard to cool down an atomic gas into the quantum degenerate regime and to control it therein. With the advances in the field of quantum optics and the fabrication of the first Bose-Einstein condensates in 1995 [1–3], predicted Einstein more than 70 years earlier [4, 5], physicists created a quantum matter that could be used as a "quantum playground" for single-, few- and many-body experiments [6].
In this class of experiments, isolated neutral atoms are trapped with the help of

electromagnetic fields and cooled down to the regime of nanokelvin. Consequently, the 10^3 to 10^8 atoms occupy a very limited number of low-energy quantum states. These atomic gases are very dilute such that their interactions are rather weak and, moreover, can simply be described by contact interaction. The systems have energy scales in the lower kilohertz regime, which makes them easily addressable. Their intrinsic time evolution happens on the order of milliseconds, which is slow enough to allow the study of the gases out of equilibrium. At the same time, the coherence of the atomic cloud could last up to seconds. For a large class of experiments, this provides enough time for the preparation and execution process. The length scales in cold-atom experiments are in the order of micrometer, such that the atoms can be accurately addressed and their states easily read out. The experimentalists can control the atoms via lasers, whose amplitude, frequency and phase can be tuned with extremely high precision and speed. Furthermore, because of their collective occupation of states and because ultra-cold atom experiments can be repeated automatically hundreds of times in a row, the state of the system can often be read out with high accuracy. Altogether, quantum experiments with ultra-cold atoms are very clean, tunable and measurable. This makes the quantum playground very lively.

Cold-atom experiments are especially interesting as they serve as analog quantum simulators for text-book models [7]. By this we mean that quantum systems realized in a cold atom experiment are described by simple models, with which a broad class of physical phenomena can be explained. Whereas such a model might be difficult to simulate on a classical computer, its dynamics or its static properties can thus be simulated in a cold-atom experiment, at least with satisfactory accuracy. By this, the quantum simulator can help to confirm or to improve our theoretical understanding of quantum physics. This is especially helpful if a system consists of many interacting quantum particles implying a huge number of degrees of freedom [8]. Then, the large size of the Hilbert space and the quick entanglement between the particles makes it often impossible to solve the Schrödinger equation by any means. In many of these situations, the quantum simulator is a unique tool to address unsolved problems in physics, without any classical counterpart. Prominent examples of physical problems where quantum simulators with ultra-cold atoms are believed to find solutions, are many-body localization [9] and the BEC-BCS

crossover [10].

A striking tool for a quantum simulation is an optical lattice. Here, equally colored lasers from different angles form standing waves[1]. If additionally the frequency of the lasers is slightly detuned to an allowed transition in the electron shell of the atoms, the particles see, via the AC stark shift, the intensity of the standing laser waves as a periodic potential. The atoms, attracted e.g. by the minima of the lattice potential, can be compared to electrons moving in a crystalline structure of ions. Hence, ulta-cold atoms in optical lattices can be used to simulate defect-free solids [8]. This analogy is astonishing. The nature of the attraction of the neutral atoms to the lattice minima, or of the electrons to the ions, is very different. Likewise, the lattice constant differs by a factor of around 10^3 and the mass of the particles by a factor of 10^5. Nevertheless, basic phenomena, for example the transition between insulating and conducting phases, are in both cases described by the celebtrated Hubbard model [11], which can be addressed by quantum simulations. Hence, ultra-cold atoms in optical lattice can be used to answer questions in solid state physics and material sciences.

Another important area where tunable many-body quantum systems, like those of ultra-cold atoms in laser fields, have a great potential, are quantum devices. By this we mean applications of quantum mechanics outside of science. A famous but rather long-term goal in this category is the realization of a scalable quantum computer. Trapping atoms and encoding qubits in a clever and stable way in this system, a quantum computer could be used to perform quantum algorithms. A quantum algorithm is an algorithm whose execution on a quantum computer scales only polynomially with the system size and which would require exponentially more ressources (e.g. time, number of gates) on a classical machine. Important quantum algorithms are Shor's algorithm to factorize any composite number [12] and Grover's algorithm to search for a single entry in a database [13]. Other important quantum devices with cold-atom systems include high-precision measurement devices, like for example gravimeters [14] and clocks [15].

---

[1]This includes laser beams that are reflected by mirrors to overlap with themselves.

1.2. Milestones in the Field

The popularity and broad applicability of cold-atom experiments of today were enabled by an impressive experimental and theoretical progress in the last twenty years. Consecutive cooling mechanisms, namely Doppler, Sysiphus and evaporative cooling, allow to reach temperatures of only a few nanokelvin [16]. By this, ultra-cold quantum gases with e.g. isotopes of Li, Na, K, Cr, Rb, Cs, Yb have been achieved, each coming with its own set of opportunities and challenges. While the present work focuses on the case where the atoms are bosons, fermi gases have attracted a similar level of interest [17]. There are also experiments comprising both species, the so called Bose-Fermi mixtures [18, 19]. While typical quantum gas experiments are performed with thousands to millions of atoms, such that their collective behaviour becomes macroscopic and well measurable, a quantum microscope provides a complementary approach [20]. Here, atoms are prepared and addressed individually with high-resolution optical imaging systems, allowing for the analysis of quantum materials on small scales.

A number of tools have been developed to read out the quantum mechanical state of the ultra-cold atoms with high precision. The spatial density of the atomic cloud can be measured via fluorescence imaging or via absorption imaging. In an optical lattice, this method allows already single-site and single-atom resolution [21]. On the other hand, the momentum of the atoms can be measured by time-of-flight expansion. Thereby, all potentials and lasers are suddenly switched off, such that the atoms freely fall under the force of gravitation. After sufficient time of flight, the density of the atoms, which can be measured by absorption imaging, reflects the momentum (i.e. velocity) distribution of their initial state.

When it comes to the investigated physics in the field, in the first years the focus laid mainly on the weakly interacting regime, where the atomic cloud can be described by a coherent matter wave (an extensive discussion can be found for example in Refs. [22–25]). Experimental milestones were the interference of condensates [26], the measurement of long-range phase correlations in a condensate [27] and the observation of quantized vortices and vortex lattices [28–30]. The matter wave can be described by the Gross-Pitaevskii equation [31, 32], which is very similar to the Schrödinger equation for a single particle. The weak interaction of the particles

leads to a non-linear term, which explains non-linear effects like vortices or solitons. Small quantum fluctuations around the macroscopic condensate wave function can be addressed within the Bogoliubov theory [33], in which the excitations can be related to non-interacting quasiparticles.

Later, the focus has shifted towards the simulation of strongly interacting systems. Here, the particles are often strongly correlated, such that the dynamics cannot necessarily be solved by simple means. Instead, the correlations lead to complex many-body (ground) states, which are hardly accessible but often of high interest. Strongly correlated systems include for example high-temperature superconductors, fractional quantum Hall systems and Luttinger liquids. The regime of strong interactions could be accessed because of two experimental advances. First of all, the use of several orthogonal laser beams creating optical lattices in each direction, could lead to a strong confinement of the atoms within each lattice site. The interaction of two atoms occupying the same lattice site can be increased while at the same time the tunneling strength is reduced. This was proposed [34] and impressively demonstrated in the famous experiment [35] where a deepening of the lattice depth induced a quantum phase transition from a superfluid to a strongly interacting Mott insulator. By the same method, a one-dimensional Tonks-Girardeau gas of hard-core bosons [36] and a Berezinskii–Kosterlitz–Thouless transition [37] could be investigated.

Another approach to enter the regime of strong interactions was made possible by the use of Feshbach resonances to tune the atomic interaction [38–40]. By this, the interaction strength between the atoms could not only be de- or increased dramatically[2], but also its sign could be inverted, making repulsive particles attractive and vice versa. Using Feshbach resonances, the contact interaction of chromium atoms in a Bose-Einstein condensate could be reduced such that the predominant interaction between the particles was dipolar. In that way a quantum ferrofluid was realized [41]. Another milestone accomplished by Feshbach resonances was the experimental exploration of the crossover between a Bose-Einstein condensate (BEC) of tightly bound molecules and a Bardeen-Cooper-Schrieffer (BCS) pairing [42–44].

---

[2]However, the strength of the interaction is limited since the number of three-body losses will eventually lead to strong heating or even vanishing of the atomic gas

The combination and interference of several standing laser waves cannot only be used for spatial confinement. Additionally, they have been applied to form various lattices in two or three dimensions, like triangular, honeycomb and Kagome lattices (see for example [45]). In these lattices, the dynamics cannot be dimensionally separated and solved independently, which could lead to interesting physical phenomena. A two-dimensional optical lattice with a honeycomb structure can, for example, be used as an analouge and thus quantum simulator of graphene, which is regarded as a super material, for its high stability, conductivity and transparency [46].

On the theoretical side, the simple contact interactions between the particles imply already a major simplification. Furthermore, ultra-cold atoms in an optical lattice can be described within the tight-binding approximation [47]. Hereby, the particles are described by so called Wannier states, which are exponentially localized at a lattice minimum. The atoms hop between neighbouring lattice sites and interact only on-site. Higher excitations within a lattice site can be disregarded since they are energetically well separated from the ground state. The resulting discrete and low-dimensional models are called Hubbard models [11]. Hubbard models often allow for a simple physical interpretation of the relevant dynamics and a number of approximative methods have been developed to solve them.

When it comes to solve many-particle models like e.g. Hubbard models, in some cases these systems can be analyzed by perturbation theory. This is for example possible if the ground state is very close to highly symmetric states, e.g. for very large interactions and away from a quantum phase transition. For the solution in non-pertubative regimes, numerical methods are indispensible. In this regard, exact diagonalization of the many-body Schrödinger equation is limited because in general the Hilbert space dimension grows exponentially with the system size. However, a number of approximative numerical methods have become standard tools in the field of cold-atom experiments. These include for example the density matrix renormalization group (DMRG) [48,49], the time-evolving block decimation (TEBD) [50–52], the quantum Monte Carlo method [53] and coupled-cluster methods [54].

1.3. Periodic Driving of the Optical Lattice

For the quantum simulation in optical lattices, it is desirable to have maximum degree of control over the parameters in the simulated models, like for example the tunneling strength or phase of the tunneling matrix element. However, only some of the experimental parameters, which determine the model parameters, are directly accessible. For an optical lattice these include for example the lattice depth and the transversal confinement. Additional light fields in some cases might increase the level of control, but on the other hand challenge the experimental setup.
Periodically modulating experimental parameters with high frequencies, on the other hand, provides an easy method to gain additional control over the internal degrees of freedom. If the frequency of the modulation does not match resonances leading to uncontrolled dynamics, and if its strength is not too high, it is possible to further manipulate the Hamiltonian of the system without inducing chaotic dynamics and significant heating on the experimentally relevant time-scale [55]. This additional degree of freedom can be used effectively in the realization of interesting many-body quantum models and has thus been established as a common tool in the context of quantum simulation with ultra-cold gases.
Because of the periodicity of the time-dependent modulation, the system can be expanded in generalized stationary states, so called Floquet states. Their existence is a consequence of the Floquet theorem [56], and they can be viewed as Bloch states in time. If the frequency of the driving is high enough, in many scenarios the driven model can be approximated by a simple time-independent effective model with effective parameters that depend on the tunable strength and frequency of the driving [57]. Therefore, the advantages of the theoretical description in optical lattices via Hubbard models can readily be transferred to the driven case.
The experimental parameters that can be modulated in an optical lattice, are for example the lattice depth, the position of the lattice (lattice shaking) or the interaction strength of the atoms with the help of time-dependent Feshbach resonances. All of these modulations can be achieved easily since they only require a modulation of the phase or the amplitude of the employed lasers and electromagnetic fields[3]. While the experimental realization of the modulation of the interaction

---

[3]Another possibility to move the lattice periodically in time is the use of piezoelectric crystals.

strength have been achieved only recently [58], there have been a number of proposals that it can be used to study novel physics (e.g. [59, 60]). Amplitude modulation is often used to access higher lying orbitals (see e.g. Ref. [61]). Lattice shaking is of special interest since it leads to a reparameterization of the tunneling strength between the lattice sites. Therefore it is possible to reduce the tunneling contact or even to make it complex, when the shaking also breaks parity symmetry in time [62]. Because of this property, lattice shaking has been employed for a broad number of experiments and theoretical proposals, which we will review in the following.

The first experiments exploiting periodic driving demonstrated this control of the tunneling strength by directly measuring the dynamical localization of a Bose-Einstein Condensate [63–65]. Controlling the tunneling strength via the frequency and strength of the lattice shaking, it was also possible to induce the quantum phase transition between the Mott insulator and the superfluid ground state in a driven lattice [66, 67]. Mimicking thereby the experiment that was done by controlling the lattice depth [35], it demonstrated that periodically driving was also applicable in the regime of strong interactions.

Another application of lattice shaking is photon-assisted tunnling over potential barriers, also known as AC-induced tunneling [68–72]. Hereby, the tunneling strength is also reparamererized. The combination of potential off-sets and photon-assisted tunnling by periodic shaking has established as a standard tool to gain dynamical control in optical lattices. Another very similar strategy to accomplish laser-assisted tunneling is the use of Raman lasers (see e.g. Ref. [73]), which, however requires additional lasers. Furthermore, photon- or shaking-assisted tunneling in systems where the interaction energy is similar to the potential off-set, can be used to make the tunneling of the particles density-dependent [74–77].

The possibility to make the tunneling parameter complex by a shaking function that breaks spatio-temporal symmetry, has led to a number of interesting proposals and experiments in two and three dimensions. First of all, by lattice shaking or by using Raman lasers, it is possible to achieve a net phase over a closed loop of lattice plaquettes [78, 79]. With these artificial gauge fields it is now possible to study magnetism even though the atoms originally have no charge [62, 73, 80–84]. A special class of these models and still a very new and active field of research are

topological insulators [85–88]. Whereas these materials are insulating in the bulk, they are conducting on the surface. These properties make the study of topological insulators in quantum simulators interesting for material sciences [89].

Other interesting situations, where the interplay of the tunneling parameter and the geometry of the lattice leads to interesting phenomena, is geometric frustration [90, 91]. While a sign change of the tunneling parameter due to lattice shaking does not lead to qualitatively new physics in one dimension or in a bipartite lattice, an inverted sign of the hopping element in a non-bipartite lattice makes the configuration of the ground-state wave degenerate. For example, a triangular lattice might have two ground states and a Kagome lattice infinitely many ones. This might lead to spontaneous symmetry breaking of the ground state, where a slight perturbation, e.g. by interactions, can have a huge impact on the properties of the system.

Another class of quantum models that can be explored by periodic driving are systems with orbital degrees of freedom. Naturally, higher orbitals are separated by a large energy gap, which is of advantage if one is only interested in the physics of the ground band of the lattice. If periodic driving is added to the system with a frequency well below this band gap, the dynamics remains limited to the ground band. If, however, the driving frequency is comparable to the energy difference towards higher orbital states and the coupling is allowed by symmetry, the dymanics leads to a mixture between several orbital states. For weak coupling, the dispersion relations are only slightly perturbed. In a weakly interacting scenario, the condensate might thus be transferred to the higher orbital if the frequency is varied slowly [92]. In another scenario, due to the admixtures of the higher orbitals the dispersion relation of the ground band forms a double-well. These two degenerate potential minima for the condensate can be studied as an effective ferromagnet [93, 94]. If the resonance condition is only fulfilled for a certain occupation of a lattice site because of the interaction energy, this leads to an interaction blockade in the other cases, which could be used as a method for density measurement [95, 96]. Nevertheless, experiments in the strong-interacting regime, in which higher orbitals are coupled in a coherent fashion, have not yet been realized. Even if experiments with ultra-cold quantum gases are well isolated and under control, unwanted heating and loss can occur and has to be accounted for. In

non-driven systems, especially three-body scattering can lead to particle excitations to higher states and consequently to heating and particle loss [97, 98]. Heating can furthermore be induced by parameter changes, which therefore have to be slow enough to reduce non-adiabatic energy exchange. Overall, in a non-driven system these phenomena are well understood and can be limited quite successfully. In periodically driven systems, the situation changes completely. If the frequency is close to the difference of two relevant energies, the external driving will couple these states and thereby pump energy into the system or take it out. These resonances can occur towards highly excited single-particle orbitals or towards highly excited collective excitations. These excitations lead to chaotic behaviour or particle loss. In fact, an unbound driven system, which is in general fully ergodic, is expected to heat up towards an infinite temperature state [99, 100]. However, if unwanted resonances are minimized successfully, there is a time period where the dynamics in a periodically driven system follows an effective description, which can be derived from Floquet physics. This provides a time window for experiments.

1.4. Agenda of the Present Work

Experiments with ultra-cold atoms in optical lattices have proven to be a versatile toolbox for quantum simulation and offer further potential in the future. A periodic driving provides additional degrees of freedom to the experimentors and renders new quantum models possible. While most proposals and experiments with periodically driven lattices work in the regime of weak interactions, the aim of this work is to explore theoretical proposals of Floquet engineering in the strong coupling regime, where the many-body nature of the system is crucial. Additionally, the work addresses the issue of heating in driven systems, which still poses a big challenge for experimentalists and is the reason why many proposals with driven systems have not yet been realized.

First of all, Chap. 2 provides the necessary theoretical framwork for the following discussion by introducing Floquet theory and the necessary tools therein, which will be used in the following chapters.

Chap. 3 studies the intriguing possibility of the coherent coupling of Bloch bands by a periodic lattice shaking. The motivation is to coherently open orbital degrees

of freedom in optical lattices, which have until now been widely neglected because of the energetic gap between the orbitals. The coherent coupling in a shaken optical lattice is possible since the driving introduces a direct coupling element between states of different Bloch bands with the same quasimomentum and is significant as long as the frequency of the driving is resonant with the energy gap separating the two Bloch bands. To explore the coherent coupling in a minimal and simple model, we focus on the lowest two Bloch bands and one dimension. To reduce excitations to even higher lying states, we propose to use a dimerized lattice, such that the resonance condition towards higher bands is not matched at the same time. Starting from the driven Hubbard model including two Bloch bands, we derive an effective Hubbard model, where the high-frequency condition is automatically fulfilled by the resonance condition. The band distance in this effective model can be tuned by the driving frequency. Hence, for strongly coupled bosons we propose to induce an orbital driven quantum phase transition between a Mott insulator and a superfluid. By presenting numerical results, we demonstrate that there exist experimentally realistic parameters where this phase transition can actually happen. These parameters also determine whether the phase transition is of first or second order. Finally, a real-time simulation of an adiabatic protocol of the orbital-driven melting of the Mott insulator is presented for small systems and it is shown that excitations to higher lying bands during the protocol can indeed be neglected. The chapter elaborates in detail the theoretical proposal that was published in Ref. [101].

In Chap. 4, we describe the possibility to realize one-dimensional anyons in a shaken optical lattice and demonstrate how these lattice anyons can be probed in an experiment. Interpolating between bosons and fermions as their wave function picks up a non-trivial phase upon particle exchange, anyons play an important role as quasiparticles of topologically ordered states. Since lattice anyons have not yet been realized within an optical lattice, we elaborate a simple scheme for this aim, which does not require additional lasers, in contrast to previous proposals [102,103]. The proposal is based on the possibilty to make the tunneling elements complex by bi-chromatic shaking on the one hand and to make them density-dependent by shaking-assisted tunneling combining a lattice tilt and strong on-site interactions of the atoms on the other. We show for which parameters lattice anyons with a tunable

statistical angle will emerge and how a simple anyonic Hubbard model can be realized effectively. Furthermore, by solving small systems via exact diagonalization, we demonstrate how Friedel oscillations in real space can be used as signatures for the anyonization of the many-particle ground state of the bosons. By simulating the full shaking protocol, we demonstrate that the preparation of this anyonic ground state is indeed possible. The work on anyons presented in this chapter is based on Ref. [104].

Finally, in Chap. 5 we study single-particle, multi-photon heating processes in periodically driven lattices. Multi-photon excitation processes in optical lattices have not been analyzed rigorously before but can have a significant strength in certain situations. We consider these processes in a shaken and in an amplitude-modulated lattice, which are very common driving schemes and lead to distinct selection rules and excitation strengths. The strength of the excitations in both cases is estimated by a Floquet perturbation theory and by a rotating-wave approximation. Furthermore, for both scenarios we analyze the time-evolution and the excitation spectrum via numerical simulations. The results for the shaken lattice are compared to the outcomes of the experiment which was performed in Hamburg and published together with our results in Ref. [105]. The section on the case of an amplitude-modulated lattice is based on the theoretical publication Ref. [106].

2. Basics and Tools of Floquet Theory

In this chapter we give an introduction to Floquet theory and present the key tools how a time-periodic Hamiltonian can be handled and solved efficiently. These methods will be used throughout the following chapters. In Sec. 2.1 we introduce Floquet theory as the main formalism to solve problems with time-periodic Hamiltonians. In Sec. 2.2 we demonstrate how Floquet theory can be used to derive an effective Hamiltonian, which reduces a time-periodic problem to a time-independent one. This is a key technique to engineer the properties of a many-body systems in the context of quantum simulation. Finally, in Sec. 2.3 we explain how to treat a slow parameter variation within a Floquet system. This is an important ingredient for many experiments with periodically driven quantum systems. The Floquet theory and methods presented here refer mainly to Refs. [57] and [55]. More specific methods in the framework of Floquet theory, like the Floquet perturbation theory, are introduced in the respective chapters and sections directly.

2.1. Solution of Quantum Systems with a Time-Periodic Hamiltonian

We start by examing a general quantum system which is time-dependent in a periodic fashion. This symmetry can be exploited when solving the system and often allows for a clear physical interpretation.

Hence, we consider a time-periodic Hamiltonian

$$\hat{H}(t) = \hat{H}(t+T) \tag{2.1.1}$$

with frequency ω and time-periodicity $T = 2\pi/\omega$, which acts in a Hilbert space $\mathcal{H}$ with finite dimension $\mathcal{D}$. Floquet's theorem [56] relates the symmetry of time-periodicity to solutions of the time-dependent Schrödinger equation

$$i\hbar\frac{\partial}{\partial t}|\psi(t)\rangle = \hat{H}(t)|\psi(t)\rangle. \tag{2.1.2}$$

The theorem states that for Eq. (2.1.2) there exists a basis of quasi-stationary solutions $|\psi_n(t)\rangle$, also called *Floquet states*, which have the form[1]

$$|\psi_n(t)\rangle = e^{-i\epsilon_n t/\hbar}|u_n(t)\rangle. \tag{2.1.3}$$

Each of these basic solutions splits into a time-periodic *Floquet mode* $|u_n(t)\rangle = |u_n(t+T)\rangle$, which governs the *micromotion* of the state within one time period, and a linearly increasing phase governed by the *quasienergy* ϵ_n. The $|\psi_n(t)\rangle$ form a complete basis of the Hilbert space. They are also called generalized eigenstates since they play the role of stationary states in a time-independent system and are transformed into them in a stationary limit of $\hat{H}(t)$, e.g. when the strength of the driving term goes to zero. Likewise, the quasienergies generalize the concept of the eigenenergies. Because of the hermiticity of the Hamiltonian, the quasienergies are real. Furthermore, they are only defined modulo $\hbar\omega$ since

$$|\psi_n(t)\rangle = e^{-i\epsilon_{nm}t/\hbar}|u_{nm}(t)\rangle \tag{2.1.4}$$

with

$$\epsilon_{nm} = \epsilon_n + m\hbar\omega \qquad \text{and} \qquad |u_{nm}(t)\rangle = |u_n(t)\rangle e^{im\omega t}. \tag{2.1.5}$$

is also a set of basic solutions. The index m is called *Fourier* or *photon index*. The transition from energies to quasienergies is thus equivalent to the transition from momenta to quasimomenta in a spatially periodic potential.

Eq. (2.1.3) reveals the general structure of the dynamics in a periodically driven quantum system. Each solution of the Schrödinger equation $|\psi(t)\rangle$ can be expanded

---

[1]This mathematical result about the solution of a linear differential equation with periodic coefficient matrix, was independently found by Gaston Floquet, George William Hill, Alexander Lyapunov and Felix Bloch in the end of the 19th and beginning of the 20th century. For spatially periodic (time-independent) Hamiltonians it is commonly known as Bloch's theorem [107].

in the Floquet basis,

$$|\psi(t)\rangle = \sum_n c_n |\psi_n(t)\rangle, \tag{2.1.6}$$

with constant coefficients $c_n = \langle \psi_n(0)|\psi(0)\rangle$. If the Floquet basis and the quasienergy spectrum are known, the time evolution of each state $|\psi(t)\rangle$ can be provided. Furthermore, if one disregards the micromotion and is only interested in the stroboscopic time-evolution in steps of T, the dynamics becomes

$$|\psi(t_0 + jT)\rangle = \sum_n e^{-\frac{i}{\hbar}\epsilon_n jT} c_n |\psi_n(t_0)\rangle, \ \ j \in \mathbb{Z}, \tag{2.1.7}$$

i.e. it is as simple as in the time-independent case. Especially in a high-frequency setting, where $\hbar\omega$ is much higher than other relevant energy scales in the Hamiltonian, this is a useful simplification.

The Floquet states $|\psi_n(t)\rangle$ diagonalize the so called monodromy operator

$$\mathcal{M}(t) = \hat{U}(t+T, t) = \mathcal{T} \exp\left(-\frac{i}{\hbar} \int_t^{t+T} \mathrm{d}\tau \hat{H}(\tau)\right) \tag{2.1.8}$$

which is the time evolution operator over one time period, i.e.

$$\mathcal{M}(t)|\psi_n(t)\rangle = e^{-\frac{i}{\hbar} m\epsilon_n T}|\psi_n(t)\rangle. \tag{2.1.9}$$

Here, $\mathcal{T}$ is the time ordering operator. Eq. (2.1.9) provides a method to calculate quasienergies and Floquet states: A complete, orthonormal basis $|\alpha\rangle$ of the Hilbert space $\mathcal{H}$ at a specific time t_0 (e.g. $t_0 = 0$) has to be propagated in time over T with $\mathcal{M}(t_0)$. The resulting states projected on the initial basis give the monodromy matrix (the monodromy operator in matrix form)

$$\mathcal{M}_{\alpha'\alpha}(t_0) = \langle \alpha'|\mathcal{M}(t_0)|\alpha\rangle \tag{2.1.10}$$

whose eigenvalues $e^{i\epsilon_n T/\hbar}$ provide the quasienergies ϵ_n and whose eigenstates are the Floquet states $|\psi_n(t_0)\rangle$ at time t_0. The micromotion of the Floquet states, i.e. the dynamics of the Floquet modes $|u_n(t_0 + t)\rangle$, can be obtained by propagating each Floquet state with $\hat{U}(t_0 + t, t_0)$.

There is another perspective on the Floquet dynamics, given by the *extended Hilbert space*, which includes an alternative way to compute Floquet states and the quasienergy spectrum. If we plug in Eq. (2.1.3) into Eq. (2.1.2), we can derive a differential equation

$$\underbrace{\left[\hat{H}(t) - i\hbar\partial_t\right]}_{\hat{Q}(t)}|u_{nm}(t)\rangle = \epsilon_{nm}|u_{nm}(t)\rangle \tag{2.1.11}$$

for the Floquet modes $|u_{nm}(t)\rangle$. Here, the operator $\hat{Q}(t)$ is called the *quasienergy operator*. Because of the time derivative, the equation is not an eigenvalue problem in the ordinary Hilbert space, but it can be regarded as one in the extended Floquet Hilbert space $\mathcal{K}$ [108]. This is the product space of the original Hilbert space $\mathcal{H}$ and the (infinite dimensional) Lebesgue space $\mathcal{L}^2(T, 0)$ of square-integrable functions within one time period, i.e.

$$\mathcal{K} = \mathcal{H} \otimes \mathcal{L}^2(T, 0). \tag{2.1.12}$$

States in $\mathcal{K}$ are denoted in the double-bra-ket notation. For example, $|u\rangle\rangle$ represents the time-periodic state $|u(t)\rangle \in \mathcal{H}$ for all $t \in [0, T]$. The scalar product in $\mathcal{K}$ between two states $|u\rangle\rangle$ and $|v\rangle\rangle$ is defined as

$$\langle\langle u|v\rangle\rangle = \frac{1}{T}\int_0^T \mathrm{d}t\, \langle u(t)|v(t)\rangle. \tag{2.1.13}$$

One possible complete basis of $\mathcal{K}$ is the set $|nm\rangle\rangle$ belonging to the Floquet modes $|u_{nm}(t)\rangle$, which fulfill

$$\langle\langle n'm'|nm\rangle\rangle = \delta_{n'n}\delta_{m'm}. \tag{2.1.14}$$

They are, however, per se not known. Another very convenient complete basis of $\mathcal{K}$ is given by the states $|\alpha m\rangle\rangle$, representing the time-periodic states $|\alpha\rangle e^{im\omega t}$ with $m \in \mathbb{Z}$ and $|\alpha\rangle$ being a complete basis in $\mathcal{H}$. With regards to the time dimension, this choice of basis is just the discrete Fourier expansion into plane waves. In this

basis, the quasienergy operator has the simple form

$$
\begin{aligned}
\langle\!\langle \alpha'm'|\hat{Q}|\alpha m\rangle\!\rangle &= \frac{1}{T}\int_0^T \mathrm{d}t\, e^{-i(m'-m)\omega t}\langle\alpha'|\big[\hat{H}(t)-i\hbar\partial_t\big]|\alpha\rangle \\
&= \langle\alpha'|\big[\hat{H}^{(m'-m)}+m\hbar\omega\delta_{m'm}\big]|\alpha\rangle.
\end{aligned}
\tag{2.1.15}
$$

Here we have introduced the Fourier components of the Hamiltonian

$$
\hat{H}^{(m)} = \frac{1}{T}\int_0^T \mathrm{d}t\, \hat{H}(t)e^{-im\omega t}
\tag{2.1.16}
$$

from the Fourier decomposition

$$
\hat{H}(t) = \sum_m \hat{H}^{(m)}e^{im\omega t}.
\tag{2.1.17}
$$

Written out with resepct to m, the quasienergy operator takes the form

$$
\hat{Q} = \begin{pmatrix}
\ddots & & \vdots & & \iddots \\
& \hat{H}^{(0)}-\hbar\omega & \hat{H}^{(-1)} & \hat{H}^{(-2)} & \\
\cdots & \hat{H}^{(1)} & \hat{H}^{(0)} & \hat{H}^{(-1)} & \cdots \\
& \hat{H}^{(2)} & \hat{H}^{(1)} & \hat{H}^{(0)}+\hbar\omega & \\
\iddots & & \vdots & & \ddots
\end{pmatrix}.
\tag{2.1.18}
$$

Here, we clearly see the block structure of the quasienergy operator: diagonal blocks comprising the static contribution $\hat{H}^{(0)}$ of $\hat{H}(t)$, are separated in quasienergy in steps of the photon energy $\hbar\omega$. These diagonal blocks are coupled to each other by the Fourier components $\hat{H}^{(m)}$, $m\neq 0$ stemming from the time-dependent part of $\hat{H}(t)$. In the extended Hilbert space, the eigenproblem Eq. (2.1.11) takes the form

$$
\hat{Q}|nm\rangle\!\rangle = \epsilon_{nm}|nm\rangle\!\rangle.
\tag{2.1.19}
$$

It resembles the problem of a quantum system where the Hamiltonian $\hat{H}^{(0)}$ is coupled to a photon-like mode. Therein, m plays the role of the photon number relative to a large background occupation and for this reason we call m the photon-index in the Floquet context. Remember that for every m, the set of quasienergies ϵ_{nm} and modes $|nm\rangle\!\rangle$ defines an equivalent solution for the dynamics of $\hat{H}(t)$. The

photon index m is just necessary to compute one of these equivalent solutions. Since m takes any integer value, $\hat{Q}$ is thus an infinitely large matrix. However, Eq. (2.1.19) can be solved for the (physically common) scenario that $\hat{H}^{(m)}$ goes to zero rapidly for increasing $|m|$. In this case, one can choose a sufficiently large cut-off m^* such that $\hat{Q}$ is reduced to to the finite matrix $\hat{Q}^*$ with $-m^* \leq m, m' \leq m^*$. One usually then picks the solution $\{\epsilon_{n0}, |n0\rangle\rangle\}$ since it is farest away from the boundaries. This provides a method to compute Floquet states and quasienergy spectrum alternative to computing and diagonalizing the monodromy operator.

2.2. Reduction to an Effective Time-Independent Model

In this section we show how $\hat{H}(t)$ or respectively $\hat{Q}$, can be reduced to an effective, time-independent Hamiltonian acting in $\mathcal{H}$. By this, the complexity of the problem is reduced and it is possible to apply standard techniques of stationary quantum mechanics. Furthermore, the derivation of an effective Hamiltonian makes it possible to separate the solution of the long-term dynamics from that of the micromotion. This allows for a clear physical interpretation and opens many possibilities for quantum simulation with periodically driven Hamiltonians [57].

Formally, for a finite-dimensional Hilbert space there always exists a time-dependent gauge transformation $\hat{U}_F(t)$ which transforms the Hamiltonian $\hat{H}(t)$ into a time-independent effective Hamiltonian

$$\hat{H}_F \;\; = \;\; \hat{U}_F^\dagger(t)\hat{H}(t)\hat{U}_F(t) - i\hbar\hat{U}_F^\dagger(t)\frac{\partial}{\partial t}\hat{U}_F(t), \tag{2.2.1}$$

see Ref. [109]. The time-evolution operator is thus decomposed as

$$\hat{U}(t_0 + t, t_0) = \hat{U}_F(t) \exp\left(-\frac{i}{\hbar}(t - t_0)\hat{H}_F\right)\hat{U}_F^\dagger(t_0). \tag{2.2.2}$$

Note that $\hat{U}_F(t)$ is absorbing the micromotion of the Floquet states, which we described in Floquet's theorem (2.1.3). For this reason, it is also called the *micromotion operator*. On the other hand, $\hat{H}_F$ describes the phase evolution due

to the quasienergies ϵ_n, which do not change under the gauge transformation. We therefore have the eigenvalue problem

$$\hat{H}_F|\tilde{u}_n\rangle = \epsilon_n|\tilde{u}_n\rangle \qquad (2.2.3)$$

in $\mathcal{H}$ for the time-independent, transformed Floquet modes

$$|\tilde{u}_n\rangle = \hat{U}_F(t)^\dagger|u_n(t)\rangle. \qquad (2.2.4)$$

The micromotion operator $\hat{U}_F(t)$ is not uniquely defined. From Eq. (2.2.1), we deduce that we can always multiply the micromotion operator by a time-independent unitary operator from the right

$$\hat{U}_F(t) \rightarrow \hat{U}_F(t)\hat{U} = \hat{U}'_F(t) \qquad (2.2.5)$$

since it only changes the stationary basis $|\tilde{u}_n\rangle$. For example, the unitary $\hat{U}$ can diagonalize $\hat{H}_F$. By choosing $\hat{U} = \hat{U}_F^\dagger(t_0)$, the time evolution operator Eq. (2.2.2) takes the simple form

$$\hat{U}(t,t_0) = \hat{U}_F(t,t_0) \exp\left(-\frac{i}{\hbar}(t-t_0)\hat{H}_{t_0}^F\right), \qquad (2.2.6)$$

where we define $\hat{U}_F(t,t_0) = \hat{U}_F(t)\hat{U}_F^\dagger(t_0)$ and

$$\hat{H}_{t_0}^F = \hat{U}_F(t_0)\hat{H}_F\hat{U}_F^\dagger(t_0). \qquad (2.2.7)$$

The effective Hamiltonian $\hat{H}_{t_0}^F$ is also called *Floquet Hamiltonian*. Considering the dynamics stroposcopically in steps of T, the time-evolution is thus simply governed by the Floquet Hamiltonian,

$$\hat{U}(t_0+T,t_0) = \exp\left(-\frac{i}{\hbar}T\hat{H}_{t_0}^F\right), \qquad (2.2.8)$$

which is very convenient in a high-frequency scenario.

However, it is not always obvious how the micromotion operator $\hat{U}_F(t)$ for an arbitrary Hamiltonian $\hat{H}(t)$ has to be constructed and it may have many and

complicated terms. Instead, it is more convenient to look for a gauge transformation $\hat{U}(t)$ that transforms the Hamiltonian

$$\hat{H}'(t) \;\; = \;\; \hat{U}^\dagger(t)\hat{H}(t)\hat{U}(t) - i\hbar\hat{U}^\dagger(t)\frac{\partial}{\partial t}\hat{U}(t) \tag{2.2.9}$$

such that the time-evolution

$$\hat{U}(t_0 + T, t_0) \approx \exp\left(-\frac{i}{\hbar}T\hat{H}'^{(0)}\right) \tag{2.2.10}$$

is approximately governed by the stationary part of the Hamiltonian

$$\hat{H}'(t) \approx \hat{H}'^{(0)} = 1/T \int_0^T \mathrm{d}t\, \hat{H}'(t). \tag{2.2.11}$$

This condition does not only depend on the higher Fourier components $\hat{H}'^{(m)}$ with $m \neq 0$ but also on the frequency ω, or respectively the photon energy $\hbar\omega$. Let us consider again the Floquet operator Eq. (2.1.18) and the block structure of $\hat{Q}$. The diagonal blocks $\hat{H}^{(0)} + m\hbar\omega$, corresponding to the stationary part of $\hat{H}(t)$, might overlap with each other in quasienergy and are coupled by the non-diagonal blocks $\hat{H}^{(m)}$. In first order perturbation theory, there are therefore two alternative possibilities such that the off-diagonal blocks, leading to non-stationary evolution, can be neglected: first of all, the off-diagonal elements $\hat{H}'^{(m)}$ should not resonantly couple states from diagonal blocks with different index m. This requirement implies that no states from different blocks are degenerate or that there exists no coupling elements between them. The other condition is that also the coupling terms $\hat{H}'^{(m)}$ should be smaller than the energy differences of the states from different blocks. If both conditions are fulfilled, the off-diagonal blocks can be neglected and the eigenvalue problem Eq. (2.1.19) can be reduced to the time-independent Schrödinger equation

$$\hat{H}'^{(0)}|n\rangle = \varepsilon_n|n\rangle \tag{2.2.12}$$

in $\mathcal{H}$. Therefore, it is a good strategy to look for all near-resonantly coupled states and apply a gauge transformation which removes the coupling between them to the stationary part $\hat{H}'^{(0)}$. This procedure is known as *Rotating Wave Approximation*

(RWA) in this context [110].

Let us demonstrate the RWA with the textbook example of a two-level system describing an atom with states $|\pm\rangle$ which have energies $E_\pm = \pm\Delta/2$. The states are coupled by a single oscillating mode (e.g. light) with strength Ω and resonant frequency $\hbar\omega = \Delta - \delta$, $\delta \ll \Delta$. The Hamiltonian

$$\hat{H}(t) = \begin{pmatrix} -\frac{\Delta}{2} & 0 \\ 0 & \frac{\Delta}{2} \end{pmatrix} + \begin{pmatrix} 0 & \Omega\cos(\omega t) \\ \Omega\cos(\omega t) & 0 \end{pmatrix} \tag{2.2.13}$$

consists of a stationary part $\hat{H}^{(0)}$ and a time-dependent part $e^{i\omega t}\hat{H}^{(1)} + e^{-i\omega t}\hat{H}^{(-1)}$, which cannot be neglected because the driving has a resonant frequency. In the RWA approximation, the Hamiltonian is transformed into the interaction picture

$$\hat{H}(t) \quad \rightarrow \quad \hat{H}'(t) = \begin{pmatrix} -\delta & \frac{\Omega}{2} \\ \frac{\Omega}{2} & \delta \end{pmatrix} + \frac{\Omega}{2}\begin{pmatrix} 0 & \exp(2i\omega t) \\ \exp(-2i\omega t) & 0 \end{pmatrix} \tag{2.2.14}$$

via the gauge transform

$$\hat{U}(t) = \begin{pmatrix} \exp\left(\frac{i}{2}\omega t\right) & 0 \\ 0 & \exp\left(-\frac{i}{2}\omega t\right) \end{pmatrix} \tag{2.2.15}$$

so that afterwards the two states are almost degenerate in energy, separated by a small off-set $\delta = \Delta - \hbar\omega$. Thus, the initial coupling $\hat{H}^{(1)}$ is transformed into a stationary part entering $\hat{H}'^{(0)}$ and a rapid-oscillating part $e^{i2\omega t}\hat{H}'^{(2)} + e^{-i2\omega t}\hat{H}'^{(-2)}$, which can be neglected if $\hat{H}^{(2)} \sim \Omega/2 \ll 2\hbar\omega$. The effective Hamiltonian $\hat{H}'^{(0)}$ can easily be solved and results in a Rabi oscillation between the original states $|+\rangle$ and $|-\rangle$, see also App. C.1.

There are further standard approximations that give an effective Hamiltonian beyond the stationary part of the Hamiltonian $\hat{H}'^{(0)}$, which may or may not be combined with a preceding gauge transformation. One of them is given by the high-frequency expansion [57, 111–116], which also provides estimates for the micromotion operator $\hat{U}_F(t)$. In this approximation, the photonic part of the Hamiltonian $\langle\langle\alpha'm'| - i\hbar\partial_t|\alpha m\rangle\rangle = \delta_{m'm}\delta_{\alpha'\alpha}m\hbar\omega$ serves as the unperturbed system while the Hamiltonian $\langle\langle\alpha'm'|\hat{H}(t)|\alpha m\rangle\rangle$ is the perturbation. Furtherore, one writes

the micromotion operator as

$$\hat{U}_F(t) = \exp(\hat{G}(t)) \tag{2.2.16}$$

with anti-Hermitian operator $\hat{G} = -\hat{G}^\dagger$, which can be perturbatively expanded

$$\hat{G}(t) = \sum_\mu \hat{G}^{(\mu)} \tag{2.2.17}$$

allowing one to derive perturbative terms for $\hat{H}_F = \sum_\mu \hat{H}_F^{(\mu)}$. The first three terms are given by

$$
\begin{aligned}
\hat{H}_F^{(1)} &= \hat{H}^{(0)}, \\
\hat{H}_F^{(2)} &= \sum_{m \neq 0} \frac{\hat{H}^{(m)}\hat{H}^{(-m)}}{m\hbar\omega}, \\
\hat{H}_F^{(3)} &= \sum_{m \neq 0} \frac{\left[\hat{H}^{(-m)}, \left[\hat{H}^{(0)}, \hat{H}^{(m)}\right]\right]}{2(m\hbar\omega)^2} + \sum_{m' \neq 0, m} \frac{\left[\hat{H}^{(-m')}, \left[\hat{H}^{(m'-m)}, \hat{H}^{(m)}\right]\right]}{3mm'(\hbar\omega)^2}.
\end{aligned}
\tag{2.2.18}
$$

Another approximation to derive an effective Hamiltonian taking into account higher Fourier modes, is the Floquet-Magnus expansion [117].

In summary, we have demonstrated methods to derive an effective Hamiltonian for a periodically time-dependent quantum system, which allow for a simplification of the solution and often allow for an interpretation of the effect of the driving, as will be seen in the proposals presented in Chap. 3 and Chap. 4.

2.3. Slow Paramater Variation in a Floquet System

Finally, we want to consider the situation where within a periodically modulated Hamiltonian one or several parameters change slowly in time. This is an important scenario in a number of experimental protocols, for example in the preparation of a specific Floquet state which represents the ground state of a target Hamiltonian. Consider therefore a time-dependent Hamiltonian $\hat{H}(t, \mu(t))$, which is almost time-periodic but also depends on a parameter (or a set of parameters) $\mu(t)$ that varies

slowly with respect to the oscillation time T and also to the time-scale determined by the energy scales of the Hamiltonian. Then it is interesting to know how the time evolution of the system deviates from the Floquet description due to $\mu(t)$. Since a time-periodic system can be reduced to an effective time-independent system, at least modulo T, it seems intuitive to generalize the adiabatic principle [118] and the Landau-Zener formula [119–121] from static quantum mechanics also to Floquet states and quasienergies in the extended Hilbert space $\mathcal{K}$. This intuitive guess is confirmed by the two-time formalism [122–124]. In this formalism we introduce a second time τ for the adiabatic parameter change, while the time of the Floquet problem is still denoted as t. Hence, we introduce instantaneous Floquet states

$$|\Psi_n^\tau(t)\rangle = \exp\left(-\frac{i}{\hbar}m\epsilon_{nm}^\tau t\right)|u_{mn}^\tau(t)\rangle \qquad (2.3.1)$$

with $|\Psi^\tau(t)\rangle|_{\tau=t} = |\psi(t)\rangle$ and instantaneous operators $\hat{H}^\tau(t) = \hat{H}(t,\mu(\tau))$ and $\hat{Q}^\tau(t) = \hat{H}^\tau(t) - i\hbar\partial_t$. Thus, we can write down the instantaneous eigenvalue problem in the extended Hilbert space

$$\hat{Q}^\tau|u_{mn}^\tau\rangle\rangle = \epsilon_{nm}^\tau|u_{mn}^\tau\rangle\rangle. \qquad (2.3.2)$$

By plugging in this relation into the full time-dependent Schrödinger equation, we see that this operator generates the time evolution with regard to τ,

$$i\hbar\frac{\partial}{\partial\tau}|\Psi^\tau\rangle\rangle = \hat{Q}^\tau|\Psi^\tau\rangle\rangle, \qquad (2.3.3)$$

for a general state $|\Psi^\tau\rangle\rangle$ in the extended Hilbert space. The structure of this equation is analogous to the time-dependent Schrödinger equation for τ, which justifies the following approximations.

Let us now consider a smooth and finite parameter varation $\mu(\tau) = \tilde{\mu}(\tau/\tau_f)$ from $\mu_0 = \tilde{\mu}(0)$ to $\mu_1 = \tilde{\mu}(1)$ so that $1/\tau_f$ defines the speed of the parameter variation. The adiabatic theorem for Floquet systems states that in the limit $\tau_f \to \infty$, i.e. $\partial_\tau H(t,\mu(\tau)) \to 0$, the system started in Floquet state $|\psi_n(0)\rangle$ with quasienergy ϵ_n remains in the Floquet state with the same index n provided its quasienergy is

separated by a finite gap from all other quasienergies[2]. This implies that after the parameter variation at time τ_f the Floquet state evolves according to

$$|\psi_n(\tau_f)\rangle \xrightarrow{\tau_f \to \infty} \exp\left(-\frac{i}{\hbar} \int_0^{\tau_f} \mathrm{d}\tau\, \epsilon_n^\tau\right) |\psi_n(0)\rangle \tag{2.3.4}$$

if $\tau_f = nT$, $n \in \mathbb{Z}$ and provided the respective Floquet mode is normalized like

$$\langle\!\langle u_{nm}^\tau | u_{nm}^\tau \rangle\!\rangle = 1 \tag{2.3.5}$$

and

$$\langle\!\langle u_{nm}^\tau | \partial_\tau | u_{nm}^\tau \rangle\!\rangle = 0. \tag{2.3.6}$$

The phase factor appearing in Eq. (2.3.4) is called the dynamic phase, as known from static quantum mechanics. Practically, if the parameter variation $\mu(\tau)$ is very slow, i.e. $\tau_f \gg T$, the system follows the Floquet state very closely. An exact definition of the term *slow* depends strongly on the specific form and time scale of the Hamiltonian. The special case where the parameter under variation μ is the frequency of the Hamiltonian ω is described in Ref. [126].

On the other hand, the Landau-Zener formula makes a quantitative statement in the important situation where the quasienergies ϵ_A^τ and ϵ_B^τ ($A = nm$, $B = n'm'$) of Floquet modes $|u_A^\tau\rangle\!\rangle$ and $|u_B^\tau\rangle\!\rangle$ come very close together in an avoided crossing. An avoided crossing happens when the two Floquet modes are very close to two orthogonal modes $|v_A^\tau\rangle\!\rangle$ and $|v_B^\tau\rangle\!\rangle$ which are coupled to each other with matrix element C in the Floquet operator. In a situation where a parameter change $\mu(\tau)$ leads to a linear crossing of the states $|v_A^\tau\rangle\!\rangle$ and $|v_B^\tau\rangle\!\rangle$, for the Floquet modes $|u_A^\tau\rangle\!\rangle$ and $|u_B^\tau\rangle\!\rangle$ this crossing is avoided due to the coupling. Close to the crossing, the situation can be represented, to good approximation, by the 2-by-2 Floquet

---

[2]The finite gap to other quasienergies is a common condition in the proof of the adiabatic theorem and can be used to give information about how fast the limit is reached. However, for the adiabatic theorem to hold it is enough to demand that there is a piecewise twice differentiable spectral projection [125].

operator in the basis of $|v_A^\tau\rangle\!\rangle$ and $|v_B^\tau\rangle\!\rangle$,

$$\hat{Q}_{\mathrm{LZ}} = \begin{pmatrix} \epsilon_0 + \epsilon'\Delta\tau & C \\ C^* & \epsilon_0 - \epsilon'\Delta\tau \end{pmatrix} \tag{2.3.7}$$

where $\Delta\tau = \tau - \tau_0$, τ_0 being the time when the crossing happens. Here ϵ_0 is the quasienergy of the state $|v_A^\tau\rangle\!\rangle$ ($|v_B^\tau\rangle\!\rangle$) and ϵ' ($-\epsilon'$) its (constant) derivative with respect to τ. The quasienergies close to the crossing are thus

$$\epsilon_{A,B}^\tau = \epsilon_0 \pm \sqrt{(\epsilon'\Delta\tau)^2 + |C|^2}, \tag{2.3.8}$$

which implies that their difference at the avoided crossing is exactly $2|C|$. The Landau-Zener formula for Floquet systems states that the probability $P_{A\to B}$ for diabatic transition, i.e. the probability for the system to transfer from state $|u_A^{\tau\to-\infty}\rangle\!\rangle$ to state $|u_B^{\tau\to+\infty}\rangle\!\rangle$ (or vice versa) is approximately given by

$$P_{A\to B} \approx \exp\left(-\frac{\pi|C|^2}{\hbar|\epsilon'|}\right). \tag{2.3.9}$$

This value becomes exact when $\hat{Q}_{\mathrm{LZ}}$ describes the whole system. The probability of adiabatic transition $P_{A\to A}$, i.e. the probability that the system remains in the initial Floquet state, is thus $P_{A\to A} = 1 - P_{A\to B}$. The requirement

$$\frac{\pi|C|^2}{\hbar|\epsilon'|} \gg 1 \tag{2.3.10}$$

provides us an important criterion if an avoided crossing will be passed adiabatically. It depends on the speed of the parameter change and the strength of the coupling of both states. The condition for diabatic passage has an inverted comparison sign, respectively.

For an increasing system size in a time-periodic system, not only the number of states grows but also the density of states within an interval of quasienergy. This implies that there is large number of avoided crossings in the quasienergy spectrum. Most of the states are generally weakly coupled to each other such that the avoided crossings are tiny and are passed diabatically. Nevertheless, the

quasienergy spectrum becomes very complex and a parameter variation can result in the excitation of a lot of Floquet states. This scenario will be discussed in more detail in Chap. 5.

3. Coherent Coupling of Orbital Degrees of Freedom

In this chapter we will demonstrate how lattice shaking can be used to coherently couple the ground band of a one-dimensional optical lattice to the first excited band, which is usually separated by a large energy gap. Hence, orbital degrees of freedom can be opened. We then show how this allows to melt a Mott insulating ground state adiabatically into a superfluid.

In Sec. 3.1 we start by giving a short introduction to orbital physics in solid state systems and optical lattices, and describe important experiments with ultra-cold atoms that include higher Bloch bands in the dynamics. In section 3.2 we derive the two-band Hubbard model for a dimerized one-dimensional optical lattice and argue that it is a reliable description of the bosonic dynamics in the tight-binding regime. Accordingly, in Sec. 3.3 we apply resonant lattice shaking to the system and show how it can be represented in the Hubbard model. By making a high-frequency approximation, we derive an effective two-band Hubbard model for the driven system, where the lowest two Bloch bands are overlapping in energy and coupled by the periodic driving. For this effective Hubbard Hamiltonian, in Sec. 3.4 we explain different methods to exactly and approximately calculate the ground state. With these methods, in Sec. 3.5 we numerically verify the orbital-driven quantum phase transition between a Mott insulator and a superfluid. In contrast to the well-known single-band version of this phase transition, we show how in the orbital driven proposal the transition can be first or second order, depending on the parameter regime. Finally, we numerically simulate an adiabatic protocol that realizes the phase transition and demonstrate that in a dimerized lattice heating to higher lying Bloch bands can be neglected for an adequate choice of parameters.

3.1. Orbital Degrees of Freedom in Optical Lattices

In this section we give a short introduction to the physics of orbital degrees of freedom in solid state physics and optical lattices.

If we consider the orbitals of the electronic wave function in an atom, the attracting potential of the nucleus can be described by a Coulomb potential. In this case the electronic orbitals can be classified by the three quantum numbers: the principle quantum number n, the azimuthal quantum number l and the magnetic quantum number m [127]. The orbitals are isotropic if $l = 0$, otherwise they allow for spatial alignment, for example as hybrid-orbitals encountered in the formation of molecules. The hybridization of orbitals is also possible since, due to the conservation of the Laplace–Runge–Lenz vector in the $1/r$ Coulomb potential, atomic orbitals with the same n are degenerate. In solid state materials, where the orbitals of the periodically ordered atoms form Bloch bands, the interplay of orbitals due to their energetic ordering leads to interesting phenomena. A prominent example are heavy-fermion compounds that emerge from the interplay between dispersive conduction-band orbitals and strongly localized orbitals, with a large effective mass and strong Coulomb interactions [128–131].

In systems of ultracold bosons in optical lattices, the orbital degrees of freedom so far have played only a minor role. The reason is that there is a crucial difference between optical lattices and solid state materials, namely the on-site potential. In contrast to the Coulomb potential, where the Runge-Lentz vector is conserved, optical lattices resemble on-site often a harmonic potential, for example in the simple cosine potential [132]. Therefore, eigenstates and -energies resemble rather those of the harmonic oscillator, where the orbital ordering in energy is different from those from atomic physics. For example, whereas in the hydrogen atom there is a genuine degeneracy between the $2s$ and the $2p$ states (p_x, p_y and p_z in three dimensions), in the harmonic oscillator the p states are energetically isolated from the s-state. In optical lattices therefore, mixing of s orbitals, related to the ground band, and p orbitals, related to the first excited band, is in many cases prevented by an energy gap. Because of this energy gap, at ultra-cold temperatures bosons all condense to the ground band, especially in the interesting tight-binding regime of strong interactions. For many cold-atom experiments within the ground

band [35, 62, 63, 66, 71, 73, 74, 133], where one explicitely wants to disregard higher orbitals, this property is an advantage. This single-band approximation has been verified by quantifying the perturbative admixture of excited bands to the ground band in theory [134–141] and experiment [142–147].

Nonetheless, the physics of atoms in higher Bloch bands of optical lattices and their orbital properties have caught considerable interest recently, especially on the theoretical side [148–154]. In the p-band of the two-dimensional square lattice one can, for example, study orbital magnetism and finds orbital ordering similar to Hund's rule in atomic physics. The orbital ordering arises from the on-site repulsion of the atoms and the degeneracy of the p_x and the p_y orbitals [149, 154]. One possibility to open the orbital degrees of freedom in an optical lattice, is to transfer atoms non-adiabatically to excited bands, see for example [61, 92, 96, 155–157]. The life-time of the atoms in isolated higher orbitals, however, is limited due to resonant scattering processes [158], which transfer atoms back into the ground band. Furthermore, the energy gap between the bands can be exploited to coherently couple the orbital degrees of freedom by external fields. Thereby, the orbitals from the different Bloch bands are coupled with each other, which is not possible in the case of an abrupt excitation of the atoms. This coherent coupling can be achieved for example by exploiting magnetic resonances [159]. A simpler scheme, however, is to achieve the coherent coupling of Bloch bands by periodically forcing the lattice, e.g. in form of lattice shaking. In the weakly interacting regime, this has already been achieved experimentally, where the condensation into two possible momentum states led to domain formation [93]. Theoretically, band coupling by periodic forcing for non or weakly interacting particles has been studied in Ref. [160–166].

In this chapter, we analyze the possibility to coherently couple Bloch bands in an optical lattice by lattice shaking for strongly interacting bosons. To provide a minimal example, we consider spinless bosons in one dimension. For this system we show how in the high-frequency regime it is possible to realize a "dressed-lattice" system, where effectively at every lattice site the strongly localized ground-band orbital is nearly degenerate and coupled to the much more dispersive first-excited-band orbital.

3.2. The Non-Driven Two-Band Hubbard Hamiltonian

In this section we show how in the tight-binding regime of a static one-dimensional optical lattice, a Hubbard model can be derived, which is a simple model to describe the dynamics of the strongly interacting bosons. In addition to the ground band, we also include the first excited Bloch band in the calculations, as it will be relevant in the dynamics due to the resonant periodic driving.

In general, the full non-relativistic three-dimensional Hamiltonian of a cold bosonic gas of atoms in an optical lattice takes the form

$$
\begin{aligned}
\hat{H}_{\text{full}} &= \hat{H}_{\text{sp}} + \hat{H}_{\text{int}} \\
&= \int d\boldsymbol{r}\,\hat{\psi}^{\dagger}(\boldsymbol{r})h_{\text{sp}}\hat{\psi}(\boldsymbol{r}) \\
&\quad + \frac{1}{2}\int d\boldsymbol{r}\,d\boldsymbol{r}'\,\hat{\psi}^{\dagger}(\boldsymbol{r})\hat{\psi}^{\dagger}(\boldsymbol{r}')U(\boldsymbol{r}'-\boldsymbol{r})\hat{\psi}(\boldsymbol{r}')\hat{\psi}(\boldsymbol{r})
\end{aligned}
\tag{3.2.1}
$$

and can be divided into a single-particle part $\hat{H}_{\text{sp}}$ with Hamiltonian density

$$
h_{\text{sp}} = -\frac{\hbar^2 k_L^2}{2m}\Delta + V(\boldsymbol{r})
\tag{3.2.2}
$$

and an interaction part $\hat{H}_{\text{int}}$. Here, we have denoted $\hat{\psi}(\boldsymbol{r})$ the bosonic field operator, k_L the wave vector of the laser, m the mass of the bosons and $U(\boldsymbol{r})$ the full interaction potential between two atoms. As energy unit we will use the recoil energy

$$
E_R = \frac{\hbar^2 k_L^2}{2m},
\tag{3.2.3}
$$

which is needed to localize a particle on a lattice constant $a = \pi/k_L$. In this chapter we consider Rb[87] atoms and a typical laser wave length of $2\pi/k_L = 852$ nm, as it is used in many experimental groups [35, 71, 167]. These parameters result in a recoil energy of $E_R = 2\pi\hbar \cdot 3.16$kHz. Since the energies are low, the interactions are approximated by contact potential. The interaction strength is determined by the s-wave scattering length a_s of the atom type. Hence, the full interaction

operator $U(\boldsymbol{r})$ is replaced by a pseudo-potential operator, which eventually gives the interaction term the simple form [168]

$$\hat{H}_{\text{int}} \approx \frac{2\hbar^2 a_s}{m} \int d\boldsymbol{r}\, \hat{\psi}^\dagger(\boldsymbol{r}) \hat{\psi}^\dagger(\boldsymbol{r}) \hat{\psi}(\boldsymbol{r}) \hat{\psi}(\boldsymbol{r}). \tag{3.2.4}$$

Because of the continuous space variable $\boldsymbol{r}$, the Hamiltonian has infinitely many degrees of freedom. However, in an optical lattice which is deep enough, $V_0 \gg E_R$, where V_0 is the difference of potential maxima and minima, we can exploit the powerful tight-binding approximation [47]. Herein, we project the atomic wave function on those Wannier orbitals $w_{\boldsymbol{\alpha}}(\boldsymbol{r} - \boldsymbol{R})$ which are real and exponentially localized around a lattice site $\boldsymbol{R}$ [169, 170]. Together with the bosonic quantum operator $\hat{b}_{\boldsymbol{R},\boldsymbol{\alpha}}$, which destroys a boson in Wannier state $\boldsymbol{\alpha}$ at site $\boldsymbol{R}$ and which fulfills the commutation relation

$$\left[\hat{b}_{\boldsymbol{R},\boldsymbol{\alpha}}, \hat{b}^\dagger_{\boldsymbol{R}',\boldsymbol{\beta}}\right] = \delta_{\boldsymbol{R},\boldsymbol{R}'} \delta_{\boldsymbol{\alpha},\boldsymbol{\beta}}, \tag{3.2.5}$$

the bosonic field operator can be expanded in the Wannier basis via

$$\hat{\psi}(\boldsymbol{r}) \;\; = \;\; \sum_{\boldsymbol{R},\alpha} w_{\boldsymbol{\alpha}}(\boldsymbol{r} - \boldsymbol{R}) \hat{b}_{\boldsymbol{R},\boldsymbol{\alpha}}. \tag{3.2.6}$$

The Wannier functions can be computed from the Bloch states $\phi_{\boldsymbol{k},\alpha}(\boldsymbol{r})$ of the lattice, which are the eigenfunctions of the single-particle Hamiltonian with quasimomenta $\boldsymbol{k}$, via

$$w_{\boldsymbol{\alpha}}(\boldsymbol{r} - \boldsymbol{R}) = \frac{1}{\sqrt{M}} \sum_{\boldsymbol{k}} e^{i\boldsymbol{R}\cdot\boldsymbol{k}} \phi_{\boldsymbol{k},\boldsymbol{\alpha}}(\boldsymbol{r}). \tag{3.2.7}$$

Note here that the phase of the Bloch functions with respect to different $\boldsymbol{k}$ is still arbitrary and results in different sets of Wannier states. Only a special choice of the normalization of the Bloch functions leads to real and exponentially localized Wannier states [169]. If the lattice is non-separable, the choice of normalization is often non-trivial and the maximally localized Wannier states have to be constructed by numerical methods from the Bloch states [171, 172]. In a separable lattice, on

the other hand, also the Wannier functions separate

$$w_{\boldsymbol{\alpha}}(\boldsymbol{r}) = w_{\alpha_x}^x(x)w_{\alpha_y}^y(y)w_{\alpha_z}^z(z), \qquad (3.2.8)$$

such that the band index $\boldsymbol{\alpha}$ is a triplet of band indices $(\alpha_x, \alpha_y, \alpha_z)$ of band indices for each direction. Hence, the Wannier function for each dimension can be computed independently. For the one-dimensional case, it has been shown how the Wannier functions can be constructed directly [173]: For an even Wannier state, all Bloch states should have vanishing imaginary parts, wheres for an odd Wannier state, the Bloch states should have vanishing real parts.

In this chapter, we consider a one-dimensional lattice (in x-direction) stemming from a separable three-dimensional lattice, where the lattices in the two orthogonal directions (y and z) are very deep ($V_\perp = 30E_R$). Because of this, the system in the orthogonal directions is always in the ground state $\alpha_y = \alpha_z = 0$, and furthermore the dynamics in these orthogonal directions is completely frozen out. Therefore we consider only direction x and do not explicitly write out the x-index.

After plugging in the Wannier expansion (3.2.6) in the Hamiltonian (3.2.1), we ignore matrix elements between Wannier states that are separated by more than one lattice site since they are very small. This reduces the number of terms dramatically. Hence, we are left only with on-site interaction terms as well as up to nearest-neighbour terms in the kinetic energy. The resulting Hamiltonian including all Bloch bands takes the form

$$\hat{H}_{\text{tb}} = -\sum_{\ell}\sum_{\alpha}(-1)^\alpha J_\alpha(\hat{b}_{\alpha(\ell+1)}^\dagger \hat{b}_{\alpha\ell} + \text{h.c.}) + \sum_{\ell}\left[\sum_{\alpha}\epsilon_\alpha \hat{n}_{\alpha\ell} + \sum_{\{\alpha\}}\frac{U_{\{\alpha\}}}{2}\hat{b}_{\alpha_1\ell}^\dagger \hat{b}_{\alpha_2\ell}^\dagger \hat{b}_{\alpha_3\ell}\hat{b}_{\alpha_4\ell}\right], \qquad (3.2.9)$$

where we have introduced the notation $\hat{b}_{j\alpha} = \hat{b}_{(jd,0,0),(\alpha,0,0)}$ for the bosonic creation and annihilation operators. The band-center energies

$$E_\alpha = \int \mathrm{d}x\ w_\alpha(x)h_{\text{sp}}(x)w_\alpha(x) \qquad (3.2.10)$$

give the energy levels of the Wannier state with index α. The tunnel parameters

$$J_\alpha = -(-1)^\alpha \int \mathrm{d}x \; w_\alpha(x) h_{\mathrm{sp}}(x) w_\alpha(x-a) \qquad (3.2.11)$$

quantify the hopping strength between two neigbouring sites. Both quantities fulfill $E_0 < E_1 < \cdots$ and $0 < J_0 < J_1 < \cdots$, respectively. The on-site interaction strengths

$$U_{\{\alpha\}} \equiv U_{\alpha_1\alpha_2\alpha_3\alpha_4} = \frac{2\hbar^2 a_s a_\perp^2}{m} \int \mathrm{d}x \; w_{\alpha_1}(x) w_{\alpha_2}(x) w_{\alpha_3}(x) w_{\alpha_4}(x) \qquad (3.2.12)$$

vanish for odd $\sum_i \alpha_i$, since $w_\alpha(x) = (-1)^\alpha w_\alpha(-x)$. Here we denote the contributions from the orthogonal lattice directions by

$$a_\perp = \int \mathrm{d}y \; \left|w_\alpha^y(y)\right|^4 = \int \mathrm{d}z \; \left|w_\alpha^z(z)\right|^4. \qquad (3.2.13)$$

Since we are interested in a minimal two-band model, we explicitly write out Hamiltonian (3.2.9) with just two Bloch bands, i.e. $\alpha = 0$ and $\alpha = 1$. This results in the two-band bosonic Hubbard model

$$\begin{aligned}
\hat{H}_0 &= \hat{H}_{\mathrm{orbital}} + \hat{H}_{\mathrm{tun}} + \hat{H}_{\mathrm{int}} \\
&= D \sum_{i=1}^{M} \hat{n}_{i,1} + \sum_{<ij>} \left(-J_0 \hat{b}_{i,0}^\dagger \hat{b}_{j,0} + J_1 \hat{b}_{i,1}^\dagger \hat{b}_{j,1} \right) \\
&\quad + \sum_i \left[\sum_{\alpha=0,1} \frac{U_{\alpha\alpha}}{2} \hat{n}_{i,\alpha}(\hat{n}_{i,\alpha}-1) + 2U_{01}\hat{n}_{i,0}\hat{n}_{i,1} + \frac{U_{01}}{2}\left(\hat{b}_{i,0}^\dagger \hat{b}_{i,0}^\dagger \hat{b}_{i,1}\hat{b}_{i,1} + \mathrm{h.c.)} \right) \right],
\end{aligned} \qquad (3.2.14)$$

where we used the short notation $U_{\alpha\beta} = U_{\alpha\alpha\beta\beta}$. Here, $D = E_1 - E_0$ denotes the energy difference between the two Bloch band centers. Note that the second interaction term in (3.2.14) has an additional prefactor of 2, which results from four different ways of assigning band indices to the four bosonic operators. The two-band Bose-Hubbard model is illustrated in Fig. 3.2.1.

Next we specify the lattice potential. In an one-dimensional one-mode optical lattice with depth V_0, created by two counter propagating laser beams of the same
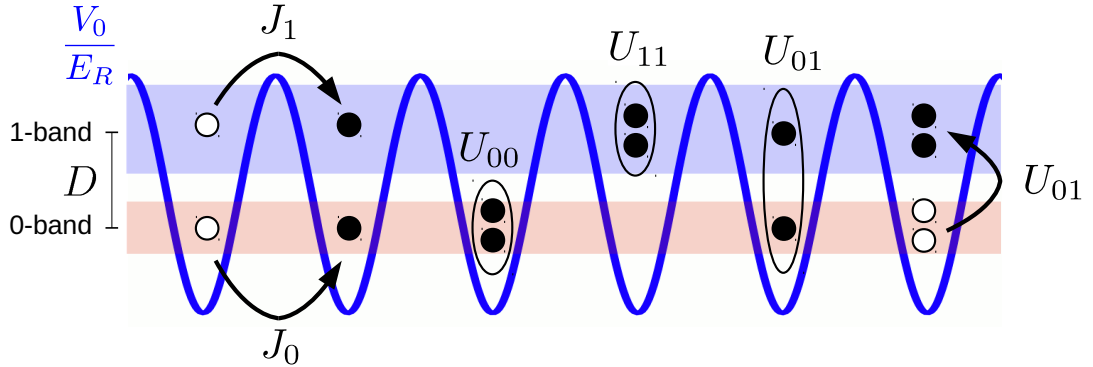
Figure 3.2.1.: Illustration of the (undriven) two-band Hubbard Hamiltonian (3.2.14).

wave length, the potential is simply a cosine [24]

$$V(x) = -\frac{V_0}{2} \cos(2k_L x). \tag{3.2.15}$$

We first consider the energy bands of the single-particle Hamiltonian with this potential as a function of the lattice depth V_0. Upper and lower edge of the lowest three bands are plotted in Fig 3.2.2. We observe that the band centers are almost equidistant. In fact, since $\cos(x)$ can be approximated by a harmonic oscillator in the center of its minima, close to the lattice minima the Wannier states are similar to the lowest eigenstates of the harmonic potential. In Fig 3.2.3 (left) we show the Wannier states of the cosine potential for the lowest three bands. In Fig 3.2.3 (right) we also show the same Wannier states with logarithmic axes to demonstrate their exponential localization.

The almost equidistance of the energy band centers inherited from the harmonic oscillator functions is problematic if we want to resonantly couple only two bands, e.g. the ground and the first excited band, without coupling to the second excited and higher bands. To illustrate this, we plot in Fig. 3.2.2(right) the three lowest energy bands as a function of the lattice depth, but this time we substract from the mth excited band m times the energy distance Δ between the ground and this first excited band, as if they were resonantly coupled. The energy distance is rather small and the bands overlap partly. Even if the energies do not exactly overlap resonantly and even if the states belonging to these energies might have
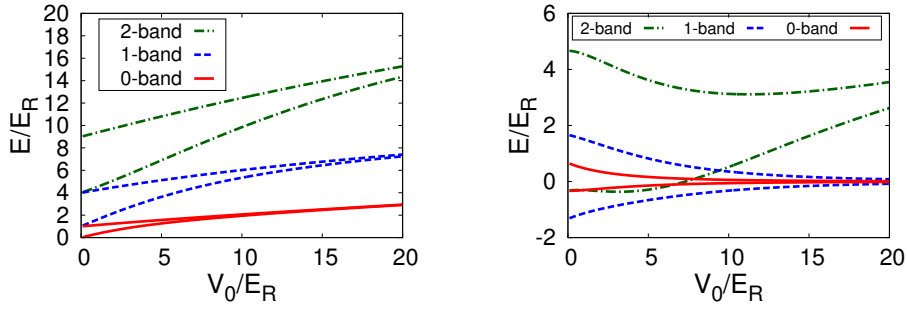
Figure 3.2.2.: Left: Minima and maxima of the lowest three bands of the simple cosine lattice. Right: The same bands but substracted by the energy difference $E_1 - E_0$ as to demonstrate the energy distance to the second excited band when the lowest to bands are in resonance with each other.
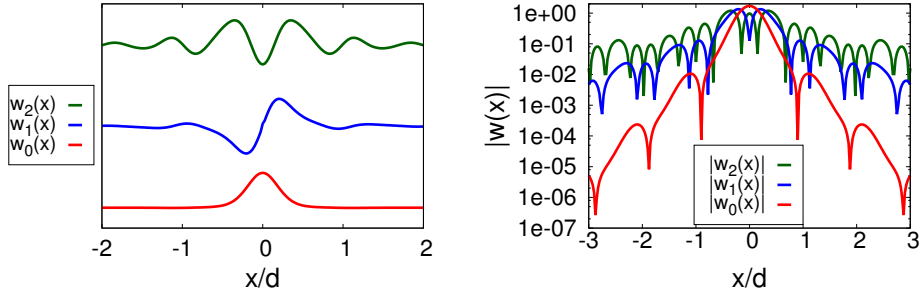
Figure 3.2.3.: Lowest three Wannier states without dimerization at a lattice depth of $V_0 = 10E_R$. The y-axes are normal (left) and logarithmic (right).

a different quasimomentum, this (almost) degeneracy poses a problem since the interaction terms shift the energies further and mix states with different quasimomenta. Consequently, if in an experiment the system starts solely in the ground band, the higher lying bands would be excited one by one, which corresponds to heating.

To avoid this problem, we engineer the band structure with a trick: We consider a potential with a second mode of half the wave length. This potential forms a dimerized lattice if both modes have a phase shift of π, taking the form

$$V(x) = -\frac{V_0}{2}\cos(2k_L x) + \frac{V_1}{2}\cos(4k_L x). \tag{3.2.16}$$

35
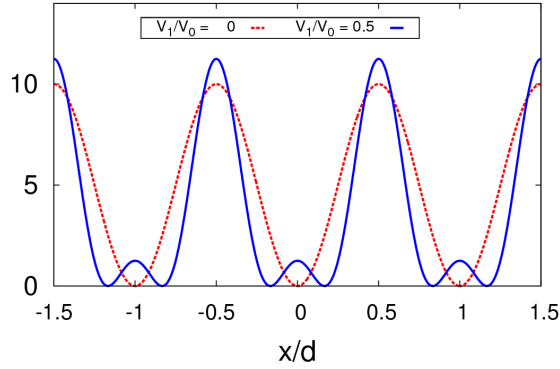
Figure 3.2.4.: Illustration of the lattice without dimerization ($V_1 = 0$, in red) and with the dimerization ($V_1 = 0.5V_0$, in blue) that is used in the calculations. A constant has been added so that the potential is positive everywhere.

The dimerized potential is illustrated and compared to the cosine potential in Fig. 3.2.4. For an increasing dimerization ratio V_1/V_0, the energy bands move together in pairs, as shown in Fig. 3.2.5 (left). Therefore, the equidistance of the energy bands is broken: the energy distance between the lowest two bands becomes smaller than the distance between first and second excited band. In Fig. 3.2.5 (right) we plot again the bands in the case of a resonant coupling between the ground and the first excited bands: Due to the dimerization, the third band gets off-resonant, which would suppress unwanted excitations to the third and higher lying bands and thus minimize heating.

In the extreme case $V_1/V_0 = \infty$ (e.g. if $V_0 = 0$), we end up with a simple cosine lattice of half the wavelength, having half the number of bands, each with twice the number of states. However, in this case we will lose the orbital degree of freedom between these two joint bands since the two orbitals would only be the even and odd superpositions of Wannier states. Thus, for large dimerizations V_1/V_0 the Hubbard parameters, like the tunneling coefficents J_0 and J_1 and the interaction parameters U_{00} and U_{11} become very similar, as it is illustrated in Fig. 3.2.7. We would like to avoid this regime since we are interested in the scenario where a rather dispersive band 1 is coupled to band 0 of well localized orbits, i.e. $J_1 \gg J_0$. This difference can lead to interesting physical phenomena and phase transitions, like the Mott insulator to superfluid transition described in Sec. 3.5. Hence, there should only be a slight dimerization coefficient like $V_1/V_0 = 0.5$. For this dimerization, the Wannier
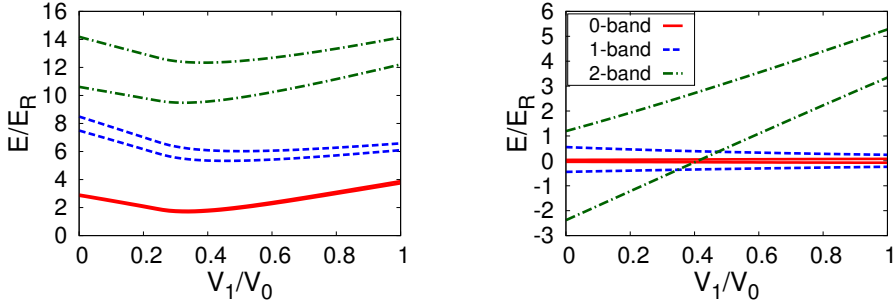
Figure 3.2.5.: Band structure (upper and lower band limits) for the cosine potential with $V_0 = 10E_R$. Left: Three lowest lying energy bands. Right: The same bands as quasi-energy bands if the ground and the first excited band get resonantly coupled. The ground band is very narrow such that upper and lower band limits merge to one line.
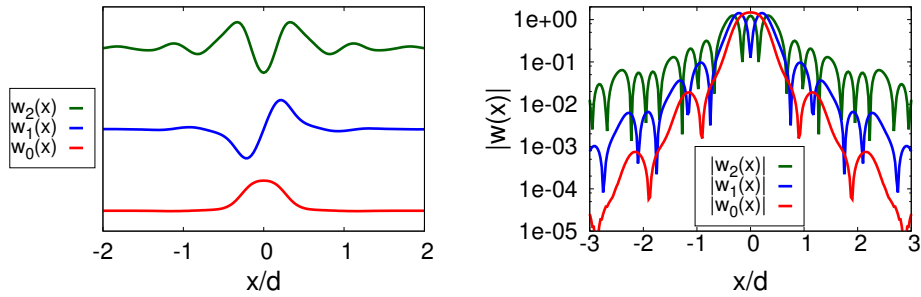

Figure 3.2.6.: Wannier states with a dimerization of $V_1 = 0.5V_0$ at a lattice depth of $V_0 = 10E_R$. The y-axes are linear (left) and logarithmic (right).

functions are altered only slightly (see Fig. 3.2.6). The band dispersions are still quite different. At the same time, the equidistance of the energy bands is already lifted to an often sufficient amount, making a resonant coupling between two bands feasable with little heating.

We fix the dimerization to $V_1/V_0 = 0.5$ in the following since it is an optimal choice. We have computed the relevant Hubbard parameter for the dimerized, static two-band Hamiltonian (3.2.14): In Fig. 3.2.8 (left) we plot the tunneling parameters J_α on a logarithmic axis as a function of the lattice depth V_0. All tunneling parameters fall off exponentially as one increases the lattice depth, as it is the case for an undimerized lattice [174]. Thus, by increasing the barrier between the lattice sites,
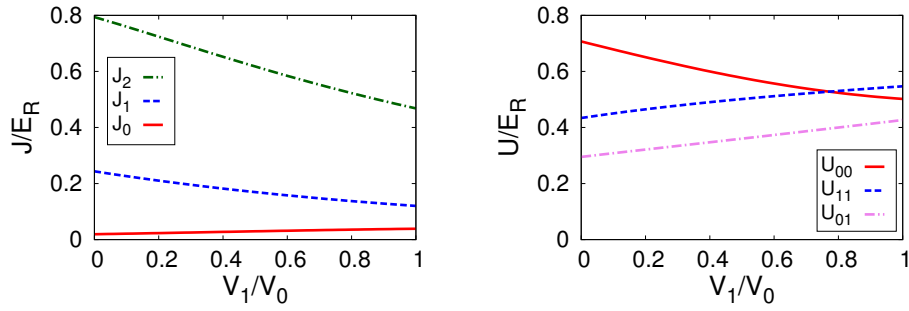
Figure 3.2.7.: Tunnel parameters (left) and interaction coefficients (right) of the dimerized lattice as a function of the normalized dimerization V_1/V_0 for $V_0 = 10E_R$.
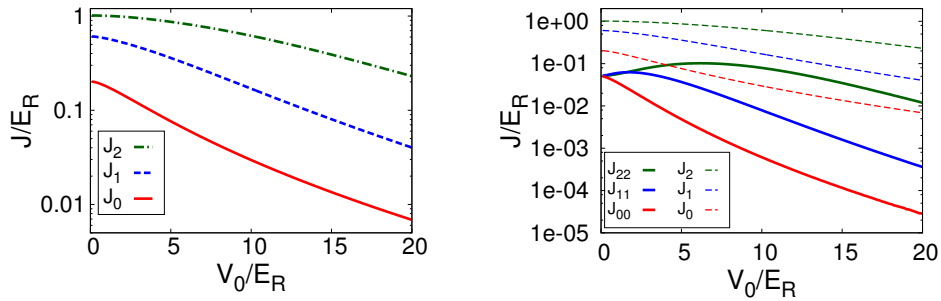
Figure 3.2.8.: Left: Tunnel parameters of the dimerized lattice with $V_1/V_0 = 0.5$ as a function of the lattice depth V_0. Right: Neglected next-nearest neighbour tunnel coefficients $J_{\alpha\alpha}$ (solid lines) compared to the nearest neighbour tunnel coefficients J_α (dashed lines).

the probablity of a tunnel process to occur falls off dramatically. To justify the tight binding approximation, where we neglected next-nearest-neighbour (NNN) tunneling, we plot the NNN tunneling parameters of bands denoted by $J_{\alpha\alpha}$ for the lowest three bands $\alpha = 0, 1, 2$ in Fig. 3.2.8 (right). We see that for each band the NNN tunneling parameters are at least one order of magnitude below the nearest-neighbour tunneling parameters, so that they indeed can be neglected. On the other hand, the on-site interaction parameters of the lattice bosons increase only moderately with the lattice depth, see Fig. 3.2.9. Thus, the ratio U_{00}/J_0 can be controlled efficiently by the lattice depth, which makes it easy to drive the phase transition between a Mott insulating and a superfluid ground state [34, 35].
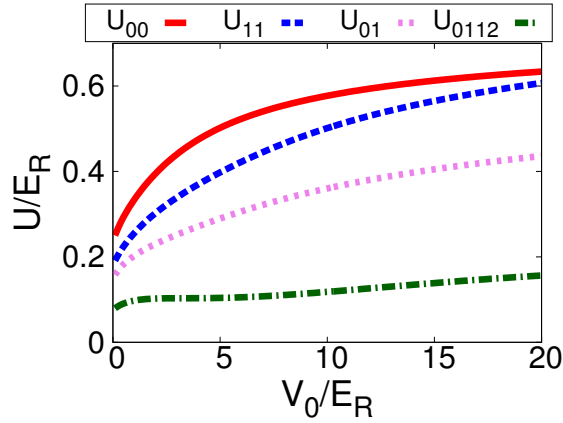
Figure 3.2.9.: Interaction parameters of the lowest two bands and U_{0112} in the dimerized lattice with $V_1/V_0 = 0.5$ as a function of the lattice depth V_0.

3.3. Effective Two-Band System in a Resonantly Shaken Lattice

In the tight-binding regime, the band distance D between ground and first excited band in Eq. (3.2.14) is typically much larger than the energy scales of the kinetics and the interaction (see Fig. 3.2.2 and Fig. 3.2.5). Therefore, the orbital degree of freedom stemming from the first and higher excited bands is frozen out. Cold bosons in non-driven optical lattices in the tight binding regime are described very accurately already by the ordinary single-band Bose-Hubbard model [34]. However, we wish to coherently open the orbital degree of freedom by means of time periodic forcing with near-resonant frequency $\hbar\omega \approx D$. In particular, the lowest band ($\alpha = 0$) shall be coupled to the more dispersive first excited band ($\alpha = 1$), without creating coupling to even higher-lying bands ($\alpha \geq 2$). As described in the previous section, these higher lying transitions can be made off-resonant by dimerizing the lattice slightly (see Fig. 3.2.5). Furthermore, we choose a driving scheme, namely sinusoidally shaking the lattice back and forth, that couples predominantly only bands $\alpha' - \alpha = n$ with odd n. On the other hand, for weak forcing the multi-"photon" interband transitions at resonances $E_{\alpha'} - E_\alpha \approx m\hbar\omega$ are strongly suppressed, especially for even integers $|m|$. This will be shown in Chap. 5. Here, we will describe how an effective, time-independent Hamiltonian can be

derived for the shaken lattice. The potential that is shaken back and force in x-direction, takes the form

$$V(x,t) = V\left[x + lk_L\cos(\omega t)\right], \tag{3.3.1}$$

where $l = K/(\pi m\omega^2)$ is the amplitude of the shaking. It is reasonable to transform the problem into the comoving frame. There, an inertial force is exerted on the atoms. The transformation to the comoving frame is accomplished by three successive gauge transformations

$$
\begin{aligned}
U_1 &= \exp\left[-\frac{i}{\hbar}l\cos(\omega t)p\right] \\
U_2 &= \exp\left[-\frac{i}{\hbar}ml\omega\sin(\omega t)x\right] \\
U_3 &= \exp\left[-\frac{i}{\hbar}\frac{1}{2}ml^2\omega^2\int_0^t\sin^2(\omega\tau)d\tau\right].
\end{aligned}
\tag{3.3.2}
$$

By these unitaries $U = U_3U_2U_1$, the single-particle Hamiltonian in (3.2.1) is transformed to

$$
\begin{aligned}
h_{\mathrm{sp}}(t) \xrightarrow{U} h'_{\mathrm{sp}}(t) &= U^\dagger h_{\mathrm{sp}}U - i\hbar U^\dagger\frac{d}{dt}U \\
&= h_{\mathrm{sp}} + ml\omega^2\cos(\omega t)x,
\end{aligned}
\tag{3.3.3}
$$

whereas the interaction part is unaltered. Now we shift again to the one dimensional Wannier representation (3.2.6). For this we write the position as $x = j + (x - j)$ with site index j. Then the Hamiltonian (3.2.14) generalizes to

$$
\begin{aligned}
\hat{H}'(t) &= \hat{H}_0 + \hat{H}_{\mathrm{dr}}(t) \\
&= \hat{H}_0 + K\cos(\omega t)\sum_{j=1}^{M}\left[\sum_{\alpha=0,1}j\hat{n}_{\alpha j} + \sum_{\alpha'\alpha=0,1}\eta_{\alpha'\alpha}\hat{b}^\dagger_{\alpha'j}\hat{b}_{\alpha j}\right].
\end{aligned}
\tag{3.3.4}
$$

The interband coupling matrix elements

$$\eta_{\alpha'\alpha} = \frac{k_L}{\pi}F\int dx\ w_{\alpha'}(x)xw_\alpha(x) \tag{3.3.5}$$
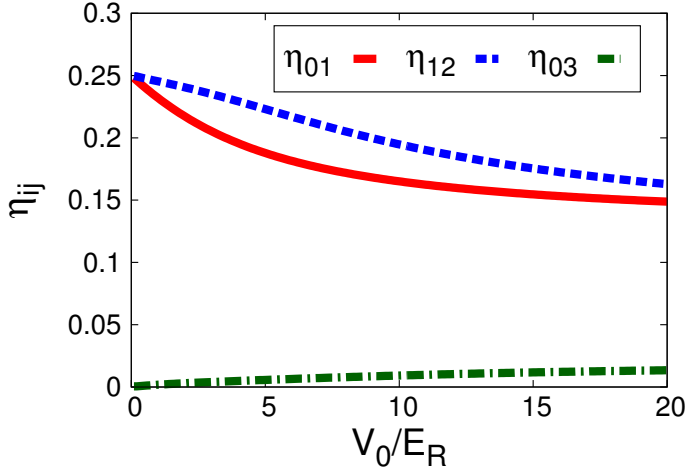
Figure 3.3.1.: Band coupling parameters η_{ij} induced by the shaking for the transitions which are relevant for the stability of the two-band model.

vanish for even $\alpha' + \alpha$ as indicated before. The coupling matrix elements for the band transitions $0 \rightarrow 1$, $1 \rightarrow 2$ and $0 \rightarrow 3$ are shown in Fig. 3.3.1. As we can see there, the coupling from the ground band to the third excited band with strength η_{03} can be neglected, though not the other two. All other coupling elements from the ground band are even weaker (not shown). The coupling matrix elements between higher lying bands are only relevant if the second excited band gets occupied which is not desirable in the first place.

Since the shaking frequency will assumed to be almost resonant between the lowest lying bands, we do another gauge transformation

$$\hat{U}_4 \quad = \quad \exp\left[-\frac{i}{\hbar}\sum_{j=1}^{M}\sum_{\alpha=0,1}\hat{n}_{\alpha,j}\ \alpha\omega t\right], \tag{3.3.6}$$

such that the eigenenergies of these two bands get close to each other. The full effect of the gauge transformation on the Hamiltonian reads

$$\hat{H}'(t) \overset{\hat{U}_4}{\rightarrow} \hat{H}''(t) \quad = \quad \hat{U}_4^{\dagger}\hat{H}'\hat{U}_4 - i\hbar\hat{U}_4^{\dagger}\frac{d}{dt}\hat{U}_4. \tag{3.3.7}$$

41

Combining the time derivative from the second term with the band distance, it is reduced by the photon energy like

$$D \overset{\hat{U}_4}{\to} \delta = D - \hbar\omega. \tag{3.3.8}$$

In the resonant case, the band distance is very small $\delta \ll D$. The transformation $\hat{U}_4$ furthermore changes those terms in the Hamiltonian that alter the occupation of the energy bands

$$\hat{H}_{\mathrm{dr}}(t) \overset{\hat{U}_4}{\to} K\cos(\omega t)\sum_{j=1}^{M}\left[\sum_{\alpha=0,1}j\hat{n}_{\alpha j} + \sum_{\alpha'\alpha=0,1}e^{i(\alpha-\alpha')\omega t}\eta_{\alpha'\alpha}\hat{b}^{\dagger}_{\alpha'j}\hat{b}_{\alpha j}\right]$$

$$\frac{U_{01}}{2}\sum_{j=1}^{M}\hat{b}^{\dagger}_{j,1}\hat{b}^{\dagger}_{j,1}\hat{b}_{j,0}\hat{b}_{j,0} \overset{\hat{U}_4}{\to} \exp(i2\omega t)\frac{U_{01}}{2}\sum_{j=1}^{M}\hat{b}^{\dagger}_{j,1}\hat{b}^{\dagger}_{j,1}\hat{b}_{j,0}\hat{b}_{j,0} \tag{3.3.9}$$

and the conjugated interaction process, respectively. Finally, we also integrate out the driving term in Hamiltonian (3.3.4) by the transformation

$$\hat{U}_5 = \exp\left[-i\frac{K}{\hbar\omega}\sin(\omega t)\sum_{j=1}^{M}\sum_{\alpha=0,1}j\hat{n}_{\alpha j}\right] \tag{3.3.10}$$

Since the driving term breaks the translational symmetry, the tunneling terms are transformed as

$$\hat{b}^{\dagger}_{j,\alpha}\hat{b}_{j+1,\alpha} \overset{\hat{U}_5}{\to} \hat{b}^{\dagger}_{j,\alpha}\hat{b}_{j+1,\alpha}\exp\left[-i\frac{K}{\hbar\omega}\sin(\omega t)\right] \tag{3.3.11}$$

$$\tag{3.3.12}$$

In total, the transformed Hamiltonian takes the form

$$\begin{aligned}
\hat{H}''' = \sum_{j=1}^{M}\Bigg\{ & \delta\hat{n}_{j,1} + \left[e^{-i\frac{K}{\hbar\omega}\sin(\omega t)}\left(-J_0\hat{b}^{\dagger}_{j,0}\hat{b}_{j+1,0} + J_1\hat{b}^{\dagger}_{j,1}\hat{b}_{j+1,1}\right) + \mathrm{h.c.}\right] \\
& + \sum_{\alpha=0,1}\frac{U_{\alpha\alpha}}{2}\hat{n}_{j,\alpha}(\hat{n}_{j,\alpha}-1) + 2U_{01}\hat{n}_{j,0}\hat{n}_{j,1} + \left[e^{i2\omega t}\frac{U_{01}}{2}\hat{b}^{\dagger}_{j,1}\hat{b}^{\dagger}_{j,1}\hat{b}_{j,0}\hat{b}_{j,0} + \mathrm{h.c.}\right] \\
& + K\cos(\omega t)\Big[\sum_{\alpha'\alpha=0,1}e^{i(\alpha-\alpha')\omega t}\eta_{\alpha'\alpha}\hat{b}^{\dagger}_{\alpha'j}\hat{b}_{\alpha j}\Big]\Bigg\}. \tag{3.3.13}
\end{aligned}$$

For weak forcing $K \ll \hbar\omega$ the driving frequency $\hbar\omega \sim \Delta_{10}$ is large compared to the intraband terms as well as to the band coupling. This allows us to average over the rapidly oscillating terms in the Hamiltonian over one driving period T and to write down an effective Hamiltonian $\hat{H}_{\text{eff}}$ that describes the dynamics on slow time scales $t \gg T = 2\pi/\omega$, to obtain

$$\hat{H}_{\text{eff}} = \frac{1}{T} \int_0^T \mathrm{d}t \; \hat{H}'''(t). \tag{3.3.14}$$

In other words, we keep only the diagonal term $m = n$ in the quasienergy operator

$$\hat{H}_{m,n} = \frac{1}{T} \int_0^T \mathrm{d}x \; \exp\left[-i(m-n)\omega t\right] \hat{H}'''(t) \tag{3.3.15}$$

or the 0-th term in the Fourier series

$$\hat{H}'''(t) = \sum_{-\infty}^{\infty} \exp(im\omega t) \hat{H}_m, \tag{3.3.16}$$

see Chap. 2. The resulting effective time-independent two-band Hamiltonian $\hat{H}_{\text{2B}} = \hat{H}_{\text{eff}}$ reads

$$
\begin{aligned}
\hat{H}_{\text{2B}} &= \delta \sum_{i=1}^{M} \hat{n}_{i,1} + \mathrm{J}_0\left(\frac{K}{\hbar\omega}\right) \sum_{<ij>} \left(-J_0 \hat{b}_{i,0}^\dagger \hat{b}_{j,0} + J_1 \hat{b}_{i,1}^\dagger \hat{b}_{j,1}\right) + \frac{\eta K}{2} \sum_{j=1}^{M} \left(\hat{b}_{j,0}^\dagger \hat{b}_{j,1} + \hat{b}_{j,1}^\dagger \hat{b}_{j,0}\right) \\
&\quad + \sum_i \left[\sum_{\alpha=0,1} \frac{U_{\alpha\alpha}}{2} \hat{n}_{i,\alpha}(\hat{n}_{i,\alpha} - 1) + 2U_{01} \hat{n}_{i,0} \hat{n}_{i,1} + \frac{U_{01}}{2} \left(\hat{b}_{i,0}^\dagger \hat{b}_{i,0}^\dagger \hat{b}_{i,1} \hat{b}_{i,1} + \hat{b}_{i,1}^\dagger \hat{b}_{i,1}^\dagger \hat{b}_{i,0} \hat{b}_{i,0}\right) \right]
\end{aligned}
\tag{3.3.17}
$$

and is illustrated in Fig. 3.3.2.

Apart from the tight-binding approximation in the last section, in this section we made two approximations: the high-frequency approximation and the neglection of bands above the first excited Bloch band. In the case of coherently coupled Bloch bands, the high-frequency approximation, where the gauge transformed, time-dependent Hamiltonian is approximated by its time average, should be reliable. The reason is that, even for the dimerized lattice, the driving energy $\hbar\omega$ is typically of the order of several E_R and therefore much larger than the lattice parameters J_α and $U_{\alpha,\beta}$, as we have seen in Figs. 3.2.5, 3.2.8 and 3.2.9. Also the band coupling
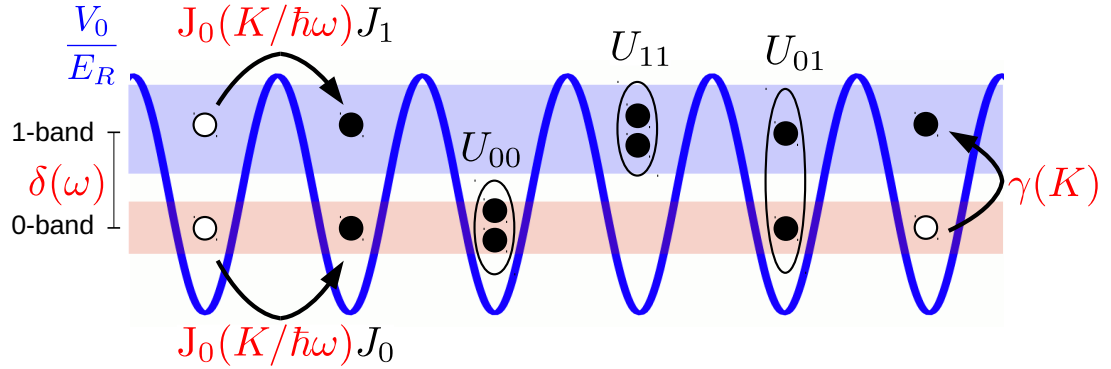
Figure 3.3.2.: Illustration of the effective two-band Hubbard Hamiltonian (3.3.17). Changes to the original Hubbard Hamiltonain (3.2.14) are marked in red. Apart from a slight parameterization of the tunneling with a 0-th order Bessel function, the band distance is reduced $D \rightarrow \delta(\omega)$ and the bands are directly coupled with strength $\gamma \sim K$. Also, the two-particle scattering term does not appear in the effective model anymore.

$K\eta_{\alpha\beta}$ stays well below $1E_R$ such that the driving amplitude K can go up to $1E_R$. For a more systematic derivation of Eq. (3.3.17), $\hat{H}_{\text{eff}}$ is defined as the generator of the time evolution over one period [109] of the shaking. It can then be computed using degenerate perturbation theory in the extended Floquet Hilbert space [108], similar like in Refs. [69,175]. In leading order one recovers Eq. (3.3.17). The leading correction contains tiny second-order coupling to bands $\alpha \geq 3$ of order $c^2/\hbar\omega$, where $c \lesssim 0.1E_R$ is a typical interband coupling matrix element and $\hbar\omega \gtrsim 3E_R$.

3.4. Methods to Analyze the Two-Band Many-Body Ground State

In this section we will present different methods that allow us to analyze the ground state of the many-body effective two-band Hamiltonian (3.3.17). The ground state properties give us information about the zero-temperature behavior of the system, which is most relevant in an experiment with ultra-cold atoms, even at finite but small temperatures. Here we are especially interested in the quantum phase of the ground state (Mott insulator or superfluid) since the quantum phase can be switched coherently by tuning the driving frequency, see Sec. 3.5. First

we will consider the single-particle problem and then the exact solution of the interacting system. However, since the Hilbert space dimension for a bosonic quantum chain grows exponentially with the system size (both for number of sites M and number of bosons N) we also need to introduce approximation methods to get reliable information about the quantum phase. Therefore, we will present also the Gutzwiller mean-field and the TEBD method in this section.

3.4.1. Solution of the Single-Particle and the On-Site Problem

It is helpful to first consider the single-particle problem of (3.3.17). The single-particle problem can be solved analytically. The solutions can be used to describe the many-body eigenstates and eigenenergies of the full interacting system. For small interactions, they are still a good approximation or can be used as a starting point for further approximations.

Hence, we consider the single-particle Hamiltonian

$$
\hat{H}_{\mathrm{sp}} = \delta \sum_{i=1}^{M} \hat{n}_{i,1} + \mathrm{J}_0\left(\frac{K}{\hbar\omega}\right) \sum_{<ij>} \left(-J_0 \hat{b}_{i,0}^\dagger \hat{b}_{j,0} + J_1 \hat{b}_{i,1}^\dagger \hat{b}_{j,1}\right) - \gamma \sum_{j=1}^{M} \left(\hat{b}_{j,0}^\dagger \hat{b}_{j,1} + \hat{b}_{j,1}^\dagger \hat{b}_{j,0}\right),
$$

$$(3.4.1)$$

where we assume periodic boundary conditions. Because of translational symmetry, we make the Ansatz for the single-particle wave function

$$
|\psi^\pm(k)\rangle = \sum_j e^{ikja}\left(\psi_0^\pm(k)|j0\rangle + \psi_1^\pm(k)|j1\rangle\right).
$$

$$(3.4.2)$$

where $|j\alpha\rangle = \hat{b}_{j,\alpha}^\dagger|\mathrm{vac}\rangle$ and k denoting the quasimomentum of the state. With this Ansatz, the Schrödinger Equation corresponding to Hamiltonian (3.4.1) in quasimomentum space reads

$$
\begin{pmatrix} -2J_0\cos(ka) & -\gamma \\ -\gamma & \delta + 2J_1\cos(ka) \end{pmatrix} \begin{pmatrix} \psi_0^\pm(k) \\ \psi_1^\pm(k) \end{pmatrix} = \epsilon_\pm(k) \begin{pmatrix} \psi_0^\pm(k) \\ \psi_1^\pm(k). \end{pmatrix}
$$

$$(3.4.3)$$

Diagonalizing this matrix gives the effective dispersion relation of the hybridized bands

$$\epsilon_\pm(k) = \frac{\delta}{2} + \cos(ka)(J_1 - J_0) \pm \sqrt{\left(\frac{\delta}{2} + \cos(k)(J_1 + J_0)\right)^2 + \gamma^2}, \qquad (3.4.4)$$

where the minus denotes the ground state and the plus denotes the excited state. The corresponding eigenstates take the form

$$\begin{pmatrix} \psi_0^-(k) \\ \psi_1^-(k) \end{pmatrix} = \begin{pmatrix} 1 \\ \frac{\epsilon_-(k) + 2J_0 \cos(ka)}{\gamma} \end{pmatrix} \frac{1}{\sqrt{1 + \left(\frac{\epsilon_-(k) + 2J_0 \cos(ka)}{\gamma}\right)^2}}$$

$$\begin{pmatrix} \psi_0^+(k) \\ \psi_1^+(k) \end{pmatrix} = \begin{pmatrix} 1 \\ \frac{\epsilon_+(k) + 2J_0 \cos(ka)}{\gamma} \end{pmatrix} \frac{1}{\sqrt{1 + \left(\frac{\epsilon_+(k) + 2J_0 \cos(ka)}{\gamma}\right)^2}}. \qquad (3.4.5)$$

In Fig. 3.4.1 we illustrate the dispersion relation, i.e. the two emerging eigenvalues as a function of the quasimomentum in a lattice of $V_0 = 10E_R$ and $K = 0.5E_R$ for different band distances $\delta = [1E_R, 0.5E_R, 0, -0.5E_R]$. The color code shows the ratio of the two bands: Red color indicates a dominant fraction of the 0-band, whereas blue represents a major fraction of the 1-band. Thus, green stands for a coherent mixture between 0- and 1-band due to the coupling term with strength $-\gamma$.

In general, one observes that if one decreases the band distance from a large positive value $\delta \gg \gamma, J_1$ to a large negative value $\delta \ll -\gamma, -J_1$, the bands pass each other, while they hybridize in the intermediate regime. Since the bands are coupled to each other with strength γ, which is independent of the quasimomentum k, the hybridization is strongest for those quasimomenta where the quasienergies lie close to each other. This happens where the bands would cross each other, e.g. at the border of the Brillouin zone for $\delta \approx 0.5E_R$ and in the center for $\delta \approx -0.5E_R$. The width of the avoided crossing is $2|\gamma|$, which can be seen in the dispersion relation (3.4.4) when the first term in the square root cancels due to band crossing.

Since we are interested in the ground state, we have to find the minimum in the dispersion relation $\epsilon_-(k)$. Note that it is an effective dispersion relation and the "ground state" is the state that is adiabatically connected to the ground state of the
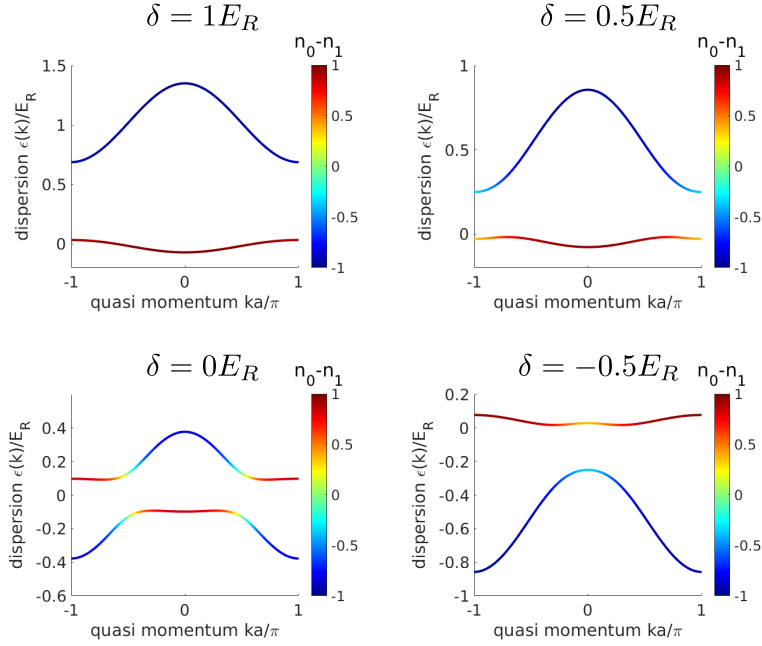
Figure 3.4.1.: Single-particle dispersion relation of Hamiltonian (3.4.1) in a lattice of $V_0 = 10E_R$ and $K = 0.5E_R$, for different band distances $\delta = [1E_R, 0.5E_R, 0, -0.5E_R]$.

non-driven system, via the chosen protocol. If for example, the two effective Bloch bands are coherently coupled the other way around, i.e. if the 1-band approaches the 0-band from below in quasi-energy, the effective ground state would be the one described here as the excited state, with a degenerate minimum in the hybridized region, see for example Ref. [93]. For $\delta \geq \delta_c$, we find the ground state at the center of the Brillouin zone at $k_{gs} = 0$, whereas for $\delta < \delta_c$, the ground state has quasimomentum $k_{gs} = \pi/a$. Assuming that at δ_c the dispersion of the ground band at $k = 0$ is almost not affected by the hybridization (since $J_1 \gg J_0$), we estimate from (3.4.4) for $\gamma/J_0 \ll 1$ by linearizing the square root,

$$\delta_c \approx 2(J_1 - J_0) + \frac{\gamma^2}{4J_0}. \tag{3.4.6}$$

For $\gamma \gg 4J_0$ we obtain

$$\delta_c \approx 2(J_1 - 3J_0) + \gamma + \frac{(\gamma - 4J_0)^2}{\gamma}. \tag{3.4.7}$$
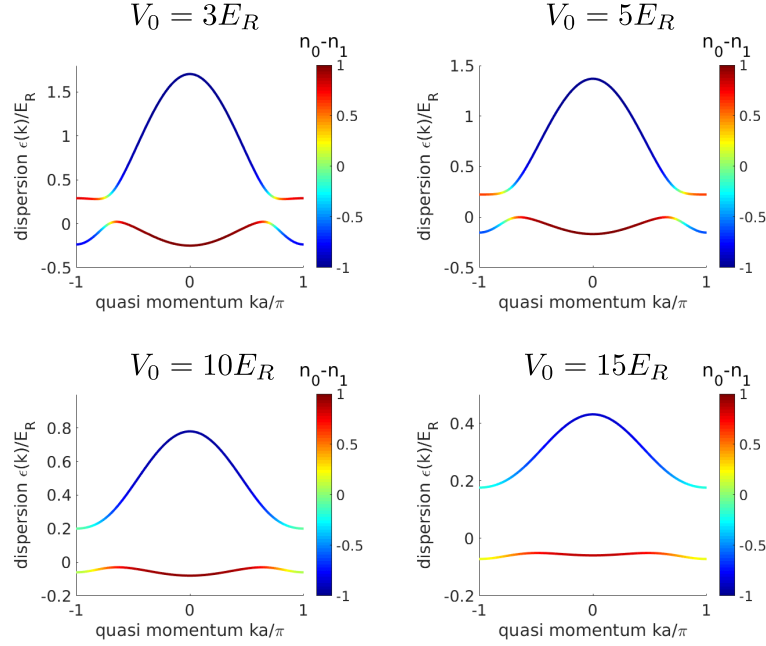
Figure 3.4.2.: Dispersion relation of the single-particle solution of Hamiltonian (3.4.1) at the critical band distance δ_c for different lattice depths $V_0/E_R = [3, 5, 10, 15]$ and $K = 0.5E_R$ giving roughly $\gamma \approx 0.121E_R$. In color we illustrate the fraction of 0- (red) and 1-band (blue), respectively.

These give critical values of $\delta_c/E_R = [0.755, 0.637, 0.421]$ for $V_0/E_R = [3, 5, 10]$ according to Eq. (3.4.6) and $\delta_c/E_R = 0.238$ for for $V_0/E_R = 15$ according to Eq. (3.4.7). In Fig. 3.4.2 we show the dispersion relations for these lattice depths at the estimated critical values. As expected, the minima approximately have the same energy and the hybridization takes place at the border of the Brillouin zone but not at the center, which justifies the approximations.

We can construct from the single-particle ground state the N-particle many-body ground state of the effective two-band model (3.3.17) in the limit of vanishing interactions. Thus, the ground state has the form

$$|\psi_{U=0}\rangle = \prod_{j=1}^{N} \left(\psi_0^-(k_{\text{gs}})\hat{a}_{0,k_{\text{gs}}}^\dagger + \psi_1^-(k_{\text{gs}})\hat{a}_{1,k_{\text{gs}}}^\dagger \right) |\text{vac}\rangle \qquad (3.4.8)$$

with the bosonic creation operators in momentum space $\hat{a}_{\alpha,k}^\dagger = \sum_j \exp(ikja)\hat{b}_{\alpha,j}^\dagger$. The ground state has energy $N\epsilon_{-,k_{\text{gs}}}$.

If on the other hand, one is interested in the limit of strong interactions, i.e. the Mott region where the bosons localize, it is instructive to diagonalize the single-site problem (3.4.1)

$$H_{\text{onsite}} = \delta \hat{n}_1 - \gamma \left(\hat{b}_0^\dagger \hat{b}_1 + \hat{b}_1^\dagger \hat{b}_0 \right),$$

(3.4.9)

for $N = 1$, where we skip the site index and the sum. The on-site energies are found to be

$$\epsilon_\pm = \frac{\delta}{2} \pm \sqrt{\frac{\delta^2}{4} + \gamma^2}$$

(3.4.10)

and the on-site eigenstates read

$$\begin{pmatrix} \psi_0^\pm \\ \psi_1^\pm \end{pmatrix} = \begin{pmatrix} 1 \\ \frac{\epsilon_\pm}{\gamma} \end{pmatrix} \frac{1}{\sqrt{1 + \left(\frac{\epsilon_\pm}{\gamma}\right)^2}}.$$

(3.4.11)

3.4.2. Exact Diagonalization

The most straightforward way to solve the effective Hubbard Hamiltonian (3.3.17) in any parameter region is by diagonalization. However, the Hilbert space dimension of a one-dimensional chain of N bosons on M lattice sites with an orbital degree of freedom of two is

$$\mathcal{D}(M, N) = \binom{N + 2M - 1}{N},$$

(3.4.12)

which can be estimated for large M, N using Stirlings formula [176] $x! \approx (x/e)^x \sqrt{2\pi x}[1 + O(1/x)]$ to be

$$\begin{aligned} \mathcal{D}(M, N) &\sim \exp\left\{ 2\left[(M + N) \ln\left(\frac{N}{M} + 1\right) - N \ln\left(\frac{N}{M}\right) \right] \right\} \\ &= \left(1 + \frac{N}{M}\right)^{2M} \left(1 + \frac{M}{N}\right)^{2N}. \end{aligned}$$

(3.4.13)

Hence, the size of the Hilbert space grows exponentially with the system size M and N. Therefore, diagonalization can be accomplished for rather small systems only. Nevertheless, if one is interested in the full spectrum or in properties of the ground state away from the theormodynamic limit, an exact diagonalization can be useful. Also, the exact diagonalization is very helpful to understand the basic behaviour of a system in the first place since it is straightforward to calculate expectation values like n-point functions and observables.

In order to perform the exact diagonalization, the first task is to find a proper ordered basis in the Hilbert space. In App. A we present one possible method to do so. With this method and by using the Lanczos algorithm for sparse matrices, the exact groundstate of a lattice with for example $N = 7$ bosons on $M = 7$ sites implying a Hilbert space dimension of $\mathcal{D}(7,7) \approx 10^5$ can be found. For a lattice with $N = 6$ bosons on $M = 6$ sites implying a Hilbert space dimension of $\mathcal{D}(6,6) \approx 10^4$, the full spectrum can be computed.

Note that in the case where the number of particles is not conserved, the Hilbert space dimension is much higher

$$\mathcal{D}_{\mathrm{nc}}(M, N_{\mathrm{max}}) = \sum_{N=1}^{N_{\mathrm{max}}} \binom{N + 2M - 1}{N}. \tag{3.4.14}$$

In this case the Hamiltonian can simply be constructed by first constructing creation $\hat{b}^{\dagger}_{j,\alpha}$, annihilation $\hat{b}_{j,\alpha}$ and number operators $\hat{n}_{j,\alpha}$ for each site j and then computing and adding all terms in the Hamiltonian (3.3.17).

3.4.3. Gutziller Mean-Field Theory

A simple approach to obtain information about the quantum phase of the ground state is to apply a Gutzwiller mean-field approximation [177], which ignores quantum fluctuations between different sites and accounts for the intersite coupling, by coupling a single site to a mean field. The Ansatz becomes exact for the two extreme cases $U/J \ll 1$ and $U/J \gg 1$, as well as in the limit of an infinite dimensional lattice.

Hence, we introduce the two order parameters $\psi_{j,0} = \langle \hat{b}_0 \rangle$ and $\psi_{j,1} = (-1)^j \langle \hat{b}_1 \rangle$ and

write the bosonic annihilation operators like

$$\hat{b}_{j,\alpha} = \left[\hat{b}_{j,\alpha} - (-1)^{j\alpha}\psi_\alpha\right] + (-1)^{j\alpha}\psi_\alpha \tag{3.4.15}$$

Here, the alternating sign for the excited band takes into account the different signs in the hopping in 0- and 1-band. Expanding the tunneling terms

$$\hat{b}_i^\dagger\hat{b}_j = \left[\hat{b}_i^\dagger - (-1)^{i\alpha}\psi_\alpha^*\right]\left[\hat{b}_j - (-1)^{j\alpha}\psi_\alpha\right] + (-1)^{i\alpha}\psi_\alpha\hat{b}_{j,\alpha} + (-1)^{(i+j)\alpha}|\psi_\alpha|^2, \tag{3.4.16}$$

the two-band Hamiltonian (3.2.14) can be decomposed into a sum of decoupled single-site Hamiltonians. Dismissing the site index j, the mean-field Hamiltonian for a single site then takes the form

$$
\begin{aligned}
\hat{H}_{\mathrm{mf}} &= -\mu(\hat{n}_0 + \hat{n}_1) + \delta\hat{n}_1 - 2\mathrm{J}_0\left(\psi_0\hat{b}_0^\dagger + \psi_0^*\hat{b}_0 - |\psi_0|^2\right) - 2\mathrm{J}_1\left(\psi_1\hat{b}_1^\dagger + \psi_1^*\hat{b}_1 - |\psi_1|^2\right) \\
&\quad -\frac{\eta K_\omega}{2}\left(\hat{b}_0^\dagger\hat{b}_1 + \hat{b}_1^\dagger\hat{b}_0\right) + U_{00}\frac{\hat{n}_0(\hat{n}_0 - 1)}{2} + U_{11}\frac{\hat{n}_1(\hat{n}_1 - 1)}{2} + 2U_{01}\hat{n}_0\hat{n}_1 \tag{3.4.17}
\end{aligned}
$$

where we have included a chemical potential term. This term is necessary to fix the particle number.

Within the Gutzwiller mean-field theory, we find the ground state by minimizing the on-site ground state energy (3.4.17) with regard to both order parameters ψ_0 and ψ_1. To achieve this, we parameterize the mean fields like $\psi_0 = |\psi|\cos(\theta)$, $\psi_1 = |\psi|\sin(\theta)\exp(\mathrm{i}\phi)$ and vary $|\psi|, \theta, \phi$. The on-site mean-field Hamiltonian (3.4.17) is then solved in the Fock basis up to a maximum particles per site of N_{max}. The order parameters with the minimal energy give the self consistent solution for the ground state.

3.4.4. Time-Evolving Block Decimation

Time-evolving Block Decimation (TEBD) is a method that was developed to efficiently describe and propagate 1D quantum systems that are only weakly entangled [50,51]. Note that by time propagating a state in imaginary time $it \to \tau$, the state of the system converges asymptotically to the ground state, which we will make use of. Furthermore, symmetries like particle conservation can be applied to the formalism. To perform the TEBD calculations, we use an open source TEBD

code package [178].

The main idea of the TEBD formalism is to rewrite quantum states in a local tensor or matrix product form. The coefficient tensor c of a multipartite (or multisite) quantum state

$$|\Psi\rangle = \sum_{i_j=1}^{d} c_{i_1 i_2 .. i_M} |i_1, i_2, .., i_M\rangle \tag{3.4.18}$$

can be decomposed by a concatenated Schmidt decomposition into the form

$$c_{i_1 i_2 .. i_M} = \sum_{\alpha_j=1, j=1...M-1}^{\chi_S(j)} \Gamma^{[1]i_1}_{\alpha_1} \lambda^{[1]}_{\alpha_1} \Gamma^{[2]i_2}_{\alpha_1 \alpha_2} \lambda^{[2]}_{\alpha_2} \cdots \Gamma^{[M-1]i_{M-1}}_{\alpha_{M-2} \alpha_{M-1}} \lambda^{[M-1]}_{\alpha_{M-1}} \Gamma^{[M]i_M}_{\alpha_{M-1}}, \tag{3.4.19}$$

called Vidal decomposition. Here d is the dimension of the "onsite" Hilbert space[1]. For a quantum gas, it is on the one hand determined by the number of particles N[2], and on the other hand depends on the internal structure, in our case the orbital degree of freedom. For example, for two bands and a maximum particle number of $N = 2$, we find a onsite dimension of $d = 6$ (a state with no particles, two states with one particle and three states with two particles). The Schmidt index $\chi_S(j) = \min(d^j, d^{(M-j)})$ is the lower of the dimensions of the Hilbert spaces of the two blocks with sites $1 \ldots j$ and $j + 1 \ldots M$, as it is in the ordinary Schmidt decomposition [179]. Each quantum state $|\psi\rangle$ is hence described by a rank 3 tensor $\Gamma^{[j]}$ and a vector $\lambda^{[j]}$ of Schmidt coefficients at every site j, or, if tensor and vector are glued together, by a matrix product. It is a local construction in the sense that the Γ's specify a local basis on each site, whereas the λ link these local states together and determine their significance. Instead of propagating the coefficient tensor $\{c_{i_1 i_2 .. i_M}\}$, one can then apply the action of the Hamiltonian on the tensors $\Gamma^{[j]}$ and the coefficients $\lambda^{[j]}$.

The Vidal decomposition (3.4.19) is exact. However, in many physical systems eigenstates are only weakly entangled states, which means that the Schmidt coefficients $\lambda^{[j]}_{\alpha_j}$ fall off exponentially at each site as a function of α_j. Hence, the weakly entangled eigenstates can be written as a sum of only a small number of

---

[1] We assume translational symmetry, i.e. d has no site index.

[2] In some cases the number of particles per site is truncated to $N_{max} < N$ or it is limited due to the nature of the particles (e.g. fermions).

product states. It is therefore enough to keep only a constant number $\chi \ll \chi_S$ of the Schmidt coefficients $\lambda^{[j]}$ and the coefficients in the tensors $\Gamma^{[j]}$ at each site. With this truncation, a weakly entangled quantum state can be described by only polynomially (in M) many coefficients $\{\Gamma^{[j]i_j}_{\alpha_{j-1}\alpha_j}, \lambda^{[j]}_{\alpha_j}\}$ instead of all d^M coefficients $\{c_{i_1 i_2 .. i_M}\}$.

Another approximation used in the TEBD formalism is the Suzuki-Trotter expansion [180] for the time evolution operator

$$
\begin{aligned}
\hat{U}(t,0) &= \exp(-i/\hbar \hat{H} t) = \exp(-i/\hbar (\hat{H}_A + \hat{H}_B) t) \\
&\approx \left[\exp(-i/\hbar t \hat{H}_A \delta_t/2) \exp(-i/\hbar t \hat{H}_B \delta_t) \exp(-i/\hbar t \hat{H}_A \delta_t/2) \right]^n \quad (3.4.20)
\end{aligned}
$$

with $n = t/\delta_t$ being the order of the decomposition. Here, $\hat{H}_A$ and $\hat{H}_B$ are non-commuting parts of the Hamiltonian, for which the action of the Hamiltonian on tensors and coefficients in the Vidal decomposition is known, in our case the on-site and tunneling terms. This decomposition allows for a fast time evolution for the tensors used in the TEBD formalism.

3.5. Orbital-Driven Mott Insulator to Superfluid Phase transition

The aim of this section is to demonstrate and analyze an orbital driven adiabatic quantum phase transition between a Mott insulator and a superfluid merely by controlling the frequency of the periodic driving, which controls the relative occupation of the excited band with regards to the ground band.

3.5.1. The Mott Insulator to Superfluid Transition in the Non-Driven Lattice

First we give a short overview about the Mott insulator to superfluid transition in the non-driven lattice, which can be induced, for example, by tuning the depth of the optical lattice [177, 181]. In the non-driven lattice, the orbital degrees of freedom stemming from excited bands can be ignored. In one dimension, the

Hubbard model thus takes the simple form

$$\hat{H}_{1B} = -J \sum_{<ij>} \hat{b}_{i,0}^{\dagger} \hat{b}_{j,0} + \sum_{j} \frac{U}{2} \hat{n}_{j,\alpha} (\hat{n}_{j,\alpha} - 1) \qquad (3.5.1)$$

and only consists of an tunneling term with strength J and an on-site interaction of strength U.

In the parameter regime where the interaction energy dominates the tunneling strength, $U \gg nJ$, which for example happens for a large lattice depth V_0, in the ground state the interaction energy is minimized by a very low mutual overlap of the bosons. In the case of an integer particle density $n = N/M \in \mathbb{N}$, this is achieved by the so called Mott insulating state, where the particles are distributed evenly over the lattice sites, where they are exponentially localized and almost uncorrelated to the particles on other lattice sites. For $n = 1$ for example, in the Mott state we find a single atom on each site and an almost vanishing interaction energy. For $n = 2$, we find exactly two particles per lattice site and an interaction energy of U per lattice site, and so on. The ground state in the Mott phase has a gap in the spectrum between ground state and first excited state of size U, since this is the energy to create a particle-hole pair. For a non-integer particle density in this parameter regime, the integer Mott state is complemented with the additional particles spread out over the lattice. If furthermore the particle number is controlled by a chemical potential μ, the particle density shows plateaus of integer n and is robust against small changes of μ. Thus, also the compressibility $\partial n/\partial \mu$ vanishes in the Mott region.

If, on the other hand, the tunneling strength dominates the interaction energy, $U \ll nJ$, which happens for a rather shallow lattice, the particles are spread out over the lattice to reduce the kinetic energy. This state is called superfluid. Deep in the superfluid region, the bosons are only weakly correlated and sit almost completely in the single-particle ground state at quasimomentum $q = 0$ (quasi-condensate). In the thermodynamic limit, $N, M \to \infty$, $N/M = $ const, the spectrum in the superfluid region is gapless. In a setting where the particle number is not conserved, the particle density changes smoothly with the chemical potential μ and thus the compressibility is always finite.

Between both regions, where the ground state is strongly correlated, a quantum
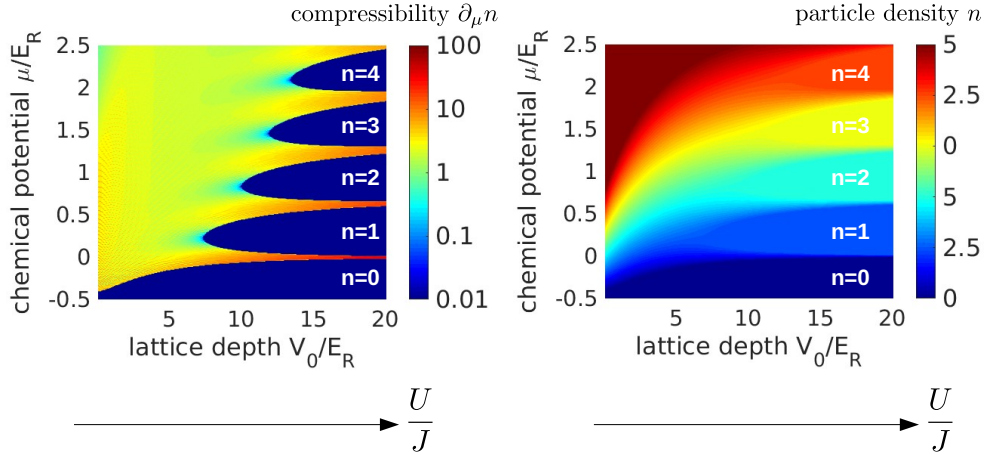
Figure 3.5.1.: Left: Phase diagram of the simple one-band Bose-Hubbard model in the dimerized lattice ($V_1/V_0 = 0.5$), controlled by chemical potential μ and the lattice depth V_0/E_R, which controls the ratio J/U. The compressibility $\partial_\mu n$ in logarithmic color scale indicates the quantum phase: If it vanishes (blue), the ground state is Mott insulating. If it has a finite value (blue to red), the system is superfluid. The ground state was calculated by the Gutzwiller-Meanfield method, see Sec. 3.4.3. Right: Particle density in the same parameter regime. The plateaus of integer particle density are clearly visible.

phase transition takes place at a critical value $(J/U)_c$, which depends on the dimension of the lattice and the particle density n. The phase transition was confirmed e.g. for a three-dimensional lattice in the experiment Ref. [35]. In one dimension, the phase transition at $n = 1$ takes place roughly at $(J/U)_c \approx 3.8$ [182], whereas the mean-field result, which becomes exact in the infinite-dimensional limit, the critical value is $(J/U)_\infty = 11.66$ [183].

To give an overview about the two quantum phases of the ground state, in Fig. 3.5.1 (left) we show the meanfield phase diagram of the ground state of the one-band Bose-Hubbard model (3.5.1). For the Hubbard model, we plugged in the model parameters J and U from the dimerized lattice with $V_1/V_0 = 0.5$ according to J_0 and U_{00} from Fig. 3.2.8 and Fig. 3.2.9. We plot the compressibility over chemical potential and lattice depth, which is closely related to the ratio J/U. The Mott lobes with vanishing compressibility are clearly visible as blue regions, whereas in the superfluid region the compressibility is finite. For $n = 1$, the phase transition roughly happens at a lattice depth of $V_0/E_R \approx 7.5$, where we find $J/U \approx 11.8$, close

to the expected critical value from mean-field theory (11.66). In Fig. 3.5.1 (right) we plot the particle density $n \equiv \langle \hat{n}_i \rangle$ of the ground state. The particle density takes integer values in the Mott lobes, which are increasing with the chemical potential. In contrast, in the superfluid region the particle density increases linearly.

3.5.2. Coherent Control of the Quantum Phase of the Ground State

In this section we demonstrate the phase transition between a Mott insulating and a superfluid state can be achieved in a qualitatively different approach, by coherently coupling the bands via lattice shaking.

This phase transition is possible since in the effective band-coupled Hamiltonian (3.2.14), the ground and excited band hybridize with strength $\gamma(K)$ depending on the driving strength K and, at the same time, their band distance $\delta(\omega)$ can be adjusted by the driving frequency ω. In addition, since both bands differ sufficiently in their tunneling strength, it is possible to find a lattice depth and dimerization such that in the ground band the ratio $J_0/U_{00} < (J/U)_c \approx 0.26$ (in one dimension) [182] is below the critical value and thus favors a Mott-insulating state, whereas in the first excited band the ratio $J_1/U_{11} > (J/U)_c$ is above the critical value and thus favors a superfluid state. Therefore, for a large positive band distance $\delta/|\gamma| \gg 1$, when band 1 lies below band 0, in the effective ground state the bosons are mainly occupying the ground band of the undriven system. In this parameter regime, the ground state of (3.2.14) is a Mott insulating state. For a large negative band distance $-\delta/|\gamma| \gg 1$ in the effective ground band the particles mainly occupy the first excited band of the undriven system. Here, the quantum phase is superfluid. In between, there has to be a quantum phase transition between these two phases, as illustrated in Fig. 3.5.2.

In the following we pick a lattice depth of $V_0 = 10 E_R$ and the dimerization $V_1/V_0 = 0.5$ such that $J_0/U_{00} \approx 0.051 < (J/U)_c$ and $J_1/U_{11} = 0.34 > (J/U)_c$ and keep the driving strength constant at $K = 0.5 E_R$. Hence, for these parameters the described orbital driven phase transition between a Mott insulator and a superfluid is theoretically possible. For comparison we will sometimes also consider the case of $V_0 = 5 E_R$,
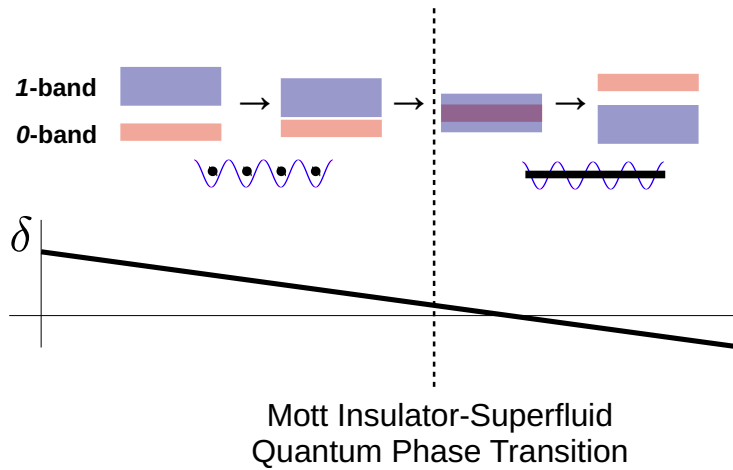
Figure 3.5.2.: Illustration of the orbital driven Mott insulator to superfluid phase transition. Starting with a large positive δ in a Mott insulating state (right), where the particles mainly occupy the ground band, the reduction of δ at some point leads to a quantum phase transition to the superfluid at a transition point δ_t. This is because the excited band favouring this phase gets occupied by the bosons.

where we have $J_0/U_{00} \approx 0.152 < (J/U)_c$ and $J_1/U_{11} = 0.903 > (J/U)_c$. For the lattice depth of $V_0 = 3E_R$ ($V_0 = 15E_R$) we do not expect the phase transition since for both 0- and 1-band, the ground state is expected to be in the superfluid (Mott insulating) phase. However, an abrupt phase transition from a superfluid in the 1-band to one in the 1-band is possible.

3.5.3. Exact Spectrum for Small Systems

By calculating exactly the low-energy spectrum of (3.2.14) for a fixed particle number N and for different band distances δ, we can already see a precursor of the transition between a Mott insulator and a superfluid. As explained earlier, in the Mott insulating ground state we expect a gap in the spectrum between the lowest two energy states of size U. In Fig. 3.5.3 we show plots of the low energy spectrum of the effective two-band model (3.2.14) for different lattice depths $V_0 = [3E_R, 5E_R, 10E_R, 15E_R]$ that result in different ratios J_0/U_{00}. The spectrum was obtained by solving a lattice of $N = 6$ particles on $M = 6$ periodically connected
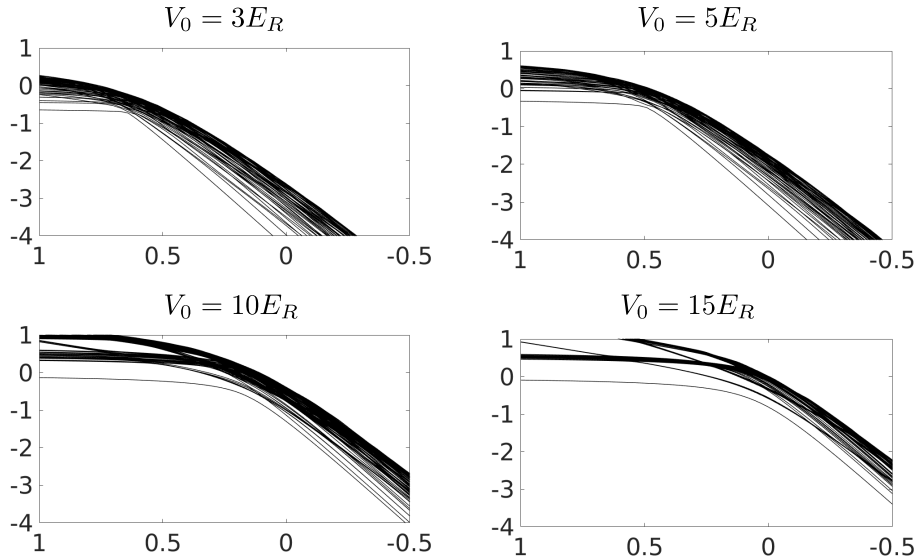
Figure 3.5.3.: Low-energy spectrum of the exactly solved (see Sec. 3.4.2) two-band Hubbard Hamiltonian for different lattice depths $V_0 = [3E_R, 5E_R, 10E_R, 15E_R$. The driving amplitude is kept at $K = 0.5E_R$. In the region dominated by the 0-band, i.e. before the bending down of the spectrum, we see a clear energy gap between ground state and first excited state, especially for $V_0 \geq 5E_R$, which becomes less pronounced in the region dominated by the 1-band.

sites by exact diagonalization. Even though this is a very small system, such that the signatures of the quantum phase are disturbed by finite size effects, the quantum phase transition is slightly indicated: For $V_0 = 5E_R$ ($V_0 = 10E_R$) the energy gap between the ground state and the excited states is rather pronounced for $\delta \gg 0$, although it is below the expected gap of $U_{00} \approx 0.50E_R$ ($U_{00} \approx 0.58E_R$). This indicates signatures of a Mott phase. For $\delta < 0$ the energy gap is larger than the difference of higher neighbouring energy states, but clearly below $U_{11} \approx 0.40$ ($U_{11} \approx 0.50$), indicating signatures of a superfluid phase. For $V_0 = 3E_R$, the gap closes, indicating a phase transition, even though both phases cannot be clearly distinguished by the gap in the spectrum. For $V_0 = 15E_R$, the differences in the energy gaps between both regions are less prononced, indicating that no quantum phase transition takes place.
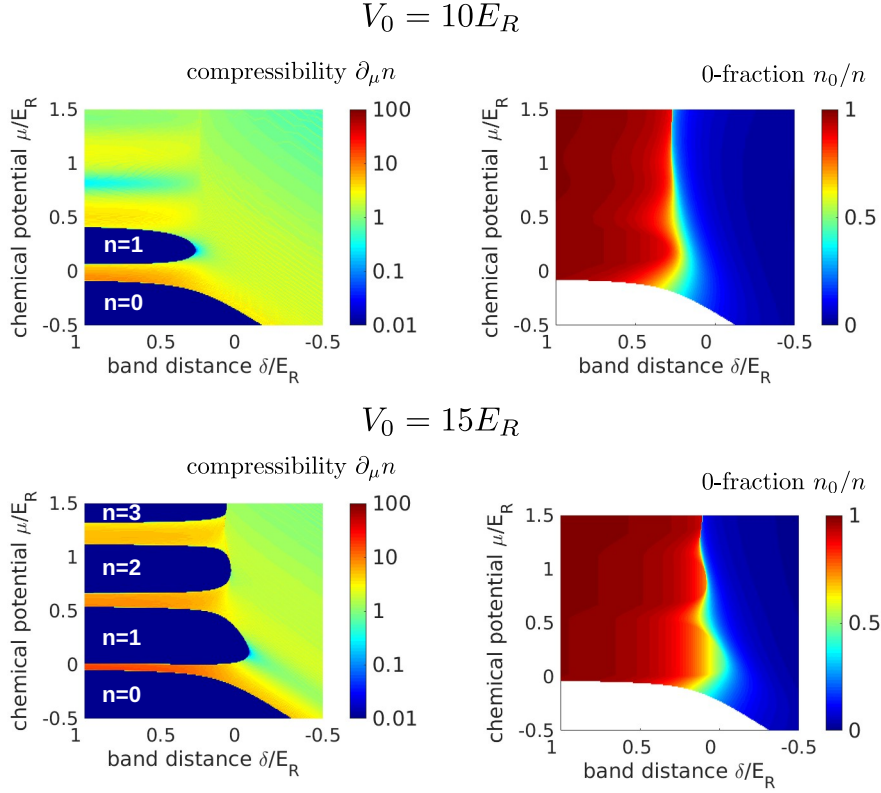
$$V_0 = 10E_R$$

$$V_0 = 15E_R$$

Figure 3.5.4.: Phase diagram (left) and band occupation (right) of the ground state of the effective band coupled model Eq. (3.2.14). Upper row: Lattice depth $V_0 = 10E_R$. Lower Row: $V_0 = 15E_R$. The dimensions of the phase space are the chemical potential μ and the band distance δ. Here, the ground state was calculated with the mean-field method, described in Sec. 3.4.3.

3.5.4. Phase Diagram

In this section, we will validate the orbital driven quantum phase transition from Mott insulator to superfluid by considering the phase diagram of the ground state of the effective two-band model Eq. (3.2.14). To do so, we consider the parameter space of chemical potential μ and band distance δ, controlled by the shaking frequency $\delta = D - \hbar\omega$, at fixed lattice depths V_0/E_R. As in Sec. 3.5.1, we distinguish the phases by plotting the particle density n and the compressibility $\partial_\mu n$ of the ground state.

In Fig. 3.5.4 (left) we plot the compressibility over band distance δ and chemical potential μ for lattice depths $V_0 = 10E_R$ and $V_0 = 15E_R$, again using the mean-field
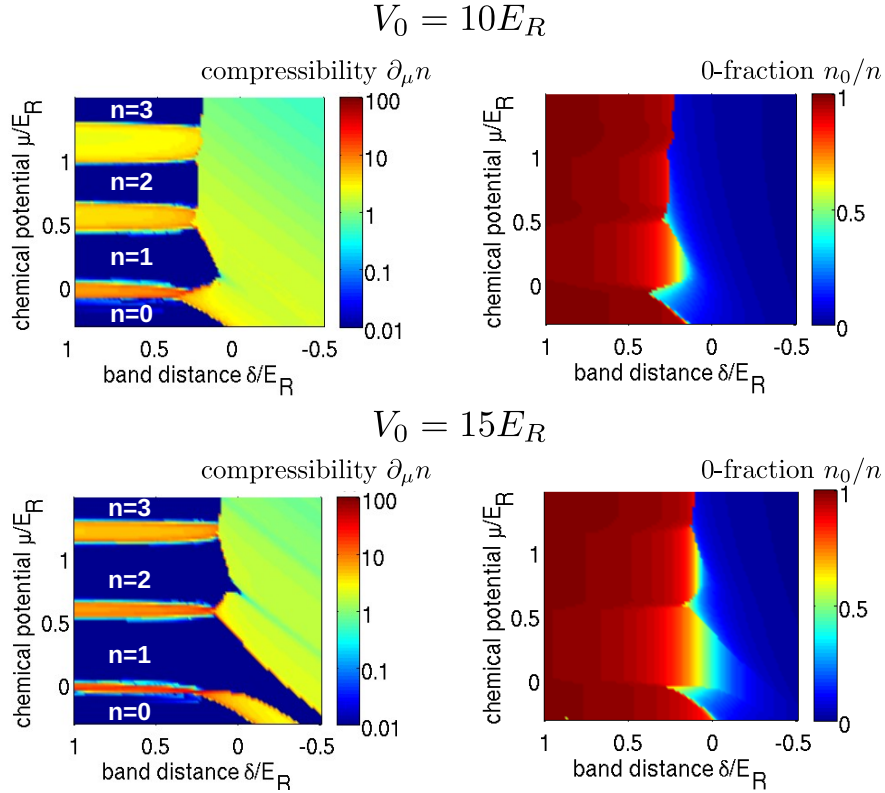
$$V_0 = 10E_R$$

$$V_0 = 15E_R$$

Figure 3.5.5.: Phase diagram (left) and band occupation (right) of the ground state of the effective band coupled model Eq. (3.2.14). Upper row: Lattice depth $V_0 = 10E_R$. Lower Row: $V_0 = 15E_R$. The dimensions of the phase space are the chemical potential μ and the band distance δ. The compressibility $\partial_\mu n$ in logarithmic color scale indicates the quantum phase: If it vanishes (blue), the ground state is Mott insulating. If it has a finite value (blue to red), the system is superfluid. The ground state was calculated with imaginary TEBD (see Sec. 3.4.4) on a system of $M = 30$ sites and a bond dimension of $\chi = 14$.

method. For $V_0 = 10E_R$, only the Mott lobe for $n = 1$ is present. Nevertheless, decreasing the band distance δ from left to right, it vanishes at a certain transition point δ_t, i.e. the Mott insulator melts into the superfluid state. The reason is, as described in the previous section, that for this set of parameters the (non-driven) ground band favors a Mott insulating state, wheras the (undriven) first excited band favors a superfluid. Hence, the quantum phase transition happens when for the particles it is energetically favourable to occupy the first excited band, taking into account the band distance as well as tunneling and interaction processes in

both bands. After the first band becomes occupied around $\delta \approx 0$, the Mott lobes are shifted downwards. This is simply because the energy goes linearly down with δ if all particles are in band 1. For $V_0 = 15E_R$, we see all Mott lobes melting at the band transition point. From Sec. 3.5.2 we actually do not expect a phase transition here, since $J_1/U_{11} < (J/U)_c$. However, as mentioned before, the meanfield method shifts the Mott region to higher J/U, therefore showing a phase transition here. To demonstrate that the quantum phase transition happens at the transfer of the particles to the first excited band, we also plot the relative band population n_0/n in Fig. 3.5.4 (right) for the same phase space.

To get a quantatively more accurate description of the orbital driven phase transition, in Fig. 3.5.5 we show the same plots as before, but calculated with the quasi-exact TEBD method. We computed the ground state of the effective two-band Hamiltonian (3.2.14) on a lattice of $M = 30$ sites and periodic boundary conditions. We again consider the cases $V_0 = 10E_R$ and $V_0 = 15E_R$. For $V_0 = 10E_R$, we observe the orbital driven phase transition for all Mott lobes. The phase transition point for $n = 1$ lies around $\delta_t \approx 0.1E_R$. This values lies behind the point of particle transition $\delta_c = 0.421E_R$ calculated for the single-particle model in Sec. 3.4.1. The reason for this is that the bands hybridize strongly due to the coupling with γ which lowers the energy of the Mott insulating state. For $V_0 = 15E_R$, we cannot observe a phase transition for the Mott lobe with $n = 1$ since the ratio $J_\alpha/U_{\alpha\alpha}$ is below the critical value $(J/U)_c$ for both bands (compare with Fig. 3.5.1). However, for higher particle densities the phase transition takes actually place. The reason is that extra particles (or holes) tunnel with strength $(n+1)J_\alpha$ (or nJ_α), which increases with the particle density n.

3.5.5. Nature of the Phase Transition

In the phase diagrams calculated by TEBD we can observe another interesting phenomenon in the phase transition, by comparing Mott lobes with different integer n. In contrast to the smooth transition for $n = 1$ at $V_0 = 10E_R$, we observe a discontinuous phase transition for the $n = 2$ Mott lobe for $V_0 = 10E_R$ and for the $n = 1$ and $n = 2$ Mott lobes for $V_0 = 15E_R$, see Fig. 3.5.5 (bottom). The order
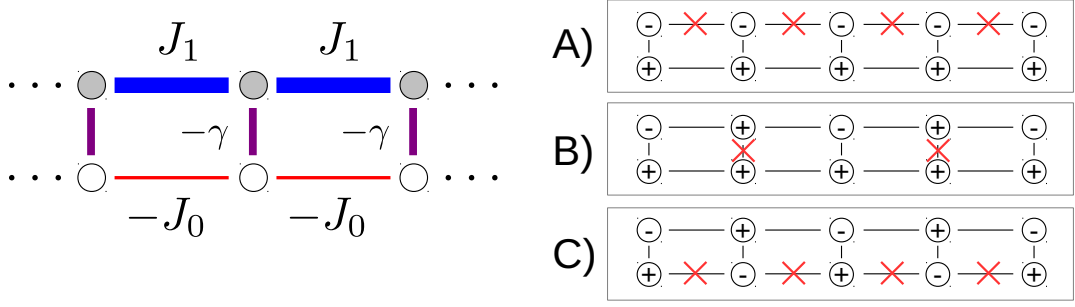
Figure 3.5.6.: Left: Illustration of the frustrated effective 2-band Hamiltonian. The horizontal legs in red and blue demonstrate tunneling in the 0- and 1-band, whereas the vertical leg in violet describes the band coupling. Because of the ladder structure and since two of the coupling elements are negative, the single-particle kinetics is frustrated. Right: Illustration of the sign of the single-particle ground-state wave function for the cases A)-C), roughly located at the center lattice site. The red crosses signify that the bond is frustrated, i.e. the energy is increased at this bond.

(first or second) of the phase transition appears to be dependent of parameters like particle density and lattice depth. This observation is a consequence of the two-band ladder-like structure of Hamiltonian (3.2.14), which can be understood by considering the ground state correlation functions

$$\chi_{\alpha'\alpha}^{\ell} = \frac{\langle \hat{b}_{\alpha'\ell}^{\dagger} \hat{b}_{\alpha 0} \rangle}{\sqrt{n_{\alpha'}n_{\alpha}}}. \tag{3.5.2}$$

We calculate the ground state of the two-band Hamiltonian (3.2.14) with fixed particle number $N = 30$ on $M = 30$ lattice sites by imaginary time TEBD. Setting $M = N$ corresponds to follow a line of constant density $n = 1$ in the phase diagrams Fig. 3.5.5. We have fixed the particle number in this case to increase the numerical precision in order to calculate also correlation functions of distant sites. Accordingly, the bond dimension is adjusted in each case such that the error is below 5% (see App. B). In Fig. 3.5.7, we plot the correlation function χ_{00}^{1}, χ_{11}^{1}, χ_{01}^{0}, χ_{00}^{8}, χ_{11}^{8} and the relative band occupation $n_0 - n_1$ for $K = 0.5$ and four lattice depths $V_0 = [3, 5, 10, 15]E_R$. The correlation function χ_{00}^{1} and χ_{11}^{1} indicate the phase between neighbouring sites within the 0- and 1-band, whereas χ_{01}^{0} give us information about
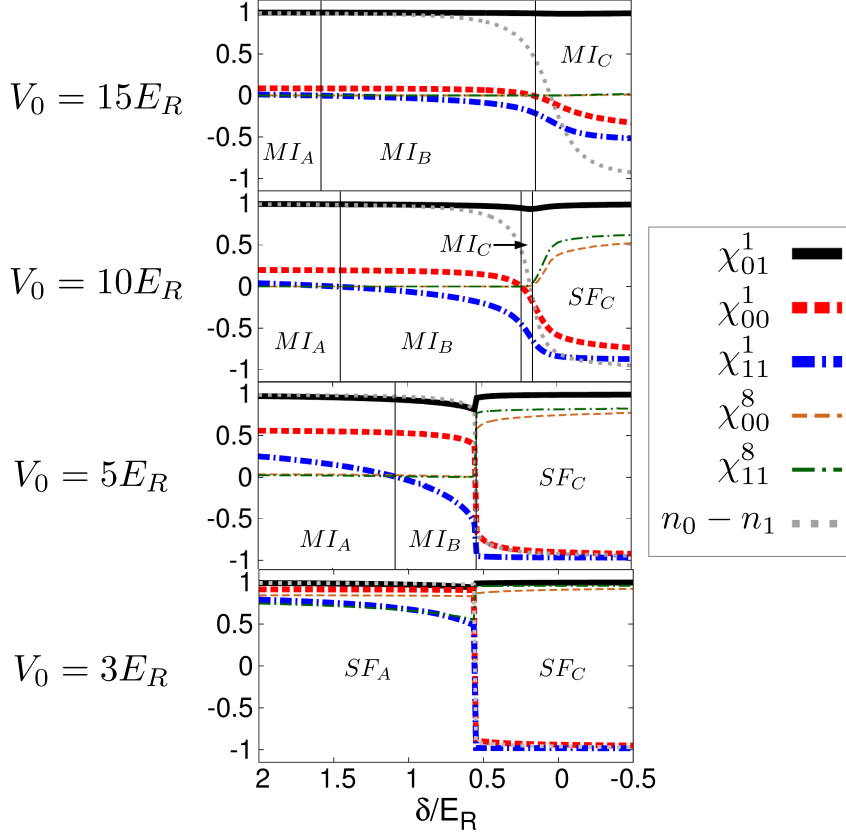
Figure 3.5.7.: Correlations $\chi^{\ell}_{\alpha'\alpha} \equiv \langle \hat{b}^{\dagger}_{\alpha'\ell} \hat{b}_{\alpha 0} \rangle / \sqrt{n_{\alpha'}n_{\alpha}}$ for fixed filling $n = 1$ versus δ, with $V_1/V_0 = 0.5$ and $V_0/E_R = 15, 10, 5$ (from top to bottom).

the on-site phase ordering between both bands. The correlation functions χ^8_{00} and χ^8_{11} indicate whether the system is in the Mott insulating or in the superfluid phase. Since the correlations fall off exponentially with the site distance ℓ, in the Mott insulating phase one expects $\chi^8_{\alpha\alpha} \approx 0$ here, whereas $\chi^8_{\alpha\alpha}$ should be finite in the superfluid phase, where the correlations fall off polynomially with ℓ in one dimension. Hence, we can confirm in Fig. 3.5.7 that for $V_0 = 15E_R$ the system remains in the Mott phase in the whole range of δ. For $V_0 = 10E_R$ and $V_0 = 5E_R$, a phase transition from a Mott insulating to a superfluid state takes place at $n_0 - n_1 \approx 0$. For $V_0 = 3E_R$ the state is always superfluid.

Whereas the correlation functions change smoothly for $V_0/E_R = 1[0, 15]$ their change is abrupt for $V_0/E_R = [3, 5]$. As confirmed Fig. 3.5.7, the nature of the

phase transition depends on the sign of χ_{11}^1 at the phase transition: If $\chi_{11}^1 < 0$ at the transition point, which is also the ordering in the superfluid of particles in band 1, the transition is continuous. If on the other hand $\chi_{11}^1 > 0$, the correlations change abruptly and the transition happens first order. The sign of χ_{00}^1 and χ_{11}^1 can be classified according to three cases[3], which are illustrated in Fig. 3.5.6 (right):

- A) $\chi_{00}^1 > 0$ and $\chi_{11}^1 > 0$

- B) $\chi_{00}^1 > 0$ and $\chi_{11}^1 < 0$

- C) $\chi_{00}^1 < 0$ and $\chi_{11}^1 < 0$

The type of ground state according to this classification depends on the band distance δ and can be explained by a frustration of the single-particle ground state, depicted in Fig. 3.5.6 (left). Since $-J_0$ and $-\gamma$ are negative and J_1 is positive, there is no way that a single-particle wave function gains a negative energy contribution from every bond at the same time. The reason is that a negative coupling element will favour a wave function with the same sign between two sites, whereas a positive coupling element will favour a different sign. Because of the ladder-like geometry, it is not possible to satisfy all four bonds around a loop to maximally minimize the energy. The orientation of the single-particle wave functions in the many-body system is consequently determined by the occupation of the bands: If almost all particles occupy the ground band, the single-particle wave function will order according to case A). If almost all bosons are in the excited band, we will find case C). Dependning on the parameters n, γ, J_0, J_1, also case B) is possible in between. Note however, that if the particle is localized strongly around one site (e.g. in the Mott phase), the frustration will have a lower impact on the state since in this case the wave function has only little contributions on the neighbouring sites, in contrast to a spread-out wave function (e.g. in the superfluid phase). Localization of the particles will favour the hybridization term with strength $-\gamma$ and the tunneling terms will be less dominant. Accordingly, since in the superfluid phase the wave function is very dispersive, the effect of J_α is much stronger than in the Mott phase, which strongly favors cases A) and C).

Hence, combining the frustration of the single-particle ground state with the particle

---

[3]The possibility of a complex wave function of the ground state is ruled out since $2U_{01} > U_{00}, U_{11}$.

occupation of the two bands, the nature of the phase transition can be described. In the next section we will employ perturbation theory to estimate the transition between regions A), B) and C).

3.5.6. Perturbative Approach

The transition point in δ between the regions A),B) and C) in the Mott region can be estimated by perturbation theory. We start with the transition between MI_A and MI_B, where $\chi_{11}^1 = \langle \hat{b}_{11}^\dagger \hat{b}_{10} \rangle / n_0$ changes its sign from positive to negative. In the limit $\delta \to -\infty$ and $J_0/H_{00} \to 0$, the ground state of (3.2.14) is the product state

$$|\psi_0\rangle = \prod_\ell \hat{b}_{0\ell}^\dagger |\text{vac}\rangle. \tag{3.5.3}$$

with the vacuum state $|\text{vac}\rangle$. Starting from this state, the ground-band tunneling and the coupling can be treated as perturbations. To find the major contribution to χ_{11}^1 in perturbation theory, we have to compute up to the order in perturbation theory where the perturbed ground state $|\psi\rangle$ acquires a finite value $\langle \psi | \hat{b}_{10}^\dagger \hat{b}_{11} | \psi \rangle$. We denote $|\psi_k\rangle$ the perturbated state correction appearing in kth order. Since a particle has to be excited to the first band from $|\psi_0\rangle$, before it can tunnel to the neighbouring site, the first non-vanishing contribution to $\langle \psi | \hat{b}_{10}^\dagger \hat{b}_{11} | \psi \rangle$ appears in third order perturbation theory. Here, the state ψ_2 involves two hopping processes, which implies four bosonic operators. In third order, we then find the contribution to the correlation function

$$\begin{aligned} \langle \psi | \hat{b}_{10}^\dagger \hat{b}_{11} | \psi \rangle &\simeq \langle \psi_1 | \hat{b}_{10}^\dagger \hat{b}_{11} | \psi_2 \rangle + \langle \psi_2 | \hat{b}_{10}^\dagger \hat{b}_{11} | \psi_1 \rangle \\ &= 2 \langle \psi_1 | \hat{b}_{10}^\dagger \hat{b}_{11} | \psi_2 \rangle. \end{aligned} \tag{3.5.4}$$

Both terms are equal because of translation invariance of the ground state. The relevant term of $|\psi_1\rangle$ coming from a single hopping process into the excited band is

$$\frac{-\gamma \hat{b}_{10}^\dagger \hat{b}_{00}}{-\delta} |\psi_0\rangle = \frac{\gamma}{\delta} \hat{b}_{10}^\dagger \prod_{\ell \neq 0} \hat{b}_{0\ell}^\dagger |\text{vac}\rangle, \tag{3.5.5}$$

where the energy difference of the connected states $E_1 - E_0 = \delta$ appears in the denominator and the coupling matrix element $-\gamma \hat{b}_{10}^\dagger \hat{b}_{00}$ in the numerator. The relevant term of $|\psi_2\rangle$, where a particle either tunnels first to the neighbouring site in the ground band and then gets excited, or gets excited first and then tunnels in the excited band, takes the form

$$\left(\frac{\gamma \hat{b}_{11}^\dagger \hat{b}_{01} \, J_0 \hat{b}_{01}^\dagger \hat{b}_{00}}{(2U_{01} + \delta)U_{00}} - \frac{J_1 \hat{b}_{11}^\dagger \hat{b}_{10} \, \gamma \hat{b}_{10}^\dagger \hat{b}_{00}}{(2U_{01} + \delta)\delta} \right) |\psi_0\rangle = \left(\frac{2J_0}{U_{00}} - \frac{J_1}{\delta} \right) \frac{\gamma}{2U_{01} + \delta} \hat{b}_{11}^\dagger \prod_{\ell \neq 0} \hat{b}_{0\ell}^\dagger |\text{vac}\rangle. \tag{3.5.6}$$

Here we have also taken into account the additional on-site interaction U_{00} and $2U_{01}$ since a particle-hole excitation is created. Plugging both contributions (3.5.5) and (3.5.6) into (3.5.4), the correlation function takes the form

$$\langle \hat{b}_{10}^\dagger \hat{b}_{11}^\dagger \rangle \simeq \left(\frac{2J_0}{U_{00}} - \frac{J_1}{\delta} \right) \frac{2\gamma^2}{(2U_{12} + \delta)\delta}. \tag{3.5.7}$$

The sign change which indicates the transition happens at

$$\delta = \frac{U_{00} J_1}{2J_0}, \tag{3.5.8}$$

where both terms in the round bracket cancel each other. For the parameter regime in Fig. 3.5.7, the M_A to M_B transition is thus estimated to happen at around $\delta \approx 1.8 E_R$ for $V_0 = 15 E_R$, for $\delta \approx 1.6 E_R$ for $V_0 = 10 E_R$ and for $\delta \approx 1.2 E_R$ for $V_0 = 5 E_R$, fitting reasonably well with the numerical values in Fig. 3.5.7.

The perturbative estimation of the MI_B-to-MI_C transition goes along the same lines. Assuming sharp filling $n = n_0 + n_1 = 1$, we again treat the tunnel terms $-J_0 \hat{b}_{01}^\dagger \hat{b}_{00} + J_1 \hat{b}_{11}^\dagger \hat{b}_{10}$ as a perturbation. The unperturbed on-site problem in the limit $\delta \to -\infty$ is then given by

$$|\psi_0\rangle = \prod_\ell |\psi_\ell^{(0)}\rangle = \prod_\ell (a_0 \hat{b}_{0\ell}^\dagger + a_1 \hat{b}_{1\ell}^\dagger)|\text{vac}\rangle. \tag{3.5.9}$$

To obtain the Mott insulating ground state in this limit, we have to solve the on-site single-particle problem,

$$\hat{H}_{\text{MI}} = \sum_{\ell} \left[\delta \hat{n}_{1\ell} + \gamma \left(\hat{b}_{1\ell}^{\dagger} \hat{b}_{0\ell} + \hat{b}_{0\ell}^{\dagger} \hat{b}_{1\ell} \right) \right] = \sum_{\ell} \hat{H}_{\text{MI}}^{(\ell)} \tag{3.5.10}$$

The solution of the 2-by-2 matrix $\hat{H}_{\text{MI}}^{(\ell)}$ of each site is the unperturbed state

$$|\psi_{\ell}^{(0)}\rangle = \left(a_0 \hat{b}_{0\ell}^{\dagger} + a_1 \hat{b}_{1\ell}^{\dagger} \right) |\text{vac}\rangle, \tag{3.5.11}$$

with energy per site

$$\varepsilon_0 = \frac{\delta}{2} - \frac{1}{2}\sqrt{\delta^2 + 4\gamma^2}. \tag{3.5.12}$$

We also have $a_1/a_0 = -\varepsilon_0/\gamma$ and the normalization condition $a_0^2 + a_1^2 = 1$. The state amplitudes give us the densities

$$n_0 \simeq a_0^2 \quad \text{and} \quad n_1 \simeq a_1^2. \tag{3.5.13}$$

For each site, we need again defect states with one particle less (a hole) and one extra particle, stemming from the tunneling processes. For $n = 1$, the on-site hole state is simply given by the vacuum

$$|\psi^{(h)}\rangle = |\text{vac}\rangle, \tag{3.5.14}$$

with energy $\varepsilon_h = 0$. The subspace with two particles on a site contains three states, depend on the band occupancies. For simplicity, we neglect the hybridization coupling γ. Thus, we approximate the eigenstates with an additional particle by states with sharp occupations of the orbitals α,

$$
\begin{aligned}
|\psi^{(20)}\rangle &= \frac{1}{\sqrt{2}} (\hat{b}_0^{\dagger})^2 |\text{vac}\rangle, \\
|\psi^{(11)}\rangle &= \hat{b}_0^{\dagger} \hat{b}_1^{\dagger} |\text{vac}\rangle, \\
|\psi^{(02)}\rangle &= \frac{1}{\sqrt{2}} (\hat{b}_1^{\dagger})^2 |\text{vac}\rangle,
\end{aligned}
\tag{3.5.15}
$$

where we skipped the site index in the operators. Neglecting the band coupling, these states with an additional particle have energies

$$
\begin{aligned}
\varepsilon_{20} &= U_{00}, \\
\varepsilon_{11} &= 2U_{01} + \delta, \\
\varepsilon_{02} &= 2U_{11} + 2\delta.
\end{aligned}
\tag{3.5.16}
$$

Since $\langle \psi | \hat{b}_{\alpha 0}^{\dagger} \hat{b}_{\alpha 1} | \psi \rangle$ has a non-zero contribution for states ψ connected to ψ_0 by a single tunneling process, we have to consider only the first order of the perturbation expansion with respect to tunneling,

$$
\begin{aligned}
\langle \psi | \hat{b}_{\alpha 0}^{\dagger} \hat{b}_{\alpha 1} | \psi \rangle &\simeq \langle \psi_0 | \hat{b}_{\alpha 0}^{\dagger} \hat{b}_{\alpha 1} | \psi_1 \rangle + \langle \psi_1 | \hat{b}_{\alpha 0}^{\dagger} \hat{b}_{\alpha 1} | \psi_0 \rangle \\
&= 2 \langle \psi_0 | \hat{b}_{\alpha 0}^{\dagger} \hat{b}_{\alpha 1} | \psi_1 \rangle.
\end{aligned}
\tag{3.5.17}
$$

The state correction $|\psi_1\rangle$ includes all states connected to $|\psi_0\rangle$ by a single hopping event. The terms relevant for (3.5.17) possess an extra particle in one of the three possible states on site 1 and a hole on site 0. Therefore, we can use relations (3.5.15) and (3.5.16) to calculate their contribution

$$
\left[\frac{a_0^2 J_0}{U_{00} - 2\varepsilon_0} (\hat{b}_{01}^{\dagger})^2 - \frac{a_1^2 J_1}{U_{11} + 2\delta - 2\varepsilon_0} (\hat{b}_{11}^{\dagger})^2 - \frac{a_0 a_1 (J_1 - J_0)}{U_{01} + \delta - 2\varepsilon_0} \hat{b}_{11}^{\dagger} \hat{b}_{01}^{\dagger} \right] \prod_{\ell \neq 0,1} (a_0 \hat{b}_0 + a_1 \hat{b}_1) |\text{vac}\rangle.
\tag{3.5.18}
$$

Plugging this into Eq. (3.5.17) and also using the relation for the densities Eq. (3.5.13), we arrive at

$$
\langle \hat{b}_{00}^{\dagger} \hat{b}_{01} \rangle \simeq \frac{2n_0}{U_{00}(2U_{01} + \delta - 2\varepsilon_0)} \Big[2n_0 J_0 (2U_{01} + \delta - 2\varepsilon_0) - n_1 (J_1 - J_0)(U_{00} - 2\varepsilon_0) \Big]
\tag{3.5.19}
$$

and

$$
\begin{aligned}
\langle \hat{b}_{10}^{\dagger} \hat{b}_{11} \rangle \simeq {}&- \frac{2n_1}{(U_{11} + 2\delta - 2\varepsilon_0)(2U_{01} + \delta - 2\varepsilon_0)} \\
&\times \Big[2n_1 J_1 (2U_{01} + \delta - 2\varepsilon_0) + n_0 (J_1 - J_0)(U_{11} + 2\delta - 2\varepsilon_0) \Big].
\end{aligned}
\tag{3.5.20}
$$

The transition from MI_B to MI_C happens at the sign change of $\langle \hat{b}_{00}^\dagger \hat{b}_{01} \rangle$. We can approximate $2U_{01} + \delta - 2\varepsilon_0 \approx 2U_{01}$ since it is consistent with our previous approximation to neglect γ on doubly occupied sites. Then, the sign change of (3.5.19) happens when

$$n_0 - n_1 \approx \frac{(J_1 - J_0)U_{00} - 4J_0U_{01}}{(J_1 - J_0)U_{00} + 4J_0U_{01}}. \tag{3.5.21}$$

Therefore, we estimate the transition for $V_0 = 15E_R$ at $n_0 - n_1 = 0.30$, for $V_0 = 10E_R$ at $n_0 - n_1 = 0.29$ and for for $V_0 = 5E_R$ at $n_0 - n_1 = 0.24$, which matches reasonably well with the numerical results in Fig. 3.5.7.

3.5.7. Preparation of the Ground State

Here we give a description how in an experiment the ground state of Hamiltonian (3.2.14) can be prepared and the orbital-driven Mott insulator-superfluid phase transition induced.

First of all, the system has to be prepared in (or close to) the undriven ground state, which would be a Mott insulator. Because of the large energy gap D to the first excited band, then almost all bosons occupy the ground band. Keeping the driving frequency constant at a value such that $\delta = D - \hbar\omega$ is still large enough to suppress any significant occupation of the excited band, the driving strength K is then ramped up smoothly to the desired value. During this step, the speed of the ramping has to be low enough to guarantee adiabatic following of the Floquet state that is (in the two-band model) connected to the undriven ground state [175]. On the other hand, the ramping cannot be too slow since it has to be diabatic with respect to tiny coupling matrix elements neglected in the high-frequency approximation leading to $\hat{H}_{2B}$. In any case, a first-order phase transition (as discussed in section 3.5.5) cannot be crossed adiabatically. For an experimental protocol therefore, a second-order transition like the one for $V_0 = 10E_R$ and $n = 1$ has to be chosen.

Apart from the demanded adiabatic following within the effective 2B model and the limitation of the high-frequency approximation made in section 3.3, we have to check that the coupling to higher bands $(b > 1)$ is indeed negligible. As described
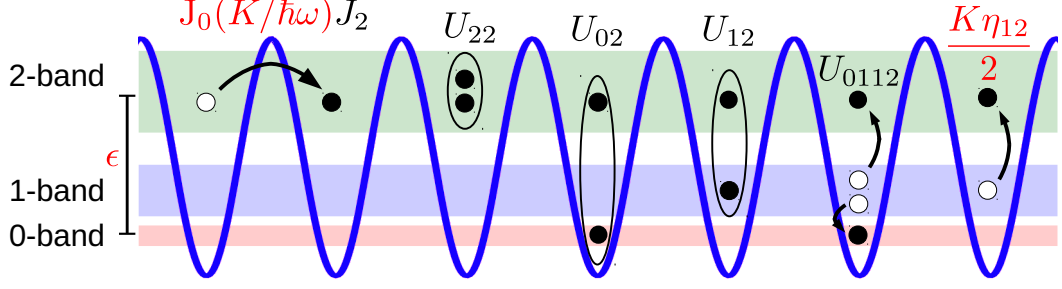
Figure 3.5.8.: Illustration of the energy terms in the effective three-band Hamiltonian (3.5.22) in the dimerized lattice. Excitation to the second excited band can occur due to direct coupling from the first excited band with strength $K\eta_{12}/2$ or due to a photon-conserving scattering event with strength U_{0112}, where two partices scatter from the first excited band to the ground band and to the second excited band, respectively.

in section 3.2, the most dominant process is the coupling to the 2nd excited band. Hence, it is important to make sure that the second excited band remains unoccupied. In the tight-binding approximation, the effective three-band (3B) Hamiltonian then takes the form

$$
\begin{aligned}
\hat{H}_{3\mathrm{B}} &= \hat{H}_{2\mathrm{B}} + \epsilon \sum_{j=1}^{M} \hat{n}_{j,2} + \mathrm{J}_0\left(\frac{K}{\hbar\omega}\right) J_2 \sum_{<ij>} \left(\hat{b}_{i,2}^\dagger \hat{b}_{j,2} + \hat{b}_{j,2}^\dagger \hat{b}_{i,2}\right) + \sum_j \left[\frac{U_{22}}{2}\hat{n}_{j,2}(\hat{n}_{j,2}-1)\right. \\
&\quad + 2U_{02}\hat{n}_{j,0}\hat{n}_{j,2} + 2U_{12}\hat{n}_{j,1}\hat{n}_{j,2} + \frac{U_{0112}}{2}\left(\hat{b}_{j,1}^\dagger \hat{b}_{j,1}^\dagger \hat{b}_{j,0}\hat{b}_{j,2} + \hat{b}_{j,0}^\dagger \hat{b}_{j,2}^\dagger \hat{b}_{j,1}\hat{b}_{j,1}\right)\right] \\
&\quad + \frac{K\eta_{12}}{2}\sum_j \left(\hat{b}_{j,2}^\dagger \hat{b}_{j,1} + \hat{b}_{j,1}^\dagger \hat{b}_{j,2}\right).
\end{aligned}
\tag{3.5.22}
$$

Here, the frequency-dependent band distance to the second excited band is

$$
\epsilon = E_2 - E_0 - 2\hbar\omega = E_2 + E_0 - 2E_1 + 2\delta.
\tag{3.5.23}
$$

All additional terms are illustrated in Fig. 3.5.8. Relevant for the heating are the two last terms in Eq. (3.5.22) where particles are excited either by possibly resonant scattering with matrix element $U_{0112} = U_a \int w_0(x)w_1(x)^2 w_2(x)dx$ or by dipole coupling from the shaking that contains the matrix element $\eta_{12} = \int w_1(x)x w_2(x)dx$. The matrix elements U_{0112} and η_{12} as a function of the lattice depth V_0 are plotted

in Fig. 3.2.9 and Fig. 3.3.1, respectively. While the scattering strength U_{0112} is rather small, the hybridization with the second excited band $\sim \eta_{12}$ is of the same order of magnitude as η_{01}. Therefore, an experiment that relocates the bosons adiabatically from the ground to the first excited band can also adiabatically excite the second excited band, provided there is a respective avoided crossing. By the dimerization of the lattice with $V_1/V_0 = 0.5$ (see section 3.2), however, avoided crossing to the second excited band are prevented since the second excited band is energetically well separated from the first two bands in resonance, i.e. ϵ is relatively large.

To verify the protocol and to demonstrate that interband heating is indeed negligible for the chosen parameter set and dimerization, we can simulate the adiabatic protocol within the effective 3B model (3.5.22) using real time propagation with the TEBD method. Again we choose $V_0 = 10E_R$, $V_0/V_1 = 0.5$ and $K = 0.5E_R$ (compare to Fig. 3.5.5 and Fig. 3.5.7), but reduce the particle number to $M = N = 16$, due to numerical limitations. The band distance is ramped from $\delta/E_R = 1$ to $\delta/E_R = -0.5$ within a time $T_r = 500\hbar/E_R \approx 25$ms so that it starts in a Mott insulator almost fully in the ground band and ends in a superfluid phase almost fully in the first excited band.

With the help of two observables we show that during the numerical simulation, the system indeed follows the effective ground state and furthermore can be sufficiently described by the 2B model. First of all, we consider the absolute value of the overlap $|\langle 3B - IT | 3B - RT \rangle|$ of the many-body wave function of the instantaneous state $|3B - RT\rangle$ in the real time protocol with the exact ground state $|3B - IT\rangle$ for the given δ calculated with imaginary time TEBD in the 3B model. By this, we see if the time evolved state follows the effective ground state adiabatically in the full 3B model. As the other observable we consider the overlap $|\langle 2B - IT | 3B - RT \rangle|$ of the instantaneous wave function with the ground state $|2B - IT\rangle$ of the two-band model (projected on the larger Hilbert space with three bands). This quantity additionally estimates the deviation between the ground states of the two-band and the three-band model. Both overlaps are plotted in Fig. 3.5.9 (top). The time propagated state accurately follows the full 3B ground state, except for a tiny dip in the overlap near the phase transition at $\delta \approx 0.15E_R$, which is typical for the passage of an avoided crossing [184]. On the other hand, the overlap
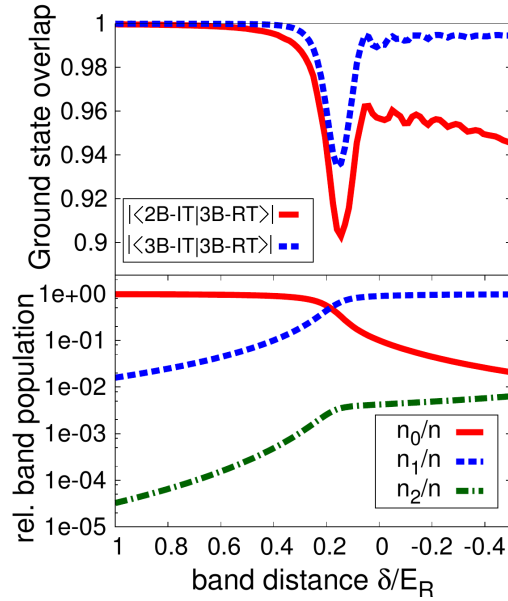
Figure 3.5.9.: Band occupations and overlaps of the instantaneous time evolved state with the (imaginary time-evolved) ground states of the 3B and 2B model. Starting in the ground state at $\delta = \epsilon_1 - \omega = 1E_R$, δ is lowered linearly to $\delta = -0.5E_R$ within a time of $T_r = 500\hbar/E_R$; for $n = 1$, $V_0/E_R = 10$, $V_1/V_0 = 0.5$, $K/E_R = 0.5$ and $M = 16$ rungs under periodic boundary condtions.

$|\langle 2\text{B} - \text{IT}|3\text{B} - \text{RT}\rangle|$ slightly drops to a value of 0.945 at the end of the protocol at $\delta/E_R = -0.5$, indicating a slight occupation of the second excited band of the 3B ground state. This assumption is verified in the bottom plot of Fig. 3.5.9, where the band occupations n_α of the three bands $\alpha = 0, 1, 2$ is plotted on a logarithmic axis for the ground state of the 3B model (3.5.22). The occupation of the second excited band n_2 starts very low, continuously increases as δ is lowered and reaches a small value of approximately 1% at $\delta/E_R = -0.5$, which explains the slight deviation of the time propagated state with the 2B ground state.

To analyze the adiabaticity of the procotol further, we plot in Fig. 3.5.10 (left) the overlap $|\langle 2\text{B} - \text{IT}|3\text{B} - \text{RT}\rangle|$ versus $T_r E_R/\hbar$ and K/E_R at the end of the protocol at $\delta/E_R = -0.5$ for a lattice with $N = M = 10$ particles. Obviously, too small T_r and too small $\gamma \propto K$ spoil the adiabatic dynamics within the 2B model since the relevant avoided crossings are not resolved anymore [175]. Furthermore, for too large K the coupling to the second excited band becomes more relevant, so that
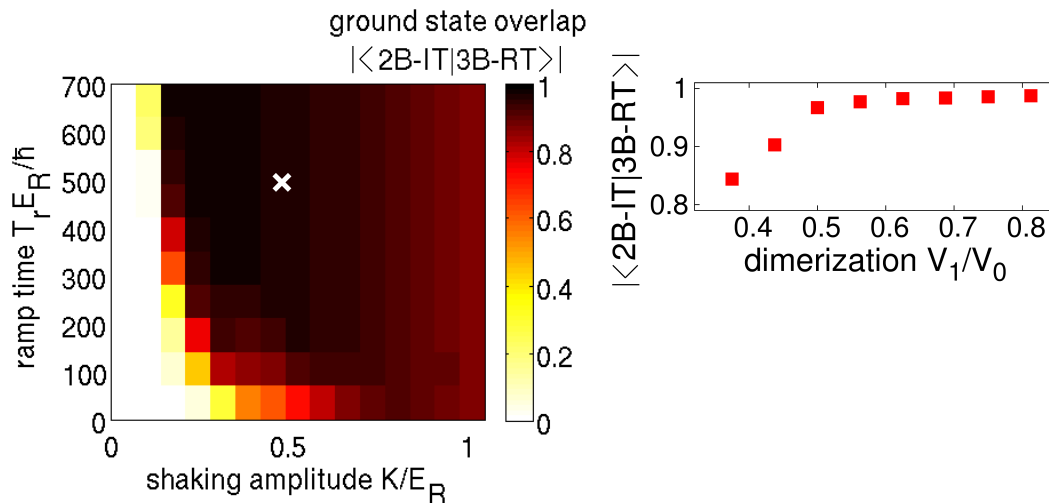
Figure 3.5.10.: After-ramp overlap of the imaginary time-evolved ground states of the 3B. Left: After-ramp overlap in color scale as a function of the ramp time $T_r E_R/\hbar$ and the shaking amplitude K/E_R. Right: After-ramp overlap as a function of the dimerization V_1/V_0.

the 2B model describes the system less accurately. For too large K and T_r also slow second-order loss processes can occur that are, however, not included in the effective models. The white cross in Fig. 3.5.10 (left) indicates the parameters for K and T_r that were used in the simulation in Fig. 3.5.9.

To demonstrate the importance of the dimerization in the proposed protocol, we plot in Fig. 3.5.10 (right) the final overlap for the ramping parameters like in Fig. 3.5.9 but with altering dimerizations. We clearly see that by lowering the dimerization below the value of $V_1/V_0 = 0.5$, the overlap is significantly reduced since a larger fraction of the particles sits in the second excited band in the 3B ground state.

In total, for the demonstrated parameter regime, the coupling to the third band does not cause detrimental heating, which justifies a description of the driven system in terms of the 2B model (3.2.14). Hence, the protocol is suitable to study the orbital driven phase transition from the Mott insulating phase to the superfluid phase. Note that this protocol can also be used as a preparation of a stable low-entropy states in the first excited Bloch band. For this purpose one has to avoid the discontinuous transition.

4. One-dimensional Lattice Anyons in a Shaken Optical Lattice

In this chapter we present a theoretical proposal where time-periodic shaking of a one-dimensional optical lattice filled with ultra-cold bosons is used to realize an effective Anyonic Hubbard Model (AHM) with tunable parameters. Furthermore, we describe signatures of these one-dimensional anyons that are easily accessible in the experiment and propose and test an experimental protocol to prepare the effective anyonic ground state. The main idea and results presented in this chapter have been published in [104].

4.1. Introduction to One-Dimensional Lattice Anyons

Anyons are particles, whose wave function picks up a phase $\theta \neq 0, \pi$ upon particle exchange [185–189]. Hence they interpolate between bosons and fermions. Mathematically, anyons can only exist in two dimensions [185]. As quasi-particles, they play a major role as topologically ordered states of matter such as fractional-quantum-Hall states [190–192]. As they might be applied in robust topological quantum information processing, anyons have caught an increasing attention during the recent years [193–200]. As shown by Haldane, the concept of anyonic, also called fractional statistics can be extended to arbitrary dimensions [201], which allows for (quasi-)anyons for example on a lattice system. One-dimensional anyons have recently attracted increasing attention. This includes theoretical studies [202–217] with a special focus on the ground state and on the hard-core limit, and a proposal to realize anyons in an optical lattice with the help of Raman lasers [102, 103].

However, the implementation of lattice anyons has not yet been accomplished. A minimal model to describe interacting anyons in a one-dimensional lattice, is the anyonic Hubbard model [102], which reads

$$\hat{H} = -J \sum_{j=2}^{M} \left(\hat{a}_j^\dagger \hat{a}_{j-1} + \text{h.c.} \right) + U \sum_{j=1}^{M} \hat{n}_j \left(\hat{n}_j - 1 \right). \tag{4.1.1}$$

So it has the same form as the Hubbard model for bosons, with a nearest-neighbour tunneling term with strength J and an on-site interaction term with strength U. The difference lies only in the anyonic commutation relation of the annihilation and creation operators, $\hat{a}_j$ and $\hat{a}_j^\dagger$, at site j that obey

$$\begin{aligned}
\hat{a}_j \hat{a}_k^\dagger - e^{-i\theta \text{sgn}(j-k)} \hat{a}_k^\dagger \hat{a}_j &= \delta_{jk} \\
\hat{a}_j \hat{a}_k - e^{-i\theta \text{sgn}(j-k)} \hat{a}_k \hat{a}_j &= 0
\end{aligned} \tag{4.1.2}$$

and are parametrized by the statistical or anyonic angle $\theta \in [0, 2\pi)$. The phase depends on the position of the lattice sites since we have $\text{sgn}(k) = -1, 0, 1$ for $k < 0, = 0, > 0$, respectively. Importantly, this implies that on-site for $j = k$, the particles behave like bosons. Thus, for $\theta = \pi$ the lattice anyons are pseudo-fermions instead of true one-dimensional fermions and several of them are allowed to occupy the same site. The anyonic or fermionic nature of the particles matters, however, in the process of two particles passing each other[1].

To make an experimental simulation of lattice anyons possible, the anyonic operators $\hat{a}_j$ and $\hat{a}_j^\dagger$ have to be mapped to bosons in a way that respects their commutation relation (4.1.2). This can be achieved via the generalized Jordan-Wigner transformation [102, 207]

$$\hat{a}_j = \hat{b}_j \, \exp\left(i\theta \sum_{k=j+1}^{M} \hat{b}_k^\dagger \hat{b}_k \right) \tag{4.1.3}$$

---

[1]Consequently, in the case of a sparsely occupied lattice, where it is very unlikely that two lattice-anyons occupy a site at the same time, the model of lattice anyons approaches a hypothetical continuous model of one-dimensional anyons.

mapping the anyons to bosons with annihilation and creation operaters fulfilling

$$\left[\hat{b}_j, \hat{b}_k^\dagger\right] = \delta_{jk}, \ \left[\hat{b}_j, \hat{b}_k\right] = \left[\hat{b}_j^\dagger, \hat{b}_k^\dagger\right] = 0. \tag{4.1.4}$$

The Jordan-Wigner transformation maps the Anyonic Hubbard model (4.1.1) to its bosonic representation,

$$\hat{H} = -J \sum_{j=2}^{M} \left(\hat{b}_j^\dagger \hat{b}_{j-1} e^{i\theta \hat{n}_j} + \text{h.c.}\right) + U \sum_{j=1}^{M} \hat{n}_j \left(\hat{n}_j - 1\right). \tag{4.1.5}$$

The anyonic exchange phase has been translated to a density-dependent Peierls phase: when tunneling one site to the right (left), a boson picks up a phase given by θ $(-\theta)$ times the number of particles occupying the site it jumps to (from). These tunneling processes are illustrated in Fig. 4.1.1. Thus, if two particles pass each other via two subsequent tunneling processes to the right (left), the many-body wave function picks up a phase of θ $(-\theta)$. Note that we implement the model on a one-dimensional lattice with open boundary conditions[2]. Since they break translational symmetry, open boundary conditions lead to density oscillations of the anyonic ground state, providing signatures for the detection of anyons in an experiment, as we will see later.

As ultra-cold atoms in optical lattices in the tight-binding regime provide a versatile tool to realize various quantum lattice models, it appears promising to also implement the anyonic Hubbard model in this way. One important proposal to realize the anyonic Hubbard model in its bosonic representation (4.1.5) with cold gases has been initially proposed by Keilman et al. [102] and has later been improved by Greschner et al. [103]. In these proposals, the density-dependent hopping is induced by Raman lasers. Here, the Fock states of neighbouring sites with different particle occupations, which are energetically decoupled by a lattice tilt, are coupled with several Raman lasers via photon-assisted tunneling, involving a change of the internal atomic state. Since laser intensities and state energies differ, the tunneling elements can be tuned to mimic the density dependence in (4.1.5), at least for tun-

---

[2]The use of periodic boundary conditions in the anyonic model (4.1.1) would be problematic with the Jordan-Wigner transformation since extra boundary terms would emerge in the transformed Hamiltonian (4.1.5) that cannot be taken care of in the experiment.
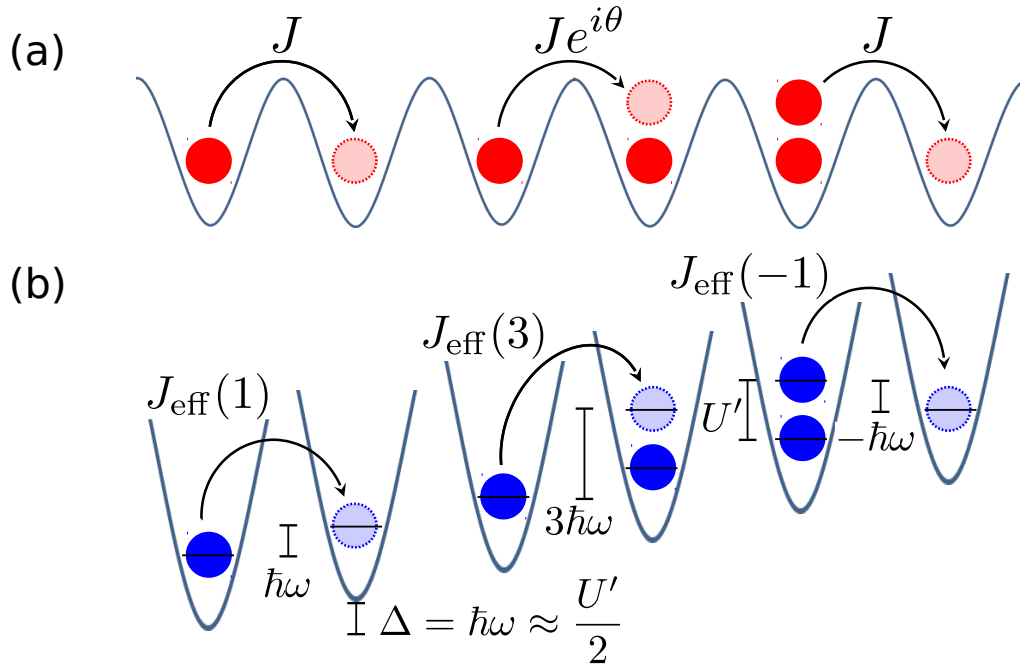
Figure 4.1.1.: (a) Basic number-dependent tunneling processes in the bosonic representation of the anyonic Hubbard model Eq. 4.1.5 involving up to two bosons. We only depict rightwards tunneling, the leftwards processes are Hermitian conjugated. (b) Realization of 1-, 3- and (−1)-photon processes in a tilted lattice with strong on-site interactions U'.

neling processes involving at maximum two particles per site. However, the scheme requires additional laser beams and has not been implemented experimentally.

In the next section, we propose an alternative scheme for the realization of the bosonic representation of the anyonic Hubbard model (4.1.5), where the photon-induced tunneling is achieved by simple lattice shaking without the need for additional lasers.

4.2. Realization of the One-Dimensional Anyonic Hubbard Model in a Shaken Lattice

In this section we will carefully describe how the bosonic Hamiltonian (4.1.5) with a number-dependent tunneling phase and an effective and tunable on-site

interaction can be implemented. The main challenge is to realize the density dependent, complex tunneling coefficients. We present a proposal where these density dependent Peierls phases are realized in the low-density limit, i.e. only for tunneling processes involving two particles at maximum. The trick is to control the tunneling of the atoms via photon-assisted tunneling by a (time-reversal breaking) lattice shaking applied to a tilted lattice. At the same time the on-site interaction of the bosons is tuned in resonance with the photon energy, such that the effective tunneling parameters depend on the occupation of both sites.

To start with, the Hamiltonian of the interacting bosons in a tilted periodically forced lattice reads

$$\hat{H}(t) \;=\; \sum_{j=1}^{M}\Big[- J' \big(\hat{b}_j^\dagger \hat{b}_{j-1} + \text{h.c.}\big) + \frac{U'}{2}\hat{n}_j(\hat{n}_j - 1) + V_j\hat{n}_j + \big(\Delta + F(t)\big) j\hat{n}_j \Big]. \tag{4.2.1}$$

The terms appearing in the Hamiltonian are illustrated in Fig. 4.1.1 b). Here $J' > 0$ and $U' > 0$ denote the tunneling and interaction parameters of the bosons in the undriven and untilted one-dimensional cosine lattice. $\Delta > 0$ quantifies the potential tilt, i.e. the potential energy difference between neighbouring sites. The V_j capture a possible weak additional on-site potential that can also be used to prepare the bosons in a specific initial state, as we will make use of later. Finally, $F(t) = F(t + T)$ incorporates a homogeneous time-periodic force with an angular frequency of $\omega = 2\pi/T$, where the cycle average vanishes, $\frac{1}{T}\int_0^T \mathrm{d}t\, F(t) = 0$. The driving term can be implemented as an inertial force $F(t)/a = -m\ddot{x}(t)$, with lattice constant a, by shaking the lattice position $x(t)$ back and forth. To achieve photon-assisted tunneling, we require for the driving frequency the resonance conditions

$$\Delta = \hbar\omega. \tag{4.2.2}$$

Furthermore, the interaction strength is set such that it is roughly twice the photon energy,

$$U' = 2\hbar\omega + U, \tag{4.2.3}$$

with a small and residual detuning U, which will play the role of the effective on-site interaction parameter later on. We demand the high-frequency condition

$$J', |U|, |V_j - V_{j-1}| \ll \hbar\omega, \tag{4.2.4}$$

such that all processes in the low-energy regime are not affected by the driving up to a parameter modulation. From Eq. (4.2.2) and Eq. (4.2.3) it becomes clear that for a vanishing driving force in Hamiltonian (4.2.1) the tunneling is energetically suppressed since any tunneling process requires at least an energy of $\approx \pm\hbar\omega$. More specifically, when a boson tunnels from site $j-1$ to site j, the system energy changes by $\hbar\omega\hat{\nu}_{j,j-1}$ with

$$\hat{\nu}_{j,j-1} = 2(\hat{n}_j - \hat{n}_{j-1}) + 3, \tag{4.2.5}$$

taking values $\pm1, \pm3, \dots$ when applied to Fock states. However, coherent tunneling processes can be induced by photon-assisted tunneling due to the driving force. Hereby the driving provides or absorbs $|\nu|$ energy quanta $\hbar\omega$, as it is illustrated in Fig. 4.1.1 b). The strength and phase of the photon-assisted tunneling is determined by an effective tunneling matrix element J_{eff} [69, 71], which depends on the occupation numbers of the two involved sites through $\hat{\nu}_{j,j-1}$. The idea of number-dependent resonant tunneling is not new but has been investigated both experimentally [74] and theoretically [60, 77, 102, 103, 218]. The tunneling coefficients can alternatively also be engineered by a modulation of the interaction strength [58, 59, 76, 166, 219, 220]. The aim of the Floquet engineering is to match the effective tunneling parameters with the number-dependent tunneling phases appearing in Eq. (4.1.5), at least in the low density limit. To explicitely calculate the effective tunneling parameters, we once more "gauge away" all terms that are resonant with the driving, as well as the driving itself. This is done using the time-periodic unitary operator

$$\hat{U}(t) = \exp\left(-i\sum_j \left[\omega t\,\hat{n}_j(\hat{n}_j - 1) + \left(\omega t - \chi(t)\right)j\hat{n}_j\right]\right), \tag{4.2.6}$$

where

$$\chi(t) = \frac{am}{\hbar}\dot{x}(t) \tag{4.2.7}$$

is proportional to the lattice velocity. Hence, $\hbar\dot{\chi}(t) = -F(t)$ is the applied force on the driven particles. Crucially, this gauge transformation is number-dependent. The gauge transformation (4.2.6) integrates out the strong on-site terms including on-site interaction and lattice tilt, as well as the periodic force. Since $\hat{U}(t)$ does not commute with the tunneling term in Eq. (4.2.1), the tunneling coefficients in the transformed Hamiltonain $\hat{H}'(t)$ become number-dependent and time-dependent,

$$
\begin{aligned}
\hat{H}'(t) &= \hat{U}^\dagger(t)\hat{H}(t)\hat{U}(t) - i\hbar\hat{U}^\dagger(t)\partial_t\hat{U}(t) \\
&= -J'\sum_j\left[\hat{b}_j^\dagger\hat{b}_{j-1}\exp\left(i\omega t\hat{\nu}_{j,j-1} - i\chi(t)\right) + \text{h.c.}\right] + \sum_j\left[\frac{U}{2}\hat{n}_j(\hat{n}_j - 1) + V_j\hat{n}_j\right].
\end{aligned}
\tag{4.2.8}
$$

The gauge transformation has moved all resonantly coupled states into a subspace with identical photon-number in the extended Floquet Hilbert space. This brings us into the position to neglect the coupling between subspaces with different photon index, i.e. to perform a rotating-wave approximation keeping only the zeroth order Fourier mode of the transformed Hamiltonian (4.2.8). It is achieved by integrating $\hat{H}'(t)$ over one driving period T to obtain the effective time-independent Hamiltonian

$$
\begin{aligned}
\hat{H}_{\text{eff}} &= \frac{1}{T}\int_0^T\mathrm{d}t\,\hat{H}'(t) \\
&= -\sum_j\left(\hat{b}_j^\dagger\hat{b}_{j-1}J_{\text{eff}}(\hat{\nu}_{j,j-1}) + \text{h.c.}\right) + \sum_j\left(\frac{U}{2}\hat{n}_j(\hat{n}_j - 1) + V_j\hat{n}_j\right). \tag{4.2.9}
\end{aligned}
$$

It contains the number-dependent tunneling parameter

$$J_{\text{eff}}(\nu) = \frac{J'}{T}\int_0^T\mathrm{d}t\,\exp\left(i\omega t\nu - i\chi(t)\right) \tag{4.2.10}$$

and the effective interaction parameter $U = U' - 2\hbar\omega$, which can be tuned by controlling the driving frequency ω such that both negative and positive values are

possible.

As already mentioned, the tunneling matrix elements $J_{\text{eff}}(\nu)$ should match the number-dependent tunneling parameters of Eq. (4.1.5) in the low density regime, as depicted in Fig. 4.1.1 a) and b). The tunneling rightwards (leftwards) from (onto) a singly or doubly occupied site onto (from) an empty site corresponds to $\nu = 1$ or $\nu = -1$, respectively. Therefore, to realize the anyonic Hubbard model for low densities the first requirement reads

$$J_{\text{eff}}(1) = J_{\text{eff}}(-1) = Je^{i\phi_g}, \tag{4.2.11}$$

where the tunneling amplitude J is set to be real and positive. The arbitrary Peierls phase ϕ_g reflects the freedom of gauge. On the other hand, tunneling rightwards (leftwards) from (onto) an empty site onto (from) an occupied site is associated with $\nu = 3$. Hence, the corresponding tunneling parameter should carry an additional phase θ, which provides a second requirement:

$$J_{\text{eff}}(3) = Je^{i\theta + i\phi_g}. \tag{4.2.12}$$

The necessary degree of freedom to fulfill conditions (4.2.11) and (4.2.12) in the proposal is the specific time function of the lattice shaking. A simple sinusoidal lattice shaking is not sufficient. Instead, we make the bichromatic ansatz

$$\chi(t) = A\cos(\omega t) + B\cos(2\omega t) \tag{4.2.13}$$

for the (integrated) driving force. However, other choices comprising more harmonics are also possible. Ansatz (4.2.13) already ensures that $J_{\text{eff}}(1) = J_{\text{eff}}(-1)$. The additional constraint

$$|J_{\text{eff}}(3)| = J = |J_{\text{eff}}(1)| \tag{4.2.14}$$

defines lines in the A-B plane, as can be seen in Fig. 4.2.1. The thickness of the line illustrates the tunneling amplitude J whereas the color of the plotted lines represents the statistical angle θ, respectively. We find three curves in the parameter regime displayed in Fig. 4.2.1. If $B = 0$, the solutions cut the axis exactly
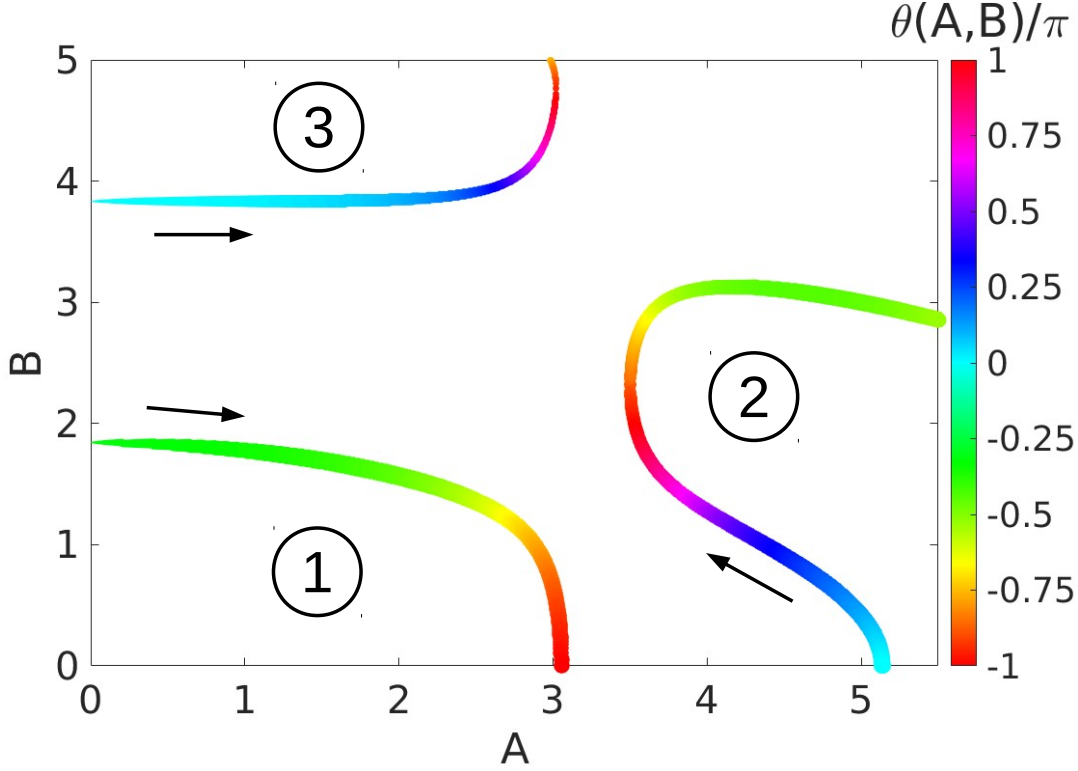
Figure 4.2.1.: Parameter curves that fulfill $|J_{\mathrm{eff}}(1)| = |J_{\mathrm{eff}}(3)|$. The color of the lines represents the statistical angle $\theta = \arg[J_{\mathrm{eff}}(3)/J_{\mathrm{eff}}(1)]$ and their thickness the tunneling amplitude $J = |J_{\mathrm{eff}}(1)|$.

at the points where $|\mathcal{J}_1(A)| = |\mathcal{J}_3(A)|$, which can be deduced from Eq. (4.2.10). At these points, the anyonic phase becomes either $\theta = 0$ or $\theta = \pi$, see also Ref. [85]. On the other hand, the B-axis is cut whenever $|\mathcal{J}_2(B)| = |\mathcal{J}_4(B)|$. The amplitude J of the tunneling vanishes here for symmetry reasons, so again a solution with a non-trivial θ from only one driving mode is not possible. The trivial solutions at the A- and B-axes suggest that there are infinitely many curves in the A-B-plane describing solutions for condition (4.2.14). We focus on the solution where the driving amplitude is as weak as possible. The three given curves in Fig. 4.2.1 together already cover the full range of possible anyonic angles $|\theta| \in [0, \pi]$. To have a closer look, we plot J and θ along the indicated curves $1, 2$ and 3 Fig. 4.2.1. The given scheme matches the anyonic Hubbard model Eq. (4.1.5) only for tun-
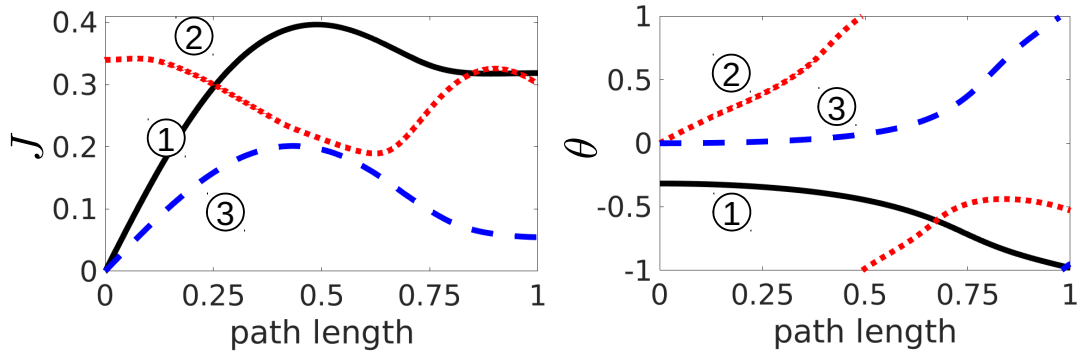
Figure 4.2.2.: Effective tunneling strength (left) and anyonic angle (right) as a function of the path length along the three curves $\alpha = 1, 2, 3$ in Fig. 4.2.1.

neling processes involving two particles at maximum, i.e. in the low-density limit. Tunneling processes with three and more particles will have a different strength $J^{(\nu)} := |J_{\text{eff}}(\nu)|$ and a different relative angle $\phi^{(\nu)} := \arg(J_{\text{eff}})(\nu) + \phi_g \neq n_j\theta$, according to Eq. (4.2.10). In Fig. 4.2.3 we plot tunneling strength and tunneling phase for processes with $\nu = 1, 3, 5, 7, 9$ and for the three given curves as a function of the path length. Note that processes with an even ν do not appear in the Hamiltonian. Depending on the strength of these higher tunneling terms and on the particle density, these processes will cause deviations from the ideal anyonic Hubbard model. As we can see in Fig. 4.2.3, for curve 1 the strengths of higher tunneling processes $J^{(\nu)}$ ($\nu > 3$) are much lower than the those for the one- and two particle tunneling $J^{(1)} = J^{(3)}$, indicating that the effective model with the parameter from the first curve is disrupted least from higher particle tunneling processes.

4.3. Ground-State Properties and Signatures of 1D Anyons

Anyonic signatures show up clearly in the (quasi-)momentum distribution of the particles (see e.g. Ref. [216]). While the non-interacting bosons occupy a single state in form of a Bose-Einstein condensate in the ground state, the ground state of pseudo fermions resembles the Fermi sea. Anyons interpolate between these two cases, see for example Ref. [216]. However, in an experiment one cannot measure

Figure 4.2.3.: Tunneling strengths $J_\alpha^{(\nu)}$ and tunneling phases $\phi_\alpha^{(\nu)}$ for photon numbers $\nu = 1, 3, 5, 7, 9$ as a function of the path length along the three curves $\alpha = 1, 2, 3$ in Fig. 4.2.1.

the anyonic momentum distribution, but only that of the atoms, bosons in our case. The reason for this is that due to the Jordan-Wigner transformation, the momentum distribution of the anyons is different from the bosonic one as $\hat{b}_i^\dagger \hat{b}_j \neq \hat{a}_i^\dagger \hat{a}_j$ for $i \neq j$. In the given proposal, also the gauge transformation (4.2.6) changes the momentum distribution. Therefore, in the following we will consider only observables that are invariant under the Jordan-Wigner and the gauge transformation (see Eq. (4.1.3) and Eq. (4.2.6)). To analyze the ground state, we exactly diagonalize a system of $N = 4$ bosons on $M = 20$ sites with open boundary conditions, both for the ideal model (4.1.5) and the effective Hamiltonian for driven bosons (4.2.9). This corresponds to a density of $n = 0.2$, which lies within the low-density regime. The interaction of the particles can be parameterized by the angle

$$\phi = 2 \arctan\left(\frac{U}{J}\right). \tag{4.3.1}$$

Thus, $\phi = 0$ implies free particles, whereas $\phi = \pi$ implies hardcore particles. The effective tunneling matrix elements (4.2.10) were obtained for the driving function corresponding either to path 1 of Fig. 4.2.1 or to path 2 (for $|\theta| < 0.4\pi$). The

real anyons   driven bosons
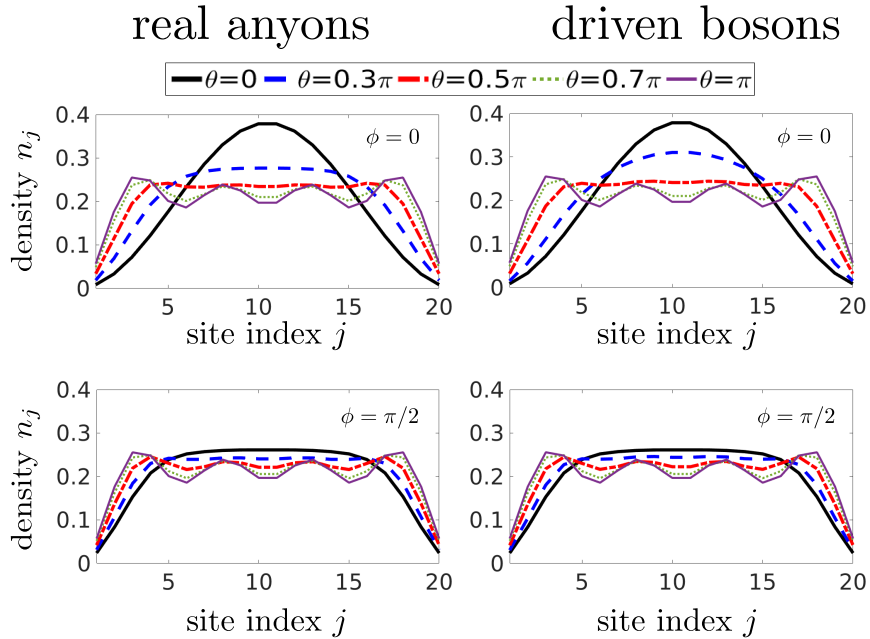
Figure 4.3.1.: Density distribution of the ground state in an exactly diago-
nalized chain of $N = 4$ particles on $M = 20$ lattice sites with open boundary
conditions for different statistical angles θ. Left: Full anyonic model accord-
ing to Eq. (4.1.5). Right: Driven bosons according to the effective model in
Eq. Eq. (4.2.9) and Eq. (4.2.10). Upper row: Non-interacting particles $\phi = 0$,
i.e. $U = 0$. Lower row: Particles with effective on-site interaction $\phi = \pi/2$, i.e.
$U = J$.

choice of path 1 is motivated by the fact that on the one hand the required driving
amplitudes are the lowest here and on the other hand matrix elements for higher
order tunneling processes are lowest for this choice, as illustrated in Fig. 4.2.3.

The first observable we look at is the local particle density $n_j = \langle \hat{n}_j \rangle = \langle \hat{b}_j^\dagger \hat{b}_j \rangle = \langle \hat{a}_j^\dagger \hat{a}_j \rangle$
of the ground state. Clearly, the local particle density is invariant under both
transformations (4.1.3) and (4.2.6). In Fig. 4.3.1, we illustrate the density of
anyons (left) and driven bosons (right) as a function of the site index j for different
statistical angles θ in the exactly diagonalized chain. Let us first discuss the
(effectively) non-interacting case $\phi = 0$, which is plotted in the upper row. Whereas
the density distribution in the bosonic case ($\theta = 0$) is rather localized in the center
of the lattice, it flattens when the statistical angle θ is switched on. This effect can
be understood, by noting that the scattering properties of the particles resulting

from the density dependent tunneling, actually resemble those of repulsive on-site interactions [103], which favor a flat density. In other words, the statistical angle θ plays a somewhat similar role as the introduced angle ϕ from the on-site interactions. For large θ, approaching the pseudo-fermionic regime, the density becomes, furthermore, modulated, with one maximum for each particle in the chain. These density oscillations correspond to Friedel oscillations, which are a hallmark of fermionic behavior [221]. They are a finite-size effect induced by the hard-wall boundary conditions which break the translation symmetry and mirror the Pauli-exclusion principle. Hence, the particle density roughly takes the form [222]

$$n(r) \approx n + \delta n \frac{\cos(2k_F r + \delta)}{r} \qquad (4.3.2)$$

where r is the distance from the wall, n is the average density, δ a phase shift and δn the oscillation depth that decreases with the lattice size M in a finite chain [223]. The oscillation wavelength is thus given by π/k_F, with Fermi wave vector k_F, the wave vector of the largest occupied quasimomentum state. This wavelength corresponds to the average particle distance, which in our system is given by $1/n = 5 \approx 2\lambda_F/a$ lattice sites. The smooth fermionization via the statistical angle θ is a fundamentally new way of approaching fermionic behavior [224], complementary to increasing the on-site interaction. The Friedel oscillations for the quasi-fermions in the low-density regime are, however, purely phase-driven and are not a consequence of the Pauli-exlusion principle. In principle, the particles could also occupy the same site, which happens for higher particle densities, as shown in the next section.

In the lower row of Fig. 4.3.1 we show the calculated density distribution for the case $\phi = \pi/2$, i.e. $J = U$. Here, both effects coming from anyonic exchange interactions and on-site interactions add up and lead to a flattened density distrubtion. In both cases, $\phi = 0$ and $\phi = \pi/2$, the densities of the driven bosons (Fig. 4.3.1 right) matches very well the one of the real anyons (Fig. 4.3.1 left), which confirms the validity of the proposal and justifies the approximations that have been made. To illustrate the difference of fermionization by on-site interaction (parameterized by ϕ) and statistical angle (induced by θ), we show in Fig. 4.3.2 the particle density
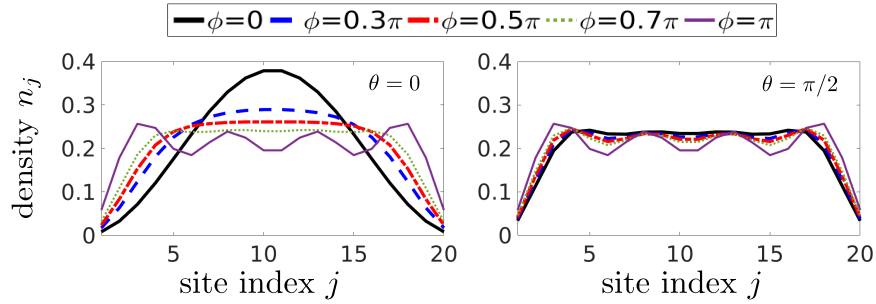
Figure 4.3.2.: Density distribution of the ground state of the same system as in Fig. 4.3.1 for the full anyonic model. Here, the statistical angle θ is fixed and the effect of the on-site interaction ϕ is illustrated. Left: Interacting bosons $\theta = 0$. Right: Interacting anyons $\theta = \pi$.

of bosons ($\theta = 0$) and anyons ($\theta = \pi/2$) with varying interactions $0 \leq \phi \leq \pi$. The transition from non-interacting bosons to hardcore bosons (or equivalently hardcore fermions) is very similar to the transition induced by the statistical angle θ.
The second observable that we consider in order to look for anyonic signatures in the ground state, is the second Rényi entropy

$$S_\ell = -\ln \operatorname{Tr}(\hat{\rho}_\ell^2). \tag{4.3.3}$$

It is the purity of the reduced density matrix $\hat{\rho}_\ell$ of the subsystem given by the first ℓ sites $j = 1, \ldots, \ell$. This quantity is especially interesting since it has recently been measured in a small chain of only four bosons on four sites, see Ref. [225]. The second Rényi entropy is a measure for how much a subsystem of the chain is entangled with the rest of the system. First, let us show that the second Rényi entropy of a one-dimensional quantum chain is invariant under the Jordan-Wigner transformation (4.1.3). Applying the Jordan-Wigner transformation, an anyonic Fock states can be written as

$$|\boldsymbol{n}\rangle = |n_1\rangle_a |n_2\rangle_a \cdots |n_M\rangle_a = \exp\left(-i\theta \sum_{j=1}^{M} \sum_{k=j+1}^{M} n_k\right) |n_1\rangle_b |n_2\rangle_b \cdots |n_M\rangle_b \tag{4.3.4}$$

where $|n_j\rangle_b$ is the bosonic Fock state of site j and $|n_j\rangle_a$ the anyonic one respectively. The transformation can also be reinterpreted as an independent site-local transfor-

real anyons driven bosons
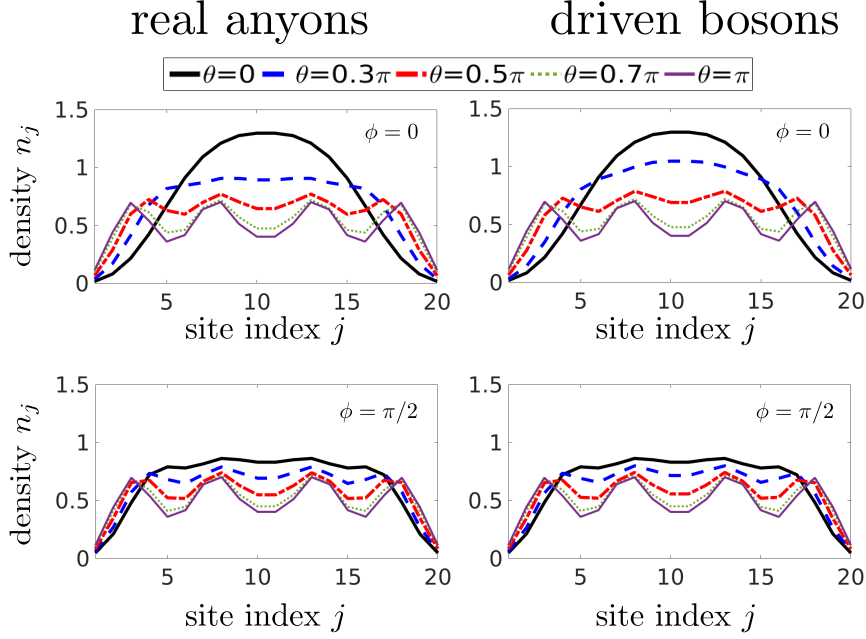
Figure 4.3.3.: Second Rényi entropy of the anyonic ground state on the chain as in Fig. 4.3.1 as a function of the size of the subsystem, for different statistical angles θ.

mation $|n_j\rangle_a = \exp(-i\theta(j-1)n_j)|n_j\rangle_b$. Therefore, tracing out a site k is identical for bosons and 1D anyons,

$$\sum_{n_k} {}_a\langle n_k| \cdot |n_k\rangle_a = \sum_{n_k} {}_b\langle n_k| \cdot |n_k\rangle_b, \qquad (4.3.5)$$

To obtain the reduced density matrix ρ_ℓ, we have to trace out all other sites $k = \ell + 1, \ldots, M$, thus we find ρ_ℓ and consequently S_ℓ, which involves further local traces, invariant. In Fig. 4.3.3, we plot the second Rényi entropy as a function of the size of the subsystem, again for real anyons (left) and driven bosons (right), for different statistical angles θ (line color and style) and for the case of non-interacting particles (upper row) and interacting particles (lower row). Once more we observe a clear broadening of the distribution and the formation of pronounced Friedel oscillations. Increasing the statistical angle, the regions on the chain disentangle from each other, demonstrating that the particles localize and avoid each other. Thus, the second Rényi entropy provides another real-space observable to track
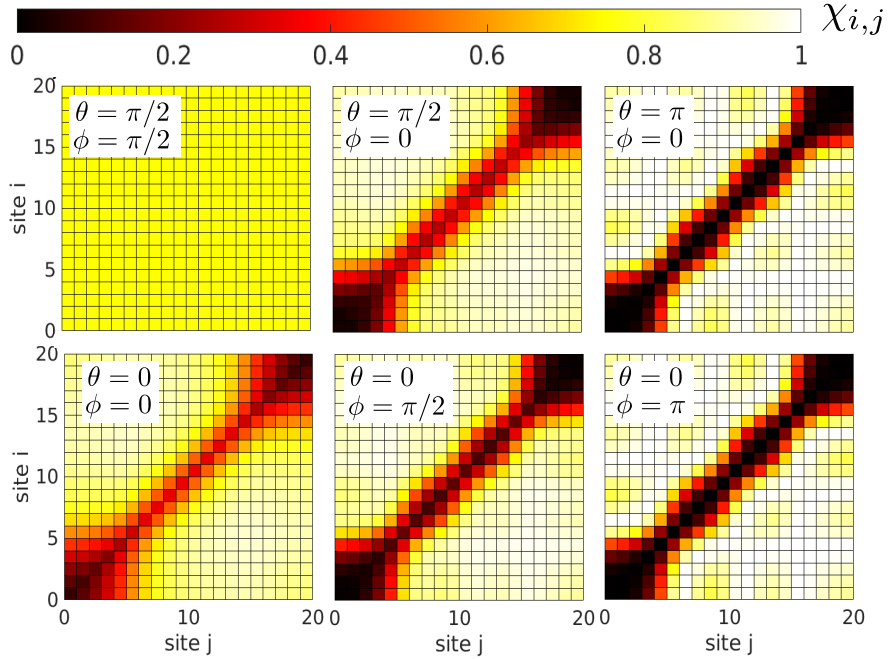
Figure 4.3.4.: Real-space two-particle correlations $\chi_{i,j}$ of the ground state of the full anyonic system for different statistical angles θ and on-site interactions ϕ.

smooth fermionization and anyonic behaviour, applicable to the given proposal of driven bosons.

The formation of Friedel oscillations allows us to monitor the continuous fermionization of the 1D anyons in our system. However, since Friedel osciallations are a finite-size effect induced by the hard-wall boundaries, their strength and visibility diminishes when going to larger systems. Therefore, a small chain like the chosen one that can be realized in an experiment like in Ref. [226] would be favourable in an experiment to detect Friedel oscillations of the anyons. An alternative would be a longer chain with a local defect, providing another form of breaking translational symmetry.

The third real space variable that reveals anyonic behaviour are the (normalized)

two-particle correlations

$$\chi_{i,j} = \frac{\langle b_i^\dagger b_j^\dagger b_j b_i \rangle}{n_i n_j}. \tag{4.3.6}$$

This quantity is related to the probability of finding a particle at site j if one has detected one at site i. In Fig. 4.3.4 we show $\chi_{i,j}$ of the ground state for the exactly diagonalized chain for the full anyonic model Eq. (4.1.5), for different statistical angles θ and on-site interactions ϕ. The white regions in the plot indicate maximum correlation, whereas in the black regions this probability vanishes. As expected, the two-particle correlations for non-interacting bosons ($\theta = \phi = 0$) are constant since the particles form a Bose condensate. While increasing the statistical angle θ (or the on-site interaction ϕ), we observe that the diagonal terms $\chi_{i,i}$ decrease and even vanish in the (pseudo-)fermionic case. So, even though on-site they behave like bosons, two pseudo-fermions do not occupy the same site in the low-density regime. The slight modulations in $\chi_{i,j}$ away from the diagonal can be explained by Friedel oscillations. Thus, also the two-particle correlations show clear signatures of anyonic behaviour in the ground state and indicate smooth fermionization for increasing θ.

Consequently, we have presented three quantities, particle density, second Rényi entropy and two-particle correlations, that show clear signatures of an anyonic ground state. Furthermore, they can directly be observed in an experiment since these quantities are invariant under the Jordan-Wigner transformation (4.1.3) and also under the unitary transformations (4.2.6) that are required to realize the anyonic Hubbard model in the shaken lattice, as presented in the previous section.

4.4. Limitations in the Simulation of Lattice Anyons

As already mentioned, the low-density limit in the effective anyonic Hubbard model is crucial for our proposal for two reasons: First of all, a large particle density will lead to multiple site occupations, which does not reflect the nature of anyons or fermions. Secondly, tunneling processes involving three and more particles in the effective Hamiltonian Eq. (4.2.9) do not reflect the tunneling of anyons, as
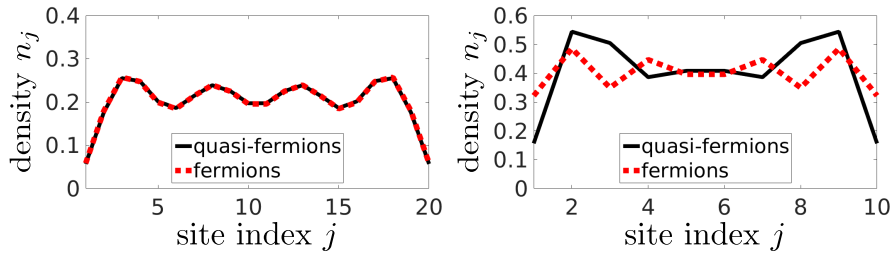
Figure 4.4.1.: Comparison of the pseudo-fermionic ($\theta = \pi$) density distrubtion of the ground state on an exactly solved open chain with the fermionic density distrubtion obtained from summing up the single-particle states in an open chain. Left: On the same system as in Fig. 4.3.1 with $N = 4$ particles on $M = 20$ sites, giving $n = 0.2$. Right: On a chain with $N = 4$ particles on $M = 10$ sites, giving $n = 0.4$.

illustrated in Fig. 4.2.3. In this section, we will distinguish both effects when going to higher particle densities and we will also estimate the effect of finite temperatures on anyonic signatures of the anyonic system.

To demonstrate the difference of anyons and (pseudo-)anyons, we consider the fermionic case $\theta = \pi$, as it can be solved analytically. Therefore, we compare the density from Fig. 4.3.1 to the density distribution of real one-dimensional fermions, which is simply the sum of the densities of single-particle densities of fermions. Each fermionic single particle state is a superposition of plain lattice waves of momenta k and $-k$, in order to match the open boundary conditions. If the number of lattices sites M is even, the single-particle states take the form

$$\psi_k(j) = \frac{1}{i\sqrt{2(M+1)}} \left[\exp(ikj) - \exp(-ikj) \right] = \sqrt{\frac{2}{M+1}} \sin(ikj) \qquad (4.4.1)$$

with quasi-momenta $k = \frac{\pi}{M+1}, \frac{2\pi}{M+1}, \ldots, \frac{N\pi}{M+1}$. Since the particles do not interact, the multi-particle state is simply the Slater determinant of the single particle states. Hence, the on-site particle density of the many-body state is just the sum of the squared wave functions of the states (4.4.1) at each site. In Fig. 4.4.1 (left) the exact fermionic result is compared to that of the quasi-fermions for the given system. Here, in the low-density regime with $n = 0.2$, both densities match perfectly. In Fig. 4.4.1 (right) we also compare densities for fermions and quasi-fermions for a
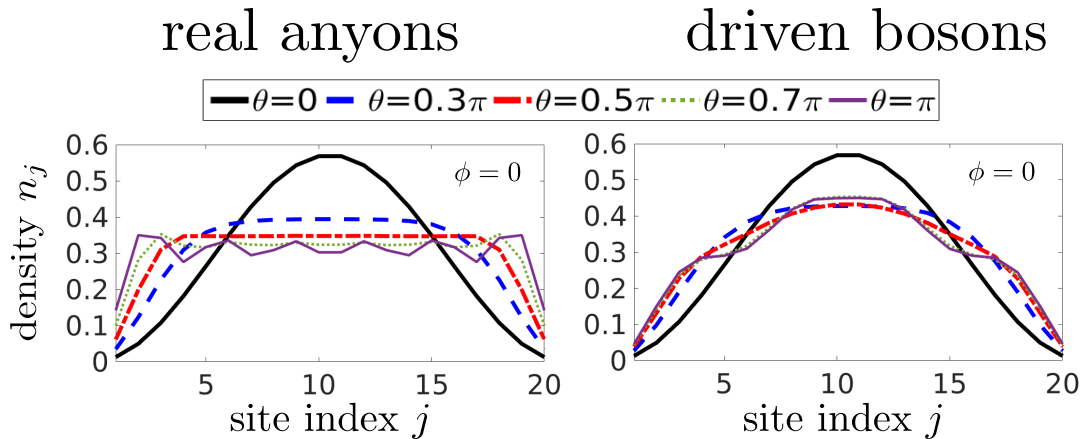
Figure 4.4.2.: Density distrubtion for an exactly solved open chain with $N = 6$ non-interacting particles on $M = 20$ sites. Left: Full anyonic Hubbard model. Right: Effective model with driven bosons.

system with 4 particles on 10 sites, i.e. $n = 0.4$. Here, the quasi-fermions indeed occupy the same sites to reduce kinetic energy and the density distribution differs notably from the fermionic one.

Next we want to illustrate the break-down of the anyonic ground state for larger particle densities due to the limitations of the effective model, i.e. the effect of tunneling processes involving more than two particles. For this, we plot in Fig. 4.4.2 the particle density of $N = 6$ non-interacting particles on the open chain with $M = 20$, which gives a total particle density of $n = 0.3$. While we show on the left the plot for the ayonic Hubbard model (4.1.1), we show on the right the same plot, but for the effective model (4.2.9). As we can see, because of the tunneling processes with more than two particles, the Friedel oscillations disappear almost completely in the effective model and the distribution does not match anymore with the expected one from the anyonic Hubbard model.

To compare both limitations on the particle density, in Fig. 4.4.3 we plot for fermions, pseudo-fermions and the effective model with $\theta = \pi$ the local particle density for a chain of $M = 14$ sites the local and different particle numbers. We clearly see that whereas the fermions always show Friedel oscillations, except for half-filling as a consequence of symmetry (see Eq. (4.4.1)), the Friedel oscillations break down first for the effective model and then for the Anyonic Hubbard model.
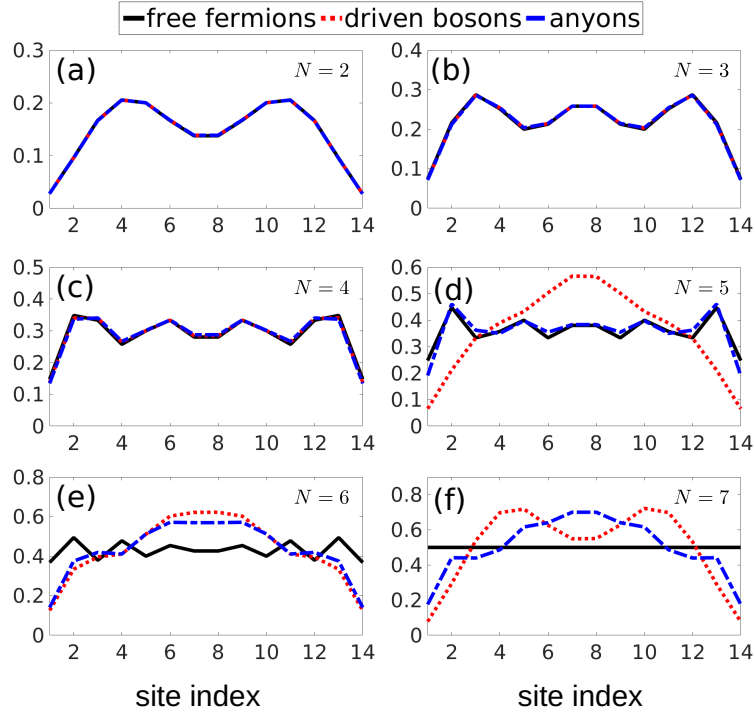
Figure 4.4.3.: Density distrubtion of fermions (solid line), anyons (dashed line) and driven bosons (dotted line) for an exactly solved open chain with $M = 6$ site and varying numbers of (pseudo-)fermions from a) to f).

Finally, we quantize the effect of finite temperatures on the proposed signatures of the ground state of the Anyonic Hubbard Model. For this, we compute the particle density $n_j(T)$ at temperatrue T by calculating the particle densities $n_j^{(\alpha)}$ of energy eigenstates with index α ($\alpha = 0$ corresponds to the ground state) and weighting the densities in the canonical ensemble

$$n_j(T) = \frac{1}{Z} \sum_j n_j^{(\alpha)} \exp\left(-\frac{E_j}{k_B T}\right). \tag{4.4.2}$$

Here,

$$Z = \sum_j \exp\left(-\frac{E_j}{k_B T}\right) \tag{4.4.3}$$
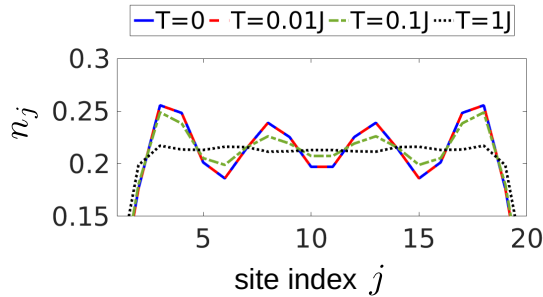
Figure 4.4.4.: Effect of the temperature on the density distribution for a system of $N = 4$ interacting pseudo-fermions $U/J = 0.5$ on $M = 20$.

is the partition function and k_B denotes Boltzmann's constant. We calculate $n_j(T)$ for the chain with $N = 4$ particles on $M = 20$ sites. We choose pseudo-fermions, i.e. $\theta = \pi$, where the Friedel oscillations are most prominent and $U/J = 0.5$, which is justified in the next section. In Fig. 4.4.4, we show the resulting densities for temperatures $k_B T = [0.01J, 0.1J, J]$ compared to the zero-temperature case, i.e. the exact ground state. While we observe perfect agreement for $k_B T = 0.01J$, the Friedel oscillations become weaker around $k_B T = 0.1J$ and vanish completely for $k_B T = J$. Hence, in an experiment realizing one-dimensional anyons in an optical lattice, the temperature has to stay well below $1J$. For $V_0 = 10E_R$ it has to lie in the lower nK-regime being explored in recent experiments (see e.g. Ref. [227]) but still a challenge.

4.5. Preparation of the Anyonic Ground State in an Experiment

In an experiment, the ground state of the effective anyonic Hamiltonian (4.2.9) has to be prepared starting from the ground state of the undriven bosonic system. In this section we will describe how this is possible in an adiabatic fashion. We assume that initially the lattice is untilted, $\Delta = F = 0$, and the system is prepared in a Mott-insulator state $|S\rangle$. In this state $|S\rangle$, the particles are localized in single
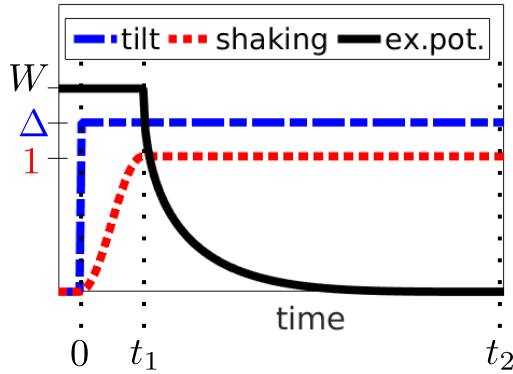
Figure 4.5.1.: Protocol for an experimental preparation of the anyonic ground state of Eq. (4.2.9). Control parameters include the lattice tilt Δ, the lattice shaking (1 corresponds to the final amplitudes A and B) and the depth of the super-lattice W.

sites $j \in S$ via a super-lattice, i.e. equally distributed along the chain,

$$|S\rangle = \prod_{j\in S} \hat{b}_j^\dagger |\text{vac}\rangle. \tag{4.5.1}$$

Here, $|\text{vac}\rangle$ denotes the vacuum state. For example, in the chain of $N = 4$ particles on $M = 20$ sites, we consider $S = \{3, 8, 13, 18\}$. The choice of equally spaced lattice sites minimizes mass transport during the adiabatic process, in contrast to, e.g., an initial state where the particles are gathered in the center of the chain. This initial state is the asymptotic ground state in the presence of an external potential $V_j = -W\delta_{j\in S}$ for $W, U' \gg J$. For finite U, this is also the ground state of the effective model (4.2.9), with $J_{\text{eff}}(\nu) = 0$. Thus, if U has at least a small value, we can adiabatically melt the Mott insulator into the ground state of $\hat{H}_{\text{eff}}$.

Now we will describe step by step how the anyonic ground state can be prepared. The proposed protocol is depicted in Fig. 4.5.1. Firstly, at time $t_0 = 0$, the lattice tilt Δ is ramped up abruptly such that the state remains in a Mott-insulating state. Secondly, between t_0 and t_1 the periodic force is ramped up adiabatically. In this step, the effective tunneling with $J_{\text{eff}}(\nu)$ is switched on. Finally, between t_1 and t_2 the external potential W is switched off continuously, which transforms $\hat{H}_{\text{eff}}$ to the desired model.
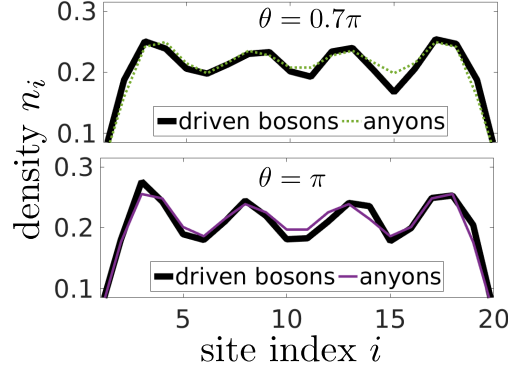
Figure 4.5.2.: Density distribution of the final state compared to the ground state of the anyon model (4.1.1). We have chosen realistic parameters for an optical lattice of depth $V_0 = 10E_R$ giving $J' = 0.0192E_R$, where the recoil energy E_R typically corresponds to frequencies of a few kilo Hertz [6]. Moreover, we chose $\hbar\omega = E_R - U$ (well below the band gap of $\approx 5E_R$), $U = 0.5J$, $W = 0.6E_R$, $t_1 = 50T$ and $t_2 = 1240T(1300T) \approx 50\hbar/J$ for $\theta = 0.7\pi(\pi)$.

We have simulated this protocol integrating the time evolution of the full time-dependent Hamiltonian (4.2.1). As anyonic angles we have chosen $\theta = 0.7\pi$ and $\theta = \pi$, for which the Friedel oscillations are quite prominent. Furthermore, we have chosen $U = 0.5J$ as it has to be finite. Note, however, that U is still small enough such that for bosons ($\theta = 0$) there are no interaction-induced Friedel oscillations for these parameter values. The times $t_1 = 50T$ and $t_2 \approx 50\hbar/J$ are picked such that the instantaneous state follows adiabatically the effective ground state in the process of switching on the driving and in the process of ramping down the super-lattice, respectively. The resulting density distribution at the end of the protocol is compared to the expected one from Eq. (4.2.9) in Fig. 4.5.2. We see good agreement between the final state and the ground state of H_{eff}. This agreement confirms both a representation of the anyonic Hubbard model by the effective Hamiltonian (4.2.9) and the possibility to actually prepare the atoms in the anyonic ground state.

5. Heating Processes in Driven Optical Lattices

In this chapter we discuss multi-photon excitation in driven optical lattices. These multi-photon excitations can lead to unwanted heating. In principal, they can also be used for a controlled population transfer between Bloch bands. The multi-photon excitations are analyzed for a shaken and for an amplitude-modulated lattice, leading to different selection rules and parameter dependencies.

In Sec. 5.1 and Sec. 5.2 we describe how multi-photon excitations emerge in a periodically driven lattice and how this leads to heating of the atomic gas. In Sec. 5.3 we analyze in detail how these excitations are induced in a shaken lattice. We calculate and approximate strength and position of the resonances of the excitations, which depend on amplitude and frequency of the shaking, using Floquet theory and numerical methods. The results are compared to experimental data. Using similar methods, in Sec. 5.4 we analyze multi-photon excitations for the case of an amplitud-modulated lattice.

5.1. Overview over Heating Processes in Periodically Driven Lattices

As we have seen in Chap. 3 and Chap. 4, high-freqency time-periodic forcing of the optical lattice is used to realize an effective Hamiltonian, whose overall form is rather simple and permits a clear interpretation [57, 67, 111, 114, 228]. The high-frequency condition states that the photon energy $\hbar\omega$ of the driving, where $\omega = 2\pi/T$ is the driving frequency and T its period, has to be significantly larger than the parameters of the static lattice Hamiltonian, like for example the

interaction parameter U or the tunneling coefficient J. An exception from this condition are those parameters that are deliberately addressed by the driving in a resonant fashion, like e.g. the lattice tilt Δ for shaking-assisted tunneling. If the high-frequency condition is not matched, the periodic forcing leads to undesired coupling between Floquet states with a different photon index m, such that the effective description breaks down or is only valid on a time scale that is too small for the desired experiment [57]. Due to these excitation processes, energy is pumped into the system in an uncontrolled fashion. Therefore we denote them as heating. The validity of the high-frequency approximation has been studied for various scenarios in references [67, 69, 175, 228–233].

Since most experiments in cold atoms are designed to engineer a system within a single or a small number of Bloch bands, the driving is also limited by a low-frequency condition: the photon energy $\hbar\omega$ has to be sufficiently small (or sometimes just not equal) compared to the energy gap to higher lying Bloch bands. For example, in Chap. 3 the lowest included Bloch band was the second and in Chap. 4 it was the first excited band. Heating that results from excitations to higher Bloch bands already occurs for a single particle, hence also for weakly interacting atomic gases. If the particles are strongly interacting, one has to combine excitation and scattering processes to describe the occuring heating processes. Previous work in this direction includes theoretical studies of resonant inter-orbital coupling due to both single-particle processes [234, 235] and two-particle scattering [165, 236]. Recently, there has been a study about how the interaction of the bosons in an shaken optical lattice affects (multi-)photon excitations and thus heating [237]. In this work, heating rates for different shaking amplitudes, frequencies and interaction strength have been measured and compared to rates obtained from many-body Floquet theory.

Note that particles can also be excited to higher lying Bloch bands for photon energies $\hbar\omega$ much lower than the relevant band gaps. This can happen if the energy differences of the Bloch states is a multiple of $\hbar\omega$. The discussion of these multi-photon transitions in driven optical lattices, which also lead to unwanted heating, will be studied in this chapter.

5.2. Single-Particle Heating Processes for Two Different Driving Schemes

We limit ourselves to the case of weakly interacting bosonic gases such that the problem can be addressed on the single-particle level. Furthermore, as long as the driving force is translationally invariant (in an adequate gauge), quasimomentum is conserved, which simplifies the analysis further. Since cold-atom experiments often take place in the lowest Bloch band of an optical lattice, we consider the scenario where the system is initialized in the ground-state $|0, q\rangle$ of the static Hamiltonian $\hat{H}_0$, whose eigenstates we denote by $|b, q\rangle$, where b and q are the indices of Bloch band and quasimomentum, respectively. Typically, we have $q = 0$ for the ground state. To quantify heating by single-particle excitations to higher Bloch bands, we introduce the parameter

$$h_\tau = \min_{t \in [0, \tau]} n_0(t) \tag{5.2.1}$$

which is the minimum over of the time-dependent occupation of the (static) ground state $n_0(t) = |\langle 0, q | \psi(t) \rangle|^2$ over the time span τ during which the periodic forcing is switched on. We take the minimum in the time-dynamics since the particles are likely to leave the atomic cloud once they are excited to higher Bloch bands. Thus, $h_\tau = 1$ means that the system remained in the ground state for the whole time τ and no heating has taken place. On the other hand, $h_\tau = 0$ means that at least at some point in time $t \in [0, \tau]$, the system left the ground state completely and the heating is maximum.

The amount of heating depends of cause on the frequency of the driving, its strength and the experimentally relevant time scale. Crucially, it also depends on the manner the periodic forcing is switched on. This can happen rather smoothly or abruptly. To better understand the implications of this, we consider two cases. In the first case the forcing strength of the Hamiltonian is switched on and increased very slowly such that the system remains approximately in a single Floquet state $|\psi_{n,q}(t)\rangle$. Calculating the Floquet spectrum gives full information about the contribution of higher Bloch bands to this Floquet state. Smoothly ramping up the amplitude of the periodic forcing, the quasienergy of the Floquet state will
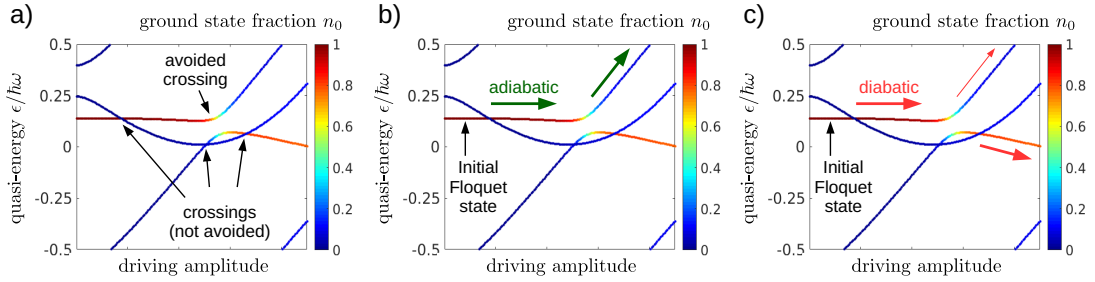
Figure 5.2.1.: An illustration of the quasienergy spectrum as a function of the driving amplitude. Shown are the three Floquet states that arise from the three lowest eigenstates in the static Hamiltonian. The color code represents the fraction of the lowest Bloch state. In a) we have marked a pronounced avoided crossing and three crossings that appear to be non-avoided since the states are very weakly coupled. As shown in b), if the driving amplitude is ramped adiabatically with regard to the avoided crossing, the system remains in the initial Floquet state. In contrast, in c) the ramping is diabatic with regard to the avoided crossing such that the system will predominantly switch to the Floquet state that has similar properties like the initial state.

encounter avoided crossings, where the hybridization of the (static) ground state with higher lying Bloch states takes place. After this passage the Floquet state has a higher contribution of these excited Bloch states. A diabatic passage leads to less heating as illustrated in Fig. 5.2.1.

An adiabatic passage of all avoided crossing is, however, not possible: There are in principal infinitely many excited states. Most of the resulting crossings in the quasienergy spectrum are very tiny since the coupling of the states is extremely weak. In these cases, even a slow turning-on of the driving leads to a diabatic passage of these crossings. Therefore, in a realistic scenario the slow switching-on of the periodic driving is always accompanied by a mixture of adiabatic and diabatic processes. This was also described in Sec. 3.5.7, where the orbital-driven quantum phase transition happened adiabatically with regard to the first excited Bloch band but diabatically with regard to the second and higher excited Bloch bands.

In the other extreme scenario, the periodic forcing is switched on instantly at $t = 0$. This setting corresponds to a quantum quench where the initial state which is a basis state $|0q\rangle$ of the old (static) basis is projected onto the new (Floquet) basis

a)   b)
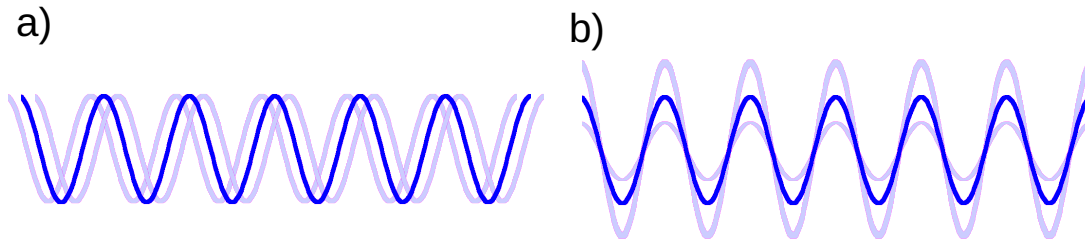
Figure 5.2.2.: The two driving schemes of the one-dimensional optical lattice that are analyzed. a) Shaken lattice: The lattice is moved back and forth in a sinusoidal fashion while the lattice depth remains constant. b) Amplitude-modulated lattice: The amplitude of the lattice is modulated sinusoidally while the lattice stays at a fixed position.

$|\psi_{n,q}(t)\rangle$ as

$$
\begin{aligned}
|\psi(t)\rangle &= \mathcal{T}\exp\left[i\int_0^t dt'\hat{H}(t')\right]|0q\rangle \\
&= \sum_n |\psi_{n,q}(t)\rangle\langle\psi_{n,q}(0)|0q\rangle,
\end{aligned}
\tag{5.2.2}
$$

where each Floquet state propagates independently in time. If more than one of the coefficients $\langle\psi_{n,q}(0)|0q\rangle$ is non-vanishing, the system that started in the ground-state at $t = 0$, excites subsequently higher lying Bloch states via the dephasing of Floquet states. Theoretically, this leads to a multi-mode oscillation between the involved Bloch-states that are also part of the excited Floquet states. In practice, the oscillations are reduced since the atoms leave the condensate via incoherent processes over time. This is the reason why we have taken the minimum in the definition of the heating parameter h_τ in Eq. (5.2.1). The amplitudes and frequencies in the oscillation spectrum after a quench can in principle be computed by the Floquet states and their quasienergies after the ramp. The strength of the heating can also be estimated by Floquet perturbative methods in Floquet space, which we will make use of in this chapter. The most common case, that only two or three states are driven near their (multi-photon) resonance is discussed in App. C. In the following, we will consider two scenarios for a periodically driven lattice: The first one is lattice shaking, which has been considered already in Chap. 3 and Chap. 4 and other theoretical and experimental works (see Chap. 1). The second

example is an amplitude modulation of the optical lattice, which has also been used in many theoretical and experimental works (see Chap. 1). Both schemes are illustrated in Fig. 5.2.2. For these two examples, we will apply analytical and numerical methods to understand the excitation processes that occur due to the periodic driving and compare them with each other.

5.3. Multi-Photon Heating in a Shaken Optical Lattice

Here we consider the scenario where the lattice is periodically driven by shaking it back and forth. Initially, the bosons "sit" in the ground state in the lowest band of the static lattice before the shaking is turned on. Heating is regarded as excitation of the particles to higher Bloch bands. We start with a Fourier expansion of the time-dependent Hamiltonian, from which we can then calculate the effective coupling parameters C that couple the ground state resonantly to excited states in diabatic heating processes. This will be done with a Floquet perturbative method and a rotating-wave approximation. Subsequently, we also compute the quasienergy spectrum of the shaken lattice numerically, in order to gain more insight into heating by continuous switching on of the shaking amplitude. A simulation of the shaking, either with continuous or smooth ramping of the amplitude, gives us then a precise description of the time-dynamics of the system and the parameters where to expect heating. Finally we will compare the numerical and analytical findings with experimental results.

5.3.1. Fourier Expansion of the Tight-Binding Hamiltonian

We start with a Floquet analysis of the single-particle Hamiltonian of the periodically shaken lattice in the tight-binding regime. As derived in Sec. 3.3, the one-dimensional bosonic lattice Hamiltonian in the co-moving reference frame takes the form

$$H_{\mathrm{sp}}(t) = -\frac{\hbar^2}{2m}\partial_x^2 + V(x) + xF_0\cos(\omega t). \qquad (5.3.1)$$
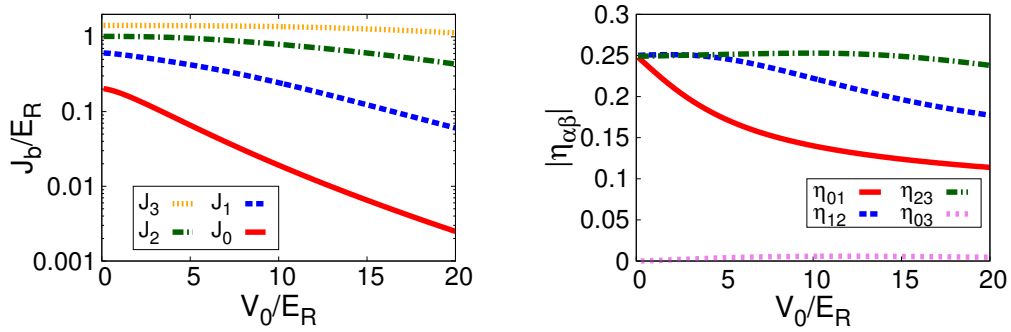
Figure 5.3.1.: Band structure of the cosine potential. Left: Tunneling coefficients of the four lowest lying energy band centers. Right: Coupling matrix elements between the first four excited states.

In contrast to Chap. 3, we consider the common case of a cosine potential $V(x) = V_0 \cos(2k_l x)$ with wave vector $k_l = \pi/a$ of the laser. As derived in Sec. 3.2, in the tight-binding approximation Hamiltonian (5.3.1) takes the form

$$
\hat{H}(t) = \sum_b \sum_{\ell=1}^{M} \Big[E_b |b\ell\rangle\langle b\ell| - (-1)^b J_b \left(|b(\ell+1)\rangle\langle b\ell| + \text{h.c.} \right) + K \cos(\omega t)\Big(\ell |b\ell\rangle\langle b\ell|
$$
$$
+ \sum_{b'} \eta_{b'b} |b'\ell\rangle\langle b\ell| \Big) \Big].
\tag{5.3.2}
$$

The tunneling coefficients J_b and the transition elements $\eta_{\alpha\beta}$ for the lowest four bands of the (non-dimerized) cosine lattice are depicted in Fig. 5.3.1. Whereas the coupling coefficients $\eta_{\alpha\beta}$ are of the same order of magnitude for adjacent bands $\alpha, \beta = \alpha \pm 1$, they are significantly lower for distant bands, e.g. $\eta_{03} \ll \eta_{01}, \eta_{12}, \eta_{23}$. The former fact leads to strong mixing of several bands at once, in regions where they are jointly brought in resonance. In the cosine potential this is likely to happen, as indicated by Fig. 5.3.2, where we plot the almost equidistant band center (i.e. orbital) energies as a function of the lattice depth.

Since we are interested in non-interacting particles and condensates with a specific quasimomentum, the precise resonance condition is determined by the dispersion relation. For a lattice depth of $V_0 = 10 E_R$, to which we will stick to in the following, we plot in Fig. 5.3.3 (left) the numerically calculated exact dispersion relation of the static lattice. Whereas the dispersion relation of the particles in the lowest
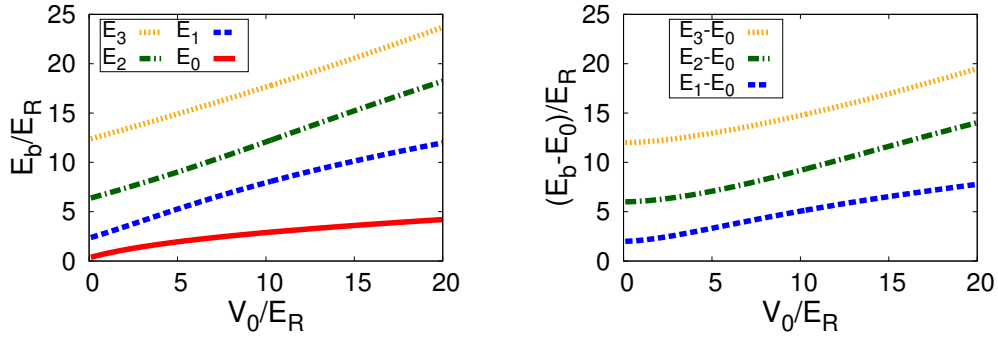
Figure 5.3.2.: Left: Band center energies of the four lowest lying Bloch bands in the cosine potential. Right: The same bands as quasienergy bands if the ground and the first excited band get resonantly coupled (with vanishing amplitude).

bands ($b = 0, 1$) are strongly affected by the lattice and band gaps are clearly visible, the particles in higher bands ($b \geq 2$) are almost free, hardly "feeling" the lattice. Also shown in the same plot are exemplified multiphoton transitions in the notation (b, m) referring to the excitation of band b in a process taking m photons. In Fig. 5.3.3 (right) we illustrate the energy difference of exited bands $b > 0$ with the ground band $b = 0$ as a function of the quasimomentum q. However, these energy differences only relate to the resonant shaking frequencies in the case of weak shaking amplitudes $\alpha = K/\hbar\omega \ll 1$. For larger shaking amplitudes the dispersion relation gets distorted, which also shifts the resonance conditions. We calculate the resulting effective tight-binding dispersion relation and the resonance condition later in this section.

Hamiltonian (5.3.2) is not translationally invariant in position space, which makes a solution very cumbersome. However, the discrete translational invariance can be achieved by making the gauge transformation

$$\hat{U}(t) = \exp\left(i \sum_{b\ell} \chi_\ell(t) |b\ell\rangle\langle b\ell| \right) \tag{5.3.3}$$

with phases

$$\chi_\ell(t) = -\frac{K\ell}{\hbar} \int_0^t \mathrm{d}t' \cos(\omega t') = -\frac{\ell K}{\hbar\omega} \sin(\omega t) \tag{5.3.4}$$
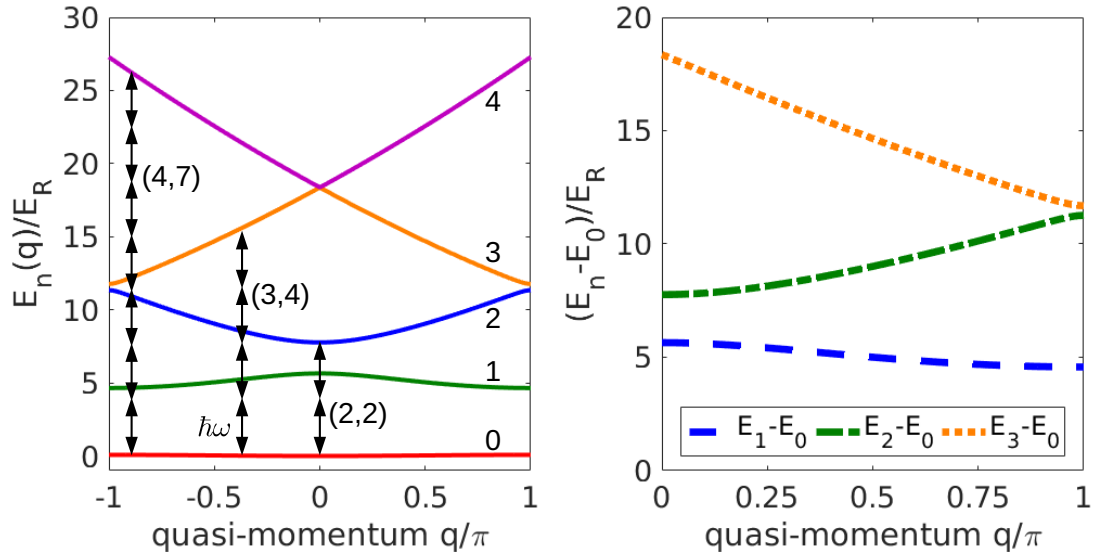
Figure 5.3.3.: Dispersion relation in the static cosine potential. Left: Five lowest lying energy bands. Also shown are exemplified multiphoton transitions in the notation (b, m) referring to band number b and photon index m. Right: The difference in energy between higher lying bands and the ground band, where an experiment typically takes place. These describe the resonance energies (i.e. frequencies) for single-particle heating in the regime with small shaking amplitude K.

Hence, we obtain the Hamiltonian

$$
\begin{aligned}
\hat{H}'(t) &= \hat{U}^\dagger \hat{H}(t)\hat{U} - i\hbar \hat{U}^\dagger \frac{d}{dt}\hat{U} \\
&= \sum_b \sum_{\ell=1}^{M} \Big[E_b |b\ell\rangle\langle b\ell| - (-1)^b J_b \left(e^{i\theta(t)} |b(\ell+1)\rangle\langle b\ell| + \text{h.c.} \right) \\
&\quad + K\cos(\omega t) \sum_{b'} \eta_{b'b} |b'\ell\rangle\langle b\ell| \Big].
\end{aligned}
\tag{5.3.5}
$$

with Peierls phases

$$
\theta(t) = \chi_\ell(t) - \chi_{\ell+1}(t) = \frac{K}{\hbar\omega}\sin(t),
\tag{5.3.6}
$$

which is now quasi-translationally invariant. We skip the apostrophe of the transformed Hamiltonian in the following. In quasimomentum represantion with states $|bq\rangle$ with M quasimomenta $q = -\pi/a, \pi/a(M-1)/M, \ldots, \pi/a$, the Hamiltonian reads

$$\hat{H}(t) = \sum_{b,q} \left[\epsilon_b \left(q - \frac{A(t)}{\hbar} \right) |bq\rangle\langle bq| + K\cos(\omega t) \sum_{b'} \eta_{b'b} |b'q\rangle\langle bq| \right]. \qquad (5.3.7)$$

Here, the vector potential reads

$$A(t) = \int_0^t dt' F_0 \cos(\omega t) = \frac{\hbar}{a}\theta(t) = \frac{\hbar}{a}\frac{K}{\hbar\omega}\sin(\omega t). \qquad (5.3.8)$$

In Eq. (5.3.7) appears the static (tight-binding) dispersion relation

$$\epsilon_b(p) = E_b - 2(-1)^b J_b \cos(ap), \qquad (5.3.9)$$

which is the roughest approximation to the exact dispersion relation plotted in Fig. 5.3.3. It is only accurate for deep lattices and low band indices where tunneling between next-nearest-neighbour lattice sites is suppressed.

Next we also expand the time-periodic Hamiltonian (5.3.7) in time by introducing plane wave states in time,

$$|bqm\rangle\rangle = \left\{ |bq\rangle e^{i\omega mt} \right\}, \qquad (5.3.10)$$

in the extended Hilbert space (see Chap. 2). Apart from the band and the quasimomentum index, the basis states have now the additional photon index m. For $K = 0$, i.e. the trivial undriven case, these basis states coincide with the actual Floquet states, which means that they then also diagonalize the quasienergy operator

$$\langle\langle b'q'm'|\hat{Q}|bqm\rangle\rangle = \langle b'q'| \left(\hat{H}_{m'-m} + \hbar\omega\delta_{m',m} \right) |bq\rangle. \qquad (5.3.11)$$

However, for finite amplitude K the plane wave states $|bqm\rangle\rangle$ do not diagonalize $\hat{Q}$. The Fourier components of the Hamiltonian appearing in (5.3.11) are found to be

$$
\begin{aligned}
\hat{H}_m &= \frac{1}{T} \int_0^T \mathrm{d}t e^{-im\omega t} \hat{H}(t) \\
&= \sum_{bq} |bq\rangle \epsilon_{bm}(q)\langle bq| + \frac{1}{2} K \delta_{|m|,1} \sum_{b'} \eta_{b,b'} |b'q\rangle\langle bq|,
\end{aligned} \tag{5.3.12}
$$

where we have written the Fourier components of the now time-dependent dispersion relation as

$$
\epsilon_{bm}(q,\alpha) = E_b \delta_{m,0} - (-1)^b J_b \mathcal{J}_m(\alpha) \left[e^{-ibq} + (-1)^m e^{ibq} \right]. \tag{5.3.13}
$$

Here and in the following we refer to the dimensionless driving strength by

$$
\alpha = \frac{K}{\hbar\omega}. \tag{5.3.14}
$$

The diagonal blocks in the quasienergy operator $\hat{Q}$ take the form

$$
\langle\langle b'q'm|\hat{Q}|bqm\rangle\rangle = \delta_{b'b}\delta_{q'q} \left[\epsilon_b^{\mathrm{eff}}(q) + m\hbar\omega \right]. \tag{5.3.15}
$$

Here appears the 0th Fourier component of the dispersion relation, that we will refer to as the effective dispersion relation

$$
\epsilon_b^{\mathrm{eff}}(q,\alpha) = \epsilon_{b0}(q) = E_b - 2(-1)^b J_b \mathcal{J}_0(\alpha) \cos(aq). \tag{5.3.16}
$$

The effective dispersion relation depends on the shaking strength α and determines quite accurately resonance conditions within the tight-binding model, up to perturbative shifts that stem from the coupling of the respective states with states of other Bloch bands. To increase the accuracy of the effective dispersion relation, especially for shallow lattices and excitation to higher bands, one has to take into account also next-nearest-neighbor-, next-next-nearest-neighbor-, etc. tunneling terms. Including next-nearest-neighbor tunneling with strength J_{bb}, the effective

dispersion relation takes the more accurate form

$$\epsilon_b^{\text{eff}}(q, \alpha) = E_b - 2(-1)^b J_b \mathcal{J}_0(\alpha)\cos(aq) - 2(-1)^b J_b \mathcal{J}_0\left(\frac{2\alpha}{\hbar\omega}\right)\cos(2aq). \quad (5.3.17)$$

The resonant frequencies for ν-photon transitions (b, ν) from the ground to the bth excited bands at quasimomentum q and for a driving strength of α are then given by

$$\omega_{(b,\nu)}(q, \alpha) = \frac{\epsilon_b^{\text{eff}}(q, \alpha) - \epsilon_0^{\text{eff}}(q, \alpha)}{\nu}. \quad (5.3.18)$$

For $\alpha = 0, 1, 2$, we list the resonance frequencies for the ν-photon transitions for $\nu = 1 \ldots 8$ in Tab. 5.3.1. Furthermore, in Fig. 5.3.4 we plot the lines of resonant frequencies according to Eq. (5.3.17) from the ground to the first (straight blue line) and the second (dotted green line) Bloch band for $\nu = 1 \ldots 8$ as a function of shaking frequency ω and strength α. In the same plot, we also draw thin horizontal lines (straight and dotted) for the values $E_b - E_0$ neglecting the band dispersion (compare to Fig. 5.3.2) so that the Bessel function $\mathcal{J}_0$ in the effective dispersion relation can clearly be seen. Note, however, that the plot is not giving any information of the strength and width of the resonances, which will be examined in the next two sections. Furthermore, due to double resonances described in Sec. 5.1, overlapping resonances might form avoided crossing, depending on the presence of a coupling element and its magnitude. If the ground state is coupled resonantly with two states at the same time, these states are necessarily coupled to each other, which does not, however, make any statement about the intensity of the coupling. The avoided crossings will be seen in the numerical simulation (see Sec. 5.3.5) and the experimental findings (see Sec. 5.3.6). Together with the direct band coupling $K\eta_{b'b}/2$, the effective dispersion relation reproduces the effective model that we have used in Chap. 3. In addition, we have now included the Fourier term in the off-diagonal blocks that take the form

$$\langle\!\langle b'q'm'|\hat{Q}|bqm\rangle\!\rangle = \delta_{q',q}\left[\delta_{b'b}\epsilon_{b(m'-m)}(q) + \frac{1}{2}K\delta_{|m'-m|,1}\eta_{b'b}\right]. \quad (5.3.19)$$

$$q = 0 \qquad\qquad q = \pi$$

$\alpha = 0$

ν \ b	1	2	3
1	5.632	7.856	17.659
2	2.816	3.928	8.830
3	1.877	2.619	5.886
4	1.408	1.964	4.415
5	1.126	1.571	3.532
6	0.939	1.309	2.943
7	0.805	1.122	2.523
8	0.704	0.982	2.207

ν \ b	1	2	3
1	4.581	10.955	12.103
2	2.290	5.478	6.052
3	1.527	3.652	4.034
4	1.145	2.739	3.026
5	0.916	2.191	2.421
6	0.763	1.826	2.017
7	0.654	1.565	1.729
8	0.573	1.369	1.513

$\alpha = 1$

ν \ b	1	2	3
1	5.468	8.051	16.907
2	2.734	4.025	8.454
3	1.823	2.684	5.636
4	1.367	2.013	4.227
5	1.094	1.610	3.381
6	0.911	1.342	2.818
7	0.781	1.150	2.415
8	0.683	1.006	2.113

ν \ b	1	2	3
1	4.664	10.422	12.656
2	2.332	5.211	6.328
3	1.555	3.474	4.219
4	1.166	2.605	3.164
5	0.933	2.084	2.531
6	0.777	1.737	2.109
7	0.666	1.489	1.808
8	0.583	1.303	1.582

$\alpha = 2$

ν \ n	1	2	3
1	5.151	8.754	15.324
2	2.576	4.377	7.662
3	1.717	2.918	5.108
4	1.288	2.188	3.831
5	1.030	1.751	3.065
6	0.859	1.459	2.554
7	0.736	1.251	2.189
8	0.644	1.094	1.916

ν \ n	1	2	3
1	4.916	9.448	14.080
2	2.458	4.724	7.040
3	1.639	3.149	4.693
4	1.229	2.362	3.520
5	0.983	1.890	2.816
6	0.819	1.575	2.347
7	0.702	1.350	2.011
8	0.614	1.181	1.760

Table 5.3.1.: Resonance frequencies in the shaken lattice of depth $V_0 = 10 E_R$ from the first to the b-th band via a ν-photon process, for different shaking strengths $\alpha = K/\hbar\omega$ and for the most important quasimomenta $q = 0$ and $q = \pi/a$.
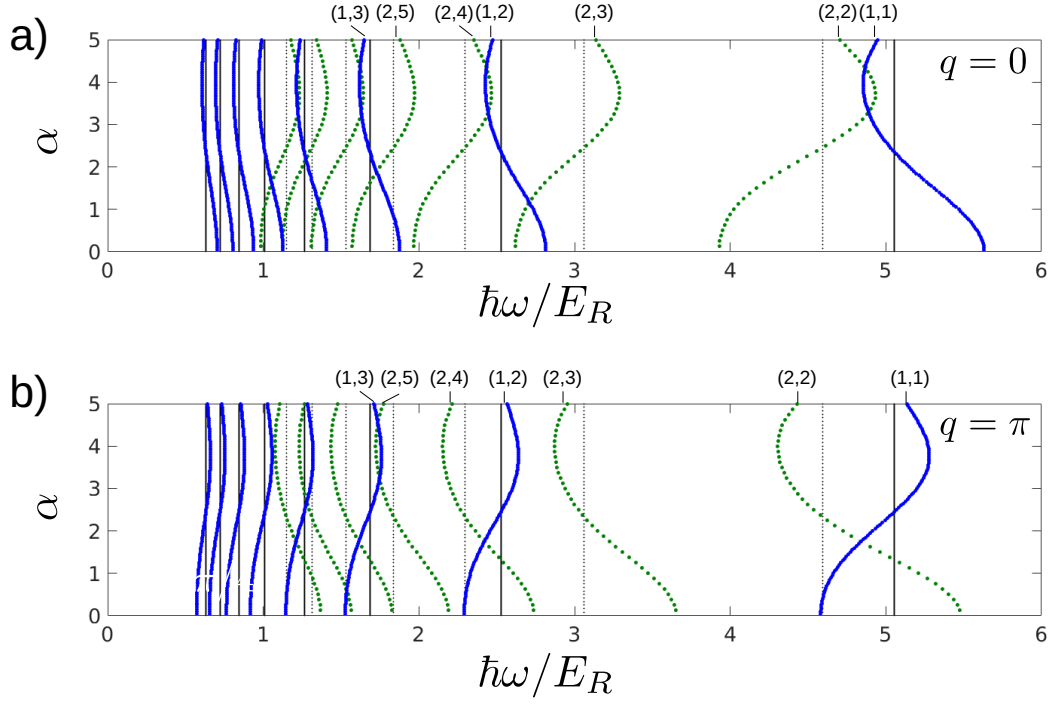
Figure 5.3.4.: Resonance frequencies in the shaken lattice of depth $V_0 = 10E_R$ from the ground to the first (straight blue line) and second (dotted green line) excited Bloch band via a ν-photon process ($\nu = 1 \ldots 8$), as a function of the shaking frequency ω and strength α and for the most important quasimomenta $q = 0$ and $q = \pi/a$. The resonances can be assigned according to Tab. 5.3.1 and are partly labeled with (b, ν). Note that the resonance $(2, 1)$ is out of range.

The first term, which is proportional to $\delta_{b'b}\epsilon_{b(m'-m)}(q)$, allows for multiphoton transitions that we ignored in Chap. 3. These multi-photon transitions only occur within the same Bloch band. However, combined with single-photon inter-band transitions they become relevant in higher-order processes. In Eq. (5.3.13), it is also important to note that for odd photon numbers $m = 1, 3, 5, \ldots$ these transitions scale like $e^{-ibq} + (-1)^m e^{ibq} \sim \sin(bq)$, which vanishes at the borders of the Brilloin zone $q = 0$ and $q = \pi/a$. On the other hand, for even photon numbers they scale like $e^{-ibq} + (-1)^m e^{ibq} \sim \cos(bq)$. This means that at $q = \pi/2a$ even and odd multi-photon transitions are equally strong.

In summary, we have Fourier transformed the shaken single-particle Hamiltonian, resulting in the quasienergy operator

$$\langle\!\langle b'q'm'|\hat{Q}|bqm\rangle\!\rangle = \delta_{q'q}\left[\delta_{b'b}\epsilon^{\text{eff}}_{b(m'-m)}(q) + \frac{1}{2}K\delta_{|m'-m|,1}\eta_{b'b} + \delta_{b'b}\delta_{m'm}m\hbar\omega\right]. \tag{5.3.20}$$

It gives us insight into the dynamics of the system in the extended Hilbert space.

5.3.2. Multi-Photon Heating from Floquet Perturbation Theory

In this section we use the quasienergy operator (5.3.20) to derive the effective coupling parameters to excited states.

In general, the resonance condition for a ν-photon transition between states $|bq\rangle$ and $|b'q\rangle$ to occur is

$$\epsilon^{\text{eff}}_{b'}(q,\alpha) - \epsilon^{\text{eff}}_{b}(q,\alpha) = \nu\hbar\omega + \delta, \tag{5.3.21}$$

with δ being a sufficiently small detuning, compared to the coupling strengths that we still have to calculate. We will set $\delta = 0$ in the following and refer to App. C for the case of a finite detuning δ. The resonance condition then corresponds to a degeneracy of the states $|bqm\rangle\!\rangle$ and $|bq(m-\nu)\rangle\!\rangle$ in the extended Hilbert space. However, there has to be a (hopping) process linking both states, i.e. a series of matrix elements in the extended Hilbert space that connects the two states with each other. Either this happens directly with strength $\frac{K\eta_{bb'}}{2}$, or there is a connection between the states across s energetically distant virtual states. In the

latter case, we can derive the effective coupling strength by degenerate perturbation theory. The unperturbed states are thus the Floquet states $|bqm\rangle\rangle$ of the undriven system, introduced in Eq. (5.3.10). Remember that their quasienergy for a finite driving strength is the effective dispersion relation Eq. (5.3.17) and not the static dispersion relation. The perturbation $\hat{V}_{\text{pert}}$ is given by the off-diagonal terms in the quasienergy operator (5.3.11)

$$
\begin{aligned}
\langle\langle bqm'|\hat{V}_{\text{pert}}|bqm\rangle\rangle &= \langle\langle bqm'|(\hat{Q}-\hat{Q}_0)|bqm\rangle\rangle \\
&= (1-\delta_{m'm})\delta_{q'q}\langle b'q|\hat{H}_{m'-m}(q)|bq\rangle.
\end{aligned}
\tag{5.3.22}
$$

Here, $\hat{Q}_0$ is the unperturbed quasienergy operator

$$
\langle\langle bqm'|\hat{Q}_0|bqm\rangle\rangle = \delta_{m'm}\delta_{q'q}\delta_{b'b}\left[m\hbar\omega + \epsilon_b^{\text{eff}}(q,\alpha)\right].
\tag{5.3.23}
$$

Following the standard expression for degenerate perturbation theory, the effective coupling element for the ν-photon transition between two degenerate states $|A\rangle\rangle = |bqm\rangle\rangle$ and $|B\rangle\rangle = |b'q(m-\nu)\rangle\rangle$ is

$$
C_{A\to B} \sim \sum_{j=1}^{\#\{\text{paths}:A\to B\}} \mathcal{C}_0 \prod_{k=1}^{s_j} \frac{\mathcal{C}_k}{\epsilon_{b_k m_k}^{\text{eff}}(q) - \epsilon_{b_0 m_0}^{\text{eff}}(q)\hbar\omega}.
\tag{5.3.24}
$$

Here, $\mathcal{C}_k$ denotes the coupling element between Floquet states with indices k and $k+1$, which is either $K\eta_{b_{k+1}b_k}/2$ or $\epsilon_{b_k, m_{k+1}-m_k}(q)$. Also we introduced the quasienergy

$$
\epsilon_{bm}^{\text{eff}}(q) = \epsilon_b^{\text{eff}}(q,\alpha) + m\hbar\omega
\tag{5.3.25}
$$

without the perturbation, but including the reparameterization by the Bessel functions. We set $m_0 = 0$ in the following.

Even though there are many paths $A \to B$ possible, only few or just one of them is significantly contributing. If the shaking fulfills $K \leq \hbar\omega$, we can approximate the Bessel functions to be $\mathcal{J}_m(\alpha) \sim \alpha^{|m|} \ll 1$. Furthermore, since the tunneling term in

Figure 5.3.5.: Illustration of the single-photon transition towards the first excited band in the extended Hilbert space. The levels represent the quasienergies of the Floquet states $|bkm\rangle\rangle$, where k denotes the quasimomentum.

the tight-binding regime is very small, $J_b \ll \eta_{b(b+1)}$, we can generally assume that

$$\epsilon_{b_k \pm 1}(q, \alpha) \ll \frac{K \eta_{b_{k+1} b_k}}{2} \tag{5.3.26}$$

in the parameter regimes that we are interested in. However, it could be that

$$\epsilon_{b_k \pm m}(q, \alpha) \approx \left(\frac{K \eta_{b_{k+1} b_k}}{2} \right)^m \tag{5.3.27}$$

so that for large ν an intra-band m-photon process contributes more significantly than a series of interband processes.

In the following we exemplify the pertubative estimate of the coupling elements by calculating the effective ν-photon coupling strengths $C_{(1,\nu)}$ between the ground state ($b = 0$) and the first excited band ($b' = 1$). The single-photon transition is obviously dominated by the direct coupling with matrix element

$$C_{(1,1)} = \frac{K \eta_{01}}{2}. \tag{5.3.28}$$

We illustrate the transition between two Floquet states with degenerate quasienergy in the extended Hilbert space in Fig. 5.3.5.

For the $\nu = 2$ photon process, there are two paths that are obviously the most significant ones, namely $|0q0\rangle\rangle \to |0q-1\rangle\rangle \to |1q-2\rangle\rangle$ and $|0q0\rangle\rangle \to |1q-1\rangle\rangle \to |1q-2\rangle\rangle$,
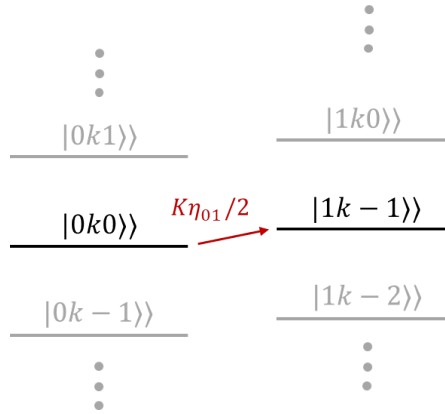
Figure 5.3.6.: Illustration of the two-photon transition towards the first excited band in the extended Hilbert space. The two shortest paths with respective coupling elements are included.

as illustrated in Fig. 5.3.6. From Eq. (5.3.24) we then find

$$
\begin{aligned}
C_{(1,2)} &= \frac{K\eta_{01}}{2\hbar\omega}\left(\epsilon_{0,-1}(q,\alpha) - \epsilon_{1,-1}(q,\alpha)\right) \\
&\sim J_1 \sin(aq)\alpha^2,
\end{aligned}
\tag{5.3.29}
$$

where the asymptotics follow from $J_1 \gg J_0$ so that the contribution of the second path is larger. Note that δ does not appear in the denominator since we have set it to zero.

For the three-photon process, the situation is more complicated. On the one hand, there are the two paths $|0q0\rangle\!\rangle \to |1q-1\rangle\!\rangle \to |0q-2\rangle\!\rangle \to |1q-3\rangle\!\rangle$ and $|0q0\rangle\!\rangle \to |1q-1\rangle\!\rangle \to |2q-2\rangle\!\rangle \to |1q-3\rangle\!\rangle$. On the other hand there are also the two paths $|0q0\rangle\!\rangle \to |0q-2\rangle\!\rangle \to |1q-3\rangle\!\rangle$ and $|0q0\rangle\!\rangle \to |1q-1\rangle\!\rangle \to |1q-3\rangle\!\rangle$ giving in total

$$
C_{(1,3)} = -\frac{(K\eta_{01}/2)^3}{(2\hbar\omega)^2} + \frac{K\eta_{01}/2(K\eta_{12}/2)^2}{2\hbar\omega(\epsilon_2^{\mathrm{eff}}(q,\alpha) - \epsilon_1^{\mathrm{eff}}(q,\alpha) - \hbar\omega)} - \frac{\epsilon_{0,-2}(q,\alpha)}{2\hbar\omega} + \frac{\epsilon_{1,-2}(q,\alpha)}{2\hbar\omega}.
\tag{5.3.30}
$$

All four paths are illustrated in Fig. 5.3.7, each in a different color. It depends on the tight-binding and the shaking parameters which of the paths contribute most
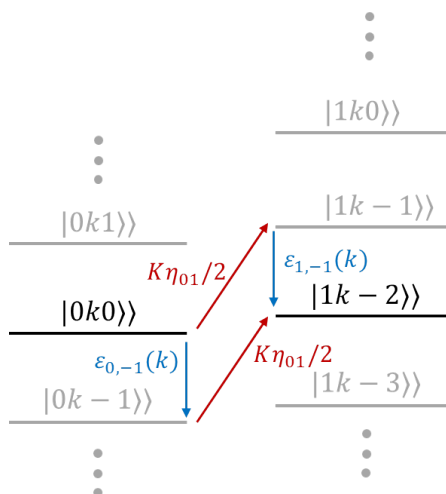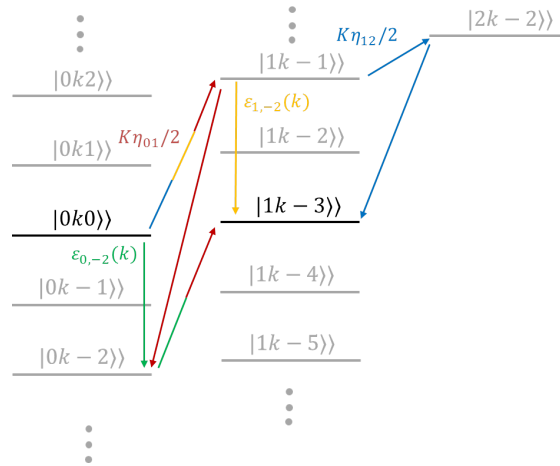
Figure 5.3.7.: Illustration of the three-photon transition towards the first excited band in the extended Hilbert space. The two shortest paths with respective coupling elements are included.

significantly.

Finally, let us also consider the resonant coupling to higher Bloch bands. As mentioned before, the coupling elements $\nu_{b,b'}$ for $b - b' > 1$ are very small, but have to be compared to higher-order processes. To give an example, the 2-photon process to the second excited band with state $|2q - 2\rangle\rangle$ has only the intermediate state $|1q - 1\rangle\rangle$, as illustrated in Fig. 5.3.8. The coupling element takes the form

$$C_{(2,2)} = \frac{K^2 \eta_{01} \eta_{12}}{4(\epsilon_1^{\text{eff}}(q,\alpha) - \epsilon_0^{\text{eff}}(q,\alpha) - \hbar\omega)}. \tag{5.3.31}$$

However, this expressions makes only sense if the denominator is sufficiently large. In other words, if the intermediate (Bloch) states (e.g. $|1q-1\rangle\rangle$ in the example above) are also degenerate with the ground state ($\gamma = 0$), the degenerate perturbation theory breaks down. In this case one can for example treat the problem by considering the corresponding 3-by-3 matrix, see for example App. C. A very important observation that we can generalize from these examples, is that every path for a ν-photon process with even ν to a band with odd b, will include at least one $\epsilon_{b_k \pm m}$ with an odd m. Since this term always comes with a factor of $\sin(aq)$, there cannot be even-photon resonances for $q = 0$ and $q = \pi/a$, being quasimomenta where the condensates is often initialized. Similarly, if ν is odd and b is even,
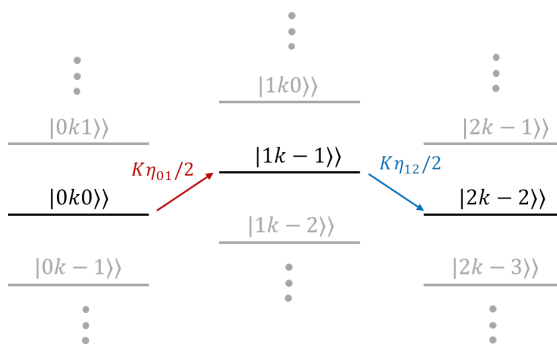
Figure 5.3.8.: Illustration of the two-photon transition towards the second excited band in the extended Hilbert space. Here, only the direct coupling elements are included since they give by far the largest conribution.

the coupling is proportional to a factor of $\sin(aq)$, such that e.g. multi-photon transitions to the second excited band are suppressed at $q = 0$ if the photon number is odd.

Summing up, via Floquet perturbation theory we have gained information about the strength of the heating and thus about the time-dynamics between the ground state and excited Bloch states.

5.3.3. Multi-Photon Heating from a Rotating-Wave Approximation

Another way of calculating effective coupling elements between two resonantly coupled states, is to perform a rotating-wave approximation, which results in a time-independent effective Hamiltonian. This procedure extends the rotating-wave approximation we have made in chapter Sec. 3.3. To this end, we will perform a gauge transformation to remove all time dependencies in the dispersion relation and then take the 0th order Fourier components of the off-diagonal terms as the effective coupling elements.

We first take the quasi-translationally invariant and time dependend Hamiltonian operator (5.3.11) and yet perform another gauge transformation

$$\hat{U}(t) = \exp\left\{ i \sum_{b,q} \chi_{b,q}(t)|bq\rangle\langle bq| \right\} \tag{5.3.32}$$

with time dependent phases

$$\chi_{b,q}(t) = \sum_{m \neq 0} \chi_{b,q}^{(m)} e^{im\omega t} \tag{5.3.33}$$

and Fourier components

$$i\chi_{b,q}^{(m)} = \frac{\epsilon_{1m}(q)}{m\hbar\omega} = (-1)^m \mathcal{J}_b(\alpha) \frac{J_b}{\hbar\omega} \begin{cases} \cos(aq), & \text{for even } m \\ -i\sin(aq), & \text{for odd } m \end{cases} \tag{5.3.34}$$

that we have already calculated in the previous section. The gauge transformation (5.3.32) removes the full time dependencies of the dispersion relation $\epsilon_b(q - A(t)/\hbar)$ (see Eq. (5.3.7)) for all Bloch states.

Applying the gauge transformation (5.3.32), the time-dependent Hamiltonian (5.3.7) is transformed to

$$\hat{H}(t) = \sum_{b,q} \epsilon_b^{\text{eff}}(q)|bq\rangle\langle bq| + \sum_{b,b'q} K\eta_{b,b'} \cos(\omega t) e^{-i[\chi_{b',q}(t) - \chi_{b,q}(t)]}|b'q\rangle\langle bq|. \tag{5.3.35}$$

Calculating the Fourier components in this new basis is not trivial. The coefficients can be found by expanding the cosine, the exponential and the time dependent arguement in (5.3.32) at once and compare the coefficients with the general Fourier expansion (with index μ) of the very same expression:

$$\begin{aligned}
\cos(\omega t) \exp\left(i\chi_{bq}(t)\right) &= \left(e^{i\omega t} + e^{-i\omega t}\right) \sum_{k=0}^{\infty} \frac{1}{k!}\left(i \sum_{m \neq 0} \chi_{bq}^{(m)} e^{im\omega t}\right)^k \\
&= \sum_{\mu=-\infty}^{\infty} A_{bq}^{(\mu)} e^{i\mu\omega t}. \tag{5.3.36}
\end{aligned}$$

In principle, each $A_{bq}^{(\mu)}$ has an infinite number of contributions. However, since $\chi_{bq}^{(m)} \sim J_b/\hbar\omega \ll 1$, we can ignore all terms that have more than a single factor of $\chi_{bq}^{(m)}$. The 0th Fourier component is thus

$$\begin{aligned}
A_{bq}^{(0)} &= \frac{i}{2}\left[\chi_{bq}^{(1)} + \chi_{bq}^{(-1)} - \chi_{b'q}^{(1)} - \chi_{b'q}^{(-1)}\right] \\
&= i\left[\chi_{bq}^{(1)} - \chi_{b'q}^{(1)}\right]. \tag{5.3.37}
\end{aligned}$$

The first Fourier component is an exception since it receives a constant in the expansion of the exponential. Hence, it is simply

$$A_{b'b,q}^{(\pm 1)} = \frac{1}{2}. \tag{5.3.38}$$

The higher Fourier components read

$$A_{b'b,q}^{(\pm|m|)} = \frac{i}{2}\left[\chi_{bq}^{(\pm(|m|-1))} - \chi_{b'q}^{(\pm(|m|-1))}\right]. \tag{5.3.39}$$

With these Fourier components, the direct coupling terms of two bands b and b' that are resonantly coupled at quasimomentum q by a ν-photon process, can be calculated. To this end, both states $|bqm\rangle\rangle$ and $|bq(m-\nu)\rangle\rangle$ that are degenerate in quasienergy have to be rotated into the same block in the extended Hilbert space. This can be done by replacing the unitary transformation (5.3.32) by the transformation

$$\hat{U}_{bb'q\nu}(t) = \exp\left\{i\nu\omega t|bq\rangle\langle bq| + i\sum_{b',q'}\chi_{b',q'}(t)|b'q'\rangle\langle b'q'|\right\}. \tag{5.3.40}$$

The time average, which is the 0th Fourier of the Hamiltonian, results in an effective Hamiltonian

$$\hat{H}_{\text{sp}}^{\text{eff}} = \sum_{b,q}\epsilon_b^{\text{eff}}(q)|bq\rangle\langle bq| + C_{b,b'}^{\nu}(q)|b'q\rangle\langle bq| \tag{5.3.41}$$

with effective coupling elements $C_{b,b'}^{\nu}(q)$. Here we neglect all other, presumably off-resonant coupling elements. Comparing with the unitary transformation (5.3.32), the Fourier components of the transformed Hamiltonian are simply shifted by ν, which gives the effective coupling

$$C_{b,b'}^{\nu}(q) = K\eta_{b,b'}A_{bq}^{(\nu)} \tag{5.3.42}$$
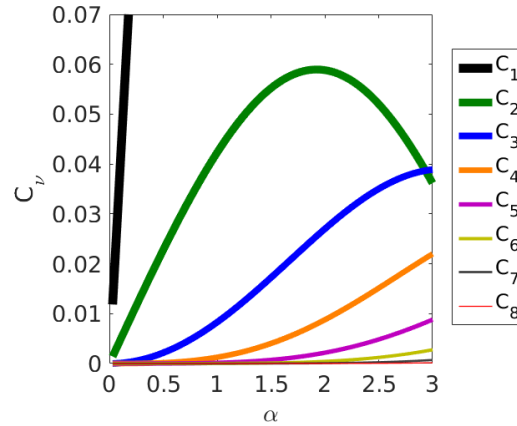
Figure 5.3.9.: Effective coupling elements from the rotating-wave approxima-
tion (5.3.44) to the first excited band at $q = 0$ and $V_0 = 10E_R$, $C_\nu = C^1_{0,1}(\pi/2)/K$.

Consequently, the effective 1-photon coupling element between two bands,

$$C^1_{b,b'}(q) = \frac{K\eta_{b,b'}}{2},\tag{5.3.43}$$

reproduces the result from Sec. 3.3 (see Eq. (5.3.28)). For higher photon numbers
ν we get

$$
\begin{aligned}
C^\nu_{b,b'}(q) &= K\eta_{b,b'}\frac{i}{2}\Big[\chi^{(\pm(|\nu|-1))}_{bq} - \chi^{(\pm(|\nu|-1))}_{b'q}\Big]\\
&= K\eta_{b,b'}\frac{J_{b'} - J_b}{(|\nu|-1)\hbar\omega}\mathcal{J}_{(|\nu|-1)}(\alpha)\begin{cases} \cos(aq), & \text{for odd } \nu\\ -i\sin(aq), & \text{for even } \nu\end{cases}
\end{aligned}\tag{5.3.44}
$$

Note that the formula only provides effective coupling elements for transitions that
are already allowed in the single-photon transition, i.e. whenever $\eta_{bb'} \neq 0$. Effective
coupling elements between states with even $b - b'$ have to be computed with e.g. the
perturbative method from the previous section. Also, we see again in Eq. (5.3.44)
that even-photon processes are suppressed by a factor of $\sin(aq)$. In Fig. 5.3.9 we
plot the effective coupling elements

$$C_\nu = \frac{C^1_{0,1}(\pi/2)}{K}\tag{5.3.45}$$

to the first excited band normalized to K for the first for photon numbers $\nu = 1\ldots8$.

5.3.4. Quasienergy Spectrum of the Shaken Lattice

In this section we numerically calculate and illustrate the exact quasienergy spectrum of the shaken lattice. The quasienergy spectrum is another way to estimate the single-particle transitions between bands leading to heating processes: At each avoided crossing, i.e. whenever two or more bands mix with each other, there will be transitions between Bloch bands in the dynamics of the shaken lattice.

We begin with rewriting the time-dependent Hamiltonian in a way that can be implemented easily on a computer, without applying any approximations. The shaken single-particle Hamiltonian (5.3.1) breaks translational symmetry because of the driving term. However, by applying the gauge transformation

$$U = \exp\left\{-ixA(t)\right\}, \tag{5.3.46}$$

with the already introduced vector potential $A(t) = \int_0^t dt' F_0 \cos(\omega t)$, we derive at the discrete translationally invariant form of the Hamiltonian

$$H_{\text{sp}}(t) = \frac{[\hat{p} - A(t)]^2}{2m} + V(x). \tag{5.3.47}$$

Here, we wrote the momentum operator explicitly as $\hat{p} = i\hbar\partial_x$. Like in the static case, Hamiltonian (5.3.47) can be solved for each quasimomentum q independently. Introducing plane waves

$$\langle x|p\rangle = \frac{1}{\sqrt{Ma}}e^{ipx}, \tag{5.3.48}$$

where the momentum is restricted to the values

$$p = q + P\frac{2\pi}{a}, \quad \text{with} \quad -\frac{\pi}{a} < q \le \frac{\pi}{a}, \quad \text{and} \quad P \in \mathbb{Z}, \tag{5.3.49}$$

the Hamiltonian can now be written as a matrix

$$
\begin{aligned}
H_{P,Q}(q,t) &= \frac{\hbar^2}{2m}\left[P\frac{\pi}{a} + q - \frac{A(t)}{\hbar}\right]^2 \delta_{P,Q} + \frac{V_0}{4}\delta_{P,Q+1} + \frac{V_0}{4}\delta_{P,Q-1} \\
&= E_R\left\{\left[2P + \frac{qa}{\pi} + \alpha\sin(\omega t)\right]^2 \delta_{P,Q} + \frac{V_0}{4E_R}\delta_{P,Q+1} + \frac{V_0}{4E_R}\delta_{P,Q-1}\right\}
\end{aligned}
\tag{5.3.50}
$$

with $P, Q \in \mathbb{Z}$. Choosing a momentum cutoff P^* with $|P| \leq P^*$, we can compute the quasienergy spectrum and also the time-evolution of the system. The latter will be done in the next section.

As we have seen in Chap. 2, there are two methods to compute the quasienergy spectrum, either by computing and diagonalizing the monodromy operator $\mathcal{M}_T$ or by diagonalizing the quasienergy operator Q in the extended Hilbert space. The quasienergy operator gives us a good insight into the physical processes and energy transfer in the system and can be treated with perturbation theory. On the other hand, calculating the eigenstates of the monodromy operator has the advantage that they can be uniquely projected onto the eigenstates of the non-driven system, without the degeneracy stemming from the photon index m. Since we are only interested in the numerical result, we use the monodromy operator to compute the Floquet states and their quasienergies.

As before, we calculate the quasienergy spectrum on a lattice of depth $V_0 = 10 E_R$ and focus on the transitions from the ground to the first excited band. We start by looking at the quasienergies as a function of the quasimomentum q. In Fig. 5.3.10 we plot the quasienergy spectrum of the shaken lattice with shaking frequency $\hbar\omega = 5 E_R$ and for increasing driving strength $\alpha = K/\hbar\omega = 0, 0.1, 0.5, 1, 3, 5$. The chosen frequency is within the 1-photon resonance to the first excited band between $\omega_{(1,1)}(q = 0, \alpha = 0) = 5.632 E_R$ and $\omega_{(1,1)}(q = \pi, \alpha = 0) = 4.581 E_R$ according to the effective dispersion relation Eq.(5.3.17) (see also Tab. 5.3.1 and Fig. 5.3.4). We illustrate the overlap of the Floquet bands to the static ground and first excited band by representing the quantity $n_0 - n_1$ of each state by color (red if $n_0 = 1$, blue if $n_1 = 1$ and green if $n_0 = n_1$ or $n_0 = n_1 = 0$). We observe that already for a very small shaking strength the avoided crossing emerges between the lowest two bands that are coupled directly with strength $\alpha\hbar\omega\eta_{01}/2$. The width of the splitting is twice the coupling strength $\alpha\hbar\omega\eta_{01} \approx 0.7\alpha E_R$, which is around $0.07 E_R$ for $\alpha = 0.1$. Note that the quasienergies in the plot are in units of $\hbar\omega = 5 E_R$. Increasing the driving strength increases the hybridization between the ground and the excited Bloch states, which can be seen by the gaps opening at the crossings and by the distribution of red. Additionally, one can see the opening of the gap between the first and second excited band in the lower part of the plot for $\alpha = 0.5$ and between the second and third excited band in the upper part. Other band crossings open
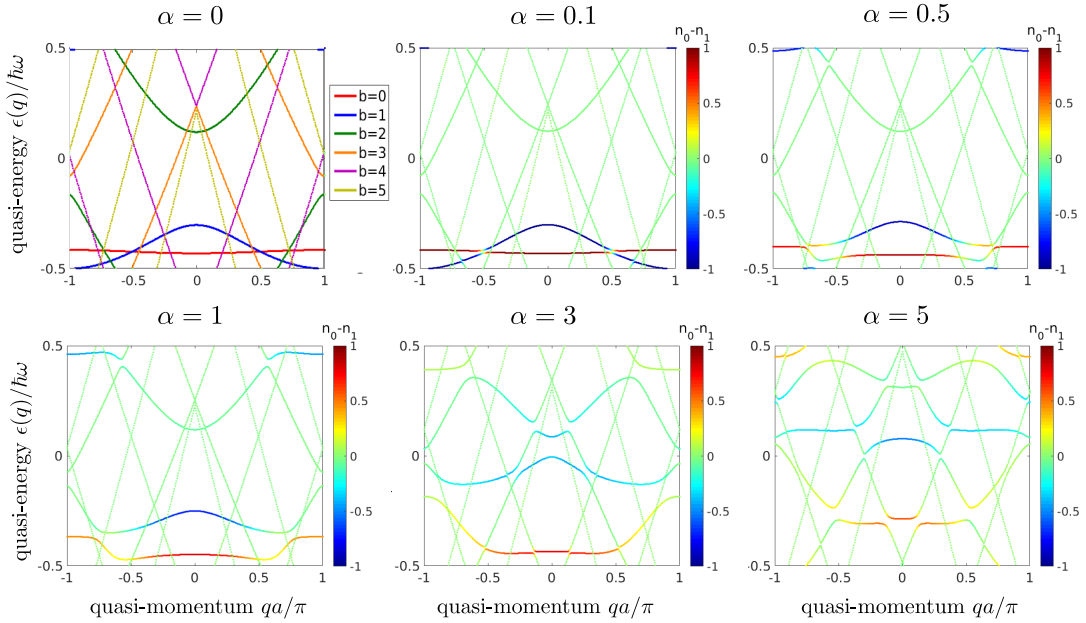
Figure 5.3.10.: Quasienergy spectrum of the shaken lattice with shaking frequency $\hbar\omega = 5E_R$ close to the 1-photon resonance at $V_0 = 10E_R$ and varying dimensionless driving strength $\alpha = K/\hbar\omega$. The calculation was done in the subspace of the six lowest bands of the non-driven system, therfore at each quasimomentum six states are shown. The color code illustrates the projection of each state on the ground minus the first excited (red to blue) state of the non-driven system. For $\alpha = 0$, where the Floquet states and the Bloch states of the static lattice coincide, we have colored each state in the color code used in all parameter plots.

significantly only for large driving strengths. Furthermore, for very high strenghts $\alpha \gg 1$ the static ground (red) and first (blue) excited bands spread over almost the entire quasienergy spectrum. Hence, for these strengths the heating of the system is expected to be very strong. Additionally, the Floquet states that correspond to Bloch states with large indices $b = 4$ and $b = 5$ apparently do not couple at all to each other and other states. The reason is that their kinetic energy is so large that they almost do not "feel" the lattice and thus also not the lattice shaking.

In Fig. 5.3.11 we plot the same quasienergy spectra, but this time with a shaking frequency of $\hbar\omega = 2.5E_R$, i.e. in the vicinity of the 2-photon resonance, which lies at $\alpha = 0$ roughly in the middle between $\omega_{(1,1)}(q = 0, \alpha = 0) = 2.816E_R$ and $\omega_{(1,1)}(q = \pi, \alpha = 0) = 2.290E_R$. Here, the splitting between the ground and the
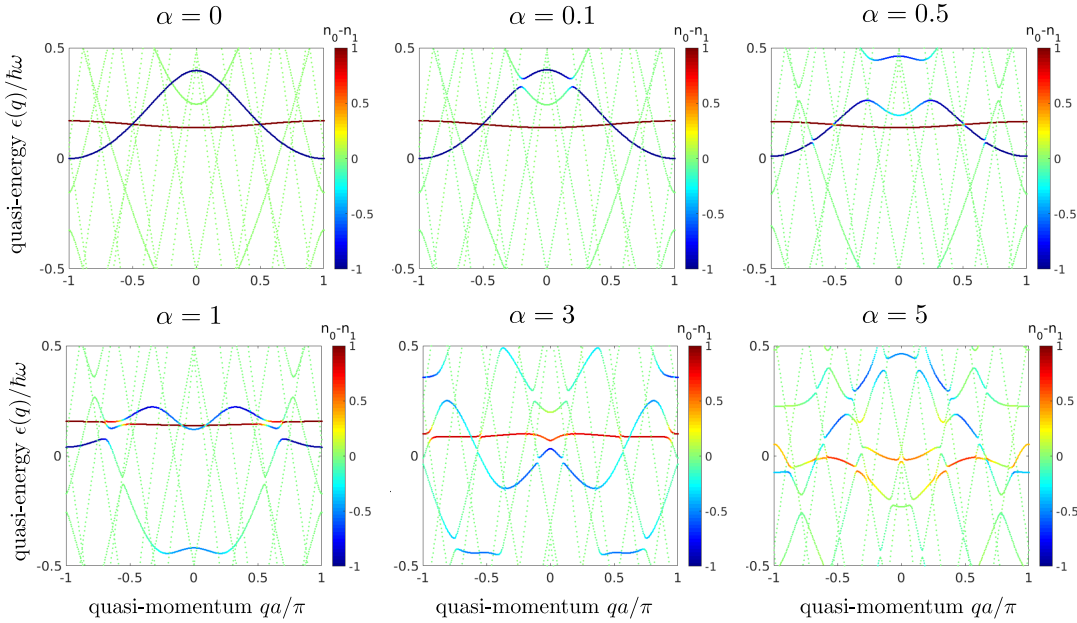
Figure 5.3.11.: Quasienergy spectrum as in Fig. 5.3.10 but with $\hbar\omega = 2.5 E_R$ close to the 2-photon resonance.

first excited band is very weak and happens only for large α. The reason for this is, as we have seen in Sec. 5.3.2, that the 2-photon coupling element is suppressed by a factor of $J_1 \sin(aq)$. This makes the gap at the avoided crossing much smaller. On the other hand, the splitting between the first and the second excited band at the band crossing is very pronounced since here the single-photon resonance is hit which is between $\epsilon_2^{\text{eff}}(q = 0, \alpha = 0) - \epsilon_1^{\text{eff}}(q = 0, \alpha = 0) = 2.224 E_R$ and $\epsilon_2^{\text{eff}}(q = \pi, \alpha = 0) - \epsilon_1^{\text{eff}}(q = \pi, \alpha = 0) = 6.3740 E_R$. These values are not shown in Tab. 5.3.1 but can be deduced from computing e.g. $\omega_{(2,1)} - \omega_{(1,1)}$.

To get a better overview on the quasienergy spectrum and to examine heating processes from the continuous ramping, we furthermore consider the quasienergies as a function of the shaking amplitude α for fixed q. We choose again $\hbar\omega = 5 E_R$ and pick quasimomentum $q = 0$ where a condensate is formed in the undriven system and $q = \pi/2a$ where the Bloch states $|0\rangle$ and $|1\rangle$ (skipping the quasimomentum q in the notation) are in resonance at $\alpha \approx 0$. In Fig. 5.3.12 we show for both quasimomenta the quasienergies as a function of α. From left to right we present the same results, but with the density of the Bloch states with index $b = 0, 1, 2$ respectively indicated
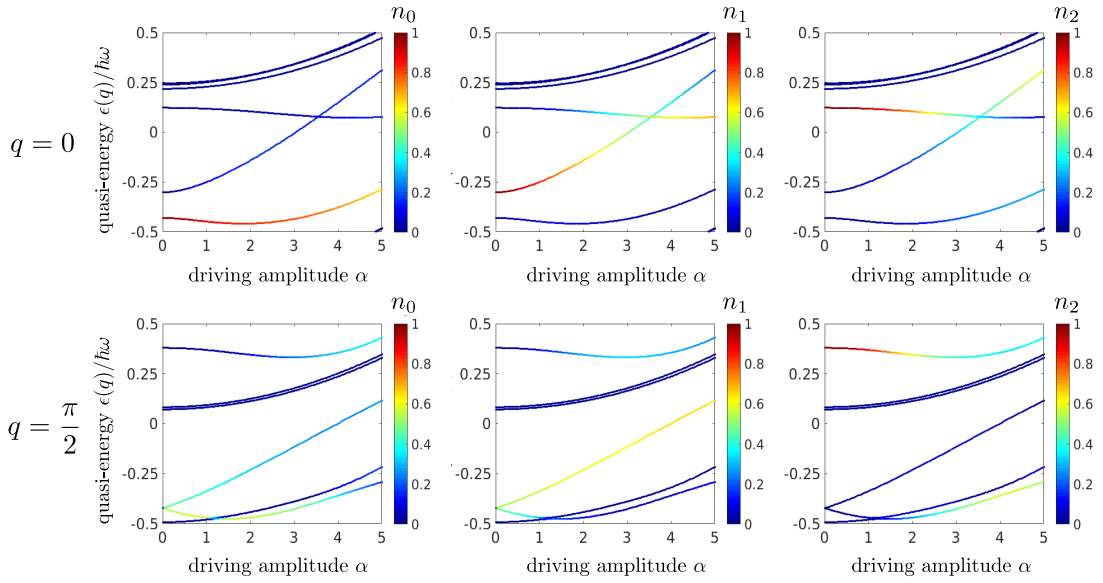
Figure 5.3.12.: Quasienergy spectrum as a function of the driving strength α for $\hbar\omega = 5E_R$, where the six lowest (in quasienergy) Bloch states were propagated in time. From left to right the projection to Bloch states $b = 0, 1, 2$ is colored in red. Upper panel: at quasimomentum $q = 0$. Lower panel: at quasimomentum $q = \frac{\pi}{2}$.

by the color in red. Remember that the course of the quasienergies is an interplay between effective dispersion relation parameterized by Bessel functions and the coupling between the Floquet states. For $\hbar\omega = 5E_R$ the coupling α, which is normalized by $\hbar\omega$, is thus very strong. Thus, the coupling distorts the eigenenergies strongly and the Bessel functions are almost not tractable. Furthermore, as we have seen in Fig. 5.3.4 (upper row), there is a double-resonance at $\alpha \approx 3.5$, which makes it hard to predict the quasienergies at this point. From this plot we can understand the difference between the two excitation mechanisms: If we quench the system to $\alpha = 5$, the ground state density n_0 will distribute over two additional Floquet states. Both states have also fractions n_1 and n_2 of the first and the second excited Bloch states. After dephasing, the system would thus oscillate between all three Bloch states $|0\rangle$, $|1\rangle$ and $|2\rangle$. On the other hand, if we follow adiabatically the Floquet state connected to $|0\rangle$ at $\alpha = 0$, at $\alpha = 5$ it has contribution of n_2, but not of n_1, even though this was the case in the intermediate regime. Therefore, Bloch
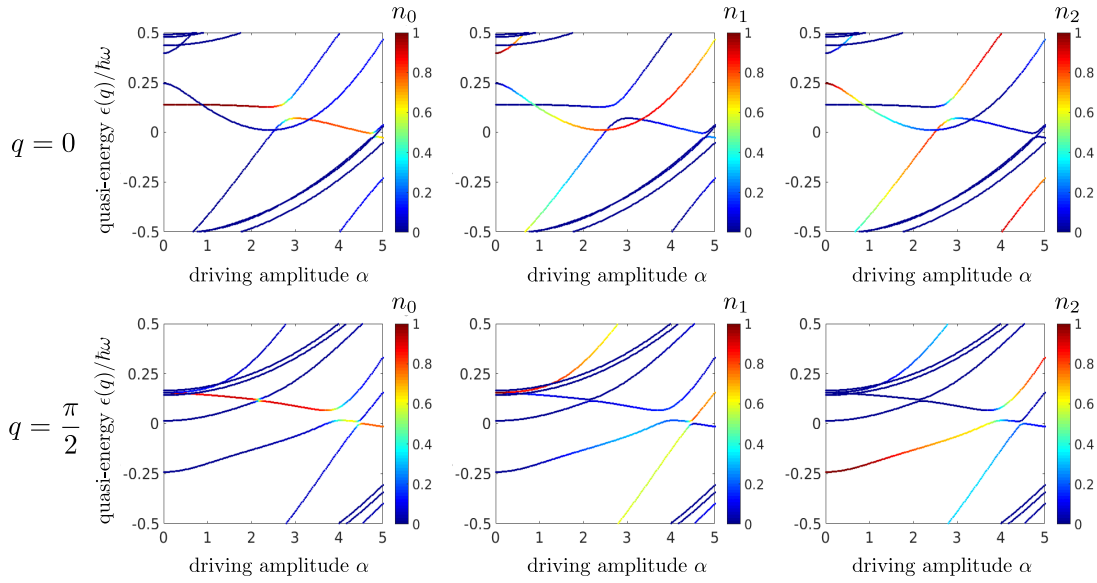
Figure 5.3.13.: Same plot as in Fig 5.3.12 but for $\hbar\omega = 2,5E_R$.

state $|1\rangle$ will be unoccupied at $\alpha = 5$. For $q = \pi/2a$ we see that the two Floquet states adiabatically connected to Bloch states $|0\rangle$ and $|1\rangle$ already mix for very small α.

In Fig. 5.3.13 we plot again the quasienergy spectrum but this time for $\hbar\omega = 2.5E_R$, close to the 2-photon resonance between ground and first excited state. Here, the effective dispersion relation is more visible since the effective couplings between the Floquet states is weaker. Because of the term $J_b\mathcal{J}_0(\alpha)\cos(aq)$ in the dispersion relation, the Bessel function renormalization is visible most strongly for $q = 0$ and $q = \pi/a$ and least strongly for $q = \pi/2a$, where $\cos(aq) = 0$ and the next nearest neighbour term $\sim J_{bb}\mathcal{J}_0\cos(2aq)$ becomes dominant. Therefore, for $q = 0$ the quasienergies vary strongly for small α, whereas for $q = \pi/2a$ they start almost constantly. For $q = 0$, we really do not see a coupling between n_0- and n_1-dominated Floquet states for small α. In contrast, the n_1- and n_2-dominated Floquet states mix strongly.

5.3.5. Numerical Simulation of Multi-Photon Heating Processes

In this section, we analyze single-particle heating in the shaken lattice by simulating the dynamics. The numerical simulation can easily be implemented based on Eq. (5.3.50). The ground state $|0q\rangle$ of the static lattice with corresponding plain wave vector $u_{0Q}(q)$ serves as the initial state for the numerical simulation. Integrating the time-dependent Schrödinger equation

$$i\hbar\dot{u}_Q(t) = \sum_Q H_{P,Q}(q,t)u_Q(t) \tag{5.3.51}$$

over a time span of τ, gives the current state of the system $|\psi(t)\rangle$ with vector $u_Q(q,t)$. The excited states $|bq\rangle$ can be projected to the current system state $|\psi(t)\rangle$ to compute the band occupation

$$n_b(t) = |\langle bq|\psi(t)\rangle|^2 = \left|\sum_Q u_Q^*(t)u_{bQ}(q)\right|^2 \tag{5.3.52}$$

during or at the end of the simulation. As discussed before, we quantify heating by $h_\tau = \min_t[n_0(t)]$, the minimum in the occupation of the ground band during the simulation time, see Eq. (5.2.1).

First we discuss the case where the shaking is turned on immediately at time $t = 0$ and held for a time τ with constant driving strength α, representing a quantum quench. Note that there are two possibilities for h_τ to have a finite value: either the coupling of the ground state to higher states is not resonant or it is resonant but so weak that the oscillation has not reached its minimum within the time τ. In Fig. 5.3.14 a) we plot the heating parameter h_τ as a function of the driving strength α and frequency $\hbar\omega$ for $q = 0$ and shaking time $\tau = 100/E_R$. The white regions correspond to parameters for which the single-particle heating is very strong, i.e. where system is oscillating between the ground state and one or more excited states. We see a number of resonance lines that broaden for increasing $\alpha \sim K$ and also for increasing ω since $K \sim \alpha\omega$. Some of the resonance lines form avoided crossings. The avoided crossings are asymmetric, i.e. they get broader towards larger α and larger $\hbar\omega$. This happens because of the normalization $\alpha = K/\hbar\omega$, as it is discussed
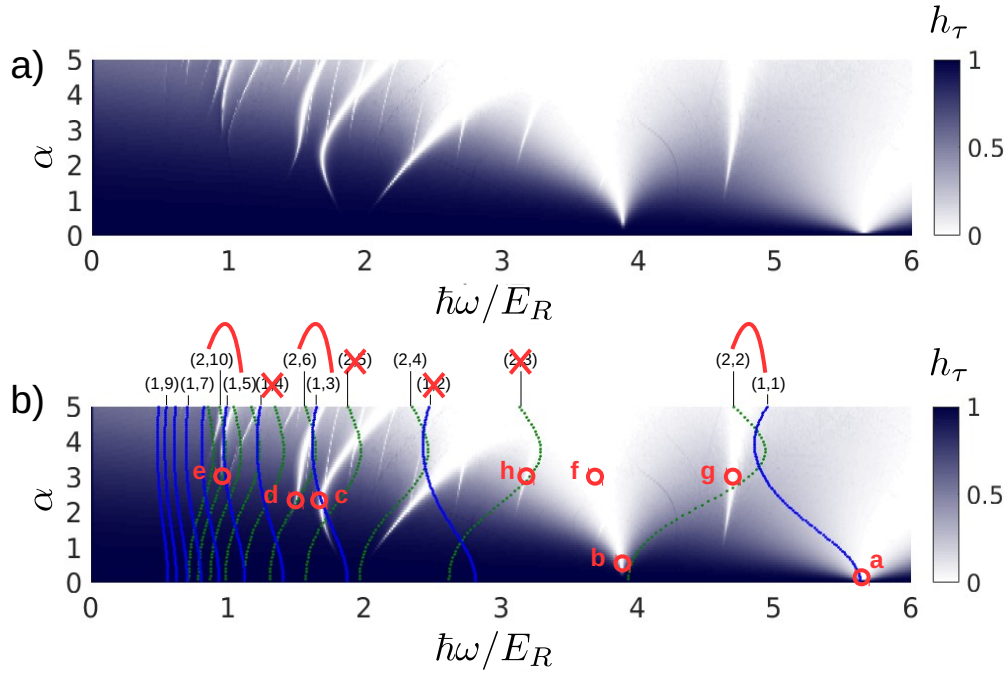
Figure 5.3.14.: Heating plot for the shaken lattice: a) Heating parameter h_τ as a function of driving strength α and frequency $\hbar\omega$ for $q = 0$, shaking time $\tau = 100/E_R$ and $V_0 = 10E_R$. The range of $\hbar\omega$ is chosen such that resonances up to the single-photon resonance to the first excited band are captured. In b) we include the resonance lines to the first and second excited band calculated by Eq. (5.3.17) and already shown in Fig. 5.3.4. Above the plot we assign the respective resonances (b, ν), cross out the forbidden resonances at $q = 0$ and also mark the resonances that are expected to couple strongly, forming a Autler–Townes splitting. Additionally, special pairs $\{\omega, \alpha\}$ are marked and numerated by a-h. In Fig. 5.3.15 we plot the time evolution corresponding to these pairs $\{\omega, \alpha\}$.

in App. C.2.

In Fig. 5.3.14 b) we include the resonance lines (b, ν) to the first (blue) and second (green) excited band, calculated from the effective dispersion relation Eq. (5.3.17). These lines help us to assign and label the resonances with (b, ν). Since $q = 0$, even (odd) photon resonances to the first (second) excited band are forbidden, which is confirmed by the heating plot. We also mark some resonance pairs $\{\omega, \alpha\}$, whose time evolution we plot in Fig. 5.3.15, though with adapted shaking times τ. For example, for very small α we see in Fig. 5.3.15 a) and b) cosine-like oscillations between the ground and the first and second excited band. These oscillations

Figure 5.3.15.: Time evolution of the Bloch band occupations $n_b(t)$ ($b = 0 \ldots 5$) for the $\{\omega, \alpha\}$ pairs a-h from Fig. 5.3.14, which all lie on resonances of different types. The shaking time differs according to the oscillation time which depends on the effective coupling to the excited state(s).

indicate almost perfect two-state resonances between the ground and the first (second) excited band with one (two) photons.

The observed avoided crossing can be well explained by Autler–Townes splittings, where the nearby resonances to first and second excited band couple to each other, forming a double-resonance, as described in App. C.2. We marked in the plot the resonances which couple with each other. Since $\eta_{01} < \eta_{12}$ and $J_1 > J_0$, typically the first excited band is coupled stronger to the second than to the ground band, which a necessary condition for an Autler–Townes splitting. In Fig. 5.3.15 c) and d) we plot the oscillations that emerge from the Autler–Townes splitting between the $(1,3)$ and $(2,6)$ resonance lines. In both cases we see a simultaneous oscillation of the ground state with the first and the excited state. Also cases e) and f) show oscillations corresponding to Autler–Townes splittings for the $(1,5)$-$(2,10)$ and
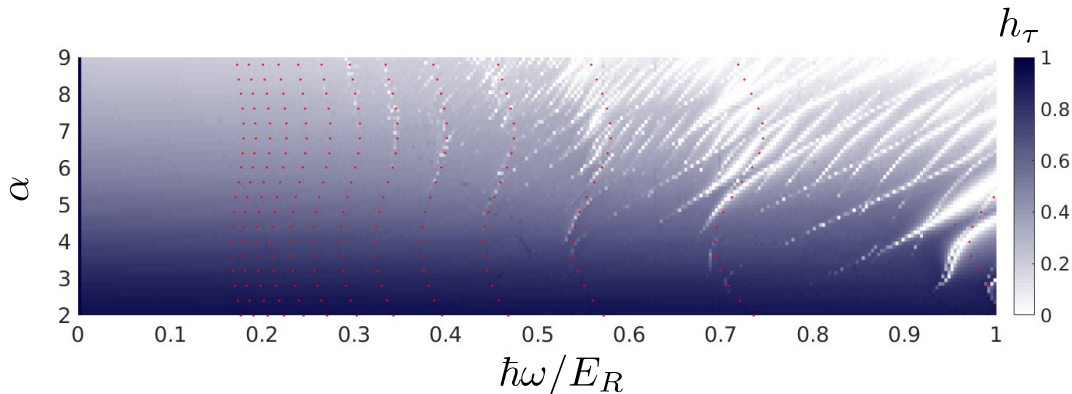
Figure 5.3.16.: Heating plot for $q = 0$ for the low-frequency and high-amplitude regime, where multi-photon transitions for large ν become visible. To this end, the shaking time is increased to $\tau = 500/E_R$. In red, the theoretical resonance lines to the first excited bands are drawn, which match very will with the shape of the numerical resonance lines.

the $(1,1)$-$(2,2)$ double-resonances. In g) and h) we see that the extra resonance lines which cannot be assigned to the first and second excited band belong to excitations to higher lying states, in this case the third and fourth Bloch band, whose occupations $n_3(t)$ and $n_4(t)$ oscillate significantly.

To have a closer look at the resonances with large photon number ν, we consider the heating plot in Fig. 5.3.16, zoomed in into the range $\hbar\omega < 1$ and for stronger couplings $2 < \alpha < 9$ and longer shaking times $\tau = 500/E_R$. Including again the resonance lines to the first excited band, one can recognize resonances up to $\nu = 19$. At the same time, all these resonances are crossed by resonances to higher lying states. This suggests that once the system is excited to the first excited band, it is very likely to excite also higher lying bands.

Next, we consider in Fig. 5.3.17 the situation at $q = \pi/2a$ to illustrate the resonances that are forbidden in the $q = 0$ and $q = \pi/a$ case. We see many more resonance lines compared to the case $q = 0$ and a main resonance $(1,1)$ that is much broader. Again we draw the resonance lines from the effective dispersion, this time also for $b = 2$. Since the nearest-neighbour tunneling term with J_b vanishes, the resonances are less pronounced and have a vertical form. For small α, where the coupling between the resonances is small, the theoretical resonance lines match very well with the numerical ones. The cases a), b) and c) for the resonances $(1,2)$, $(2,3)$ and
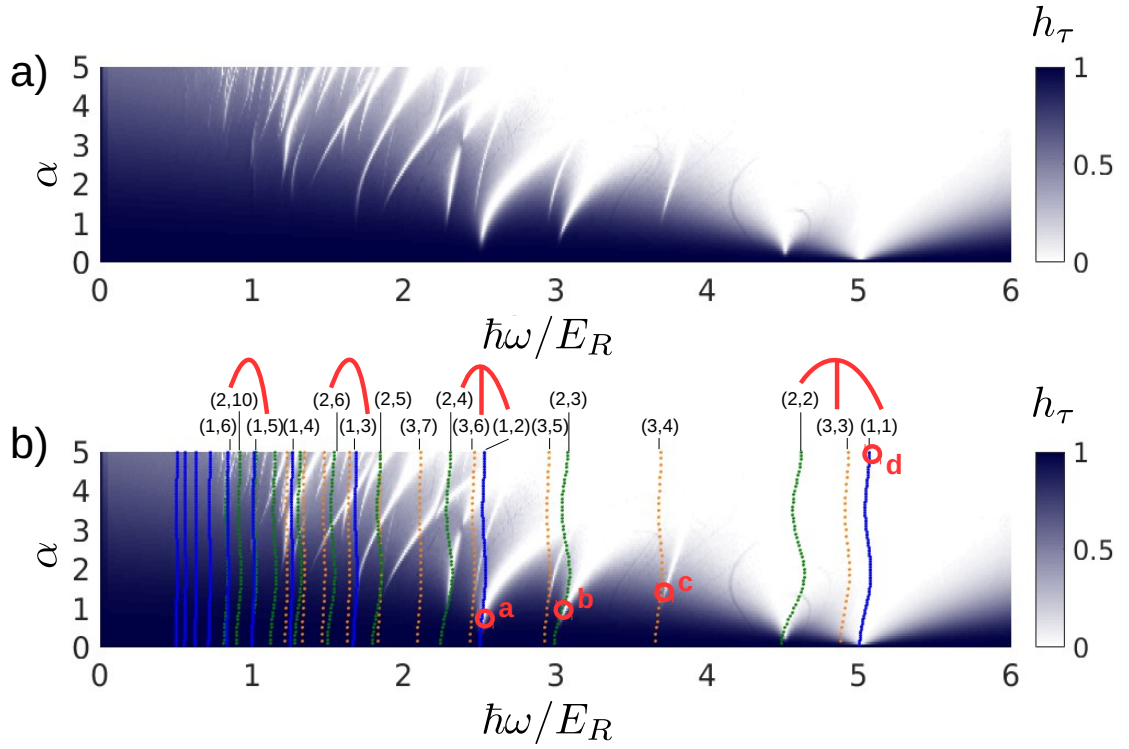
Figure 5.3.17.: Heating plot as in Fig. 5.3.14 but for $q = \pi/2a$ where all transitions to higher bands are allowed. We again picked specific pairs $\{\omega, \alpha\}$ whose time evolution is plotted in Fig. 5.3.18.
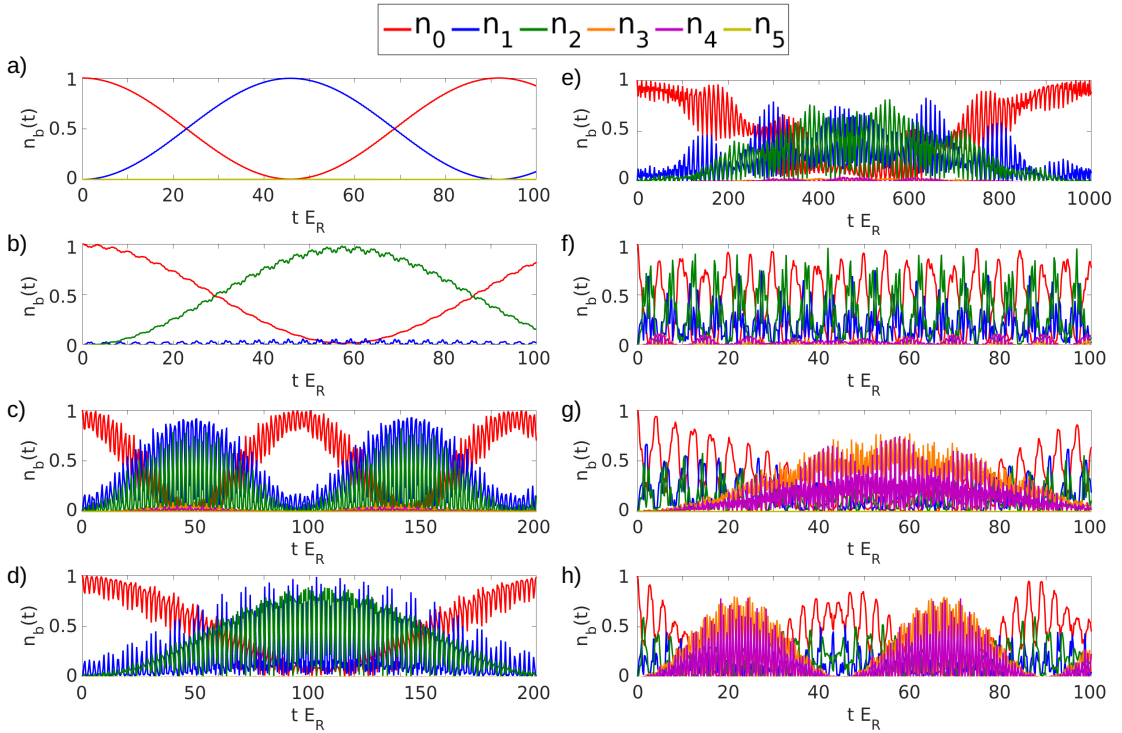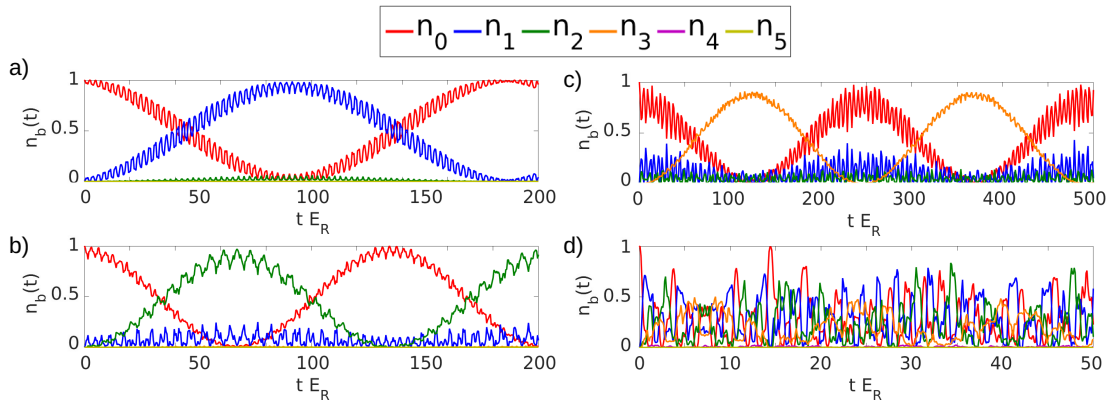

Figure 5.3.18.: Time evolution of the Bloch band occupations $n_b(t)$ ($b = 0 \ldots 5$) for the $\{\omega, \alpha\}$ pairs a-d from Fig. 5.3.17.

$(3,4)$ are time-resolved in Fig. 5.3.18. They show very clean cosine-like oscillations. In contrast, case d) shows the $(1,1)$ resonance for a very strong $\alpha = 5$. Due to
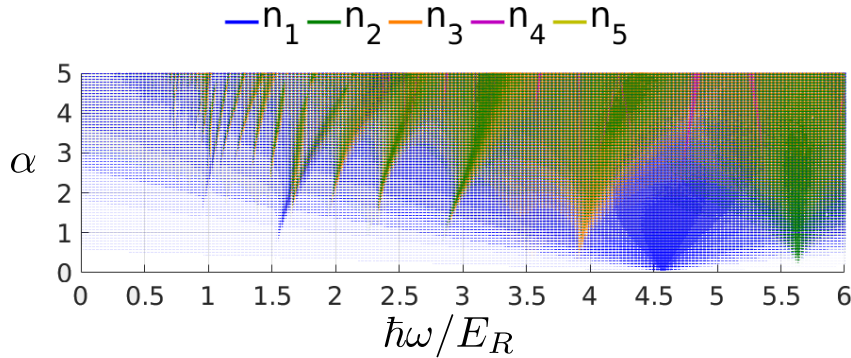
Figure 5.3.19.: Heating plot for $q = \pi/2a$ as in Fig. 5.3.18, where the transitions to the different Bloch bands are colorized. The color represents the Bloch band b, where the particle is excited to whereas the circle size illustrates the maximum occupation $\max_{t\in[b,\tau]} n_b(t)$ of the respective Bloch band b during the time span τ.

the strong coupling and the large frequency, the dynamics is complex. However, the oscillation is almost fully restricted to the four lowest bands and does not occupy even higher lying bands. To give a better intuition about the proportion of the differen Bloch bands in the heating process and in order to track better multi-resonances, in Fig. 5.3.19 we plot the heating plot where we overlay the maximum of the density of each Bloch band $\max_{t\in[b,\tau]} n_b(t)$ during the time span τ, colorized in the usual color code. Here we see that only for small shaking amplitudes $\alpha \lesssim 1.5$ the resonances are to a single band only. For higher shaking amplitudes, the bands strongly mix and several bands get excited at once.

Finally, we want to have a look on the situation where the shaking amplitude α is switched on in a finite ramping time t_r. Here, the avoided crossing in the quasienergy spectrum (see the previous section, Sec. 5.3.4) are partly resolved such that whenever an avoided crossing of quasienergies is passed by, higher lying bands are excited, even if at the final value of α a quantum quench would not lead to strong heating. In Fig. 5.3.20 we show the heating plot ($\hbar\omega \leq 3$) with a shaking that is linearly switched on for a time $t_r = 100/E_R$ before it is kept constant for another $t_s = 40/E_R$ to let oscillations dispread. We see that the regions above diagonal resonances are not dark, i.e. they show heating. To observe the effect of the ramping time in a specific example, we pick a pair $\{\omega, \alpha\} = \{1.7/\hbar, 3.5\}$ at $q = 0$,
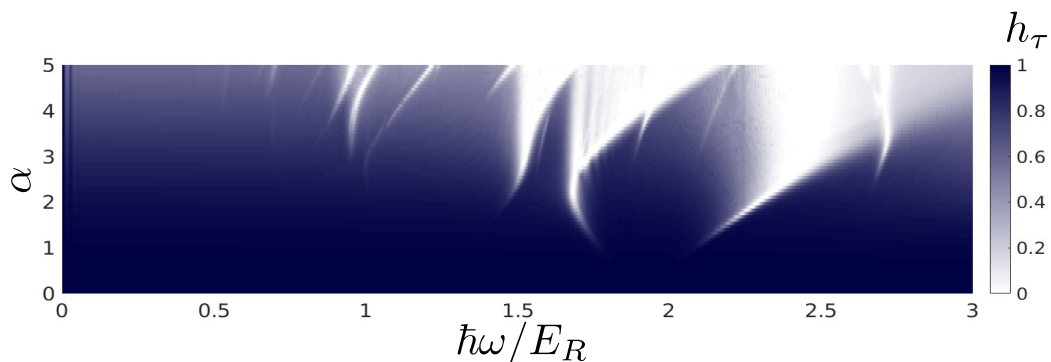
Figure 5.3.20.: Heating plot for $\tau = 40/E_R$ but with an initial ramping time $t_r = 100/E_R$. We set again $q = 0$ and $V_0 = 10E_R$.
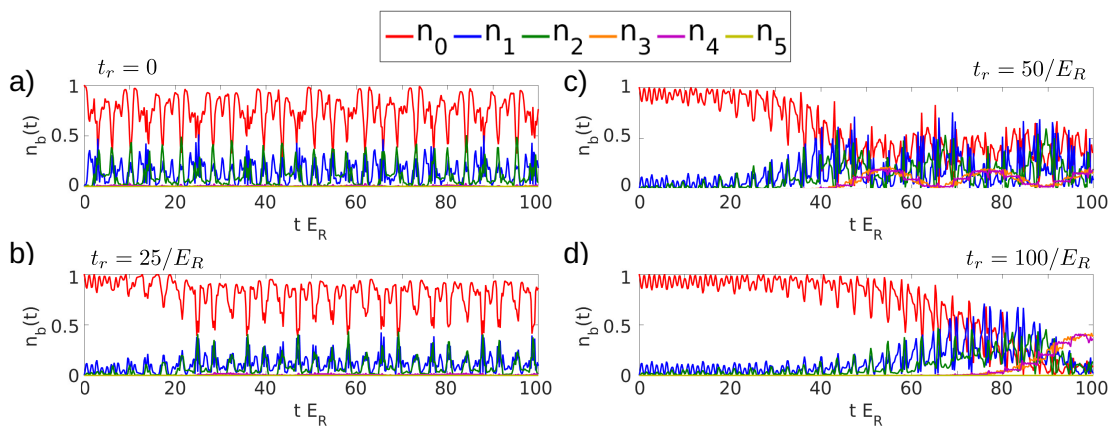
Figure 5.3.21.: Time evolution of the Bloch band occupations $n_b(t)$ ($b = 0 \ldots 5$) for $\{\omega, \alpha\} = \{1.7/\hbar, 3.5\}$ at $q = 0$ for different ramping times $t_r = [0, 25, 50, 100]/E_R$, while $\tau = 100/E_R$.

which lies not exactly on a resonance in the heating plot, and vary the ramping time t_r, while the total time $\tau = t_r + t_s = 100/E_R$ remains fixed. The resulting time dynamics for $t_r = [0, 25, 50, 100]/E_R$ is plotted in Fig. 5.3.21. As the ramping time is increased, we see a growing fraction of the third and fourth band. The reason for this is that a respective resonance is crossed during the ramping, as can be seen in Fig. 5.3.14.

5.3.6. Comparison of the Numerical Simulations with Experimental Findings

Finally, we compare the numerical findings to experimental results on heating in a weakly-interacting gas of ultra-cold bosonic ^{87}Rb atoms which were obtained in the group of Klaus Sengstock in Hamburg, see Ref. [105]. There, the optical lattice was realized by a pair of $\lambda_L = 830$nm wavelength that were arranged at an angle of 117.1°, giving a lattice spacing of $a = 486.5$nm. We therefore define the effective recoil energy in this section by the lattice spacing $E_R = \frac{\pi^2 \hbar^2}{2ma^2}$. The lattice depth for the experiment was $V_0 = 13.05 E_R$.

In the experiment, the atomic cloud was initially prepared in the ground state of the static lattice at $q = 0$. Then the shaking strength was ramped up in a time of $t_r = 50$ms and kept fixed at the desired value of α for another $t_s = 20$ms, while the frequency ω was kept constant for the whole time $\tau = 70$ms. Thereafter, all fields have been switched off so that the atoms fall under the influence of gravity for 40ms time-of-flight until an absorption image was taken. The heating parameter in the experiment was defined by the optical density of the atoms, which decreases if atoms leave the cloud due to excitation to higher Bloch bands.

It is important to note that the quasimomenta of the bosons in this experimental setup are not fully conserved due to small interactions of the atoms and because of the presence of the trapping potential. As a consequence, during the switching-on of the shaking amplitude within time t_a the interaction of the atoms leads to partly relaxing of the condensate into the new ground state at $q = \pi/a$ of the effective dispersion relation, which happens at the first zero of the 0th order Bessel function around $\alpha \approx 2.42$. Therefore in the numerics we switch at $\alpha = 2.42$ from the heating plot at $q = 0$ to the one for $q = \pi/a$. Another consequence of the trapping potential, the interaction of the atoms and the finite temperature of the atomic cloud is that the condensate has a finite width of around $\omega_q = 0.1\pi/a$ in quasimomentum. Therefore we assume the cloud to be Gaussian shaped with width ω_q. In the numerics this is addressed by superimposing heating plots for several q around $q = 0$.

As the ramp-up time of the driving is rather long (50ms), we will see a mixture of excitations stemming from adiabatic and diabatic excitation processes. While in
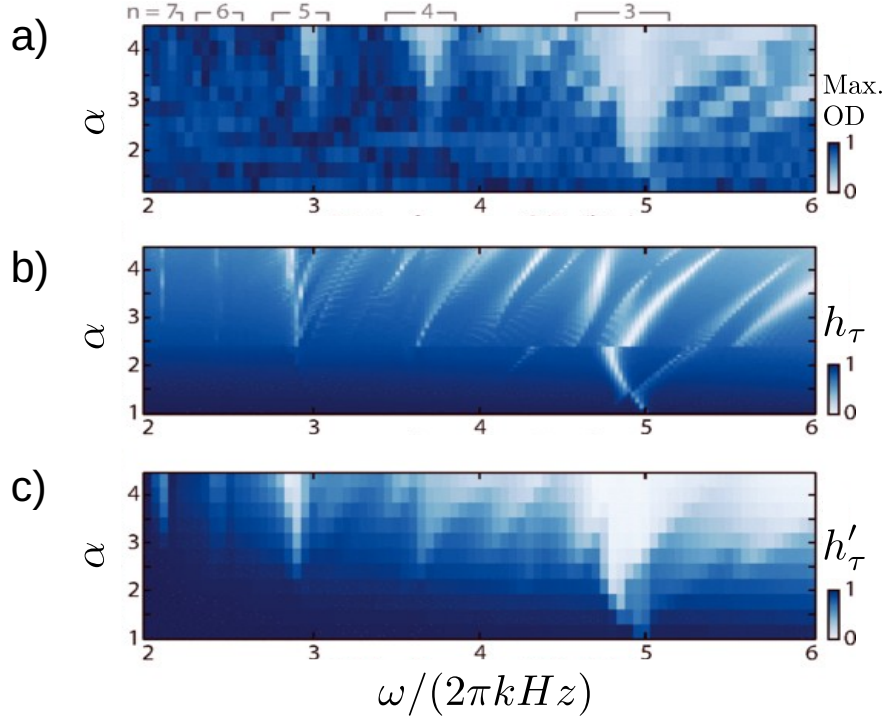
Figure 5.3.22.: Comparison of numerical and experimental data for heating of weakly-interacting bosons in a shaken optical lattice. a) Experimental data, where the heating parameter is the optical density. b) Numerical data. Here, to describe the finite width of the condensate of around $\omega_q \approx 0.1\pi/a$, heating plots for different q are superposed in a Gaussian shape. c) To cover the effect of adiabatic excitations in the experiment, the heating parameter h_τ has been summed along the α-axis. Furthermore, the resolution has been reduced to maximize the resemblence with the experimental data.

the single-particle model we can simulate the ramping for fixed q, we cannot do so if the minimum changes to $q = \pi/a$ at $\alpha = 2.42$. To include the adiabatic excitation processes approximately, we sum the heating parameter h_τ upwards along the α axis

$$h'_\tau(\alpha_n) = \sum_{i=1}^{n} h_\tau(\alpha_i). \tag{5.3.53}$$

In Fig. 5.3.22 we compare the experimental data with the numerics. Whereas Fig. 5.3.22 a) shows the experimental data, in b) we show the numerical heating

plot as it is expected for the given parameters and with the broadening of the cloud of ω_q, allowing also for resonances which are forbidden at $q = 0$. In the experimental data we can recognize resonances up to $\nu = 7$. The odd resonances show up more clearly, as it is expected since most of the condensate lies around $q = 0$. Also, the avoided crossings are visible in the experimental data. Especially the crossing between band 1 and 2 around $\omega/2\pi\mathrm{kHz} \approx 5$ that was discussed in the previous section, is visible and leads to enhanced heating. Even a couple of diagonal resonances to bands > 2 are visible around $\omega/2\pi\mathrm{kHz} \approx 4.5$ and $\omega/2\pi\mathrm{kHz} \approx 5.5$. In c) we show the heating parameter h'_τ to include the ramping procedure. Furthermore, we have reduced the resolution in both ω and α to maximize the resemblence between experrimment and numerics, which is astonishing good in total.

To sum up, the experimental data is very well reproduced by the numerical simulation and can be very well described by the presented theoretical findings.

5.4. Multi-Photon Heating in an Amplitude-Modulated Lattice

Next we consider the scenario where the lattice is periodically driven by modulating its amplitude. Again we start with a Fourier expansion of the time-dependent Hamiltonian, from which we can then calculate the effective coupling parameters C that couple the ground state resonantly to excited states in diabatic heating processes. We use the Floquet perturbative method and a rotating-wave approximation. Subsequently, we also compute the quasienergy spectrum of the shaken lattice numerically. A numerical simulation, here only for the quenched scenario, reveals the precise information about where and how strong the heating is taking place.

5.4.1. Fourier Expansion of the Tight-Binding Hamiltonian

As in the case of a shaken lattice, we start with the single-particle Hamiltonian

$$H_{\mathrm{sp}}(t) = -\frac{\hbar^2}{2m}\partial_x^2 + V(x,t). \tag{5.4.1}$$

The amplitude of the cosine potential is now modulated sinusoidally

$$V(x,t) = V_0 \left[1 + \beta \sin(\omega t)\right] \cos(k_l x), \qquad (5.4.2)$$

which can be achieved by a modulation of the lattice depth. In contrast to Chap. 5.3, we take a different approach to expand the Hamiltonian in time and to derive the quasienergy operator. Namely, we transform the Hamiltonian to the basis of its instantaneous eigenstates denoted by $|bq, t\rangle$ that fulfill

$$\hat{H}(t)|bq, t\rangle = E_b(q, t)|bq, t\rangle. \qquad (5.4.3)$$

Thus, they are Bloch waves of the lattice system at the instantaneous lattice depth $V_0[1 + \beta \sin(\omega t)]$ labeled by the same quantum numbers, quasimomentum q and band index b, as the eigenstates of the undriven system $|bq\rangle = |bq, 0\rangle$. The transformation is achieved by the gauge transformation

$$\hat{U}(t) = \sum_{q,b} |bq, t\rangle\langle bq| \qquad (5.4.4)$$

Consequently, the Hamiltonian is transformed to

$$
\begin{aligned}
\hat{H}'(t) &= \hat{U}^\dagger(t)\hat{H}(t)\hat{U}(t) - i\hbar\hat{U}^\dagger(t)\dot{\hat{U}}(t) \\
&= \sum_b |bq\rangle E_b(q, t)\langle bq| + \sum_{bb'} |b'q\rangle M_{b'b}(q, t)\langle bq| \qquad (5.4.5)
\end{aligned}
$$

with matrix elements

$$M_{b'b}(q, t) = -i\hbar\langle b'q, t|\partial_t|bq, t\rangle. \qquad (5.4.6)$$

For the sake of a light notation, in the following we will suppress the quasimomentum label q, when denoting states, energies, and matrix elements. Applying the transformation (5.4.4) is a standard procedure when treating slow parameter variations in quantum systems. Following this standard procedure further, we can bring the matrix elements $M_{b'b}(t)$ in a more convenient form. Their diagonal elements $M_{bb}(t)$ describe Berry phase effects. Since we are varying a single parameter only, the diagonal terms can be removed by a simple gauge transformation. Namely, we

can write the diagonal matrix elements like

$$M_{bb}(t) = -i\hbar\langle b, t|\partial_t|b, t\rangle = -\hbar A_b(V)\dot{V}(t) \tag{5.4.7}$$

in terms of the Berry connection

$$A_b(t) = i\langle b, V|\partial_V|b, V\rangle \tag{5.4.8}$$

for a variation of the lattice depth V. Here we have written the eigenstates as $|b, V\rangle$ for a lattice of depth V, so that $|b, t\rangle = |b, V(t)\rangle$ with $V(t) = V_0[1 + \beta\sin(\omega t)]$. A gauge transformation

$$|b, V\rangle' = e^{i\theta_b(V)}|b, V\rangle \tag{5.4.9}$$

changes the Berry curvature to

$$A'_b(V) = A_b(V) - \partial_V\theta_b(V), \tag{5.4.10}$$

which vanishes for the choice

$$\theta_b(V) = \int_0^V dW\, A_b(W). \tag{5.4.11}$$

Thus, for a suitable definition of the phase of the instantaneous eigenstates, the diagonal matrix elements vanish,

$$M_{bb}(t) = 0. \tag{5.4.12}$$

Berry phase effects can matter, however, in more complicated driving scenarios where several parameters are varied.

In order to evaluate the off diagonal matrix elements $M_{b'b}(t)$ with $b' \neq b$, we consider the quantity

$$
\begin{aligned}
\langle b', t|\frac{\mathrm{d}}{\mathrm{d}t}\left(\hat{H}'(t)|b, t\rangle\right) &= \langle b', t|\dot{\hat{H}}(t)|b, t\rangle + E_{b'}(t)\langle b', t|\partial_t|b, t\rangle \\
&= E_b(t)\langle b', t|\partial_t|b, t\rangle, \tag{5.4.13}
\end{aligned}
$$

where $\hat{H}'$ denotes the Hamiltonian after the previous gauge transformation. From this equation we can derive an expression for $\langle b', t | \partial_t | b, t \rangle$, which gives in total

$$M_{b'b}(q, t) = -i \frac{\hbar \langle b'q, t | \dot{\hat{H}}(t) | bq, t \rangle}{E_{b'}(q, t) - E_b(q, t)} \tag{5.4.14}$$

as long as $E_{b'}(q, t) \neq E_b(q, t)$. Here we have reintroduced the quasimomentum q. All in all, the system is described by the time-periodic Hamiltonian

$$\hat{H}'(q, t) = \sum_b \left[|bq\rangle E_b(q, t) \langle bq| + \sum_{b' \neq b} |b'q\rangle M_{b'b}(q, t) \langle bq| \right]. \tag{5.4.15}$$

Note that no approximation has been made so far and that the Hamiltonian in the present form is valid for a large class of driving schemes with a single parameter variation.

The properties of the matrix elements (5.4.14) become more transparent, when expressing the instantaneous Bloch waves in terms of instantaneous Wannier states $|b\ell, t\rangle$,

$$|bq, t\rangle = \frac{1}{\sqrt{M}} \sum_\ell e^{iqa\ell} |b\ell, t\rangle. \tag{5.4.16}$$

Remember that their wave functions

$$\langle x | b\ell, t \rangle = w_b(x - \ell a, t) \tag{5.4.17}$$

are real and exponentially localized at the lattice minima $x = \ell a$ with integer ℓ. Moreover, $w_b(x)$ is even (odd) for b even (odd), $w_b(-x) = (-1)^b w_b(x)$ [173]. As the width of the Wannier orbitals decreases slightly with increasing lattice depth, the time dependence describes a breathing motion of the Wannier functions. Transforming to the Wannier states, the numerator on the right-hand side of Eq. (5.4.14) can be expressed like

$$\hbar \langle b'q, t | \dot{\hat{H}}(t) | bq, t \rangle = \beta V_0 \hbar \omega \cos(\omega t) \sum_\ell e^{iqa\ell} W_{b'b}^{(\ell)}(t), \tag{5.4.18}$$

with matrix elements

$$W_{b'b}^{(\ell)}(t) = \int \mathrm{d}x \, w_{b'}(x + \ell a, t) \cos(k_l x) w_b(x, t). \qquad (5.4.19)$$

Similar to the $\eta_{b'b}$ in the shaken lattice, the $W_{b'b}^{(\ell)}$ describe how strong the Wannier states are coupled with each other by the driving term. Since they obey

$$W_{b'b}^{(-\ell)}(t) = (-1)^{b+b'} W_{b'b}^{(\ell)}(t), \qquad (5.4.20)$$

for even $(b' + b)$ the sum on the right-hand side of Eq. (5.4.18) reads

$$W_{b'b}^{(0)}(t) + 2W_{b'b}^{(1)}(t) \cos(qa) + 2W_{b'b}^{(2)}(t) \cos(2qa) + \cdots, \qquad (5.4.21)$$

whereas for odd $(b' + b)$ the leading $\ell = 0$ term vanishes and one finds

$$2iW_{b'b}^{(1)}(t) \sin(qa) + 2iW_{b'b}^{(2)}(t) \sin(2qa) + \cdots. \qquad (5.4.22)$$

These equations indicate that transitions to odd bands are suppressed completely for $q = 0$ and $q = \pi/a$. This is complementary to the case of lattice shaking, where excitations from the ground state $(b = 0)$ are only possible to bands with odd b' at $q = 0$. The missing $\ell = 0$ term for odd transitions, which is related to parity conservation within a single lattice site, also leads to a relative suppression of transitions from the lowest to odd bands for other values of q. Namely, due to the exponential localization of the Wannier functions, the matrix elements $W_{b'b}^{(\ell)}(t)$ drop rapidly with ℓ. It is, therefore, reasonable to keep only the leading term and to approximate

$$\hbar \langle b'q, t | \dot{\hat{H}}(t) | bq, t \rangle = \beta V_0 \hbar \omega \cos(\omega t) W_{b'b}^{(0)}(t) \qquad (5.4.23)$$

for even $(b' + b)$ and

$$\hbar \langle b'q, t | \dot{\hat{H}}(t) | bq, t \rangle = i2 \sin(qa) \beta V_0 \hbar \omega \cos(\omega t) W_{b'b}^{(1)}(t) \qquad (5.4.24)$$

for odd $(b' + b)$.

In the following we will focus on transitions from the lowest to the second excited band. For small quasimomenta $q \ll \pi/a$ these transitions constitute the dominant
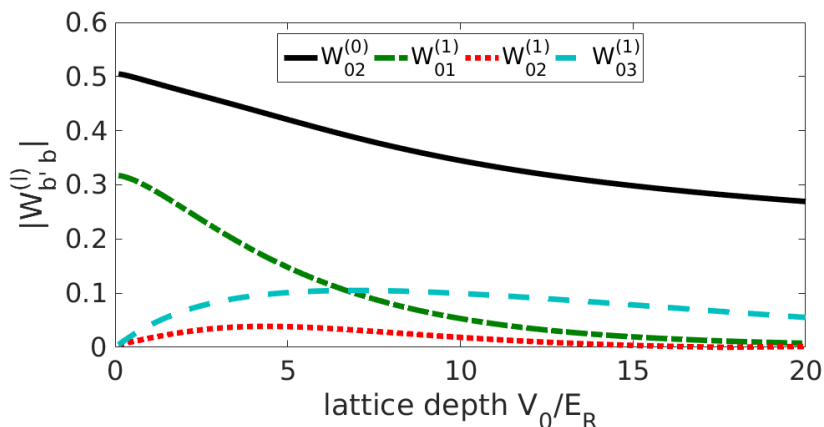
Figure 5.4.1.: Coupling matrix elements $W_{b0}^{(0)}$ and $W_{b0}^{(1)}$ as defined in Eq. (5.4.19) versus lattice depth V_0/E_R.

heating channel. The relevant matrix elements $W_{b'b}^{(0)}$ and $W_{b'b}^{(1)}$ has a rather weak dependence on the lattice depth (see Fig. 5.4.1), so that we can approximate

$$W_{b'b}^{(0)}(t) \approx \mathcal{W}_{b'b} - \beta \mathcal{W}'_{b'b} \sin(\omega t), \tag{5.4.25}$$

for even $b' + b$ and

$$W_{b'b}^{(1)}(t) \approx \mathcal{V}_{b'b} - \beta \mathcal{V}'_{b'b} \sin(\omega t), \tag{5.4.26}$$

for odd $(b' + b)$ neglecting higher harmonics. The coefficients $\mathcal{W}_{b'b}$, $\mathcal{W}'_{b'b}$, $\mathcal{V}_{b'b}$ and $\mathcal{V}'_{b'b}$ have a very weak dependence on β only and one has $\mathcal{W}'_{b'b} \ll \mathcal{W}_{b'b} \sim 1$ and $\mathcal{V}'_{b'b} \ll \mathcal{V}_{b'b} \sim 1$. At a ν-photon resonance, we can likewise approximate the instantaneous energy difference between both bands like

$$E_b(q,t) - E_{b'}(q,t) \approx \nu\hbar\omega + \beta\mathcal{F}_{b'b}(q)\sin(\omega t) \tag{5.4.27}$$

and its inverse like

$$\frac{1}{E_b(q,t) - E_{b'}(q,t)} \approx \frac{1}{\nu\hbar\omega} - \beta\frac{\mathcal{F}_{b'b}(q)}{(\nu\hbar\omega)^2}\sin(\omega t). \tag{5.4.28}$$

Taking terms up to β^2, the matrix element $M_{b'b}(q,t)$ then reads

$$M_{b'b}(q,t) \approx -i\frac{V_0}{\nu}\left[\beta\mathcal{W}_{b'b}\cos(\omega t) - \beta^2\frac{1}{2}X_{b'b}(q)\sin(2\omega t)\right], \tag{5.4.29}$$

for even $b + b'$ and

$$M_{b'b}(q,t) \approx 2\sin(qa)\frac{V_0}{\nu}\left[\beta\mathcal{V}_{b'b}\cos(\omega t) - \beta^2\frac{1}{2}Y_{b'b}(q)\sin(2\omega t)\right], \tag{5.4.30}$$

for odd $b + b'$. Here we used the notation

$$X_{b'b}(q) = \left[\mathcal{W}'_{b'b} + \frac{\mathcal{F}_{b'b}(q)}{\Delta_{b'b}(q)}\right], \quad Y_{b'b}(q) = \left[\mathcal{V}'_{b'b} + \frac{\mathcal{F}_{b'b}(q)}{\Delta_{b'b}(q)}\right]. \tag{5.4.31}$$

In the derivation we have explicitly used the resonance condition

$$\Delta_{b'b}(q) = \epsilon_{b'}(q) - \epsilon_b(q) = \nu\hbar\omega, \tag{5.4.32}$$

where $\epsilon_b(q)$ is the static dispersion relation, which has been plotted in Fig. 5.3.3 and which is not renormalized by a Bessel function as it is the case for the shaken lattice. At the ν-photon resonance between bands b and b', it is sufficient to describe the system within the subspace spanned by these two states, as all other Bloch states can be neglected. This approximation is justified, as it will be confirmed later in the numerical simulation, since most of the resonances are between two states only. Up to a time-dependent energy constant, the relevant Hamiltonian is thus given by

$$\begin{aligned}\hat{H}'(q,t) &\approx& \left[\nu\hbar\omega + \beta\mathcal{F}_{b'b}(q)\sin(\omega t)\right]|b'q\rangle\langle b'q| \\ &&+ M_{b'b}(q,t)|b'q\rangle\langle bq| + M^*_{b'b}(q,t)|bq\rangle\langle b'q|.\end{aligned} \tag{5.4.33}$$

These can be expanded in Fourier components

$$\hat{H}'(q,t) = \sum_m \hat{H}_m(q)e^{im\omega t}, \tag{5.4.34}$$

$$\hat{H}_m(q) = \frac{1}{T}\int_0^T dt\, e^{-im\omega t}\hat{H}'(q,t), \tag{5.4.35}$$

with driving period $T = 2\pi/\omega$. For the most relevant transition from the ground to the second excited band, we find

$$\hat{H}_0(q) = \nu\hbar\omega|2q\rangle\langle 2q|, \tag{5.4.36}$$

$$\hat{H}_1(q) = -i\frac{\beta\mathcal{F}_{20}(q)}{2}|2q\rangle\langle 2q| + \frac{\beta V_0 \mathcal{W}_{20}}{2\nu}\big(|2q\rangle\langle 0q| - |0q\rangle\langle 2q|\big), \tag{5.4.37}$$

$$\hat{H}_2(q) = \frac{\beta^2 V_0 X_{20}(q)}{2\nu}\big(|2q\rangle\langle 0q| - |0q\rangle\langle 2q|\big), \tag{5.4.38}$$

as well as the conjugated terms $\hat{H}_{-m} = \hat{H}_m^\dagger$. The terms $\hat{H}_m$ become smaller with increasing m and depend on the driving strength like $\beta^{|m|}$. This applies also to the higher harmonics that we neglected.

With the Fourier components of the Hamiltonian we can readily write down the quasienergy operator

$$\langle\langle b'q'm'|\bar{Q}|bqm\rangle\rangle = \langle b'q'|(\delta_{m'm}m\hbar\omega + \hat{H}'_{m'-m}(q))|bq\rangle, \tag{5.4.39}$$

of the amplitude modulated lattice. We write $\hat{Q}$ in the basis $|bqm\rangle\rangle$ in the extended Hilbert space, where $|bqm\rangle\rangle$ represents the time-dependent state $|bq\rangle e^{im\omega t}$ in the original state space. The relevant coupling matrix elements of the perturbation $\hat{V}_{\text{pert}}$ change the photon number m by ± 1 or by ± 2. At the ν-photon resonance between states $|bq\rangle$ and $|b'q\rangle$ they are given by

$$\langle\langle 2(m\pm 1)|\hat{V}_{\text{pert}}|2m\rangle\rangle = \mp i\frac{\beta\mathcal{F}_{b'b}}{2} \tag{5.4.40}$$

$$\langle\langle 2(m\pm 1)|\hat{V}_{\text{pert}}|0m\rangle\rangle = -i\frac{\beta V_0 \mathcal{W}_{b'b}}{2\nu} \tag{5.4.41}$$

$$\langle\langle 2(m\pm 2)|\hat{V}_{\text{pert}}|0m\rangle\rangle = \pm\frac{\beta^2 V_0 X_{b'b}}{2\nu} \tag{5.4.42}$$

for even $b + b'$ and

$$\langle\langle 2(m\pm 1)|\hat{V}_{\text{pert}}|2m\rangle\rangle = \pm 2\sin(qa)\frac{\beta\mathcal{F}_{b'b}}{2} \tag{5.4.43}$$

$$\langle\langle 2(m\pm 1)|\hat{V}_{\text{pert}}|0m\rangle\rangle = 2\sin(qa)\frac{\beta V_0 \mathcal{V}_{b'b}}{2\nu} \tag{5.4.44}$$

$$\langle\langle 2(m\pm 2)|\hat{V}_{\text{pert}}|0m\rangle\rangle = \pm i2\sin(qa)\frac{\beta^2 V_0 Y_{b'b}}{2\nu} \tag{5.4.45}$$

for odd $b + b'$, see Eqs. (5.4.37) and (5.4.38).

Comparing the Fourier components of the Hamiltonian in the amplitude modulated scenario with that of the shaken lattice scenario, we see that the groundstate couples stronger to the second than not the first excited band, since $\mathcal{W}_{20} \approx W_{20}^{(0)}(t) > W_{10}^{(1)}(t) \approx \mathcal{V}_{10}$, see Fig. 5.4.1. For the transitions to first excited band, the coupling terms have an additional factor of $i2\sin(qa)$ compared to those to the second excited band. Also, the Hamiltonian has more non-vanishing Fourier components than in the case of the shaken lattice, such that direct coupling elements are present not just for single-photon processes but also for higher m.

5.4.2. Multi-Photon Heating from a Rotating-Wave Approximation

The rotating-wave approximation for the amplitude modulated lattice is justified if the coupling matrix element $M_{b0}(q,t)$ is small compared to the driving frequency $\hbar\omega$. Both quantities scale like $1/\nu$. Therefore this condition depends mainly on the driving strength β.

As in the case of the shaken lattice, we first perform another gauge transformation, with the unitary operator

$$\hat{U}'(t) = \exp\left(-i\sum_q \left[\nu\omega t - \frac{\beta\mathcal{F}_{b0}(q)}{\hbar\omega}\cos(\omega t)\right]|bq\rangle\langle bq|\right). \tag{5.4.46}$$

such that the resonant states have the same photon index m and such that the time dependency of the dispersion relation is removed. Assuming the resonance condition (5.4.32), the transformed Hamiltonian reads

$$\hat{H}''(q,t) = M_{20}(q,t)e^{i\nu\omega t - i\frac{\beta\mathcal{F}_{b0}(q)}{\hbar\omega}\cos(\omega t)}|2q\rangle\langle 0q| + \text{ h.c. }. \tag{5.4.47}$$

In the following, we will again drop the label q on all quantities. Employing the relation

$$\exp(-ia\cos(b)) = \sum_{k=-\infty}^{\infty} (-i)^k \mathcal{J}_k(a)e^{-ikb}, \tag{5.4.48}$$

where $\mathcal{J}_k(x)$ denotes the Bessel function of first kind, we find the Fourier components of the time-dependent matrix element

$$M_{b0}(q,t)e^{i\nu\omega t - i\frac{\beta\mathcal{F}_b(q)}{\hbar\omega}\cos(\omega t)} = \sum_r M_{b,r}^{(\nu)} e^{ir\omega t} \tag{5.4.49}$$

to be given by

$$
\begin{aligned}
M_{b,r}^{(\nu)} &= -i\frac{\beta V_0 \mathcal{W}_b}{2\nu}(-i)^{\nu+1-r}\mathcal{J}_{\nu+1-r}\left(\frac{\beta\mathcal{F}_b}{\hbar\omega}\right) - i\frac{\beta V_0 \mathcal{W}_b}{2\nu}(-i)^{\nu-1-r}\mathcal{J}_{\nu-1-r}\left(\frac{\beta\mathcal{F}_b}{\hbar\omega}\right) \\
&\quad + \frac{\beta^2 V_0 X_b}{2\nu}(-i)^{\nu+2-r}\mathcal{J}_{\nu+2-r}\left(\frac{\beta\mathcal{F}_b}{\hbar\omega}\right) - \frac{\beta^2 V_0 X_b}{2\nu}(-i)^{\nu-2-r}\mathcal{J}_{\nu-2-r}\left(\frac{\beta\mathcal{F}_b}{\hbar\omega}\right)
\end{aligned}
\tag{5.4.50}
$$

for even b and

$$
\begin{aligned}
M_{b,r}^{(\nu)} &= \sin(qa)\Bigg[\frac{\beta V_0 \mathcal{V}_b}{\nu}(-i)^{\nu+1-r}\mathcal{J}_{\nu+1-r}\left(\frac{\beta\mathcal{F}_b}{\hbar\omega}\right) + \frac{\beta V_0 \mathcal{V}_b}{\nu}(-i)^{\nu-1-r}\mathcal{J}_{\nu-1-r}\left(\frac{\beta\mathcal{F}_b}{\hbar\omega}\right) \\
&\quad + i\frac{\beta^2 V_0 Y_b}{\nu}(-i)^{\nu+2-r}\mathcal{J}_{\nu+2-r}\left(\frac{\beta\mathcal{F}_b}{\hbar\omega}\right) - i\frac{\beta^2 V_0 Y_b}{\nu}(-i)^{\nu-2-r}\mathcal{J}_{\nu-2-r}\left(\frac{\beta\mathcal{F}_b}{\hbar\omega}\right)\Bigg]
\end{aligned}
\tag{5.4.51}
$$

for odd b. For the rotating-wave approximation, we now neglect the rapidly rotating phases of the coupling matrix element and keep only the 0th component of the Fourier expansion of the Hamiltonian

$$M_{20}(q,t)e^{i\nu\omega t - i\frac{\beta\mathcal{F}_b(q)}{\hbar\omega}\cos(\omega t)} \approx M_{0,b}^{(\nu)}. \tag{5.4.52}$$

Thus, the effective coupling parameter is given by

$$C_{(b,\nu)} = M_{0,b}^{(\nu)}. \tag{5.4.53}$$

In order to interpret this result and estimate the scaling of $C_{(b,\nu)}$, it is useful to make further approximations. First of all, let us consider only the leading order with respect to the driving strength β. For this purpose, we remember again that for small arguments x (and $k \geq 0$) the Bessel function is asymptotically given by

$$\mathcal{J}_k(x) \simeq \frac{1}{k!}\left(\frac{x}{2}\right)^k. \tag{5.4.54}$$

Hence, in leading order only the second and the fourth term of Eq. (5.4.50) and Eq. (5.4.51) contribute to $M_{0,b}$ and we find

$$M_{0,b}^{(\nu)} \simeq (-i)^{\nu} \frac{\beta V_0}{\nu} \left[\frac{\mathcal{W}_b}{2} + \frac{(\nu - 1) X_b \hbar \omega}{\mathcal{F}_b} \right] \frac{\left(\frac{\beta \mathcal{F}_b}{2 \hbar \omega} \right)^{\nu - 1}}{(\nu - 1)!} \qquad (5.4.55)$$

for even b. For large photon numbers ν, we can now use Stirling's formula

$$k! \simeq \sqrt{2\pi k} \left(\frac{k}{e} \right)^k \qquad (5.4.56)$$

valid for large k. Employing Eqs. (5.4.32), we obtain

$$C_{(b,\nu)} \simeq \beta V_0 \sqrt{\frac{\pi}{2\nu^3}} \left(\mathcal{W}_b + \frac{\mathcal{W}_b' \Delta_b}{\mathcal{F}_b} + 1 \right) \left(\frac{\beta}{\beta_{\text{thresh},b}} \right)^{\nu - 1}, \qquad (5.4.57)$$

for even b and

$$C_{(b,\nu)} \simeq \beta i 2 \sin(qa) V_0 \sqrt{\frac{\pi}{2\nu^3}} \left(\mathcal{V}_b + \frac{\mathcal{V}_b' \Delta_b}{\mathcal{F}_b} + 1 \right) \left(\frac{\beta}{\beta_{\text{thresh},b}} \right)^{\nu - 1}, \qquad (5.4.58)$$

for odd b. Here we introduced the threshold value

$$\beta_{\text{thresh},b} = \frac{2\Delta_b}{e\mathcal{F}_b} \qquad (5.4.59)$$

for the driving strength. From Eq. (5.4.57) and Eq. (5.4.57) we conclude that for large a photon-number ν heating occurs in a rather sharp transition when the driving strength is increased and reaches the threshold. Namely, for $\beta < \beta_{\text{thresh},b}$ the coupling parameter is exponentially suppressed with respect to $\nu = \Delta_b/\hbar\omega$. This result is favorable for Floquet engineering, as it tells us that for sufficiently low frequencies and not too strong driving, interband heating becomes very small. However, the predicted threshold is only valid as long as $M_{20}(t)$ is small compared to $\hbar\omega$ for $\beta = \beta_{\text{thresh},b}$. If this is not the case, we have to go beyond the rotating-wave approximation. This can be done using once more the degenerate perturbation theory in Floquet space, as we will do in the next chapter.

5.4.3. Multi-Photon Heating from Floquet Perturbation Theory

In this section we use degenerate perturbation theory in the Floquet space to estimate the effective coupling parameter $C_{(b,\nu)}(q)$ for the resonant ν-photon coupling of the states $|0q\rangle$ and $|bq\rangle$. We will first explicitly calculate the first effective coupling parameters for the transition to the second excited band since this is the most relevant heating channel at $q = 0$, where the condensate is often initialized in an experiment. Then we will derive the asymptotics for the general case and show that there is a cut-off in the driving strengths, below which interband excitations are suppressed exponentially for large ν.

As in the case of the shaken lattice, we define the perturbation in the extended Hilbert space is given by the operator

$$
\begin{aligned}
\langle\!\langle bqm'|\hat{V}_{\text{pert}}|bqm\rangle\!\rangle &= \langle\!\langle bqm'|(\hat{Q} - \hat{Q}_0)|bqm\rangle\!\rangle \qquad\qquad (5.4.60) \\
&= (1 - \delta_{m'm})\delta_{q'q}\langle b'q\|\hat{H}_{m'-m}(q)|bq\rangle.
\end{aligned}
$$

where the unperturbed quasienergy operator in this case takes the form

$$
\begin{aligned}
\langle\!\langle bqm'|\hat{Q}_0|bqm\rangle\!\rangle &= \delta_{m'm}\langle b'q'|(m\hbar\omega + \hat{H}_0')|bq\rangle \qquad\qquad (5.4.61) \\
&= \delta_{m'm}\delta_{q'q}\delta_{b'b}\big[m\hbar\omega + \varepsilon_b(q)\big].
\end{aligned}
$$

The unperturbed quasienergy $\varepsilon_{bm}(q)$ is thus given by the photonic energy $m\hbar\omega$ plus the static dispersion relation

$$
\varepsilon_{bm}(p) = m\hbar\omega + \varepsilon_b(p). \qquad\qquad (5.4.62)
$$

The relevant coupling matrix elements of the perturbation in the quasienergy operator change the photon number m by ± 1 or by ± 2 so that for $n > 2$ necessarily higher-order processes have to be taken into account in order to describe the coupling between $|0m\rangle\!\rangle$ and $|2(m-n)\rangle\!\rangle$. For this we assume that we do not hit any double-resonance so that the intermediate states do not have a different band index than b or b'. This assumption is justified since there are only few double-resonances in the case of the amplitude-modulated lattice, as we will demonstrate in Sec. 5.4.4. Double-resonances are discussed in App. C. Only with this assumption it is sufficient

that we have calculated the matrix elements of the quasienergy operator Q only at the ν-photon resonance.

For the single-photon resonance with $\nu = 1$, hence, both states are directly coupled by the matrix element (5.4.41), so that the coupling parameter reads

$$C_{(2,1)} = \langle\!\langle 2(m-1)|\hat{V}_{\text{pert}}|0m\rangle\!\rangle = \frac{\beta V_0 \mathcal{W}_b}{2}. \tag{5.4.63}$$

For the two-photon resonance with $\nu = 2$, we have two relevant contributions to the coupling parameter, namely

$$C_{(2,2)} = C_{(2,2)}^{(1)} + C_{(2,2)}^{(2)}. \tag{5.4.64}$$

The first contribution directly corresponds to the matrix element (5.4.42) describing a two-photon process,

$$C_{(2,2)}^{(1)} = \langle\!\langle 2(m-2)|\hat{V}_{\text{pert}}|0m\rangle\!\rangle = -\frac{\beta^2 V_0 X_b}{4}. \tag{5.4.65}$$

The second contribution stems from the second-order processes $|0m\rangle\!\rangle \to |2(m-1)\rangle\!\rangle \to |2(m-2)\rangle\!\rangle$, where both states are coupled via the energetically distant intermediate state $|2(m-1)\rangle\!\rangle$. The unperturbed quasienergy of this intermediate state, $\varepsilon_{2(m-1)} = n\hbar\omega + (m-1)\hbar\omega$, lies $\hbar\omega$ above the quasienergy $\varepsilon_{0m} = \varepsilon_{2(m-n)} = m\hbar\omega$ of the degenerate doublet. According to the rules of degenerate perturbation theory (see Eq. (5.3.24), or e.g., Ref. [57]), the effective coupling element is

$$
\begin{aligned}
C_{(2,2)}^{(2)} &= \frac{\langle\!\langle 2(m-2)|\hat{V}_{\text{pert}}|2(m-1)\rangle\!\rangle\langle\!\langle 2(m-1)|\hat{V}_{\text{pert}}|0m\rangle\!\rangle}{\varepsilon_{0m} - \varepsilon_{2(m-1)}} \\
&= -\frac{\beta^2 F V_0 \mathcal{W}_b}{8\hbar\omega}.
\end{aligned}
\tag{5.4.66}
$$

Let us finally consider the excitation process with $\nu = 3$. The coupling parameter is a combination of three contributions,

$$C_{(2,3)} = C_{(2,3)}^{(2)} + C_{(2,3)}^{(3a)} + C_{(2,3)}^{(3b)}. \tag{5.4.67}$$

The first contribution stems from the second-order process $|0m\rangle\!\rangle \to |2(m-2)\rangle\!\rangle \to |2(m-3)\rangle\!\rangle$. The intermediate state $|2(m-2)\rangle\!\rangle$ have a quasienergy lying $\hbar\omega$ above the degenerate doublet and the resulting coupling is given by

$$
\begin{aligned}
C_{(2,3)}^{(2)} &= \frac{\langle\!\langle 2(m-3)|\hat{V}_{\text{pert}}|2(m-2)\rangle\!\rangle\langle\!\langle 2(m-2)|\hat{V}_{\text{pert}}|0m\rangle\!\rangle}{\varepsilon_{0m} - \varepsilon_{2(m-2)}} \\
&= -\frac{\beta^3 \mathcal{F}_2 V_0 X_2}{4n\hbar\omega}.
\end{aligned}
\tag{5.4.68}
$$

The second contribution stems from the third-order processes $|0m\rangle\!\rangle \to |2(m-1)\rangle\!\rangle \to |0(m-1)\rangle\!\rangle \to |2(m-3)\rangle\!\rangle$. The quasienergies of both intermediate states $|2(m-1)\rangle\!\rangle$ and $|0(m-1)\rangle\!\rangle$ are separated by $2\hbar\omega$ and $-\hbar\omega$ from the degenerate doublet of states to be coupled. The matrix element is, thus, is roughly

$$
C_{(2,3)}^{(3a)} \approx \left(-i\frac{\beta V_0 \mathcal{W}_2}{2\nu}\right)^3 \frac{1}{(-2\hbar\omega)(\hbar\omega)} = -i\frac{\beta^3 V_0^3 \mathcal{W}_2^3}{432(\hbar\omega)^2}.
\tag{5.4.69}
$$

The third contribution stems from the third order process $|0m\rangle\!\rangle \to |2(m-1)\rangle\!\rangle \to |2(m-2)\rangle \to |2(m-3)\rangle\!\rangle$. The quasienergies of both intermediate states are separated by $2\hbar\omega$ and $\hbar\omega$ from the degenerate doublet. The corresponding coupling parameter is roughly

$$
C_{(2,3)}^{(3b)} \approx \left(\frac{i\beta\mathcal{F}_2}{2}\right)^2 \frac{-i\beta V_0 \mathcal{W}_2}{2\nu} \frac{1}{(-2\hbar\omega)(-\hbar\omega)} = i\frac{\beta^3 \mathcal{F}_2^2 V_0 \mathcal{W}_2}{32(\hbar\omega)^2}.
\tag{5.4.70}
$$

Extending the perturbative arguments used here to higher orders of the perturbation theory, one can estimate also the coupling parameters $C_{(2,\nu)}$ for multi-photon transitions with $\nu > 3$. The same approach can also be applied for transitions to the first excited band or higher lying bands. In leading order in the driving strengths β, we can again bring the coupling parameters into the very same form

$$
C_{(b,\nu)} = \beta B_{(b,\nu)}\left(\frac{\beta}{\beta_{(b,\nu)}}\right)^{\nu-1}
\tag{5.4.71}
$$

encountered already within the rotating-wave approximation (5.4.57) and (5.4.58). Here the coefficient $B_{(b,\nu)}$ sets the energy scale. Once more for the driving strength

β we find a threshold value, which we denote $\beta_{(b,\nu)}$. For a driving strength below the threshold, interband excitation processes are suppressed exponentially for large photon numbers $\nu = \Delta_b/(\hbar\omega)$, that is for low frequencies. While Eq. (5.4.71) is of the same form as the rotating-wave result from Sec. 5.4.2, the coefficient $B_{(b,\nu)}$ and the threshold value $\beta_{(b,\nu)}$ will generally be different.

Finally, let us estimate how $\beta_{(b,\nu)}$ scales when ν becomes large. For that purpose, the first quantity to be studied are the energy denominators of the perturbatively computed coupling parameters. They are given by the product of the quasienergy difference $\epsilon_{b_k m_k}(q)$ of intermediate states with respect to the quasienergy $\epsilon_{b_0 m_0}(q)$ of the degenerate doublet of states. Taking, for simplicity, a sequence of processes that lower the photon number in steps of one, these denominators provide a factor of

$$\frac{1}{(\nu-1)!(\hbar\omega)^{\nu-1}} \simeq \frac{1}{\sqrt{2\pi(\nu-1)}}\left(\frac{e}{(\nu-1)\hbar\omega}\right)^{(\nu-1)}, \qquad (5.4.72)$$

where we have again used Stirling's formula (5.4.56). This result indicates that the energy denominators contribute a factor of $\nu\hbar\omega/e = \Delta_b/e$ to $\beta_{(b,\nu)}$, which for fixed Δ_b is independent of ν. Similar results are obtained for sequences involving individual processes that lower the photon number in steps larger than one.[1] Apart from the energy denominators also the matrix elements contribute to $\beta_{(b,\nu)}$. In the present example of a lattice with modulated lattice depth, we must expect that the $1/\nu$-dependence of the matrix elements Eq. (5.4.41)-(5.4.45) leads to an increase of $\beta_{(b,\nu)}$ with ν. This effect is not captured by the rotating-wave approximation, which takes these matrix elements into account in linear order only. In order to systematically improve the result (5.4.57) and (5.4.58) obtained within the rotating-wave approximation, one can also start from the transformed Hamiltonian $\hat{H}''(q,t)$ given by Eq. (5.4.47). In this case we would recover the result (5.4.53) already in first order. Note that the coupling matrix element (5.4.53) contains infinite powers of the matrix element (5.4.40) [(5.4.43)] for even [odd] $b + b'$, while it is linear in the matrix elements (5.4.41) and (5.4.42 [(5.4.44) and (5.4.45)]. Transforming from

---

[1] One example is the case, where for an even value of ν we combine $\nu/2$ processes with matrix elements $\propto \beta^2$ that individually lower the photon number by two. In this case the energy denominator can take the form $(\nu-2)!!(\hbar\omega)^{\nu/2-1} = (\nu/2-1)!(2\hbar\omega)^{\nu/2-1} \simeq \sqrt{\pi(\nu-2)}[(\nu-2)\hbar\omega/e]^{\nu/2-1}$. It contributes a factor of $\sqrt{\Delta_b/e}$ to $\beta_{(b,\nu)}$, which is again independent of ν.

$\hat{H}'(q,t)$ to $\hat{H}''(q,t)$, thus, corresponds to a resummation of part of the perturbation series obtained for $\hat{H}'(q,t)$ to infinite order.

5.4.4. Quasienergy Spectrum

In this section we compute and illustrate the quasienergy spectrum of the amplitude-modulated lattice. We will describe the spectrum and compare it to the one obtained for the shaken lattice. The interpretation will be done in the next section. Introducing again plain waves (see Eq. (5.3.48)) with momenta $p = q + P2\pi/a, -\pi/a < q \le \pi/a, P \in \mathbb{Z}$ the Hamiltonian matrix takes the form

$$
H_{P,Q}(q,t) = E_R \left\{ \left[\frac{qa}{\pi} + 2P \right]^2 \delta_{P,Q} + \frac{V_0}{4} [1 + \beta \sin(\omega t)] \left(\delta_{P,Q+1} + \delta_{P,Q-1} \right) \right\}.
$$
(5.4.73)

where we, for convenience, factored out the recoil energy $E_R = \hbar^2 \pi^2 / 2ma^2$. With a momentum cut-off $|P| \le P^*$, Eq. (5.4.73) can be diagonalized for each quasimomentum q independently. The quasienergies are computed by solving and diagonalizing the monodromy operator $\mathcal{M}_T$. We choose $V_0 = 10 E_R$ as the lattice depth.

In Fig. 5.4.2 we plot the quasienergy spectrum of the amplitude-modulated lattice for $\hbar\omega = 8 E_R$, which lies close to the important transition to the second excited band between $\omega_{(2,1)}(q = 0, \beta = 0) = 7.856 E_R$ and $\omega_{(2,1)}(q = \pi, \beta = 0) = 10.955 E_R$, as a function of the quasimomentum q for increasing driving strength $\beta = 0, 0.1, 0.5, 1, 1.5, 2$. Note that it is difficult to compare the driving strengths β of the shaken lattice and β of the amplitude modulated lattice since the former is normalized by $\hbar\omega$ and also since the relation between the driving strengths and the resulting effective couplings strengths between the states are of very different nature. Whereas ground and first excited bands are well separated in quasienergy for $\beta = 0$, the second band is crossed close to $q = 0$. Already for a small driving strength of $\beta = 0.1$ this crossing opens and the bands hybridize. At the same time the first and the third excited band hybridize close to $q = \pm\pi/a$. For a larger driving strength the density of the Bloch band with index $b = 0$ distributes fairly over several Floquet states, indicating strong heating processes in a quantum quench scenario. In general the Floquet states increasingly deform for increasing β. Only the Bloch states with
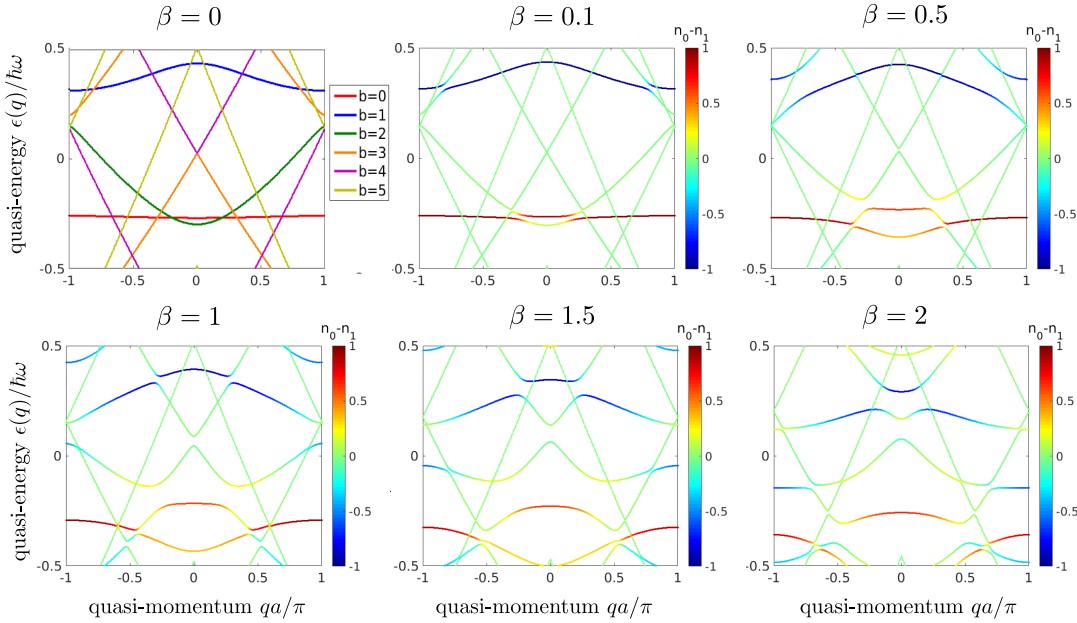
Figure 5.4.2.: Quasienergy spectrum of the amplitude-modulated lattice with shaking frequency $\hbar\omega = 8E_R$ close to the 1-photon resonance to the second excited band at $V_0 = 10E_R$ and varying driving strength β. The calculation was done in the subspace of the six lowest bands of the non-driven system and their continuiation in Floquet space, therfore at each quasimomentum six states are shown. The color code illustrates the projection of each state on the ground (red) and first excited (blue) state of the non-driven system.

index $b = 4$ and $b = 5$ do not mix with the other Bloch bands since their kinetic energy is so large that the lattice modulation hardly affects them.

In Fig. 5.4.3 we plot the quasienergies corresponding to the same Floquet states but as a function of β for $q = 0$ and $q = \pi/2a$. For $q = 0$ the Bloch states with $b = 0$ and $b = 2$ start close together at $\beta = 0$ and therefore mix already for small β. For $q = \pi/2a$ the states lie further apart in quasienergy and therefore start to mix only for larger β. Also here the Floquet state connected with the ground state at $\beta = 0$ passes two avoided crossings with the Floquet states stemming from the Bloch states with $b = 3$ and $b = 4$. This would be relevant in an adiabatic protocol, where a smooth switching-on of the driving strength would excite to these two Bloch states.

In Fig. 5.4.4 we plot the quasienergy spectrum of the amplitude-modulated lattice
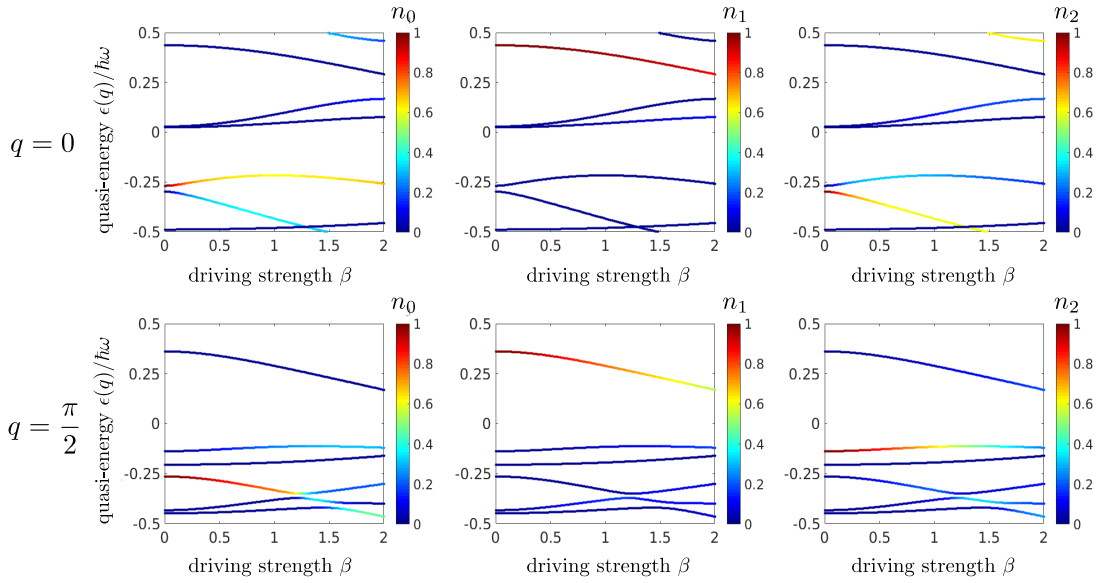
Figure 5.4.3.: Quasienergy spectrum of the Floquet states shown in Fig. 5.4.2 as a function of the driving strength β for $\hbar\omega = 8E_R$. From left to right the density of the Bloch states $b = 0, 1, 2$ is colored in red. Upper panel: at quasimomentum $q = 0$ where the coupling between bands with odd $b+b'$ vanishes completely. Lower panel: at quasimomentum $q = \frac{\pi}{2}$.

for $\hbar\omega = 5E_R$, close to the 1-photon resonance to the first excited band and the 2-photon resonance to the second excited band. Since the frequency is smaller, the photon number of most couplings is higher, making the couplings smaller in general. Apart from the 2-photon resonance with the first excited band for small β, however, it is very difficult to draw further information from these plot.

Finally we consider in Fig. 5.4.5 the quasienergy as a function of β for $\hbar\omega = 5E_R$. We observe that at $q = 0$, which is slightly off-resonant with respect to the transition between ground and second excited band, only for large driving strength β the Bloch bands with $b = 0$ and $b = 2$ mix. At the same time they do not couple to other bands, even for strong driving strengths $\beta \approx 2$ which implies that the lattice amplitude is modulated three times as high as the depth of the static lattice. At $q = \pi/2a$ the situation is different: Already for small β the Bloch states with $b = 0$ and $b = 1$, which lie very close together at $\beta = 0$, mix. For large β the density n_0 is distributed over three Floquet states. Again we see avoided crossings with Floquet
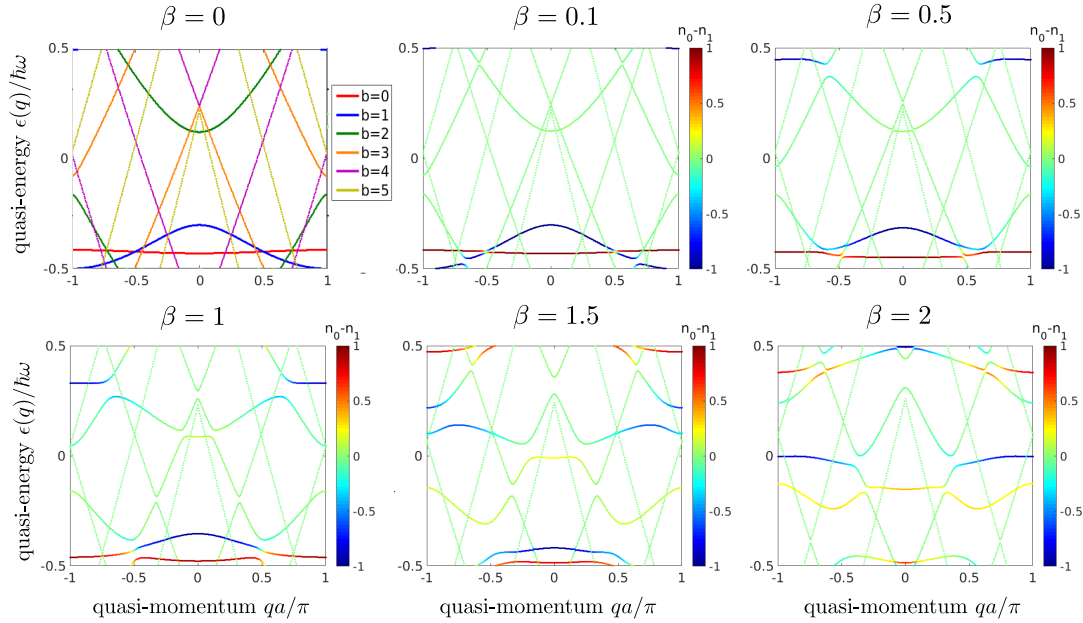
Figure 5.4.4.: Same plots as in Fig. 5.4.2 but with $\hbar\omega = 5E_R$, close to the 1-photon resonance to the first excited band and the 2-photon resonance to the second excited band.

states stemming from Bloch bands with high band index.

5.4.5. Numerical Simulation of Multi-Photon Heating Processes

Finally we will consider the numerical simulation of the amplitude-modulated lattice in the quench scenario and the respective heating plots that can be understood well with the analyical and numerical results from Sec. 5.4.1 - Sec. 5.4.4 and App. C. We compare the resonances to those of the shaken lattice.

To this end we integrate the time-dependent Schrödinger equation Eq. (2.1.2) over a time span of τ, starting from the initial $|0q\rangle$ with corresponding vector $u_{0Q}(q)$. In Fig. 5.4.6 a)-e) we plot the heating parameter h_τ as a function of both driving strength β and driving frequency $\hbar\omega$ within the range of the 1-photon resonance to the first excited band. Again we assign the respective multiphoton resonances (b, ν) via the resonance condition Eq. (5.4.32). The resonance lines do not shift
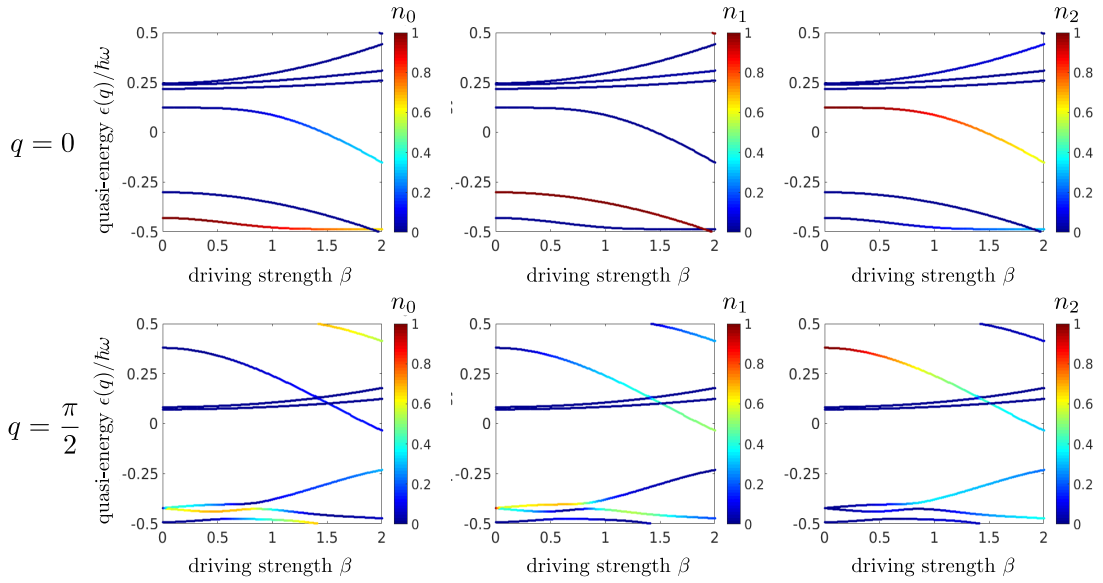
Figure 5.4.5.: Same figure as Fig. 5.4.3 but with $\hbar\omega = 5E_R$, close to the 1-photon resonance to the first excited band and the 2-photon resonance to the second excited band.

for increasing β, as in the shaken case, since the bands are not renormalized with Bessel functions. This happens only slightly if resonances repel each other. The resonances only shift with q where the resonance condition follows the dispersion relation of both states. Furthermore, the driving strength is not reparameterized by $\hbar\omega$. Therefore the width of the resonance (b, ν) is directly proportional to the effective coupling element $C_{(b,\nu)}$. Remember that the coupling from the ground state to bands with odd b is parameterized by a factor of $2\sin(qa)$, so it vanishes at the edges of the Brilloin zone at $q = 0$ and $q = \pi/a$, which explains the vanishing resonance lines at those quasimomenta. On the other hand, and in contrast to the shaken lattice, there is no such factor depending on the photon index ν. Therefore, resonance lines for even and odd ν are visible for all q and their thickness decreases monotoneosly for increasing ν for each band. Furthermore, we see that the resonance lines appear rather abruptly for a specific $\beta \approx \beta_{(b,\nu)}$, below which the heating is suppressed. This $\beta_{(b,\nu)}$ apparently increases with ν and can be identified with the threshold value that we predicted by the rotating-wave approximation and the Floquet perturbation theory.
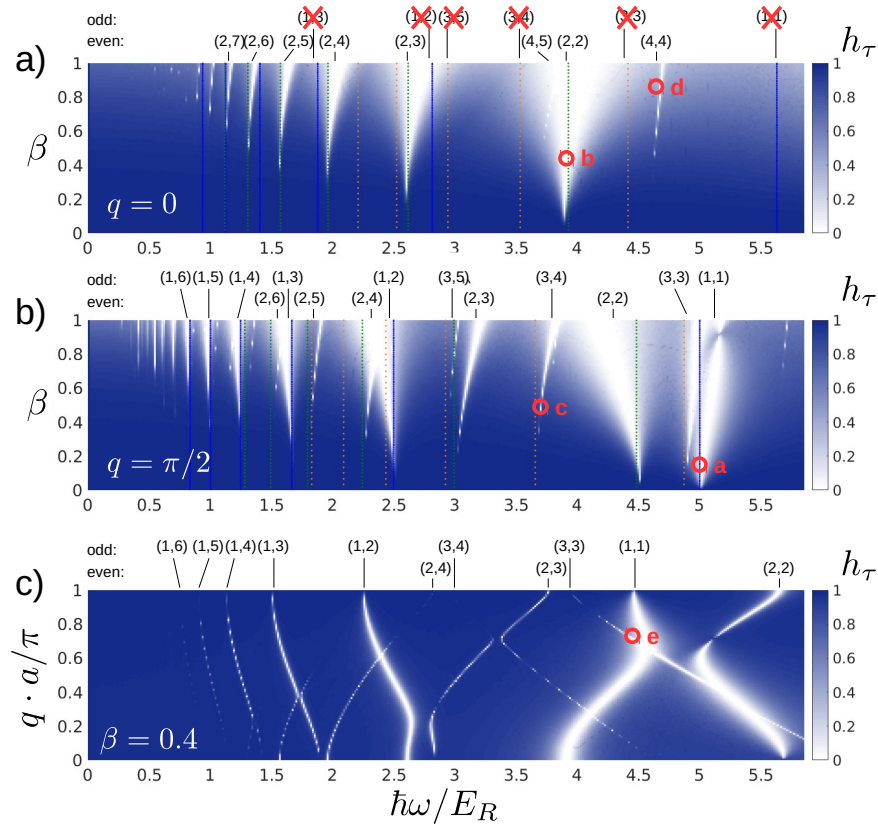
Figure 5.4.6.: Heating plot for the amplitude-modulated lattice: Minimum occupation of the ground state $\min_{\Delta t}[n_0(t)]$ during a time span of $\tau = 418/E_R$ (corresponding to 20ms for $E_R = 3.33 \cdot 2\pi\hbar\text{kHz}$), plotted versus driving frequency $\hbar\omega/E_R$ and driving amplitude β in a) for $q = 0$, in b) for $q = \pi/2$ and in c) versus quasimomentum q with $\beta = 0.4$. The lattice depth is again $V_0/E_R = 10$. Resonances corresponding to an ν-photon transition from band 0 to b are visible as white stripes and labeled by (b, ν). For the points marked by a, b, c, d and e the evolution of the probabilities $n_b(t)$ is depicted in panels a), b), c), d) and e) of Fig. 5.4.7, respectively. Above the plot we assign the respective resonances (b, ν) and cross out the forbidden resonances at $q = 0$.

Let us now compare the resonance lines with $b = 1$ and $b = 2$ for intermediate $0 < q < \pi/a$. Remember that in the amplitude modulated lattice the most dominant matrix element coupling the ground state to the first excited band is much smaller than the one to the second excited band, $W_{02}^{(0)} \approx 5 W_{01}^{(1)}$ at $V_0 = 10 E_R$, see Fig. 5.4.1. With the additional factor of $2\sin(qa)$, the direct (single-photon) coupling elements
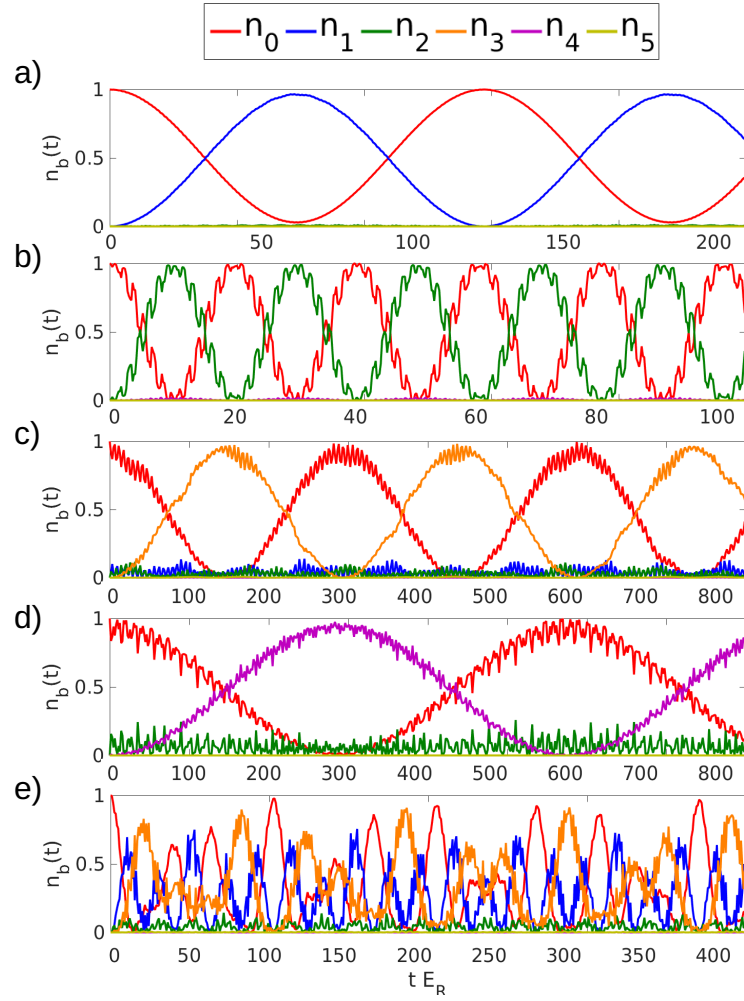
Figure 5.4.7.: Time evolution of the populations $n_b(t)$ of the six lowest bands. From top to bottom, the five plots correspond to the parameters marked by a, b, c, d and e in Fig. 5.4.6, respectively. The plotted time-span has been adapted to optimize visibility.

to the first excited band will be similar to that to the second excited band. However, the driving frequency suppresses the effective coupling for multiphoton transitions with $\nu > 1$, see Eq. (5.4.57)-(5.4.58) and Eq. (5.4.69)-(5.4.70). Therefore, the ν-photon resonance to the second excited band is additionally suppressed with respect to the resonance to the first excited band since the latter happens always at a lower frequencies. This is best visible for $q = \pi/2a$, where the $(2, \nu)$ resonances are
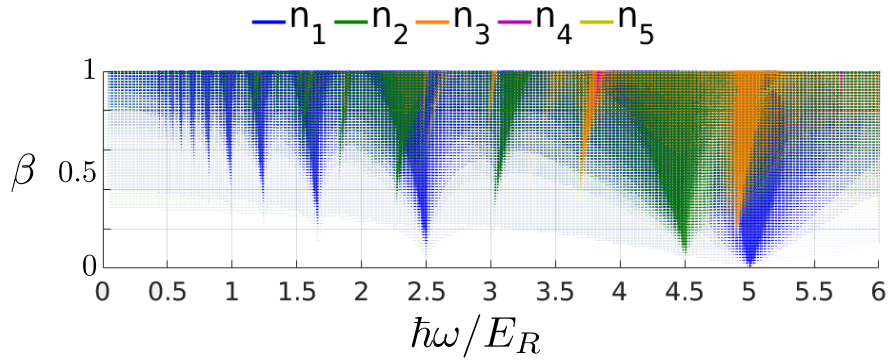
Figure 5.4.8.: Heating plot for $q = \pi/2a$ as in Fig. 5.4.6 b), where the transitions to the different Bloch bands are colorized. The color represents the Bloch band b, where the particle is excited to whereas the circle size illustrates the maximum occupation $\max_{t\in[b,\tau]} n_b(t)$ of the respective Bloch band b during the time span τ.

strong for $\nu = 2$ and $\nu = 3$ but fall off quickly with ν, whereas the $(1,\nu)$ resonances are visible even until $\nu = 9$.

In Fig. 5.4.6 f) we plot for fixed $\beta = 0.4$ the heating parameter h_τ as a function of $\hbar\omega$ and the quasimomentum q. Again we see that the resonances $(2,\nu)$ for $\nu > 1$ become weaker for increasing ω, as q is increased, shifting the resonances towards higher frequencies. This is best visible for the $(2,2)$ resonance and the $(2,4)$ and $(2,5$ resonances that are even invisible above a certain ω, since the threshold value $\beta_{(2,\nu)}$ has then become lower. Furthermore, we observe how resonances cross and avoid crossings. As explained in App. C, this depends on how the three involved states are coupled to each other. If the excited states belonging to the two resonances are coupled stronger to each other than to the ground state, they form an avoided crossing. If, otherwise, the strongest coupling involves the ground state, the resonances cross, but can still be deformed.

In Fig. 5.4.7 we plot the time evolution for four isolated multiphoton resonances to each of the first four excited bands, which are marked in Fig. 5.4.6. We observe very clean sinusoidal oscillations, which are rather difficult to find in the case of the shaken lattice. This enables us to extract easily the coupling strength from the time evolution and compare it to the estimations from the rotating-wave approximation and Floquet perturbation theory. From the evolution shown in Fig. 5.4.7(a), we can

extract the period $T^{\mathrm{sim}}_{(2,2)} \approx 2.56\,\mathrm{ms}$ for $\beta = 0.3$, $\hbar\omega = 3.9 E_R$, $q = 0$, $V_0/E_R = 10$ and $E_R = 3.33 \cdot 2\pi\hbar\mathrm{kHz}$. For these parameters, we obtain $\Delta_2 \approx 7.77 E_R$, $F(0) \approx 5.51 E_R$, $W \approx 0.345$, as well as $W' \approx 0.12$. Using the rotating-wave approximation for the coupling parameter (5.4.55) and (5.4.53), we obtain the estimate $T^{\mathrm{RW}}_{(2,2)} \approx 2.03\,\mathrm{ms}$ for the oscillation period, which lies about twenty percent below the numerically observed value. In Fig. 5.3.19 we plot the heating plot again with colorized Bloch band occupation $\max_{t\in[b,\tau]} n_b(t)$. In contrast to the shaken case, for the amplitude-modulated lattice the resonances most of the times are really isolated, i.e. only a single Bloch band is getting excited at a resonance.

6. Conclusion

In this work, we have presented two proposals where periodic driving of an optical lattice leads to interesting many-body phenomena in the strongly-interacting regime. In the first proposal, lattice shaking has been used to coherently couple the lowest two Bloch bands of a one-dimensional, dimerized lattice and thus orbital degrees of freedom have been opened. Thereby, an orbital driven phase transition from a Mott insulating to a superfluid ground state could be achieved by controlling the frequency of the shaking, and thus, the relative occupation of the two Bloch bands. In the second proposal, we have shown how interacting, one-dimensional lattice anyons can be simulated by bichromatically shaking a tilted cosine lattice, which contains strongly interacting bosons. We have demonstrated how real-space Friedel oscillations can be used as experimental signatures for anyonization, especially in a system of a small number of atoms using a quantum microscope. The feasibility of proposals has been tested via real-time simulations, thereby testing the robustness towards heating and the major approximations that were applied. The experimental realization of the proposals is thus promising and it would be very interesting to see the predicted phenomena be observed. Both, the coherent opening of orbital degrees of freedom, as well as the creation of one-dimensional lattice anyons in an optical lattice, have a rather fundamental character. Hence, they could trigger follow-up experiments, which explore more involved many-body quantum models with similar properties.

Furthermore, we have made a detailed analysis of single-particle, multi-photon heating processes in a shaken and in an amplitude-modulated lattice. As we have seen, there are several methods, including numerical and analytical ones, to analyze and estimate the position and the strength of resonances of particle transitions from the ground to excited Bloch states. Moreover, the excellent agreement with the experimental results in the shaken case, even for large photon numbers, as well

as the existence of resonances with high photon numbers with very clean two-state oscillations, suggest that multi-photon transitions in a driven lattice can possiby be used to accurately address and excite higher lying Bloch bands.

The results for single-particle, multi-photon heating processes are relevant for the case of driven systems with weakly interacting particles. However, the much more involved case of multi-photon heating in a driven system of strongly interacting particles has to be understood on a similar level. Accomplishing this, optimal parameter regimes for Floquet proposals with strongly interacting systems can be provided in a sufficient manner. An important step in this direction has been made by the experiment described in Ref. [237]. Herein, shaking-induced heating of interacting bosons was measured as a function of the shaking frequency, the driving amplitude and the interactiong strength. While the functional dependencies of the heating rates could be explained quite well with the help of many-body Floquet theory, other experimentally relevant effects like e.g. the depth of the trapping potential, multi-scattering of the bosons and the density of states of the whole atomic cloud, have also been shown to be relevant for the overall multi-photon heating rates.

All in all, the ever growing toolbox of Floquet theory, the successful realization of a range of proposals using driven lattices in the recent years, and the better comprehension of heating processes in these experiments, demonstrate how a periodic driving has become a standard tool in the field of quantum simulations with cold atoms, and it will help to understand many more phenomena of many-body quantum physics.

A. Implementation of Exact Diagonalization of the Two-Band Model

In this section we present one possibility to implement the diagonalization of the effective two-band Hubbard Hamiltonian (3.3.17). For the two-band bosonic chain we choose as basis an outer occupation-number basis that counts the particle occupation of each site and an inner occupation-number basis that locally counts the occupation of the orbital states. More specifically, each component of the outer occupation-number basis

$$|N_1, \ldots, N_j, \ldots, N_M\rangle = |N_1\rangle \otimes \ldots \otimes |N_j\rangle \otimes \ldots \otimes |N_M\rangle \qquad (A.0.1)$$

is not a scalar, but a vector from the inner basis

$$|N_j\rangle = \left(n_j^{(N_j,0)}, n_j^{(N_j-1,1)}, \ldots, n_j^{(0,N_j)}\right). \qquad (A.0.2)$$

Here $n_j^{(a,b)}$ gives the local amplitude of having a particles in orbital 0 and b particles in orbital 1 on site j with both adding up to the number of particles on site j in this state $a + b = N_j$. The outer state is then a tensor product of the inner basis. So, for example, on a system with $N = 6$ particles on $M = 4$ sites we find the state

$$|0, 3, 1, 2\rangle = n_1^{(0,0)} \otimes \left(n_2^{(3,0)}, n_2^{(2,1)}, n_2^{(1,2)}, n_2^{(0,3)}\right) \otimes \left(n_3^{(1,0)}, n_3^{(0,1)}\right) \otimes \left(n_4^{(20)}, n_4^{(11)}, n_4^{(02)}\right)$$

$$(A.0.3)$$

The outer occupation-number basis is numerated according to how much the particles are remote from the first site, starting with the state where they are all on the first site:

$$
\begin{aligned}
\psi_1 &= |N, 0, \ldots, 0\rangle \\
\psi_2 &= |N - 1, 1, 0, \ldots, 0\rangle \ldots \\
&\vdots \\
\psi_\alpha &= |N_1, \ldots, N_j, \ldots, N_M\rangle \ldots \\
&\vdots \\
\psi_{\mathcal{D}(M,N)} &= |0, \ldots, 0, N\rangle
\end{aligned}
$$

When constructing the Hamiltonian we have to know which of these states (or rather set of states) are connected via a tunnel process. While it is easy to construct from a state $|N_1, N_2, \ldots, N_M\rangle$ with index α the state that is connected via the tunneling process of a particle from site j to site $j + 1$

$$
|N_1, \ldots, N_j, N_{j+1}, \ldots, N_M\rangle \rightarrow |N_1, \ldots, N_j - 1, N_{j+1} + 1, \ldots, N_M\rangle, \qquad \text{(A.0.4)}
$$

it is not trivial to get the index β of such a state. This index is needed to put the respective tunneling term (which is a matrix in general) at the respective position α, β in the Hamiltonian. The formula that gives out the index of a given state for the indexing (A.0.4) is [238]

$$
f_\alpha(\{N\}) = \sum_{j=1}^{M} \Gamma\left(N - 1 - \sum_{i=1}^{j} N_i, M + 1 - i\right), \qquad \text{(A.0.5)}
$$

where

$$
\Gamma(M, N) = \binom{M + N - 1}{N} \qquad \text{(A.0.6)}
$$

counts the number of outer occupation-number states for a 1D lattice. Note that $\mathcal{D}(M, N) = \Gamma(2M, N)$. The local tunneling matrices have to be constructed for each combination of particle occupations N_j, N_{j+1} of two neighbouring sites, i.e.

$N_j + N_{j+1} = 1, \ldots N$. Also for the other terms in the Hamiltonian, like interaction and band coupling terms, local Hamiltonians depending on possible occupations $N_j = 1, \ldots N$ of a site are constructed. The full Hamiltonian is then constructed by a tensor product of these local Hamiltonians together, adding the tunneling terms and summing over all outer occupation-number states.

B. Relevance of the Bond Dimension in TEBD Calculations

Here we analyze how the accuracy of the numerical TEBD results, both real and imaginary time, depends on the bond dimension. The bond dimensions used in the simulation are limited by the large on-site state space, resulting from both the facts that we take into account up to three orbital states per site and that we are dealing with bosonic particles allowing for onsite occupation numbers larger than one. For the different numerical results, we will therefore show how the reults converges with respect to the bond dimensions, thereby justifying the choices of bond dimensions we have made.

In Fig. B.0.1 we demonstrate how the correlations shown in Fig. 3.5.7 behave if we reduce the bond dimension χ. A bond dimension of $\chi = 1$ disregards all two-particle correlations. For a bond dimension of $\chi = 2$, short-distance correlations are captured, though not very accurately. Long-distance correlations like $\chi_{\alpha\alpha}^8$ are disregarded though. In the rage $\chi = 10 \ldots 20$ we observe the correlations still alter considerably, especially the long-distance ones. The plots for higher bond dimensions ($\chi > 20$) can hardly be distinguished from each other.

A closer look at the converngence behavior in the transition region can be found in Fig. B.0.2 below. Here we plot the correlation functions of Fig. 3.5.7 directly with respect to the bond dimension, for different values of the detuning close to the transition.

Let us now illustrate how the results of our real-time simulations change with respect to the bond dimension. In Fig. 3.5.9 the preparation dynamics is investigated. In Fig. B.0.3 we compare the numerical results of Fig. 3.5.9 (for which $\chi = 24$ was used) with results for the lower bond dimension $\chi = 20$ and $\chi = 22$. Whereas the general adiabadicity is captured quite well for both bond dimensions, the
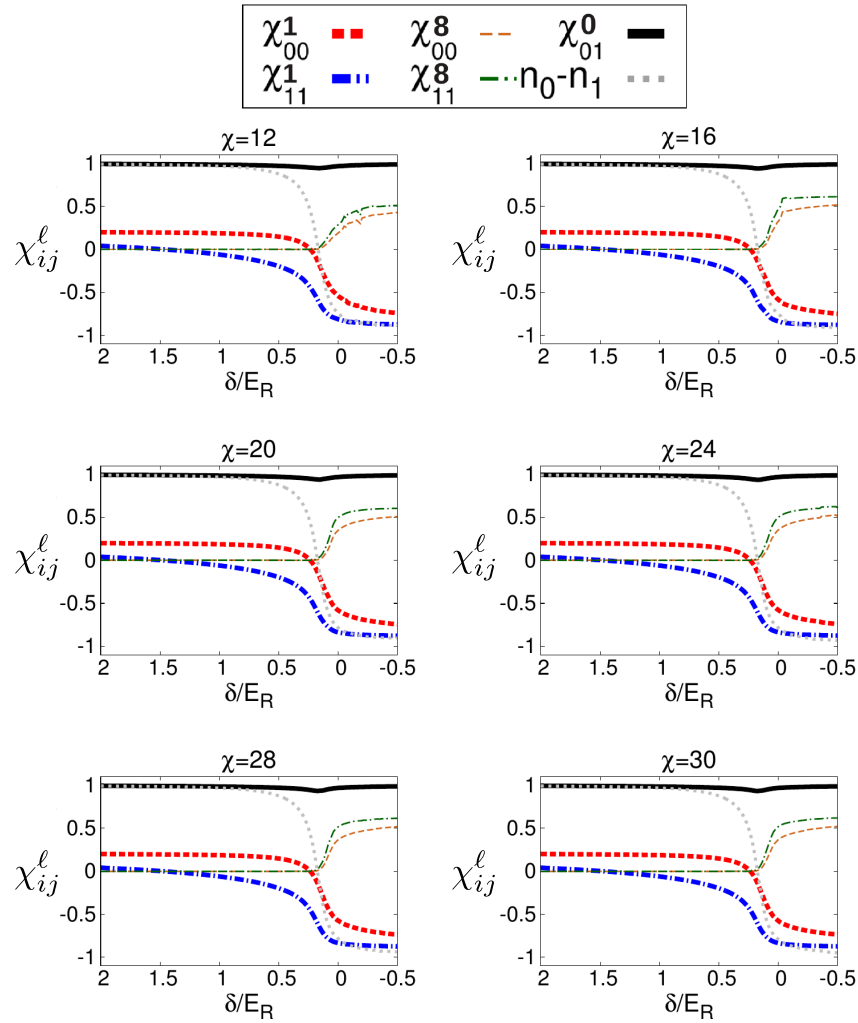
Figure B.0.1.: Correlations $\chi^\ell_{\alpha'\alpha} \equiv \langle \hat{b}^\dagger_{\alpha'\ell} \hat{b}_{\alpha 0} \rangle / \sqrt{n_{\alpha'} n_\alpha}$ as a function of δ for different bond dimensions χ for $V_0/E_R = 10$ (see Fig. 3.5.7).

expected Landau-Zeener oscialltions are only resolved for $\chi = 24$. The oscillations are expected to be smoother for even higher χ.

For imaginary TEBD, we could go even to $\chi = 28$ on the given system. Therefore, in Fig. B.0.4 we plot the overlap between the ground states of the two- and the three-band model comparing results obtained for bond dimesions $\chi = 20, 24, 28$. The curves obtained for the larger to bond dimensions are hardly distinguishable. Therefore we assume that going to a bond dimension of > 24 does not give any significant improvement of the accuracy of the numerical results.
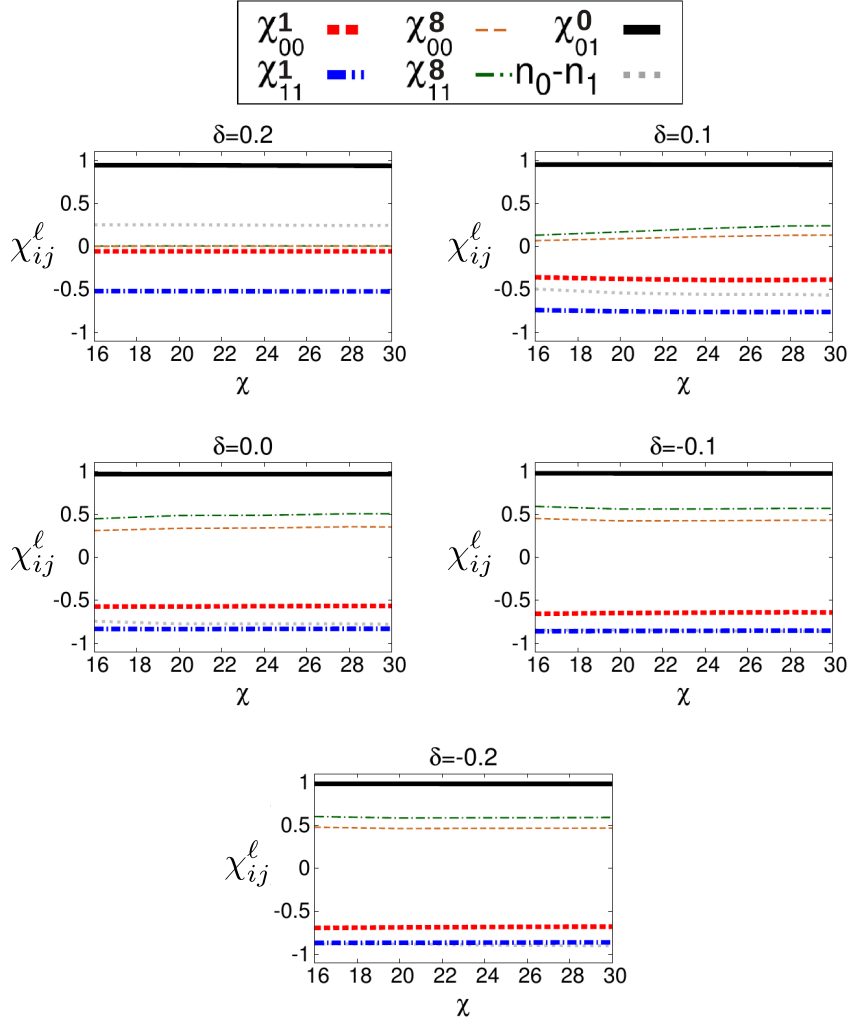
Figure B.0.2.: Correlations $\chi^{\ell}_{\alpha'\alpha} \equiv \langle \hat{b}^{\dagger}_{\alpha'\ell} \hat{b}_{\alpha 0} \rangle / \sqrt{n_{\alpha'} n_{\alpha}}$ as a function of the bond dimension χ at different δ close to the phase transition for $V_0/E_R = 10$ (see Fig. 3.5.7).
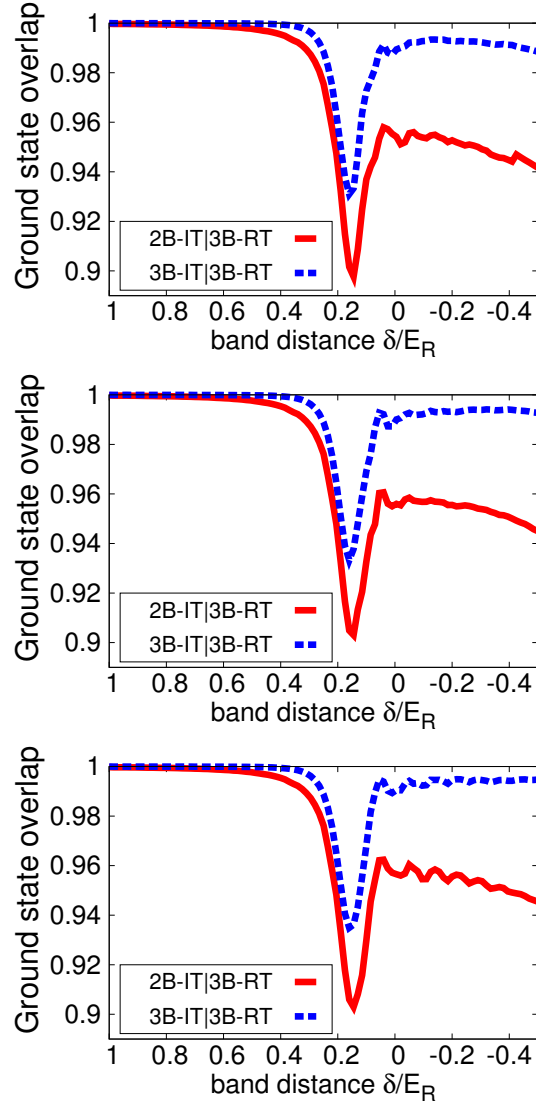
Figure B.0.3.: Inner products of ground states of three-band real time evolution with three- and two-band imaginary time evolved ground state for a linear decreasing of δ. Upper: bond dimension $\chi = 20$ Middle: $\chi = 22$ Lower: $\chi = 24$ (as in Fig. 3.5.9)
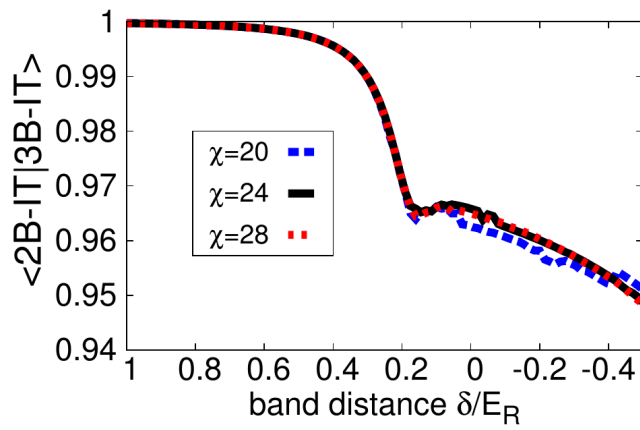
Figure B.0.4.: Inner product of the imaginary-time evolved ground state of three- and two-band models for a linear decreasing of δ (see Fig. 3.5.9 for bond dimension $\chi = 20, 24, 28$ ($\chi = 24$ in the main text).

C. Ground-State Dynamics of Few-State Systems

Here we analyze the time-dynamics for simple two- and three-state quantum systems. These systems describe simple and double resonances in periodically driven lattices and can explain their resonance spectrum. Therefore, we are especially interested in the occupation dynamics of the ground state and its minimal occupation.

C.1. The Rabi Problem for Two Coupled States

If a quantum system is effectively described by only two coupled states $|0\rangle$ ("ground state") and $|1\rangle$ ("excited state"), its Hamiltonian can be written as

$$\hat{H}^{\text{eff}} = \begin{pmatrix} 0 & C \\ C^* & \delta \end{pmatrix} \tag{C.1.1}$$

with coupling strength C and detuning δ. Diagonalizing this Hamiltonian results in the two eigenenergies

$$\epsilon_\pm = \frac{\delta \pm \sqrt{|2C|^2 + \delta^2}}{2} \tag{C.1.2}$$

for the eigenvectors

$$\begin{pmatrix} v_\pm^{(0)} \\ v_\pm^{(1)} \end{pmatrix} = \begin{pmatrix} C \\ \epsilon_\pm \end{pmatrix} \frac{1}{\sqrt{|C|^2 + \epsilon_\pm^2}} \tag{C.1.3}$$

where we used the notation $v_\pm^{(j)} = \langle j|\pm\rangle$, $j = 0, 1$. We are interested in the time evolution of the system that starts in the ground state $|0\rangle = v_+^{(0)}|+\rangle + v_-^{(0)}|-\rangle$ at $t = 0$

and then evolves in time as

$$|\psi(t)\rangle = v_+^{(0)} e^{-i\epsilon_+ t}|+\rangle + v_i^{(0)} e^{-i\epsilon_- t}|-\rangle. \qquad (C.1.4)$$

Consequently, if both states are coupled in perfect resonance $\delta = 0$, we find a perfect oscillation with frequency $\Omega_0 = |2C|$ between them,

$$n_0(t) = |\langle 0|\psi(t)\rangle|^2 = \cos^2\left(\frac{\Omega_0}{2}t\right), \quad n_1(t) = |\langle 1|\psi(t)\rangle|^2 = \sin^2\left(\frac{\Omega_0}{2}t\right). \qquad (C.1.5)$$

For finite detuning $\delta > 0$, we observe the time dynamics

$$n_0(t) = \frac{\Omega_0^2}{\Omega_\delta^2}\cos^2\left(\frac{\Omega_\delta}{2}t\right) + \left(1 - \frac{\Omega_\delta^2}{\Omega_0^2}\right), \quad n_1(t) = \frac{\Omega_0^2}{\Omega_\delta^2}\sin^2\left(\frac{\Omega_\delta}{2}t\right) \qquad (C.1.6)$$

with oscillation (Rabi) frequency

$$\Omega_\delta = \epsilon_+ - \epsilon_- = \sqrt{\Omega_0^2 + \delta^2}. \qquad (C.1.7)$$

Note that there is only an incomplete particle transfer. The ground state is not depleted anymore but its population has a non-zero minimum

$$\min_t[n_0(t)] = 1 - \frac{\Omega_0^2}{\Omega_\delta^2}. \qquad (C.1.8)$$

Both Eq. (C.1.7) and Eq. (C.1.6) are well-known but nevertheless important results, since these equations provide the relation between amplitude and frequency (including the detuning) of the periodic forcing on the one hand and coupling strength and detuning of the coupled states on the other hand.

C.2. Three-State Cascade

Next we want to discuss the case of three states $|0\rangle$, $|1\rangle$ and $|2\rangle$ that are coupled in a cascade, i.e. $|0\rangle$ is coupled to $|1\rangle$ with strength C_1 and $|1\rangle$ is coupled to $|2\rangle$ with strength C_2. This situation appears often in double resonances in the shaken

optical lattices, where the coupling between adjacent states is much stronger than between states more distant in energy. The Hamiltonian for a cascade can be written as

$$\hat{H}^{\text{eff}} = \begin{pmatrix} -\delta & C_1 & 0 \\ C_1^* & -\gamma & C_2 \\ 0 & C_2^* & \delta \end{pmatrix} \tag{C.2.1}$$

where we have chosen a parameterization for the detunings δ and γ that is motivated by a periodically driven system.

For non-vanishing coupling strengths C_i, we always have three distinct eigenvalues $\epsilon_- < \epsilon_X < \epsilon_+$ with eigenstates $|-\rangle, |X\rangle$ and $|+\rangle$. Again we use the notation $v_{i,X,+}^{(j)} = \langle j|-, X, +\rangle$, $j = 0, 1, 2$. Assuming again the initial condition $|\psi(t = 0)\rangle = |0\rangle$, the ground state-occupation dynamics is

$$n_0(t) = \left| |v_-^{(0)}|^2 e^{-i\epsilon_- t} + |v_X^{(0)}|^2 e^{-i\epsilon_X t} + |v_+^{(0)}|^2 e^{-i\epsilon_+ t} \right|^2 \tag{C.2.2}$$

resulting in three harmonics with frequencies $\epsilon_- - \epsilon_X$, $\epsilon_X - \epsilon_+$ and $\epsilon_+ - \epsilon_-$. The analytical expressions of eigenvalues and eigenstates of Hamiltonian (C.2.1) are in general complicated. However, for $\delta = 0$ the solution does have a simple form. Therefore we first consider special cases and in the end make statements about the general case.

If $\delta = 0$, the eigenvalues take the form

$$\epsilon_\pm = -\frac{\gamma}{2} \pm \frac{1}{2}\sqrt{\gamma^2 + \Omega_1^2 + \Omega_2^2} = \frac{-\gamma \pm \Omega_\gamma}{2}, \quad \epsilon_X = 0 \tag{C.2.3}$$

with the notation $\Omega_1 = |2C_1|$, $\Omega_2 = |2C_2|$ and $\Omega_\gamma = \sqrt{\gamma^2 + \Omega_1^2 + \Omega_2^2}$. The corresponding eigenstates read

$$\begin{pmatrix} v_\pm^{(0)} \\ v_\pm^{(1)} \\ v_\pm^{(2)} \end{pmatrix} = \frac{1}{\sqrt{\Omega_0^2 + \epsilon_\pm^2}} \begin{pmatrix} \Omega_1 \\ \epsilon_\pm \\ \Omega_2 \end{pmatrix}, \quad \begin{pmatrix} v_X^{(0)} \\ v_X^{(1)} \\ v_X^{(2)} \end{pmatrix} = \frac{1}{\Omega_0} \begin{pmatrix} \Omega_2 \\ 0 \\ -\Omega_1 \end{pmatrix} \tag{C.2.4}$$

where $\Omega_0 = \sqrt{\Omega_1^2 + \Omega_2^2}$. Note that if $C_2 > C_1$, from $|v_-^{(0)}|^2 + |v_X^{(0)}|^2 + |v_+^{(0)}|^2 = 1$ it follows that

$$|v_X^{(0)}|^2 > |v_-^{(0)}|^2 + |v_+^{(0)}|^2 \tag{C.2.5}$$

implying also $v_X^{(0)} > v_\pm^{(0)}$.

We will consider further special cases to obtain an overview how the parameters C_1, C_2, δ and γ determine the dynamics of the ground state. It is instructive to start with the most simple case.

Case A: $\gamma = \delta = 0$ and $C_1 = C_2 = C$

In this situation both states are in resonance and are coupled equally. The resulting dynamics is simply

$$n_0^A(t) = \cos^4\left(\frac{\Omega_0}{2}t\right) \tag{C.2.6}$$

with the oscillation frequency $\Omega_0 = \sqrt{2}|2C|$. Here we find a perfect ground state depletion, i.e.

$$\min_t\left[n_0^A(t)\right] = 0. \tag{C.2.7}$$

Case B: $\gamma = \delta = 0$, $C_1 \neq C_2$

For a double resonance with different coupling strengths we find

$$n_0^B(t) \quad = \quad \frac{\Omega_1^4}{\Omega_0^4}\left[\cos\left(\frac{\Omega_0}{2}t\right) + \frac{\Omega_2^2}{\Omega_1^2}\right]^2. \tag{C.2.8}$$

Here, both harmonics add constructively so that again the oscillation frequency is Ω_0. Note that for $C_1 > C_2$, the term in the bracket takes negative and positive values and thus also zeros. This leads to ground state depletion. If $C_1 < C_2$, the bracket is always positive and the minimum of the ground state occupation is finite.

In total we have

$$\min_t[n_0^B(t)] = \max\left\{0, \left(\frac{\Omega_2^2 - \Omega_1^2}{\Omega_2^2 + \Omega_1^2}\right)\right\}^2. \tag{C.2.9}$$

Case C: $\gamma = \delta \gg |C_i|$

In this case states $|0\rangle$ and state $|1\rangle$ are in resonance whereas state $|2\rangle$ is largely off-resonant. This sitation is a simple two state-resonance and was treated in the previous section with time evolution

$$n_0^C(t) = \cos^2\left(\frac{\Omega_1}{2}t\right), \ n_1(t) = |\langle 1|\psi(t)\rangle|^2 = \sin^2\left(\frac{\Omega_1}{2}t\right). \tag{C.2.10}$$

Case D: $\gamma \gg |C_i|, \ \delta = 0$

In this case, states $|0\rangle$ and $|2\rangle$ are in resonance but state $|1\rangle$ is separated by a large energy gap of size γ. Since $\gamma \gg 0$, we have that $|\epsilon_-| \gg |\epsilon_+| \approx 0$ and thus $v_+^{(0)} \gg v_-^{(0)} \approx 0$. Therefore, in the time evolution is mainly governed by $|+\rangle$ and $|X\rangle$ and can be approximated by

$$n_0^D(t) = \frac{4\Omega_1^2\Omega_2^2}{\Omega_0^4}\cos^2\left(\frac{\epsilon_+}{2}t\right) + \left(\frac{\Omega_2^2 - \Omega_1^2}{\Omega_2^2 + \Omega_1^2}\right)^2, \ n_2^D(t) = \frac{4\Omega_1^2\Omega_2^2}{\Omega_0^4}\sin^2\left(\frac{\epsilon_+}{2}t\right). \tag{C.2.11}$$

where the system is oscillating mainly between states $|0\rangle$ and $|2\rangle$. Therefore, the situation resembles a two-state system (see previous section) but with an oscillation slowed down by the energy barrier γ and a ground state minimum occupation of

$$\min_t[n_0^D(t)] = \left(\frac{\Omega_2^2 - \Omega_1^2}{\Omega_2^2 + \Omega_1^2}\right)^2. \tag{C.2.12}$$

Case E: $\delta = 0$

While we cannot make any statement for $C_1 > C_2$, for $|C_2| > |C_1|$ we have that

$$\min_t[n_0^E(t)] > 0 \tag{C.2.13}$$

The reason is from the inequality (C.2.5) it follows that the constant in the bracket of the time evolution is larger than the prefactor of the oscillating terms altogether.

General Cascade

For the general three-state cascade with finite δ and γ, we will not give analytic values for the amplitude and frequency of the oscillation. However, we can ask the question if there is a finite value for $\pm|\delta|$ that leads to full ground state depletion in the case $|C_2| > |C_1|$, in contrast to the case $\delta = 0$ when the ground state is always partly occupied (Case E).

Without loss of generality, we can always choose $\epsilon_- = -\epsilon_X$ by adding a constant to all eigenvalues. For $\delta = 0$ we have (see Eq. (C.2.5)) that $|v_X| > |v_+|, |v_-|$, whereas for $\delta \to +\infty$, we obviously have $|v_-^{(0)}| = 1$ and $v_+^{(0)} = v_X^{(0)} = 0$. Since the eigenvalues change smoothly with δ, there must be a value $\delta > 0$ for which $|v_-^{(0)}| = |v_X^{(0)}| > |v_+^{(0)}|$ resulting in the dynamics

$$n_0(t) = 4|v_-^{(0)}|^4 \left| \cos(t\epsilon_-) + \frac{|v_+^{(0)}|^2}{2|v_-^{(0)}|^2} e^{-it\epsilon_+} \right|^2 \qquad \text{(C.2.14)}$$

Since $\frac{|v_+^{(0)}|^2}{2|v_-^{(0)}|^2} < 1$ in this situation, we conclude that

$$\lim_{t \to \infty} \min_t \left[n_0(t) \right] = 0. \qquad \text{(C.2.15)}$$

Furthermore, since $\epsilon_+ > \pm\epsilon_-$ it follows that the minimum approaches zero rather quickly. The same arguement holds for $\delta < 0$ for which $|v_+^{(0)}| = |v_X^{(0)}| > |v_-^{(0)}|$ giving another resonance. Thus we confirmed that for $|C_2| > |C_1|$ we see an avoided crossing. To illustrate this result, in Fig. C.2.1 we plot the minimum of the time dynamics as a function of both detunings δ and γ for $C_1 = 4$ and $C_2 = 9$. The avoided crossing, as well as the two resonance lines corresponding to cases C (diagonal resonance) and D (vertical resonance) are clearly visible. Each of the cases B-E is marked in the plot. For these cases and case A ($C_1 = C_2 = 4$) and a case in the shifted resonance (case F) we show in Fig. C.2.2 the time evolution of the state occupations $n_b(t)$. Note that we have only presented results about $n_0(t)$ and not about the occupations of the other two states. The avoided resonance crossing can be called
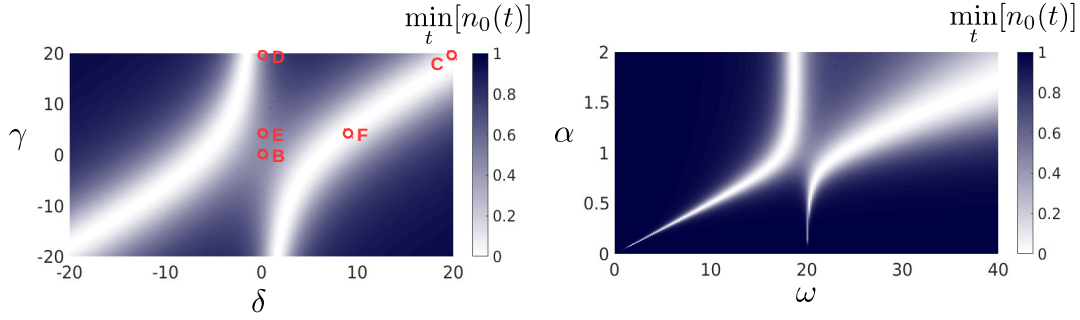
Figure C.2.1.: a) Resonance plot in the δ-γ-parameter space in the (dimensionless) three-state model with fixed coupling $C_1 = 4$ and $C_2 = 9$. The cases B-E described in this section and a shifted resonance (Case F) are marked. Their time dynamics is plotted in Fig.C.2.2b) The same plot but with renormalized couplings C_1 and C_2, mirroring the situation and format that we encounter in a shaken lattice.
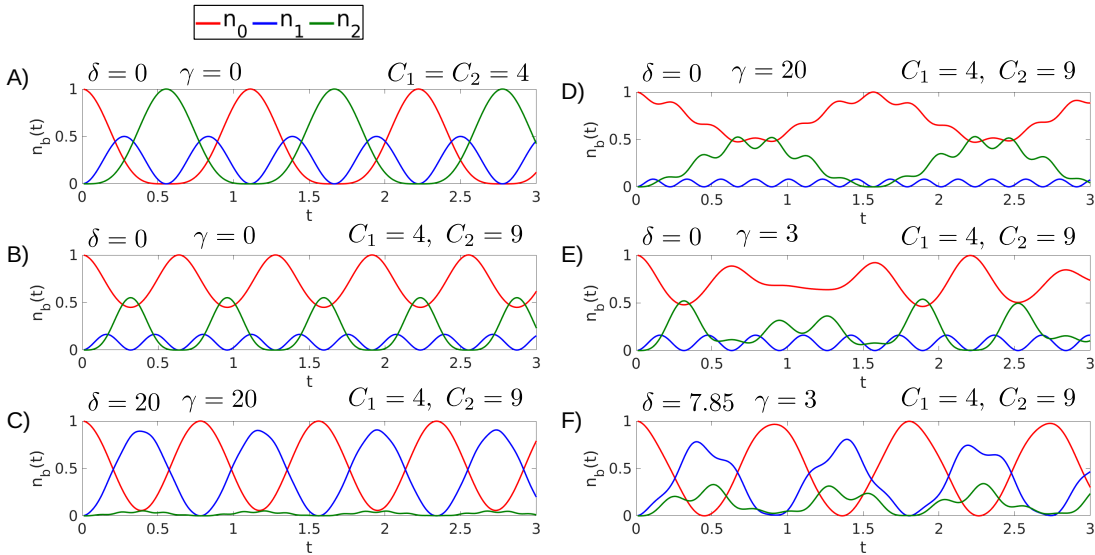

Figure C.2.2.: Examples of the time dynamics in the three-state models for the cases A-E and the case of a shifted resonance where $|v_-| = |v_X|$ (case F). Whereas for cases A-D the frequency and amplitude of the ground-state oscillation have a simple analytical form, they can always be calculated numerically by diagonalizing the corresponding 3-by-3 matrix.

an Autler–Townes splitting (see Refs. [239, 240]). In the standard Autler-Townes effect, the states $|1\rangle$ and $|2\rangle$ are resonantly coupled such that the quasienergies
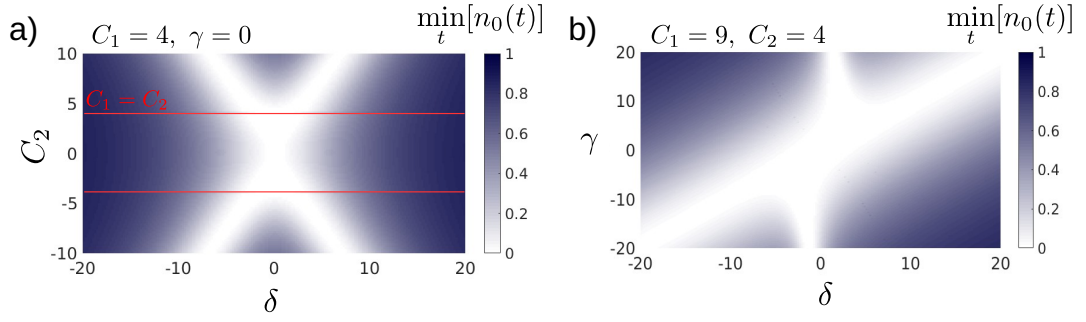
Figure C.2.3.: a) Resonance plot for varying C_2 and δ. If $|C_2| < |C_1|$, the avoided crossing at $\delta = 0$ is closed. b) In the δ-γ-parameter space for fixed $C_1 > C_2$ we confirm the resonance crossing.

split. This splitting is then observed spectroscopically with a different field from the initial state $|0\rangle$ which is energetically well seperated from states $|1\rangle$ and $|2\rangle$. For this energy separation both transitions can be treated independently such that the problem can be reduced to the Rabi problem. In our case though, the states are coupled by the same driving field and all states are on the same energy scale. Therefore, one has to solve the full 3-by-3 matrix. However, for $|C_2| > |C_1|$ we can understand the avoided crossing like in the Autler-Townes effect, such that states $|1\rangle$ and $|2\rangle$ form an avoided crossing that is spectroscopically probed by state $|0\rangle$. To illustrate the situation that we encounter in a shaken lattice, we further assume that a) the resonance condition depends on the coupling strength and b) the plotted coupling strength is normalized by the frequency ω that leads to the detuning $\delta = \omega - \omega_0$. To this end, we parameterize $C_1 = \alpha C_1^{(0)} \omega / \omega_0$, $C_2 = \alpha C_2^{(0)} \omega / \omega_0$ and $\gamma = -\omega_0(\alpha - 0.5)$. In Fig. C.2.1 we plot for $\omega_0 = 20$, $C_1^{(0)} = 4$ and $C_2^{(0)} = 9$ the minimum of the oscillation. From the construction, the couling strengths get stronger (resonances get broader) if one moves upwards or rightwards in the plot. Finally, let us examine the variation of the coupling strengths C_1 and C_2. In the upper plot Fig. C.2.3 a) we show the minimum of $n_0(t)$ when C_2 and δ are varied, keeping $\gamma = 0$ and $C_1 = 4$ fixed. We see that for $|C_2| < |C_1|$ the avoided crossing around $\delta = 0$ vanishes, as we have predicted in case B. To illustrate this in the parameter space related to the periodic driving, we plot in Fig. C.2.3 b) the oscillation minimum as a function of α and ω. We see that the two resonances really cross.
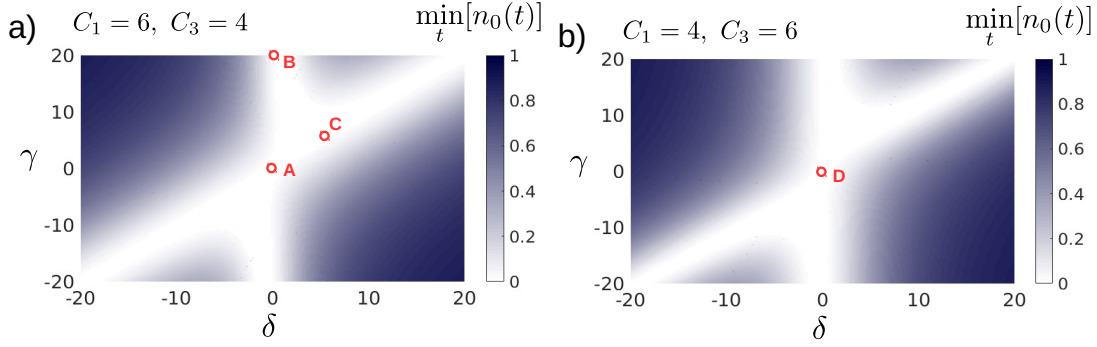
Figure C.3.1.: Resonance plot for varying δ and γ in the V-type three-level system. a) $C_1 = 6$ and $C_3 = 4$. b) $C_1 = 4$ and $C_3 = 6$. In both cases we do not see an avoided crossing. For marked δ- and γ-pairs (A-D) we plot the time-dynamics in Fig. C.3.2.
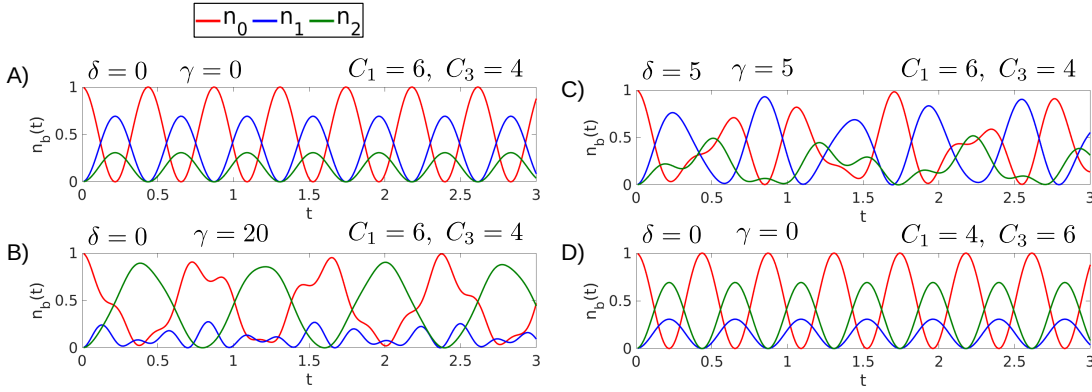

Figure C.3.2.: Time-dynamics for marked δ- and γ-pairs (A-D) from Fig. C.3.1. If $C_1 > C_3$ the oscillation of the ground state $|0\rangle$ is stronger to state $|1\rangle$ than to state $|2\rangle$ and vice versa.

C.3. Three-State V-type

Here we will also shortly discuss the case of a double-resonance, where the ground state $|0\rangle$ is coupled simultaneously to two states $|1\rangle$ (with strength C_1) and $|2\rangle$ (with strength C_3) higher lying in energy, resulting in the Hamiltonian

$$\hat{H}^{\text{eff}} = \begin{pmatrix} -\delta & C_1 & C_3 \\ C_1^* & -\gamma & 0 \\ C_3^* & 0 & \delta \end{pmatrix} \tag{C.3.1}$$

This case is called V-type and it is specially relevant in the resonance spectrum of the amplitude-modulated lattice, where the ground state is coupled to the first and second excited state with similar strength for some q. Except discussing special cases we will directly look at the resonance plot that turns out to be simpler than in the cascade-type. In Fig C.3.1 we plot again the minimum in the ground state dynamics as a function of δ and γ, a) for $C_1 > C_3$ and b) for $C_1 < C_3$. In both cases the resonances cross non-avoided, though being slightly deformed at the crossing. This finding can be understood intuitively since both excited states are for all C_1 and C_3 fully "accessible" from the ground state. Nevertheless, the dynamics at the crossing of the resonances will be more complex than any simple combination of the Rabi-oscillations stemming from the individual resonances. This is confirmed in Fig. C.3.2, where we plot some special pairs of δ and γ from Fig. C.3.1. If $C_1 > C_3$ the oscillation of the ground state $|0\rangle$ is stronger to state $|1\rangle$ than to state $|2\rangle$ and vice versa. Only if one state becomes largly off-resonant, the dynamics returns to a simple sine-like oscilattion, as can be seen in case B).

C.4. Three-State General Case

Finally, we want to discuss what happens if both $C_2 > 0$ and $C_3 > 0$ such that the Hamiltonian takes the form

$$\hat{H}^{\text{eff}} = \begin{pmatrix} -\delta & C_1 & C_3 \\ C_1^* & -\gamma & C_2 \\ C_3^* & C_2 & \delta \end{pmatrix}. \tag{C.4.1}$$

We consider the case $|C_2| > |C_1|$, which is the common case in periodically driven lattices and also since for $|C_2| < |C_1|$ we can expect from Sec. C.2 and Sec. C.3 that the resonance lines simply cross. In Fig. C.4.1 a) we plot the resonance plot varying δ and γ for a small $C_3 = 5$. We see that the avoided crossing is still there and that there is additionally a point where one of the resonances even vanishes. In Fig. C.4.1 b) we keep $\gamma = 0$ fixed and vary C_3. The avoided crossing vanishes at the point where $|C_3| > |C_2|$. Therefore, we see that the Autler-Townes splitting only emerges if both, $|C_2| > |C_1|$ and $|C_2| > |C_3|$. This is the main result of this section.
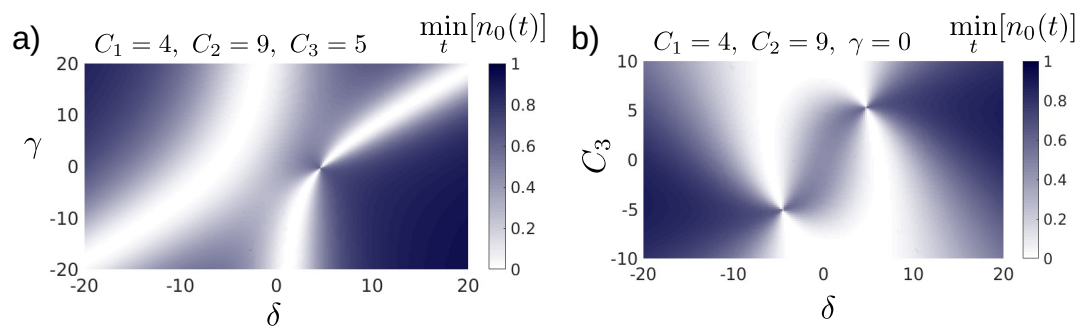
Figure C.4.1.: a) Resonance plot for varying δ and γ for the general system if $|C_1|, |C_3| < |C_2|$. b) Resonance plot for varying C_3 and δ if $|C_1| < |C_2|$ and $\gamma = 0$.

183

Acknowledgements

Publication List

[1] A. Faribault, O. El Araby, C. Sträter, and V. Gritsev, "Gaudin models solver based on the correspondence between Bethe ansatz and ordinary differential equations," *Phys. Rev. B*, vol. 83, p. 235124, Jun 2011.

[2] C. Sträter, O. Tsyplyatyev, and A. Faribault, "Nonequilibrum dynamics in the strongly excited inhomogeneous Dicke model," *Phys. Rev. B*, vol. 86, p. 195101, Nov 2012.

[3] C. Sträter and A. Eckardt, "Orbital-driven melting of a bosonic Mott insulator in a shaken optical lattice," *Phys. Rev. A*, vol. 91, p. 053602, May 2015.

[4] M. Weinberg, C. Ölschläger, C. Sträter, S. Prelle, A. Eckardt, K. Sengstock, and J. Simonet, "Multiphoton interband excitations of quantum gases in driven optical lattices," *Phys. Rev. A*, vol. 92, p. 043621, Oct 2015.

[5] C. Sträter and A. Eckardt, "Interband heating processes in a periodically driven optical lattice," *Zeitschrift für Naturforschung A*, vol. 71, pp. 909–920, Sep 2016.

[6] C. Sträter, S. C. L. Srivastava, and A. Eckardt, "Floquet Realization and Signatures of One-Dimensional Anyons in an Optical Lattice," *Phys. Rev. Lett.*, vol. 117, p. 205303, Nov 2016.

[7] E. Anisimovas, M. Račiūnas, C. Sträter, A. Eckardt, I. B. Spielman, and G. Juzeliūnas, "Semisynthetic zigzag optical lattice for ultracold bosons," *Phys. Rev. A*, vol. 94, p. 063632, Dec 2016.

[8] M. Reitter, J. Näger, K. Wintersperger, C. Sträter, I. Bloch, A. Eckardt, and U. Schneider, "Interaction Dependent Heating and Atom Loss in a Periodically Driven Optical Lattice," *Phys. Rev. Lett.*, vol. 119, p. 200402, Nov 2017.

Versicherung

Hiermit versichere ich, dass ich die vorliegende Arbeit ohne unzulässige Hilfe Dritter und ohne Benutzung anderer als der angegebenen Hilfsmittel angefertigt habe; die aus fremden Quellen direkt oder indirekt übernommenen Gedanken sind als solche kenntlich gemacht. Die Arbeit wurde bisher weder im Inland noch im Ausland in gleicher oder ähnlicher Form einer anderen Prüfungsbehörde vorgelegt. Diese Arbeit wurde unter der wissenschaftlichen Betreuung von Prof. Dr. Roland Ketzmerick am Max-Planck-Institut für Physik komplexer Systeme in Dresden angefertigt. Ich erkläre hiermit, dass keine früheren erfolglosen Promotionsverfahren stattgefunden haben. Ich erkenne die Promotionsordnung der Fakultät für Mathematik und Naturwissenschaften der Technische Universität Dresden an.

Dresden, January 2, 2018

Bibliography

[1] M. H. Anderson, J. R. Ensher, M. R. Matthews, C. E. Wieman, and E. A. Cornell, "Observation of Bose-Einstein condensation in a dilute atomic vapor," *Science*, vol. 269, p. 198, 1995.

[2] C. C. Bradley, C. A. Sackett, J. J. Tollet, and R. G. Hulet, "Observation of Bose-Einstein condensation in a dilute atomic vapor," *Phys. Rev. Lett.*, vol. 75, p. 1687, 1995.

[3] K. B. Davis, M. O. Mewes, M. R. Andrews, N. J. van Druten, D. S. Durfee, D. M. Kurn, and W. Ketterle, "Bose-Einstein condensation in a gas of sodium atoms," *Phys. Rev. Lett.*, vol. 75, p. 3969, 1995.

[4] S. Bose, "Plancks Gesetz und Lichtquantenhypothese," *Zeitschrift für Physik*, vol. 26, pp. 178–181, Dec. 1924.

[5] A. Einstein, "Quantentheorie des einatomigen idealen Gases," *Sitz. Ber. Preuss. Akad. Wiss.*, vol. 22, p. 261, 1924.

[6] I. Bloch, J. Dalibard, and W. Zwerger, "Many-Body Physics with Ultracold Gases," *Rev. Mod. Phys.*, vol. 80, p. 885, 2008.

[7] R. P. Feynman, "Simulating Physics with Computers," *Int. J. Theor. Phys.*, vol. 21, p. 467, 1982.

[8] I. Bloch, J. Dalibard, and S. Nascimbène, "Quantum simulations with ultracold quantum gases," *Nat. Phys.*, vol. 8, p. 267, 2012.

[9] J. Eisert, M. Friesdorf, and C. Gogolin, "Quantum many-body systems out of equilibrium," *Nat. Phys.*, vol. 11, no. 2, pp. 124–130, 2015.

[10] W. Zwerger, *The BCS-BEC crossover and the unitary Fermi gas*, vol. 836. Springer Science & Business Media, 2011.

[11] J. Hubbard, "Electron Correlations in Narrow Energy Bands," *Proceedings of the Royal Society of London Series A*, vol. 276, pp. 238–257, Nov. 1963.

[12] P. W. Shor, "Algorithms for quantum computation: Discrete logarithms and factoring," in *Foundations of Computer Science, 1994 Proceedings., 35th Annual Symposium on*, pp. 124–134, IEEE, 1994.

[13] L. K. Grover, "A fast quantum mechanical algorithm for database search," in *Proceedings of the twenty-eighth annual ACM symposium on Theory of computing*, pp. 212–219, ACM, 1996.

[14] N. Poli, F.-Y. Wang, M. G. Tarallo, A. Alberti, M. Prevedelli, and G. M. Tino, "Precision Measurement of Gravity with Cold Atoms in an Optical Lattice and Comparison with a Classical Gravimeter," *Phys. Rev. Lett.*, vol. 106, p. 038501, Jan 2011.

[15] M. Takamoto, F.-L. Hong, R. Higashi, and H. Katori, "An optical lattice clock," *Nature*, vol. 435, no. 7040, pp. 321–324, 2005.

[16] S. Chu, "Cold atoms and quantum control," *Nature*, vol. 416, no. 6877, pp. 206–210, 2002.

[17] W. Ketterle and M. W. Zwierlein, "Making, probing and understanding ultracold Fermi gases," *arXiv*, vol. cond-mat, p. 0801.2500, 2008.

[18] M. Lewenstein, L. Santos, M. A. Baranov, and H. Fehrmann, "Atomic Bose-Fermi mixtures in an optical lattice," *Phys. Rev. Lett.*, vol. 92, p. 050401, 2004.

[19] K. Günter, T. Stöfferle, H. Moritz, M. Köhl, and T. Esslinger, "Bose-Fermi Mixtures in a Three-Dimensional Optical Lattice," *Phys. Rev. Lett.*, vol. 96, p. 180402, 2006.

[20] W. S. Bakr, J. I. Gillen, A. Peng, S. Foelling, and M. Greiner, "Quantum Gas Microscope detecting single atoms in a Hubbard regime optical lattice," *Nature*, vol. 462, p. 74, 2009.

[21] J. F. Sherson, C. Weitenberg, M. Endres, M. Cheneau, I. Bloch, and S. Kuhr, "Single-atom-resolved fluorescence imaging of an atomic Mott insulator," *Nature*, vol. 467, no. 7311, pp. 68–72, 2010.

[22] F. Dalfovo, S. Giorgini, L. P. Pitaevskii, and S. Stringari, "Theory of Bose-Einstein condensation in trapped gases," *Rev. Mod. Phys.*, vol. 71, pp. 463–512, Apr 1999.

[23] A. J. Leggett, "Bose-Einstein condensation in the alkali gases: Some fundamental concepts," *Rev. Mod. Phys.*, vol. 73, p. 307, 2001.

[24] C. J. Pethick and H. Smith, *Bose-Einstein Condensation in Dilute Gases*. Cambridge UK: Cambridge University Press, 2002.

[25] L. Pitaevskii and S. Stringari, *Bose-Einstein Condensation*. Oxford New York: Oxford Science Publications, 2003.

[26] M. R. Andrews, C. Townsend, H. J. Miesner, D. S. Durfee, D. M. Kurn, and W. Ketterle, "Observation of Interference Between Two Bose Condensates," *Science*, vol. 275, p. 637, 1997.

[27] I. Bloch, T. W. Hänsch, and T. Esslinger, "Measurement of the spatial coherence of a trapped Bose gas at the phase transition," *Nature*, vol. 403, no. 6766, pp. 166–170, 2000.

[28] M. R. Matthews, B. P. Anderson, P. C. Haljan, D. S. Hall, C. E. Wieman, and E. A. Cornell, "Vortices in a Bose-Einstein Condensate," *Phys. Rev. Lett.*, vol. 83, p. 2498, 1999.

[29] K. W. Madison, F. Chevy, W. Wohlleben, and J. Dalibard, "Vortex Formation in a Stired Bose-Einstein-Condensate," *Phys. Rev. Lett.*, vol. 84, p. 806, 2000.

[30] J. R. Abo-Shaeer, C. Raman, J. M. Vogels, and W. Ketterle, "Observation of Vortex Lattices in Bose-Einstein Condensates," *Science*, vol. 292, p. 476, 2001.

[31] L. Pitaevskii, "Vortex lines in an imperfect Bose gas," *Sov. Phys. JETP*, vol. 13, no. 2, pp. 451–454, 1961.

[32] E. P. Gross, "Hydrodynamics of a superfluid condensate," *Journal of Mathematical Physics*, vol. 4, no. 2, pp. 195–207, 1963.

[33] N. N. Bogoliubov, "On the theory of superfluidity," *J. Phys. (USSR)*, vol. 11, p. 23, 1947. reprinted in: D. Pines, *The Many-Body Problem* (W.A. Benjamin, New York, 1961), p. 292.

[34] D. Jaksch, C. Bruder, J. I. Cirac, C. W. Gardiner, and P. Zoller, "Cold Bosonic Atoms in Optical Lattices," *Phys. Rev. Lett.*, vol. 81, p. 3108, 1998.

[35] M. Greiner, O. Mandel, T. Esslinger, T. W. Hänsch, and I. Bloch, "Quantum phase transition from a superfluid to a Mott isolator in a gas of ultracold atoms," *Nature*, vol. 415, p. 39, 2002.

[36] T. Kinoshita, T. Wenger, and D. S. Weiss, "Observation of a One-Dimensional Tonks-Girardeau Gas," *Science*, vol. 305, p. 1125, 2004.

[37] Z. Hadzibabic, P. Krüger, M. Cheneau, B. Battelier, and J. Dalibard, "Berezinskii–Kosterlitz–Thouless crossover in a trapped atomic gas," *Nature*, vol. 441, no. 7097, pp. 1118–1121, 2006.

[38] H. Stoof, M. Houbiers, C. Sackett, and R. Hulet, "Superfluidity of spin-polarized 6 Li," *Phys. Rev. Lett.*, vol. 76, no. 1, p. 10, 1996.

[39] S. Inouye, M. R. Andrews, J. Stenger, H. J. Miesner, D. M. Stamper-Kurn, and W. Ketterle, "Observation of Feshbach resonances in a Bose-Einstein condensate," *Nature*, vol. 392, p. 151, 1998.

[40] P. Courteille, R. S. Freeland, D. J. Heinzen, F. A. van Abeelen, and B. J. Verhaar, "Observation of a Feshbach Resonance in Cold Atom Scattering," *Phys. Rev. Lett.*, vol. 81, p. 69, 1998.

[41] T. Lahaye, T. Koch, B. Fröhlich, M. Fattori, J. Metz, A. Griesmaier, S. Giovanazzi, and T. Pfau, "Strong dipolar effects in a quantum ferrofluid," *Nature*, vol. 448, no. 7154, pp. 672–675, 2007.

[42] M. Bartenstein, A. Altmeyer, S. Riedl, S. Jochim, C. Chin, J. H. Denschlag, and R. Grimm, "Collective Excitations of a Degenerate Gas at the BEC-BCS Crossover," *Phys. Rev. Lett.*, vol. 92, p. 203201, May 2004.

[43] T. Bourdel, L. Khaykovich, J. Cubizolles, J. Zhang, F. Chevy, M. Teichmann, L. Tarruell, S. Kokkelmans, and C. Salomon, "Experimental study of the BEC-BCS crossover region in lithium 6," *Phys. Rev. Lett.*, vol. 93, no. 5, p. 050401, 2004.

[44] M. W. Zwierlein, C. A. Stan, C. H. Schunck, S. M. F. Raupach, A. J. Kerman, and W. Ketterle, "Condensation of Pairs of Fermionic Atoms near a Feshbach Resonance," *Phys. Rev. Lett.*, vol. 92, p. 120403, 2004.

[45] L. Tarruell, D. Greif, T. Uehlinger, G. Jotzu, and T. Esslinger, "Creating, moving and merging Dirac points with a Fermi gas in a tunable honeycomb lattice," *Nature*, vol. 483, pp. 302–305, Mar. 2012.

[46] A. K. Geim and K. S. Novoselov, "The rise of graphene," *Nature materials*, vol. 6, no. 3, pp. 183–191, 2007.

[47] N. W. Ashcroft and N. D. Mermin, *Festkörperphysik*. München Wien: Oldenbourg Verlag, 2001.

[48] S. R. White, "Density matrix formulation for quantum renormalization groups," *Phys. Rev. Lett.*, vol. 69, pp. 2863–2866, Nov 1992.

[49] U. Schollwöck, "The density-matrix renormalization group," *Rev. Mod. Phys.*, vol. 77, p. 259, 2005.

[50] G. Vidal, "Efficient Classical Simulation of Slightly Entangled Quantum Computations," *Phys. Rev. Lett.*, vol. 91, p. 147902, Oct 2003.

[51] G. Vidal, "Efficient Simulation of One-Dimensional Quantum Many-Body Systems," *Phys. Rev. Lett.*, vol. 93, p. 040502, Jul 2004.

[52] U. Schollwöck, "The density-matrix renormalization group in the age of matrix product states," *Annals of Physics*, vol. 326, no. 1, pp. 96–192, 2011.

[53] M. Suzuki, *Quantum Monte Carlo methods in condensed matter physics*. World scientific, 1993.

[54] R. Bishop, "An overview of coupled cluster theory and its applications in physics," *Theoretica chimica acta*, vol. 80, no. 2-3, pp. 95–148, 1991.

[55] A. Eckardt, "Colloquium: Atomic quantum gases in periodically driven optical lattices," *Rev. Mod. Phys.*, vol. 89, p. 011004, Mar 2017.

[56] G. Floquet, "Sur les équations différentielles linéaires à coefficients périodiques," in *Annales scientifiques de l'École normale supérieure*, vol. 12, pp. 47–88, 1883.

[57] A. Eckardt and E. Anisimovas, "High-frequency approximation for periodically driven quantum systems from a Floquet-space perspective," *New J. Phys.*, vol. 17, p. 093039, 2015.

[58] F. Meinert, M. J. Mark, K. Lauber, A. J. Daley, and H.-C. Nägerl, "Floquet Engineering of Correlated Tunneling in the Bose-Hubbard Model with Ultracold Atoms," *Phys. Rev. Lett.*, vol. 116, p. 205301, May 2016.

[59] A. Rapp, X. Deng, and L. Santos, "Ultracold Lattice Gases with Periodically Modulated Interactions," *Phys. Rev. Lett.*, vol. 109, p. 203005, Nov 2012.

[60] S. Greschner, G. Sun, D. Poletti, and L. Santos, "Density-Dependent Synthetic Gauge Fields Using Periodically Modulated Interactions," *Phys. Rev. Lett.*, vol. 113, p. 215303, Nov 2014.

[61] G. Wirth, M. Ölschläger, and A. Hemmerich, "Evidence for orbital superfluidity in the P-band of a bipartite optical square lattice," *Nat. Phys.*, vol. 7, p. 147, 2011.

[62] J. Struck, C. Ölschläger, M. Weinberg, P. Hauke, J. Simonet, A. Eckardt, M. Lewenstein, K. Sengstock, and P. Windpassinger, "Tunable Gauge Poten-

tial for Neutral and Spinless Particles in Driven Optical Lattices," *Phys. Rev. Lett.*, vol. 108, p. 225304, May 2012.

[63] H. Lignier, C. Sias, D. Ciampini, Y. Singh, A. Zenesini, O. Morsch, and E. Arimondo, "Dynamical Control of Matter-Wave Tunneling in Periodic Potentials," *Phys. Rev. Lett.*, vol. 99, p. 220403, 2007.

[64] A. Eckardt, M. Holthaus, H. Lignier, A. Zenesini, D. Ciampini, O. Morsch, and E. Arimondo, "Exploring dynamic localization with a Bose-Einstein condensate," *Phys. Rev. A*, vol. 79, p. 013611, 2009.

[65] C. E. Creffield, F. Sols, D. Ciampini, O. Morsch, and E. Arimondo, "Expansion of matter waves in static and driven periodic potentials," *Phys. Rev. A*, vol. 82, p. 035601, 2010.

[66] A. Zenesini, H. Lignier, D. Ciampini, O. Morsch, and E. Arimondo, "Coherent control of dressed matter waves," *Phys. Rev. Lett.*, vol. 102, p. 100403, 2009.

[67] A. Eckardt, C. Weiss, and M. Holthaus, "Superfluid-Insulator Transition in a Periodically Driven Optical Lattice," *Phys. Rev. Lett.*, vol. 95, p. 260404, 2005.

[68] A. Eckardt, T. Jinasundera, C. Weiss, and M. Holthaus, "Analog of Photon-Assisted Tunneling in a Bose-Einstein Condensate," *Phys. Rev. Lett.*, vol. 95, p. 200401, 2005.

[69] A. Eckardt and M. Holthaus, "AC-induced superfluidity," *EPL*, vol. 80, p. 50004, 2007.

[70] V. V. Ivanov, A. Alberti, M. Schioppo, G. Ferrari, M. Artoni, M. L. Chiofalo, and G. M. Tino, "Coherent Delocalization of Atomic Wave Packets in Driven Lattice Potentials," *Phys. Rev. Lett.*, vol. 100, p. 043602, 2008.

[71] C. Sias, H. Lignier, Y. Singh, A. Zenesini, D. Ciampini, O. Morsch, and E. Arimondo, "Observation of photon-assisted tunneling in optical lattices," *Phys. Rev. Lett.*, vol. 100, p. 040404, 2008.

[72] Alberti, V. V. Ivanov, G. M. Tino, and G. Ferrari, "Engineering the quantum transport of atomic wavefunctions over macroscopic distances," *Nat. Phys.*, vol. 5, p. 547, 2009.

[73] M. Aidelsburger, M. Atala, S. Nascimbène, S. Trotzky, Y.-A. Chen, and I. Bloch, "Experimental Realization of Strong Effective Magnetic Fields in an Optical Lattice," *Phys. Rev. Lett.*, vol. 107, p. 255301, Dec 2011.

[74] R. Ma, M. E. Tai, P. M. Preiss, W. S. Bakr, J. Simon, and M. Greiner, "Photon-Assisted Tunneling in a Biased Strongly Correlated Bose Gas," *Phys. Rev. Lett.*, vol. 107, p. 095301, Aug 2011.

[75] Y.-A. Chen, S. Nascimbène, M. Aidelsburger, M. Atala, S. Trotzky, and I. Bloch, "Controlling Correlated Tunneling and Superexchange Interactions with ac-Driven Optical Lattices," *Phys. Rev. Lett.*, vol. 107, p. 210405, Nov 2011.

[76] S. Greschner, L. Santos, and D. Poletti, "Exploring Unconventional Hubbard Models with Doubly Modulated Lattice Gases," *Phys. Rev. Lett.*, vol. 113, p. 183002, Oct 2014.

[77] L. Cardarelli, S. Greschner, and L. Santos, "Engineering interactions and anyon statistics by multicolor lattice-depth modulations," *Phys. Rev. A*, vol. 94, p. 023615, Aug 2016.

[78] D. Jaksch and P. Zoller, "Creation of effective magnetic fields in optical lattices: the Hofstadter butterfly for cold neutral atoms," *New J. Phys.*, vol. 5, no. 1, p. 56, 2003.

[79] A. R. Kolovsky, "Creating artificial magnetic fields for cold atoms by photon-assisted tunneling," *EPL*, vol. 93, p. 20003, 2011.

[80] J. Struck, M. Weinberg, C. Ölschläger, P. Windpassinger, J. Simonet, K. Sengstock, R. Höppner, P. Hauke, A. Eckardt, M. Lewenstein, and L. Mathey, "Engineering Ising-XY spin models in a triangular lattice via tunable artificial gauge fields," *Nat. Phys.*, vol. 9, p. 738, 2013.

[81] M. Aidelsburger, M. Atala, M. Lohse, J. T. Barreiro, B. Paredes, and I. Bloch, "Realization of the Hofstadter Hamiltonian with ultracold atoms in optical lattices," *Phys. Rev. Lett.*, vol. 111, p. 185301, 2013.

[82] H. Miyake, G. A. Siviloglou, C. J. Kennedy, W. C. Burton, and W. Ketterle, "Realizing the Harper Hamiltonian with Laser-Assisted Tunneling in Optical Lattices," *Phys. Rev. Lett.*, vol. 111, p. 185302, Oct 2013.

[83] M. Atala, M. Aidelsburger, M. Lohse, J. T. Barreiro, B. Paredes, and I. Bloch, "Observation of chiral currents with ultracold atoms in bosonic ladders," *Nat. Phys.*, vol. 10, p. 588, 2014.

[84] C. J. Kennedy, W. C. Burton, W. C. Chung, and W. Ketterle, "Observation of Bose-Einstein condensation in a strong synthetic magnetic field," *Nat. Phys.*, vol. 11, p. 859, 2015.

[85] P. Hauke, O. Tieleman, A. Celi, C. Ölschläger, J. Simonet, J. Struck, M. Weinberg, P. Windpassinger, K. Sengstock, M. Lewenstein, and A. Eckardt, "Non-Abelian Gauge Fields and Topological Insulators in Shaken Optical Lattices," *Phys. Rev. Lett.*, vol. 109, p. 145301, Oct 2012.

[86] G. Jotzu, M. Messer, T. U. Rémi Desbuquois, Martin Lebrat, D. Greif, and T. Esslinger, "Experimental realization of the topological Haldane model with ultracold fermions," *Nature*, vol. 515, p. 237, 2014.

[87] M. Aidelsburger, M. Lohse, C. Schweizer, M. Atala, J. T. Barreiro, S. Nascimbène, N. R. Cooper, I. Bloch, and N. Goldman, "Measuring the Chern number of Hofstadter bands with ultracold bosonic atoms," *Nauture Physics*, vol. 1, p. 162, 2015.

[88] N. Fläschner, B. Rem, M. Tarnowski, D. Vogel, D.-S. Lühmann, K. Sengstock, and C. Weitenberg, "Experimental reconstruction of the Berry curvature in a Floquet Bloch band," *Science*, vol. 352, no. 6289, pp. 1091–1094, 2016.

[89] M. Z. Hasan and C. L. Kane, "Colloquium," *Rev. Mod. Phys.*, vol. 82, pp. 3045–3067, Nov 2010.

[90] A. Eckardt, P. Hauke, P. Soltan-Panahi, C. Becker, K. Sengstock, and M. Lewenstein, "Frustrated quantum antiferromagnetism with ultracold bosons in a triangular lattice," *EPL*, vol. 89, p. 10010, 2010.

[91] J. Struck, C. Ölschläger, R. Le Targat, P. Soltan-Panahi, A. Eckardt, M. Lewenstein, P. Windpassinger, and K. Sengstock, "Quantum Simulation of Frustrated Classical Magnetism in Triangular Optical Lattices," *Science*, vol. 333, p. 996, 2011.

[92] N. Gemelke, E. Sarajlic, Y. Bidel, S. Hong, and S. Chu, "Parametric Amplification of Matter Waves in Periodically Translated Optical Lattices," *Phys. Rev. Lett.*, vol. 95, p. 170404, 2005.

[93] C. V. Parker, L.-C. Ha, and C. Chin, "Direct observation of effective ferromagnetic domains of cold atoms in a shaken optical lattice," *Nat. Phys.*, vol. 9, p. 769, 2013.

[94] L.-C. Ha, L. W. Clark, C. V. Parker, B. M. Anderson, and C. Chin, "Roton-Maxon Excitation Spectrum of Bose Condensates in a Shaken Optical Lattice," *Phys. Rev. Lett.*, vol. 114, p. 055301, Feb 2015.

[95] P. Cheinet, S. Trotyky, M. Feld, U. Schnorrberger, M. Moreno-Cardoner, S. Fölling, and I. Bloch, "Counting Atoms Using Interaction Blockade in an Optical Lattice," *Phys. Rev. Lett.*, vol. 101, p. 090404, 2008.

[96] W. S. Bakr, P. M. Preiss, M. E. Tai, R. Ma, J. Simon, and M. Greiner, "Orbital excitation blockade and algorithmic cooling in quantum gases," *Nature*, vol. 480, no. 7378, p. 500, 2011.

[97] A. Daley, J. Taylor, S. Diehl, M. Baranov, and P. Zoller, "Atomic three-body loss as a dynamical three-body interaction," *Phys. Rev. Lett.*, vol. 102, no. 4, p. 040402, 2009.

[98] P. Johnson, E. Tiesinga, J. Porto, and C. Williams, "Effective three-body interactions of neutral bosons in optical lattices," *New J. Phys.*, vol. 11, no. 9, p. 093022, 2009.

[99] A. Lazarides, A. Das, and R. Moessner, "Equilibrium states of generic quantum systems subject to periodic driving," *Phys. Rev. E*, vol. 90, p. 012110, Jul 2014.

[100] L. D'Alessio and M. Rigol, "Long-time Behavior of Isolated Periodically Driven Interacting Lattice Systems," *Phys. Rev. X*, vol. 4, p. 041048, Dec 2014.

[101] C. Sträter and A. Eckardt, "Orbital-driven melting of a bosonic Mott insulator in a shaken optical lattice," *Phys. Rev. A*, vol. 91, p. 053602, May 2015.

[102] T. Keilmann, S. Lanzmich, I. McCulloch, and M. Roncaglia, "Statistically induced phase transitions and anyons in 1D optical lattices," *Nat. Comm.*, vol. 2, p. 361, 2011.

[103] S. Greschner and L. Santos, "Anyon Hubbard Model in One-Dimensional Optical Lattices," *Phys. Rev. Lett.*, vol. 115, p. 053002, Jul 2015.

[104] C. Sträter, S. C. L. Srivastava, and A. Eckardt, "Floquet Realization and Signatures of One-Dimensional Anyons in an Optical Lattice," *Phys. Rev. Lett.*, vol. 117, p. 205303, Nov 2016.

[105] M. Weinberg, C. Ölschläger, C. Sträter, S. Prelle, A. Eckardt, K. Sengstock, and J. Simonet, "Multiphoton interband excitations of quantum gases in driven optical lattices," *Phys. Rev. A*, vol. 92, p. 043621, Oct 2015.

[106] C. Sträter and A. Eckardt, "Interband heating processes in a periodically driven optical lattice," *Zeitschrift für Naturforschung A*, vol. 71, pp. 909–920, Sep 2016.

[107] F. Bloch, "Über die Quantenmechanik der Elektronen in Kristallgittern," *Zeitschrift für Physik*, vol. 52, pp. 555–600, 1929.

[108] H. Sambe, "Steady States and Quasienergies of a Quantum-Mechanical System in an Oscillating Field," *Phys. Rev. A*, vol. 7, p. 6, 1973.

[109] J. H. Shirley, "Solution of the Schrödinger Equation with a Hamiltonian Periodic in Time," *Phys. Rev.*, vol. 138, p. B979, 1965.

[110] L. Mandel and E. Wolf, *Optical Coherence and Quantum Optics*. Cambridge, New York, Melbourne: Cambridge University Press, 1995.

[111] N. Goldman and J. Dalibard, "Periodically Driven Quantum Systems: Effective Hamiltonians and Engineered Gauge Fields," *Phys. Rev. X*, vol. 4, p. 031027, Aug 2014.

[112] N. Goldman, J. Dalibard, M. Aidelsburger, and N. R. Cooper, "Periodically driven quantum matter: The case of resonant modulations," *Phys. Rev. A*, vol. 91, p. 033632, Mar 2015.

[113] T. P. Grozdanov and M. J. Raković, "Quantum system driven by rapidly varying periodic perturbation," *Phys. Rev. A*, vol. 38, pp. 1739–1746, Aug 1988.

[114] T. Mikami, S. Kitamura, K. Yasuda, N. Tsuji, T. Oka, and H. Aoki, "Brillouin-Wigner theory for high-frequency expansion in periodically driven systems: Application to Floquet topological insulators," *Phys. Rev. B*, vol. 93, p. 144307, Apr 2016.

[115] A. P. Itin and M. I. Katsnelson, "Effective Hamiltonians for Rapidly Driven Many-Body Lattice Systems: Induced Exchange Interactions and Density-Dependent Hoppings," *Phys. Rev. Lett.*, vol. 115, p. 075301, Aug 2015.

[116] S. Rahav, I. Gilary, and S. Fishman, "Effective Hamiltonians for periodically driven systems," *Phys. Rev. A*, vol. 68, p. 013820, Jul 2003.

[117] F. Casas, J. A. Oteo, and J. Ros, "Floquet theory: exponential perturbative treatment," *Journal of Physics A: Mathematical and General*, vol. 34, no. 16, p. 3379, 2001.

[118] M. Born and V. Fock, "Beweis des Adiabatensatzes," *Z. Phys.*, vol. 51, p. 165, 1928.

[119] L. Landau, "Zur Theorie der Energieübertragung II," *Phys. Z. Sowjetunion*, vol. 2, p. 46, 1932.

[120] C. Zener, "Non-Adiabatic Crossing of Energy Levels," *Proc. R. Soc. Lond. A*, vol. 137, p. 696, 1932.

[121] E. C. G. Stueckelberg, "of inelastic collisions between atoms, using two simultaneous differential equations," *Helv. Phys. Acta*, vol. 5, p. 369, 1932.

[122] P. Pfeifer and R. D. Levine, "A stationary formulation of time-dependent problems in quantum mechanics," *The Journal of Chemical Physics*, vol. 79, no. 11, pp. 5512–5519, 1983.

[123] H. P. Breuer and M. Holthaus, "Quantum phases and Landau-Zener transitions in oscillating fields," *Phys. Lett. A*, vol. 140, p. 507, 1989.

[124] U. Peskin and N. Moiseyev, "The solution of the time-dependent Schrödinger equation by the (t,t') method: Theory, computational algorithm and applications," *The Journal of Chemical Physics*, vol. 99, no. 6, pp. 4590–4596, 1993.

[125] J. E. Avron and A. Elgart, "Adiabatic Theorem without a Gap Condition," *Communications in Mathematical Physics*, vol. 203, no. 2, pp. 445–463, 1999.

[126] K. Drese and M. Holthaus, "Floquet theory for short laser pulses," *Eur. J. Phys. D*, vol. 5, p. 119, 1999.

[127] L. D. Landau and E. M. Lifschitz, *Lehrbuch der Theoretischen Physik III — Quantenmechanik*. Berlin: Akademie-Verlag Berlin, 1979.

[128] A. C. Hewson, *The Kondo problem to heavy fermions*, vol. 2. Cambridge university press, 1997.

[129] P. Coleman, *Heavy Fermions: Electrons at the Edge of Magnetism*. John Wiley & Sons, Ltd, 2007.

[130] Q. Si and F. Steglich, "Heavy fermions and quantum phase transitions," *Science*, vol. 329, no. 5996, pp. 1161–1166, 2010.

[131] M. Gulácsi, "The one-dimensional Kondo lattice model at partial band filling," *Advances in Physics*, vol. 53, pp. 769–937, 2004.

[132] M. Lewenstein, A. Sanpera, and V. Ahufinger, *Ultracold Atoms in Optical Lattices: Simulating quantum many-body systems.* Oxford (UK): Oxford University Press, 2012.

[133] E. Haller, R. Hart, M. J. Mark, J. G. Danzl, , L. Reichsöllner, and H.-C. Nägerl, "Inducing Transport in a Dissipation-Free Lattice with Super Bloch Oscillations," *Phys. Rev. Lett.*, vol. 104, p. 200403, 2010.

[134] J. Li, Y. Yu, A. M. Dudarev, and Q. Niu, "Interaction broadening of Wannier functions and Mott transitions in atomic BEC," *New J. Phys.*, vol. 8, p. 154, 2006.

[135] D.-S. Lühmann, K. Bongs, K. Sengstock, and D. Pfannkuche, "Self-Trapping of Bosons and Fermions in Optical Lattices," *Phys. Rev. Lett.*, vol. 101, p. 050402, 2008.

[136] P.-I. Schneider, S. Grishkevich, and A. Saenz, "Ab initio determination of Bose-Hubbard parameters for two ultracold atoms in an optical lattice using a three-well potential," *Phys. Rev. A*, vol. 80, p. 013404.

[137] H. P. Büchler, "Microscopic Derivation of Hubbard Parameters for Cold Atomic Gases," *Phys. Rev. Lett.*, vol. 104, p. 090402, 2010.

[138] K. R. A. Hazzard and E. Mueller, "On-site correlations in optical lattices: Band mixing to coupled quantum Hall puddles," *Phys. Rev. A*, vol. 81, p. 031602(R), 2010.

[139] O. Dutta, A. Eckardt, P. Hauke, B. Malomed, and M. Lewenstein, "Bose–Hubbard model with occupation-dependent parameters," *New J. Phys.*, vol. 13, p. 023019, 2011.

[140] M. Łacki and J. Zakrzewski, "Fast Dynamics for Atoms in Optical Lattices," *Phys. Rev. Lett.*, vol. 110, p. 065301, 2013.

[141] O. Dutta, M. Gajda, P. Hauke, M. Lewenstein, D.-S. Lühmann, B. A. Malomed, T. Sowiński, and J. Zakrzewski, "Non-standard Hubbard models in optical lattices: a review," *Reports on Progress in Physics*, vol. 78, no. 6, p. 066001, 2015.

[142] G. K. Campbell, J. Mun, M. Boyd, P. Medley, A. E. Leanhardt, L. G. Marcassa, D. E. Pritchard, and W. Ketterle, "Imaging the Mott Insulator Shells by Using Atomic Clock Shifts," *Science*, vol. 313, p. 649, 2006.

[143] T. Best, S. Will, U. Schneider, L. Hackermüller, D. van Oosten, I. Bloch, and D.-S. Lühmann, "Role of Interactions in Rb87-K40 Bose-Fermi Mixtures in a 3D Optical Lattice," *Phys. Rev. Lett.*, vol. 102, p. 030408, 2009.

[144] S. Will, T. Best, U. Schneider, L. Hackermüller, D.-S. Lühmann, and I. Bloch, "Time-resolved observation of coherent multi-body interactions in quantum phase revivals," *Nature*, vol. 465, p. 197, 2010.

[145] M. Mark, E. Haller, K. Lauber, J. Danzl, A. Daley, and H. Nägerl, "Precision Measurements on a Tunable Mott Insulator of Ultracold Atoms," *Phys. Rev. Lett.*, vol. 107, p. 175301, 2011.

[146] J. Heinze, S. Götze, J. Krauser, B. Hundt, N. Fläschner, D.-S. Lühmann, C. Becker, and K. Sengstock, "Multiband Spectroscopy of Ultracold Fermions: Observation of Reduced Tunneling in Attractive Bose-Fermi Mixtures," *Phys. Rev. Lett.*, vol. 107, p. 135303, 2011.

[147] O. Jürgensen, F. Meinert, M. J. Mark, H.-C. Nägerl, and D.-S. Lühmann, "Observation of Density-Induced Tunneling," *Phys. Rev. Lett.*, vol. 113, p. 193003, Nov 2014.

[148] A. Isacsson and S. M. Girvin, "Multiflavor bosonic Hubbard models in the first excited Bloch band of an optical lattice," *Phys. Rev. A*, vol. 72, p. 053604, 2005.

[149] C. Wu, W. V. Liu, J. Moore, and S. D. Sarma, "Quantum Stripe Ordering in Optical Lattices," *Phys. Rev. Lett.*, vol. 97, p. 190406, 2006.

[150] C. Wu, "Orbital Ordering and Frustration of p-Band Mott Insulators," *Phys. Rev. Lett.*, vol. 100, p. 200406, 2008.

[151] C. Wu, "Orbital Analogue of the Quantum anomalous Hall Effect in p-Band Systems," *Phys. Rev. Lett.*, vol. 101, p. 186807, 2008.

[152] X. Li, E. Zhao, and W. V. Liu, "Topological states in a ladder-like optical lattice containing ultracold atoms in higher orbital bands," *Nat. Comm.*, vol. 4, p. 1523, 2012.

[153] X. Li, Z. Zhang, and W. V. Liu, "Time-Reversal Symmtry Breaking of p-Orbital Bosons in a One-Dimensional Optical Lattice," *Phys. Rev. Lett.*, vol. 108, p. 175302, 2012.

[154] F. Pinheiro, G. M. Bruun, J.-P. Martikainen, and J. Larson, "XYZ Quantum Heisenberg Models with p-Orbital Bosons," *Phys. Rev. Lett.*, vol. 111, p. 205302, 2013.

[155] T. Müller, S. Fölling, A. Widera, and I. Bloch, "State Preparation and Dynamics of Ultracold Atoms in Higher Lattice Orbitals," *Phys. Rev. Lett.*, vol. 99, p. 200405, 2007.

[156] C. Sias, A. Zenesini, H. Lignier, S. Wimberger, D. Ciampini, O. Morsch, and E. Arimondo, "Resonantly Enhanced Tunneling of Bose-Einstein condensates in Periodic Potentials," *Phys. Rev. Lett.*, vol. 98, p. 120403, 2007.

[157] M. Ölschläger, G. Wirth, and A. Hemmerich, "Unconventional Superfluid Order in the F Band of a Bipartite Optical Square Lattice," *Phys. Rev. Lett.*, vol. 106, p. 015302, 2011.

[158] I. B. Spielman, P. R. Johnson, J. H. Huckans, C. D. Fertig, S. L. Rolston, W. D. Phillips, and J. V. Porto, "Collisional deexcitation in a quasi-two-dimensional degenerate bosonic gas," *Phys. Rev. A*, vol. 73, p. 020702, Feb 2006.

[159] J. Pietraszewicz, T. Sowiński, M. Brewczyk, J. Zakrzewski, M. Lewenstein, and M. Gajda, "Two-component Bose-Hubbard model with higher-angular-momentum states," *Phys. Rev. A*, vol. 85, p. 053638, 2012.

[160] S. Arlinghaus and M. Holthaus, "Generalized acclearation theorem for spatiotemporal Bloch waves," *Phys. Rev. B*, vol. 84, p. 054301, 2011.

[161] S. Arlinghaus and M. Holthaus, "ac Stark shift and multiphotonlike resonances in low-frequency-driven optical lattices," *Phys. Rev. A*, vol. 85, p. 063601, 2012.

[162] T. Sowiński, "Creation on Demand of Higher Orbital States in a Vibrating Optical Lattice," *Phys. Rev. Lett.*, vol. 108, p. 165301, Apr 2012.

[163] S.-L. Zhang and Q. Zhou, "Shaping topological properties of the band structures in a shaken optical lattice," *Phys. Rev. A*, vol. 90, p. 051601, Nov 2014.

[164] W. Zheng, B. Liu, J. Miao, C. Chin, and H. Zhai, "Strong Interaction Effects and Criticality of Bosons in Shaken Optical Lattices," *Phys. Rev. Lett.*, vol. 113, p. 155303, Oct 2014.

[165] S. Choudhury and E. J. Mueller, "Stability of a Floquet Bose-Einstein condensate in a one-dimensional optical lattice," *Phys. Rev. A*, vol. 90, p. 013621, Jul 2014.

[166] M. D. Liberto, C. E. Creffield, G. I. Japaridze, and C. M. Smith, "Quantum simulation of correlated-hopping models with fermions in optical lattices," *Phys. Rev. A*, vol. 89, p. 013624, Jan 2014.

[167] F. Brennecke, S. Ritter, T. Donner, and T. Esslinger, "Cavity Optomechanics with a Bose-Einstein Condensate," *Science*, vol. 322, no. 5899, pp. 235–238, 2008.

[168] K. Huang and C. Yang, "Quantum-Mechanical Many-Body Problem with Hard-Sphere Interaction," *Phys. Rev.*, vol. 105, p. 767, 1956.

[169] G. H. Wannier, "The Structure of Electronic Excitation Levels in Insulating Crystals," *Phys. Rev.*, vol. 52, pp. 191–197, Aug 1937.

[170] G. H. Wannier, "Wave Functions and Effective Hamiltonian for Bloch Electrons in an Electric Field," *Phys. Rev.*, vol. 117, p. 432, 1960.

[171] N. Marzari and D. Vanderbilt, "Maximally localized generalized Wannier functions for composite energy bands," *Phys. Rev. B*, vol. 56, pp. 12847–12865, Nov 1997.

[172] N. Marzari, A. A. Mostofi, J. R. Yates, I. Souza, and D. Vanderbilt, "Maximally localized Wannier functions: Theory and applications," *Rev. Mod. Phys.*, vol. 84, pp. 1419–1475, Oct 2012.

[173] W. Kohn, "Analytic Properties of Bloch Waves and Wannier Functions," *Phys. Rev.*, vol. 115, p. 809, 1959.

[174] M. Abramowitz and I. A. Stegun, *Pocketbook of mathematical functions.* Thun, Frankfurt am Main: Verlag Harri Deutsch, 1984.

[175] A. Eckardt and M. Holthaus, "Avoided level crossing spectroscopy with dressed matter waves," *Phys. Rev. Lett.*, vol. 101, p. 245302, 2008.

[176] I. N. Bronstein, K. A. Semendjajew, G. Musiol, and H. Mühlig, *Taschenbuch der Mathematik.* Frankfurt am Main: Verlag Harri Deutsch, 1997.

[177] M. P. A. Fisher, P. B. Weichman, G. Grinstein, and D. S. Fisher, "Boson localization and the superfluid-insulator transition," *Phys. Rev. B*, vol. 40, p. 546, 1989.

[178] M. Wall and L. Carr *Open Source TEBD, http://physics.mines.edu/downloads/software/tebd*, 2009.

[179] E. Schmidt, "Zur Theorie der linearen und nichtlinearen Integralgleichungen.," *Mathematische Annalen*, vol. 65, pp. 370–399, 1908.

[180] M. Suzuki, "Fractal decomposition of exponential operators with applications to many-body theories and Monte Carlo simulations," *Physics Letters A*, vol. 146, no. 6, pp. 319–323, 1990.

[181] W. Zwerger, "Mott-Hubbard transition of cold atoms in optical lattices," *J. Opt. B: Quantum Semiclass. Opt.*, vol. 5, p. 9, 2003.

[182] N. Elstner and H. Monien, "Dynamics and thermodynamics of the Bose-Hubbard model," *Phys. Rev. B*, vol. 59, p. 12184, 1999.

[183] S. Sachdev, *Quantum Phase Transitions.* Cambridge (UK): Cambridge University Press, 1999.

[184] R. Lim and M. V. Berry, "Superadiabatic tracking of quantum evolution," *J. Phys. A: Math. Gen.*, vol. 24, p. 3255, 1991.

[185] J. Leinaas and J. Myrheim, "On the theory of identical particles," *Il Nuovo Cimento B (1971-1996)*, vol. 37, no. 1, pp. 1–23, 1977.

[186] G. A. Goldin, R. Menikoff, and D. H. Sharp, "Representations of a local current algebra in nonsimply connected space and the Aharonov-Bohm effect," *Journal of Mathematical Physics*, vol. 22, pp. 1664–1668, Aug. 1981.

[187] F. Wilczek, "Quantum Mechanics of Fractional-Spin Particles," *Phys. Rev. Lett.*, vol. 49, pp. 957–959, Oct 1982.

[188] D. C. Tsui, H. L. Stormer, and A. C. Gossard, "Two-Dimensional Magnetotransport in the Extreme Quantum Limit," *Phys. Rev. Lett.*, vol. 48, pp. 1559–1562, May 1982.

[189] G. S. Canright, S. M. Girvin, and A. Brass, "Statistics and flux in two dimensions," *Phys. Rev. Lett.*, vol. 63, pp. 2291–2294, Nov 1989.

[190] R. B. Laughlin, "Anomalous Quantum Hall Effect: An Incompressible Quantum Fluid with Fractionally Charged Excitations," *Phys. Rev. Lett.*, vol. 50, pp. 1395–1398, May 1983.

[191] B. I. Halperin, "Statistics of Quasiparticles and the Hierarchy of Fractional Quantized Hall States," *Phys. Rev. Lett.*, vol. 52, pp. 1583–1586, Apr 1984.

[192] F. E. Camino, W. Zhou, and V. J. Goldman, "Realization of a Laughlin quasiparticle interferometer: Observation of fractional statistics," *Phys. Rev. B*, vol. 72, p. 075342, Aug 2005.

[193] A. Kitaev, "Fault-tolerant quantum computation by anyons," *Annals of Physics*, vol. 303, no. 1, pp. 2 – 30, 2003.

[194] S. Das Sarma, M. Freedman, and C. Nayak, "Topologically Protected Qubits from a Possible Non-Abelian Fractional Quantum Hall State," *Phys. Rev. Lett.*, vol. 94, p. 166802, Apr 2005.

[195] P. Bonderson, A. Kitaev, and K. Shtengel, "Detecting Non-Abelian Statistics in the $\nu = 5/2$ Fractional Quantum Hall State," *Phys. Rev. Lett.*, vol. 96, p. 016803, Jan 2006.

[196] A. Stern and B. I. Halperin, "Proposed Experiments to Probe the Non-Abelian $\nu = 5/2$ Quantum Hall State," *Phys. Rev. Lett.*, vol. 96, p. 016802, Jan 2006.

[197] C. Nayak, S. H. Simon, A. Stern, M. Freedman, and S. D. Sarma, "Non-Abelian anyons and topological quantum computation," *Rev. Mod. Phys.*, vol. 80, p. 1083, 2008.

[198] J. Alicea, Y. Oreg, G. Refael, F. von Oppen, and M. P. Fisher, "Non-Abelian statistics and topological quantum information processing in 1D wire networks," *Nat. Phys.*, vol. 7, no. 5, pp. 412–417, 2011.

[199] A. Stern and N. H. Lindner, "Topological quantum computation—from basic concepts to first experiments," *Science*, vol. 339, no. 6124, pp. 1179–1184, 2013.

[200] J. C. Matthews, K. Poulios, J. D. Meinecke, A. Politi, A. Peruzzo, N. Ismail, K. Wörhoff, M. G. Thompson, and J. L. O'Brien, "Observing fermionic statistics with photons in arbitrary processes," *Scientific reports*, vol. 3, 2013.

[201] F. D. M. Haldane, ""Fractional statistics" in arbitrary dimensions: A generalization of the Pauli principle," *Phys. Rev. Lett.*, vol. 67, pp. 937–940, Aug 1991.

[202] Z. N. C. Ha, "Exact Dynamical Correlation Functions of Calogero-Sutherland Model and One-Dimensional Fractional Statistics," *Phys. Rev. Lett.*, vol. 73, pp. 1574–1577, Sep 1994.

[203] M. V. N. Murthy and R. Shankar, "Thermodynamics of a One-Dimensional Ideal Gas with Fractional Exclusion Statistics," *Phys. Rev. Lett.*, vol. 73, pp. 3331–3334, Dec 1994.

[204] Y.-S. Wu and Y. Yu, "Bosonization of One-Dimensional Exclusons and Characterization of Luttinger Liquids," *Phys. Rev. Lett.*, vol. 75, pp. 890–893, Jul 1995.

[205] J.-X. Zhu and Z. D. Wang, "Topological effects associated with fractional statistics in one-dimensional mesoscopic rings," *Phys. Rev. A*, vol. 53, pp. 600–603, Jan 1996.

[206] L. Amico, A. Osterloh, and U. Eckern, "One-dimensional XXZ model for particles obeying fractional statistics," *Phys. Rev. B*, vol. 58, no. 4, p. R1703, 1998.

[207] A. Kundu, "Exact Solution of Double δ Function Bose Gas through an Interacting Anyon Gas," *Phys. Rev. Lett.*, vol. 83, pp. 1275–1278, Aug 1999.

[208] M. T. Batchelor, X.-W. Guan, and N. Oelkers, "One-Dimensional Interacting Anyon Gas: Low-Energy Properties and Haldane Exclusion Statistics," *Phys. Rev. Lett.*, vol. 96, p. 210402, Jun 2006.

[209] M. D. Girardeau, "Anyon-Fermion Mapping and Applications to Ultracold Gases in Tight Waveguides," *Phys. Rev. Lett.*, vol. 97, p. 100402, Sep 2006.

[210] P. Calabrese and M. Mintchev, "Correlation functions of one-dimensional anyonic fluids," *Phys. Rev. B*, vol. 75, p. 233104, Jun 2007.

[211] A. del Campo, "Fermionization and bosonization of expanding one-dimensional anyonic fluids," *Phys. Rev. A*, vol. 78, p. 045602, Oct 2008.

[212] Y. Hao, Y. Zhang, and S. Chen, "Ground-state properties of one-dimensional anyon gases," *Phys. Rev. A*, vol. 78, p. 023631, Aug 2008.

[213] Y. Hao, Y. Zhang, and S. Chen, "Ground-state properties of hard-core anyons in one-dimensional optical lattices," *Phys. Rev. A*, vol. 79, p. 043633, Apr 2009.

[214] Y. Hao and S. Chen, "Dynamical properties of hard-core anyons in one-dimensional optical lattices," *Phys. Rev. A*, vol. 86, p. 043631, Oct 2012.

[215] L. Wang, L. Wang, and Y. Zhang, "Quantum walks of two interacting anyons in one-dimensional optical lattices," *Phys. Rev. A*, vol. 90, p. 063618, Dec 2014.

[216] G. Tang, S. Eggert, and A. Pelster, "Ground-state properties of anyons in a one-dimensional lattice," *New J. Phys.*, vol. 17, p. 123016, 2015.

[217] W. Zhang, E. Fan, T. C. Scott, and Y. Zhang, "Beats, broken-symmetry superfluid on a one dimensional anyon Hubbard model," *arXiv*, vol. cond-mat, p. 1511.01712, 2015.

[218] A. Bermudez and D. Porras, "Interaction-dependent photon-assisted tunneling in optical lattices: a quantum simulator of strongly-correlated electrons and dynamical Gauge fields," *New J. Phys.*, vol. 17, p. 103021, 2015.

[219] J. Gong, L. Morales-Molina, and P. Hänggi, "Many-Body Coherent Destruction of Tunneling," *Phys. Rev. Lett.*, vol. 103, p. 133002, Sep 2009.

[220] T. Wang, X.-F. Zhang, F. E. A. d. Santos, S. Eggert, and A. Pelster, "Tuning the quantum phase transition of bosons in optical lattices via periodic modulation of the *s*-wave scattering length," *Phys. Rev. A*, vol. 90, p. 013633, Jul 2014.

[221] J. Friedel, "Metallic alloys," *Nuovo Cimento*, vol. 7, p. 287, 1958.

[222] G. Griiner, "Density waves in solids," *Front. Phys*, vol. 89, 1994.

[223] B. Dóra, "Boundary effect on CDW: Friedel oscillations, STM image," *EPL*, vol. 70, no. 3, p. 362, 2005.

[224] B. Paredes, A. Widera, V. Murg, O. Mandel, S. Fölling, I. Cirac, G. V. Shlyapnikov, T. W. Hänsch, and I. Bloch, "Tonks-Girardeau gas of ultracold atoms in an optical lattice," *Nature*, vol. 429, p. 277, 2004.

[225] R. Islam, R. Ma, P. M. Preiss, M. E. Tai, A. Lukin, M. Rispoli, and M. Greiner, "Measuring entanglement entropy through the interference of quantum many-body twins," *Nature*, vol. 528, p. 77, 2015.

[226] P. M. Preiss, R. Ma, M. E. Tai, J. Simon, and M. Greiner, "Quantum gas microscopy with spin, atom-number, and multilayer readout," *Phys. Rev. A*, vol. 91, p. 041602, Apr 2015.

[227] S. Baier, M. J. Mark, D. Petter, K. Aikawa, L. Chomaz, Z. Cai, M. Baranov, P. Zoller, and F. Ferlaino, "Extended Bose-Hubbard models with ultracold magnetic atoms," *Science*, vol. 352, no. 6282, pp. 201–205, 2016.

[228] M. Bukov, L. D'Alessio, and A. Polkovnikov, "Universal High-Frequency Behavior of Periodically Driven Systems: from Dynamical Stabilization to Floquet Engineering," *Adv. in Phys.*, vol. 64, p. 139, 2015.

[229] D. Poletti and C. Kollath, "Slow quench dynamics of periodically driven quantum gases," *Phys. Rev. A*, vol. 84, p. 013615, 2011.

[230] M. Genske and A. Rosch, "Floquet-Boltzmann equation for periodically driven Fermi systems," *Phys. Rev. A*, vol. 92, p. 062108, Dec 2015.

[231] T. Bilitewski and N. R. Cooper, "Scattering theory for Floquet-Bloch states," *Phys. Rev. A*, vol. 91, p. 033601, Mar 2015.

[232] T. Bilitewski and N. R. Cooper, "Population dynamics in a Floquet realization of the Harper-Hofstadter Hamiltonian," *Phys. Rev. A*, vol. 91, p. 063611, Jun 2015.

[233] E. Canovi, M. Kollar, and M. Eckstein, "Stroboscopic prethermalization in weakly interacting periodically driven systems," *Phys. Rev. E*, vol. 93, p. 012130, Jan 2016.

[234] K. Drese and M. Holthaus, "Ultracold atoms in modulated standing light waves," *Chem. Phys.*, vol. 217, p. 201, 1997.

[235] M. Holthaus, "Floquet engineering with quasienergy bands of periodically driven optical lattices," *J. Phys. B: At. Mol. Opt. Phys.*, vol. 49, p. 013001, 2015.

[236] S. Choudhury and E. J. Mueller, "Transverse collisional instabilities of a Bose-Einstein condensate in a driven one-dimensional lattice," *Phys. Rev. A*, vol. 91, p. 023624, Feb 2015.

[237] M. Reitter, J. Näger, K. Wintersperger, C. Sträter, I. Bloch, A. Eckardt, and U. Schneider, "Interaction Dependent Heating and Atom Loss in a Periodically Driven Optical Lattice," *Phys. Rev. Lett.*, vol. 119, p. 200402, Nov 2017.

[238] A. Eckardt, "Zum Mott-Übergang im Bose-Hubbard-Modell: Kritische Parameter und kohärente Kontrolle," *PhD thesis, Universität Oldenburg, Fakultät für Mathematik und Naturwissenschaften*, 2007.

[239] S. H. Autler and C. H. Townes, "Stark Effect in Rapidly Varying Fields," *Phys. Rev.*, vol. 100, pp. 703–722, Oct 1955.

[240] C. N. Cohen-Tannoudji, "The Autler-Townes effect revisited," in *Amazing Light*, pp. 109–123, Springer, 1996.